Numerical simulation of depth-averaged flow models : a class of Finite Volume and discontinuous Galerkin approaches.

Arnaud Duran

Collège Doctoral du Languedoc-Roussillon

THÈSE

Pour obtenir le grade de

Docteur

Délivré par l'**Université Montpellier II**

Préparée au sein de l'école doctorale **I2S**
Et de l'unité de recherche **I3M - ACSIOM**

Spécialité: **Mathématiques Appliquées**

Présentée par **Arnaud Duran**

Numerical simulation of depth-averaged flow models : a class of Finite Volume and discontinuous Galerkin approaches.

Soutenue le 17 octobre 2014 devant le jury composé de

M. Pascal AZERAD	Maître de Conférences, *Université Montpellier II*	Co-directeur de thèse
M. Christophe BERTHON	Professeur des Universités, *Université de Nantes*	Examinateur
M. Daniele DI-PIETRO	Professeur des Universités, *Université Montpellier II*	Examinateur
M. Jean-Luc GUERMOND	Professeur des Universités, *Texas A& M University*	Rapporteur
M. Fabien MARCHE	Maître de Conférences, *Université Montpellier II*	Co-directeur de thèse
M. Nicolas SEGUIN	Maître de Conférences, *Laboratoire J.-L. Lions*	Rapporteur
M. Jean-Paul VILA	Professeur des Universités, *INSA Toulouse*	Examinateur

UNIVERSITÉ MONTPELLIER 2
SCIENCES ET TECHNIQUES

ABSTRACT

This work is devoted to the development of numerical schemes to approximate solutions of depth averaged flow models.

We first detail the construction of Finite Volume approaches for the *Shallow Water* system with source terms on unstructured meshes. Based on a suitable reformulation of the equations, we implement a well-balanced and positive-preserving approach, and suggest adapted MUSCL extensions. The method is shown to handle irregular topography variations and demonstrates strong stabilities properties. The inclusion of friction terms is subject to a thorough analysis, leading to the establishment of some *Asymptotic Preserving* property through the enhancement of another recent Finite Volume scheme.

The second aspect of this study concerns discontinuous Galerkin Finite-Element methods. Some of the ideas advanced in the Finite Volume context are employed to broach the *Shallow Water* system on triangular meshes. Numerical results are exposed and the method turns out to be well suited to describe a large variety of flows. On these observations we finally propose to exploit its features to extend the approach to a new family of *Green-Nadghi* equations. Numerical experiments are also proposed to validate this numerical model.

Keywords : Shallow Water, Depth averaged models, Well balanced methods, Finite Volume methods, Discontinuous Galerkin methods, Source terms, High order schemes.

RESUME

Ce travail est consacré au développement de schémas numériques pour approcher les solutions de modèles d'écoulement type "*depth averaged*".

Dans un premier temps nous détaillons la construction d'approches Volumes Finis pour le système *Shallow Water* avec termes sources sur maillages non structurés. En se basant sur une reformulation appropriée des équations, nous mettons en place un schéma équilibré et préservant la positivité de la hauteur d'eau, et suggérons des extensions MUSCL adaptées. La méthode est capable de gérer des topographies irrégulières et exhibe de fortes propriétés de stabilité. L'inclusion des termes de friction fait l'objet d'une analyse poussée, aboutissant à l'établissement d'une propriété type "*Asymptotic Preserving*" à travers l'amélioration d'un autre récent schéma Volumes Finis.

La seconde composante de cette étude concerne les méthodes Elements Finis type Galerkin discontinu. Certaines des idées avancées dans le contexte Volumes Finis sont employées pour aborder le système *Shallow Water* sur maillages triangulaires. Des résultats numériques sont exposés et la méthode se révèle bien adaptée à la description d'une large variété d'écoulements. Partant de ces observations nous proposons finalement d'exploiter ces caractéristiques pour étendre l'approche à une nouvelle famille d'équations type *Green-Nadghi*. Des validations numériques sont également proposées pour valider le modèle numérique.

Mots clés : Shallow Water, Modèles type *depth averaged*, Schémas équilibrés, Méthodes Volumes Finis, Méthodes Galerkin Discontinu, Termes source, Schémas d'ordre élevé.

Contents

Remerciements

Ces travaux de thèse ont été effectués à l'Université Montpellier II, au sein de l'Equipe ACSIOM de l'Institut de Mathématiques et de Modélisation de Montpellier.

Mes premières pensées se dirigent naturellement vers Fabien Marche, qui a encadré ces travaux. Pouvoir s'appuyer sur quelqu'un d'aussi compétent, sincère et agréable est quelque chose de rare. Sur bien des plans ces trois années n'ont pas été évidentes, et Fabien a toujours su se rendre disponible pour m'apporter une aide précieuse et parfaitement dosée. A l'issue de ces travaux je réalise sans doute un peu plus quelle a été ma chance de travailler avec lui. Cette collaboration m'a énormément apporté, tant sur un plan scientifique que sur un plan humain.

Je tiens aussi à remercier chaleureusement Pascal Azerad pour son soutien et son implication dans la mise en place de mon parcours scientifique. Ses conseils avisés m'ont été d'une grande utilité. J'ai, par ailleurs, eu la chance de l'avoir comme enseignant, et il n'est certainement pas étranger aux motivations qui m'ont poussé à poursuivre dans le domaine de l'analyse numérique et du calcul scientifique.

Je voudrais exprimer mes plus sincères remerciements à Jean-Luc Guermond et Nicolas Seguin pour m'avoir fait l'honneur d'être les rapporteurs de cette thèse. Leurs conseils ont permis d'améliorer considérablement la qualité de ce travail. Outre la précision de leurs remarques sur les aspects techniques et généraux, j'ai pu m'inspirer de leur recul et de leur appréhension du domaine pour initier un réel questionnement sur mon travail.

J'aimerais ensuite témoigner ma gratitude à Daniele Di-Pietro pour avoir accepté de participer à ce jury. Ces dernières années, j'ai eu la chance de pouvoir bénéficier de sa présence au laboratoire et prendre la mesure de ses immenses connaissances sur les méthodes employées dans ce travail, que ce soit à travers son livre, ou bien directement par l'acuité de ses observations et la pertinence de ses remarques.

A bien des égards, les compétences scientifiques de Christophe Berthon ont joué un rôle décisif au cours de ces années. Bien que nos entretiens n'aient pas été nombreux, ses idées lumineuses ont systématiquement permis de

grandes avancées dans mes travaux. Il n'a pas non plus hésité à m'apporter son soutien lorsque c'était nécessaire. Un grand merci donc.

A cette occasion, je voudrais associer Rodolphe Turpault à ces remerciements pour son investissement au cours de notre collaboration. Il s'est toujours montré disponible pour me conseiller et me faire partager ses connaissances, et je veux le saluer pour sa patience et la clarté de ses explications.

J'adresse un grand merci Jean-Paul Vila pour être présent dans ce jury. Je lui suis profondément reconnaissant de m'avoir fait confiance en me donnant la chance d'intégrer son équipe l'année prochaine. Je veux joindre Florent Chazel à ces pensées, pour son aide, pour son soutien, pour m'avoir offert la possibilité d'exposer mes travaux et son accueil chaleureux au sein du laboratoire.

Intégrer l'équipe INRIA Lemon m'a permis de riches rencontres et l'entretien d'une activité très épanouissante. Merci donc à Antoine Rousseau, qui emploie un dynamisme inépuisable au sein de cette équipe, pour m'avoir permis, avec Fabien, de prendre part au projet.

Je tiens à saluer l'efficacité et la bienveillance de Bernadette Lacan, qui a dû développer des trésors de patience et de compréhension pour m'accompagner dans mes tâches administratives. Un grand merci à Sophie Cazanave, Nathalie Quintin et Myriam Debus, qui s'occupent aussi d'une manière admirable des membres de l'équipe. J'adresserai une pensée particulière à Baptiste, toujours disponible, efficace et de bonne humeur, ainsi qu'à Eric pour son sourire, son dynamisme et sa profonde gentillesse. Nos folles virées de course à pied vont assurément me manquer.

Pour avoir réussi à me supporter durant ces trois années, je voudrais rendre hommage à ceux qui ont eu l'immense privilège de partager mon bureau, Christian, Myriam, Guillaume, et plus récemment Jérémie. Travailler à leurs côtés fut un réel plaisir, et je tiens à les remercier pour avoir apporté cette alchimie idéale entre bonne humeur et travail. Je n'oublierai pas non plus mes autres "copains" et "copines" du laboratoire, notamment Christophe, Mickaël, Guillaume, Gautier, Joubine, Etienne, Elsa, sans qui ces dernières années n'auraient sans doute pas été aussi drôles et agréables. Je rajouterai enfin Vanessa, de peur qu'elle ne m'en veuille si elle n'est pas mentionnée!

Mes amis de longue date ont tous, à leur manière, contribué à l'aboutissement de ces travaux. Leur présence a été d'un grand secours dans les nombreux moments de doute. Un grand merci à Jo, Adeline, Ben, Anne, Vinche, Alex, Charlotte, Céline qui ont toujours su être là pour me transmettre leur enthousiasme et leur confiance. Un merci particulier à Alain et Caro pour avoir été présents ces dernières semaines, délicates. Un soutien précieux. Je tiens aussi à saluer Kévin, Mathieu et Sébastien et compte sur eux pour m'accompagner dans ma future aventure Toulousaine. J'en viens ensuite à Yohan, qui, au delà de ses aptitudes à savoir me soutenir (à sa manière) dans la difficulté, a su trouver le

temps pour m'aider sur des points techniques, notamment en ce qui concerne mes aptitudes à programmer, quasi nulles au départ. Enfin, une tendre pensée à Nancy, dont le courage a été mis à rude épreuve ces derniers mois.

Mon frère Guillaume reste un modèle, sur tous les plans. Je le remercie d'être à mes côtés pour me montrer la voie, et lui souhaite d'être heureux avec Sophie et Léon dans sa toute nouvelle vie à trois. Il est pour moi difficile d'exprimer toute la dimension de la gratitude ressentie envers mes parents. Je vois leur aide permanente et inconditionnelle comme une chance inouie, appui sans lequel il m'aurait été impossible de mener ces travaux à terme.

Je veux enfin adresser mes dernières pensées à mon grand père, Louis Duran, décédé le 30 mars 2006. Peu d'occasions me sont offertes d'exprimer ma profonde admiration à son égard ainsi que l'extrême reconnaissance pour la richesse de l'héritage moral qu'il nous a légué. Il reste pour moi une référence et son exemple m'inspire constamment dans les moments difficiles.

Je lui dois l'aboutissement de cette thèse. Ce travail, c'est le sien.

Introduction Générale

L'étude des phénomènes d'évolution hydrodynamiques multidimensionnels représente aujourd'hui un enjeu scientifique de grande importance à plusieurs niveaux. L'étendue des applications possibles, couplée à la richesse des problématiques qui sont soulevées, suscite un intérêt croissant et mobilise ainsi un grand nombre de chercheurs. De nos jours, la nécessité d'une description précise et efficace de tels mécanismes est indissociable de domaines clés tels que l'hydrodynamique côtière et l'ingénierie hydraulique, avec l'analyse de rupture de barrages, de phénomènes de crues dans les lits de rivière, l'étude des tsunamis, et leur impact possible sur les populations et les infrastructures. Sur un plan scientifique, les difficultés posées par la modélisation et la simulation de tels problèmes sont de taille. La complexité persistante des mécanismes mis en jeu engendre une quantité de contraintes numériques qui, couplées aux éventuelles astreintes directement liées au domaine d'étude (géométrie, dimensions, changements d'échelle...), poussent à opter pour des équations simplifiées, permettant, sous certaines hypothèses d'échelle, d'obtenir des résolutions réalistes tout en allégeant les efforts d'implémentation. En particulier, c'est ici qu'interviennent les modèles type "depth-averaged", obtenus en intégrant les équations de Navier-Stokes selon la verticale afin de se ramener à un problème d'écoulement à surface libre bi-dimensionnel.

Parmi les équations appartenant à ce type de modèle, nous nous intéresserons majoritairement dans ces travaux aux équations de Saint Venant [87], dont nous donnerons la formulation et étudierons les principales caractérisiques dans le premier chapitre. Elles expriment la dynamique des eaux dites *peu profondes* (la terminologie *Shallow Water* est d'ailleurs couramment employée), c'est à dire sous l'hypothèse que la profondeur totale de la couche de fluide est petite par rapport à la longueur d'onde caractéristique. Jouissant d'une formulation simple et d'un domaine de validité relativement large, ces équations sont très fréquemment utilisées pour étudier la circulation des masses d'eau dans les océans et les rivières, et s'invitent de surcroît dans une multitude d'autres secteurs, avec entre autres, des applications pratiques aux problèmes de transport de polluant ou de sédiments, aux avalanches, ou encore à l'analyse du ruissellement d'eau de pluie dans les bassins agricoles.

Parmi les objectifs principaux visés dans cette thèse figure la mise en place

de modèles numériques pour approcher de manière efficace les solutions de ces équations. En vue d'applications à des situations réelles, nous choisissons de profiter des atouts que peuvent présenter les maillages non structurés vis à vis de géométries complexes, avec la possibilité d'affiner les résolutions dans des zones d'intérêt bien précises. La contrepartie majeure de cette stratégie réside sans doute dans un effort d'analyse et de conception plus important que dans le cadre de grilles cartésiennes. En réalité, ces aspects canalisent presque à eux seuls les motivations principales à l'origine de ces travaux, en ce sens que la construction des schémas proposés visera majoritairement à étendre des approches mono-dimensionnelles à des maillages généraux. Cet exercice s'avère en effet plus délicat que sur maillages cartésiens, où le schéma 1d peut être directement intégré dans les deux directions privilégiées.

S'agissant des méthodes numériques, il convient de mentionner que le système de Saint-Venant est un système de loi de conservation hyperbolique, que nous aborderons dans un premier temps par la voie classique des Volumes Finis. Présentant des facilités de mise en oeuvre et un faible coût calculatoire, cette approche est communément utilisée pour ce type d'EDP, car elle permet en outre une gestion naturelle des chocs via la résolution de problèmes de Riemann aux interfaces, et peut tolérer une certaine latitude par rapport à l'inclusion des termes sources. A cet égard, la prise en compte des variations du fond et des effets de friction fera l'objet d'une attention particulière.

En second lieu, et avec l'objectif de gagner en précision notamment, nous présenterons une méthode Eléments-Finis type Galerkin discontinu (dG) pour ce même système. Ce schéma s'inspire du contexte précédent mais l'on se trouve confronté à de nouvelles difficultés numériques, inhérentes à la montée en ordre. Ces différents points seront abordés en détail et des outils de résolution seront proposés. Enfin, bien qu'il soit légèrement moins simple, dans ce cadre, de satisfaire l'ensemble des propriétés demandées à un schéma type *Shallow Water* moderne, l'exploration de telles méthodes numériques s'est révélée prometteuse pour des problèmes obéissant à des lois plus complexes. Dans la pratique en effet, l'approche dG s'est montrée adaptée pour intégrer les termes dispersifs dans le modèle mathématique. Nous en arrivons ainsi à traiter un modèle d'écoulement type Green Naghdi, plus riche, permettant d'étendre la portée des applications à des eaux plus profondes.

La présentation de ces travaux s'articule autour de 5 chaptires. A l'exception du premier, ayant une dimension introductive, chacun d'entre eux détaillera la construction d'une méthode numérique destinée à répondre à des objectifs spécifiques, et s'ouvrira sur une description précise des motivations et enjeux liés à ces orientations. Les schémas obtenus seront systématiquement évalués à travers une série de validations numériques. Une grande variété de cas

tests seront ainsi proposés, permettant d'aborder une multitude de contextes.

CHAPITRE I

Cette partie préliminaire est destinée à une présentation des équations de Saint-Venant. Nous partons d'une approche Volumes Finis classique sur un maillage type *vertex-centered* pour étudier leur strucure et les spécificités liées à ce type de support géométrique. La résolution se base en réalité sur la considération de problèmes de Riemann 1d dans chacune des directions propres aux arêtes et à cet effet nous donnons quelques rappels sur les solveurs de Riemann. Nous abordons ensuite d'autres points clés tels que le problème des conditions aux limites et la sélection du pas de temps. Enfin, nous énumérons les principales contraintes spécifiques à ces équations, à savoir la préservation des états d'équilibre, la préservation de la positivité de la hauteur d'eau et la gestion des zones sèches, et dressons un inventaire des techniques ayant été introduites pour les intégrer au sein d'un modèle numérique, notamment sur ce type de maillage.

CHAPITRE II

Nous choisissons ici d'envisager les équations de Saint-Venant sous un angle légèrement différent, en changeant de variable conservative. Sous leur forme classique, la hauteur d'eau est liée au débit via les équations de conservation de la masse et de la quantité de mouvement. Ici, nous faisons le choix de substituer l'élévation totale de la surface libre à la hauteur d'eau. Cette option a pour avantage de ne pas modifier la structure des équations et d'offir un cadre de travail adapté au problème de la préservation des états d'équilibre. Ces aspects pratiques sont exploités dans la conception d'un premier modèle numérique. La seconde ligne de travail concerne l'introduction de méthodes d'ordre élevé. A l'issue d'une brève présentation générale, nous proposons la mise en place de deux méthodes MUSCL en veillant à ne pas détériorer les propriétés d'origine du schéma de premier ordre. Nous présentons en particulier un résultat général de stabilité pour ces reconstrutions.

CHAPITRE III

La popularité des équations de Saint-Venant est en partie expliquée par l'amplitude de son champ d'applications, à travers l'inclusion de termes sources additionnels notamment. S'il est parfois possible de les incorporer sans trop de difficultés aux modèles numériques, la prise en compte des forces de résistance se révèle plus compliquée. Il s'agit là d'un aspect important car les lois de friction tiennent compte des caractéristiques physiques et mécaniques des domaines

d'étude et jouent à ce titre un rôle de premier plan dans la majorité des configurations réalistes. Nous développons ainsi une méthode permettant d'inclure ces termes de manière appropriée, en particulier sans altérer la stabilité de l'approche Volumes Finis précédemment introduite. Dans un second temps nous tentons d'apporter certains élements de réponse quant au problème de la prise en compte du comportement en temps long observé par les équations continues. Plus précisément, l'objectif est de développer une nouvelle approche Volumes Finis permettant de respecter au niveau discret le régime asymptotique du système soumis aux lois de résistance. Il en résulte un schéma type "*Asymptotic Preserving*", dont nous étudions les caractéristiques et les différences avec les approches traditionnelles. Dans des contextes précis, ces disparités peuvent devenir réellement significatives. Notons qu'à l'heure actuelle, il semblerait qu'une telle piste n'ait pas encore été explorée dans le contexte 2d non structuré. Néanmoins, les premiers résultats numériques se montrent en accord avec certains travaux menés en 1d.

CHAPITRE IV

Le reste de ces travaux est consacré aux méthodes Galerkin discontinu. Nos premiers efforts se sont dirigés vers une approche du système sur maillages triangulaires. Ici, nous proposons également de remplacer la hauteur d'eau par la surface libre, de sorte que la stratégie développée peut s'interpréter comme une extension du schéma Volumes Finis introduit dans le Chapitre II à un ordre arbitraire. Le modèle est discrétisé en utilisant une base d'expansion nodale. Bien que la préservation des équilibres statiques soit encore automatique, et ce indépendamment du degré du polynôme d'approximation, des nouveaux enjeux émergent avec le contrôle des effets déstabilisants des modes élevés, nécessitant l'introduction de procédés de limitation adaptés, ou encore la préservation de la positivité de la hauteur d'eau. Cette dernière propriété sera assurée en s'inspirant de techniques récentes basées sur le principe du maximum et des règles de quadratures adéquates. A l'occasion de la partie expérimentale, nous explorons plusieurs situations d'intérêt permettant d'apprécier la robustesse et la précision de cette approche, et évaluons entre autres les performances relatives des méthodes Volumes Finis MUSCL et dG d'ordre 2.

CHAPITRE V

La qualité des résultats numériques obtenus atteste la capacité de la méthode à gérer des géométries complexes et les contraintes numériques propres au système de Saint-Venant. Ceci étant, les méthodes dG se montrent aussi efficaces dans l'évaluation des dérivées d'ordre élevé. Exploitant ces caractéristiques, dans la dernière partie nous décrivons une extension du schéma précédent pour approximer les solutions d'une nouvelle famille de modèles Green-Naghdi. Nous visons ainsi à augmenter l'applicabilité de la méthode aux équations dispersives, dans

l'optique de décrire des écoulements de nature plus complexe. Les équations type Green-Naghdi sont plus complètes et réquisitionnent naturellement plus d'efforts en termes d'implémentation et de coût calculatoire. Gardant ceci à l'esprit, nous entendons travailler sur des nouveaux modèles plus efficaces sur ces plans, tout en étant asymptotiquement équivalents à la formulation initiale. La nouveauté tient dans la formulation de l'opérateur elliptique agissant sur le système, pour lequel la dépendance en temps est révoquée, offrant ainsi des gains importants en terme de temps de calcul. Nous devons préciser ici qu'en dépit d'une plus grande précision, ces équations en l'état ne peuvent être utilisées pour décrire le déferlement des vagues, contrairement au modèle de Saint-Venant pour lequel il est possible d'exploiter l'aptitude naturelle à la capture des chocs. Nous proposons donc un procédé numérique simple pour la gestion du déferlement, basé sur un détecteur de forts gradients pour délimiter des zones de transition entre ces deux modèles.

Chapter I

Focus on the Shallow Water system

I.1 Introduction

The description of hydrodynamic processes is present in a wide variety of scientific fields such as coastal oceanography, river modelling or hydraulic engineering. From a practical point of view, the simulation of tsunami waves, dam break problems or pollutant transport in high density population regions for example has become a major concern in hydraulic urbanism. This motivates the introduction of numerical tools providing accurate descriptions of these phenomena, which are notably able to handle correctly partly dry domains, irregular bottom variations and complicated geometries, and computationally efficient in the perspective of large scale applications.

A quite simple and relevant model for such environmental flows is provided by the well known system of Non linear Shallow Water equations (NSW). This system expresses the dynamic of a free surface shallow layer of homogeneous incompressible fluid. It is used to describe vertically averaged flows in terms of horizontal velocity and depth variation. Historically, the physical model was first proposed by de Saint Venant in 1871 ([87]), obtained from asymptotic analysis and indeed depth-averaging the Navier-Stokes equations (see also [122, 210]). In practice, the model is truly well-suited for the simulation of geophysical phenomena, such as river and oceanic flows. It is also extensively used in coastal engineering, for the study of nearshore flows involving run-up and run-down on sloping beaches or coastal structures. Under its conservative form, the NSW equations consist of a set of PDE's involving the total water height h and the discharge $\mathbf{q} = {}^t(q_x, q_y)$ as vector variable. In a 2d context, denoting z the bottom height and $\mathbf{u} = {}^t(u, v)$ the velocity vector, these equations are commonly written as follows :

$$\frac{\partial U}{\partial t} + \nabla \cdot G(U) = B(U, z)\,, \tag{I .1}$$

with

$$U = \begin{pmatrix} h \\ q_x \\ q_y \end{pmatrix}\ ,\ G(U) = \Big(G^1(U), G^2(U)\Big) = \begin{pmatrix} q_x & q_y \\ uq_x + \dfrac{1}{2}gh^2 & vq_x \\ uq_y & vq_y + \dfrac{1}{2}gh^2 \end{pmatrix}, \tag{I .2}$$

and the topography source term defined by :

$$B(U, z) = \begin{pmatrix} 0 \\ -gh\partial_x z \\ -gh\partial_y z \end{pmatrix}\ , \tag{I .3}$$

A sketch of a 1d configuration is proposed in Fig. I .1, where we also define the new variable η as the total free surface (i.e. $\eta = h + z$). In what follows,

$$\Theta := \{(h, \mathbf{q})\,,\ h \geq 0\}\,. \tag{I .4}$$

will denote the convex set of admissible states.

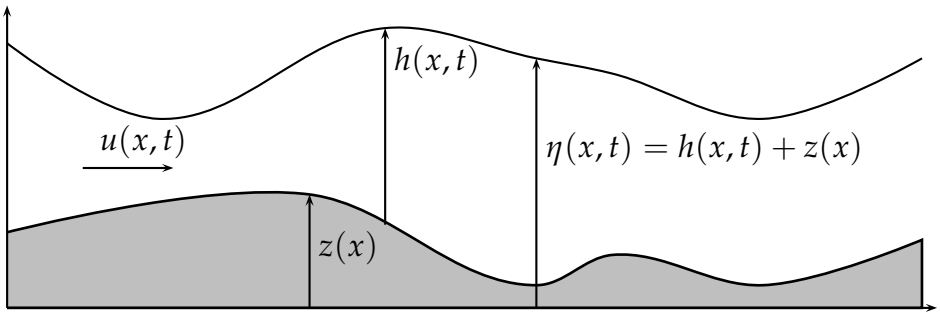

Figure I .1: Non conservative variables for NSW equations.

Note that in equations (I .1), some minor physical effects have been consciously neglected, as the source terms related to the wind or rainfall contribution for instance. Formulations taking such phenomena into account can be found in [63, 73, 89], or even [91], where a new Shallow Water model is introduced, including viscosity. In this work, we also choose to set the Coriolis force to zero ; numerical investigations shown that their impact was insignificant within the considered scales. The inclusion of such long scale physical effects is performed in [5, 32, 41, 73, 144, 200] for instance. As for the inclusion of resistance terms, an entire part will be devoted to this subject (Chapter III).

More specifically, since years, a growing number of theoretical and numerical investigations are run by the scientific community in order to develop suitable approximations for weak solutions of the Shallow Water system. The NSW equations being part of the wide family of hyperbolic systems of conservation laws, our work naturally follows the general orientations issuing from the analysis and resolution of such class of problems (see [39, 128, 130, 131, 189, 188] for some reference studies). These works generally emphasize on the performances of Finite Volume Methods, often preferred for their natural ability in capturing shocks, and an interesting latitude regarding the treatment of convective fluxes and source terms. In addition of the necessity of handling shocks that may arise from their hyperbolic structure, several additional concerns have to be taken into account when seeking approximations of these equations. In this connexion, the central issues of steady states preservation, conservation of positive water heights, and occurrence of dry cells will be addressed in detail.

In the same time, it is worth mentioning the recent interest of some applied scientists, in oceanography or hydraulic for instance, for the unstructured meshes discretizations, allowing natural refinement possibilities and a great versatility with respect to the geometry of the computational domain. One of the major motivations of this work is driven by the challenging objective of proposing efficient methods on general meshes in view of real life applications, where such a capacity to adapt may be of broad interest.

This preliminary chapter aims at giving an overall presentation of the NSW equations, simultaneously oriented toward the specificities of unstructured meshes and the well-established numerical concerns unique to the model. Through the consideration of a trivial Finite Volume approach of the homogeneous equations, we first introduce general notations and propose some recalls on the characteristics theory and Riemann problems. We then detail the set of Riemann solvers employed in our numerical experiments. In Section §I.4 we make an inventory of some techniques for the treatment of boundary conditions. After having discussed about the time step criterion, we end by a survey on well balanced and positive preserving Finite Volume Methods (FVM) for the NSW equations.

I.2 Finite Volume Method on unstructured meshes

We give here the general outlines relative to the Finite Volume formalism on unstructured meshes. The notations introduced here will be reused throughout the different chapters. Let $\mathcal{T}$ be a partition of the computational domain Ω. For the sake of simplicity, it is assumed that Ω is a polygonal domain in two space dimensions, so that $\mathcal{T}$ covers Ω exactly. To illustrate the problem, we consider the dual cells $(C_i)_{i\in\mathbb{Z}}$ issuing from $\mathcal{T}$, but all the subsequent notations and developments can of course be adapted to the *cell-centered* mesh directly extracted from the initial triangulation. We refer to Chapter IV for a construction based on triangular meshes. Let $\mathbf{x}$ refer to the (x, y) coordinates in Ω. Denoting by $(M_i)_{i\in\mathbb{Z}}$ the nodes of $\mathcal{T}$, we set (see Fig. I .2) :

- $\Lambda(i)$: number of triangles surrounding M_i.
- $j(k)$: the index of the cell $C_{j(k)}$ neighboring C_i, for each $k \in \{1, \dots, \Lambda(i)\}$.
- $K(i)$: set of subscripts k for which $C_{j(k)}$ is adjacent to C_i (that is : $K(i) = \{1\,, \cdots\,, \Lambda(i)\}$).
- $|C_i|$: area of C_i.
- Γ_{ij} : boundary interface defined by C_i and C_j.
- ℓ_{ij} : length of Γ_{ij}.
- $\vec{n}_{ij}$: unit normal to Γ_{ij}, pointing to C_j.
- $\mathfrak{d}_i$: diameter of C_i.
- $\mathfrak{p}_i$: perimeter of C_i.
- $T_{ij(k)}$: triangle defined by the edge $\Gamma_{ij(k)}$ and the node M_i.

The starting point of our investigations concerns the case of a flat bottom. Denoting U_i a piecewise constant interpolation of the weak solution of (I .1) on the cell C_i, we classically obtain a semi-discrete Finite Volume formulation by integrating by part over a cell C_i :

$$|C_i|\frac{d}{dt}U_i + \sum_{k=1}^{\Lambda(i)} \int_{\Gamma_{ij(k)}} G(U).\vec{n}_{ij(k)}\, ds = 0\,. \tag{I .5}$$

Written at time level t^n, a numerical scheme associated with (I .5) takes the form :

$$|C_i|\frac{d}{dt}U_i + \sum_{k=1}^{\Lambda(i)} \ell_{ij(k)}\mathcal{G}_{ij(k)}\, ds = 0\,, \tag{I .6}$$

where

$$\mathcal{G}_{ij} = \mathcal{G}(U_i^n, U_j^n, \vec{n}_{ij}) \tag{I .7}$$

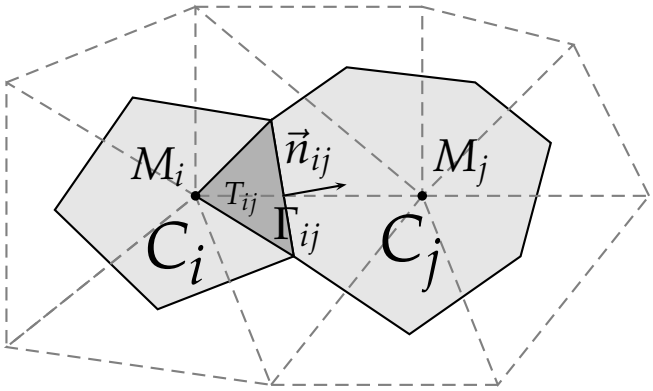

Figure I .2: Vertex centered formalism - focus on the interface Γ_{ij}.

is a numerical flux function through the interface between cells C_i and C_j, so that $\mathcal{G}(U_i^n, U_j^n, \vec{n}_{ij})$ approximates $\frac{1}{\ell_{ij}} \int_{\Gamma_{ij}} G(U).\vec{n}_{ij}\, ds$. Here the subscript "$n$" is employed in the writing of U to refer to the approximate solution at time t^n.

We are consequently left with the evaluation of $\Lambda(i)$ numerical fluxes in the normal direction of each boundary interface. Thus, on these aspects, the principles of resolution in the context of polygonal meshes are not so distant from the 1d case. Accordingly, our aim is to get a better understanding of the structure of the problem at the level of each edge, before engaging in their integration within a numerical model.

I.2.1 Structural considerations

Before delving into the matter of Riemann problems, we propose a brief recall regarding the general characteristics of the 2d Shallow Water system. In the context of unstructured meshes, the computation of each numerical flux is accompanied by a change of coordinates, to pass from the original reference to the one associated with the outward normal of the boundary interface. We first propose to explore the behaviour of the system with regard to these induced rotations. Let's first rewrite the homogeneous system extracted from (I .1) as :

$$\frac{\partial U}{\partial t} + A_x(U)\frac{\partial U}{\partial x} + A_y(U)\frac{\partial U}{\partial y} = 0\,, \tag{I .8}$$

where we have set :

$$A_x(U) = \begin{pmatrix} 0 & 1 & 0 \\ c^2 - u^2 & 2u & 0 \\ -uv & v & u \end{pmatrix} \quad , \quad A_y(U) = \begin{pmatrix} 0 & 0 & 1 \\ -uv & v & u \\ c^2 - u^2 & 0 & 2v \end{pmatrix} ,$$

and $c = \sqrt{gh}$ the speed of gravity waves. For a given unit outward normal vector $\vec{n} = (n_x, n_y)$, the passing from the original reference to the $(n,\, \tau)$ coordinates

system attached to $\vec{n}$ is governed by the classical relations (Fig. I .3) :

$$\frac{\partial U}{\partial x} = \frac{\partial U}{\partial n}\frac{\partial n}{\partial x} + \frac{\partial U}{\partial \tau}\frac{\partial \tau}{\partial x} = \frac{\partial U}{\partial n}n_x - \frac{\partial U}{\partial \tau}n_y\,,$$
$$\frac{\partial U}{\partial y} = \frac{\partial U}{\partial n}\frac{\partial n}{\partial y} + \frac{\partial U}{\partial \tau}\frac{\partial \tau}{\partial y} = \frac{\partial U}{\partial n}n_y + \frac{\partial U}{\partial \tau}n_x\,.$$

Then, the projection of (I .8) in the direction $\vec{n}$ is :

$$\frac{\partial U}{\partial t} + A_n(U)\frac{\partial U}{\partial n} = 0\,, \tag{I .9}$$

where $A_n(U)$ is the projection of the flux onto $\vec{n}$:

$$A_n(U) := A_x(U)n_x + A_y(U)n_y = \begin{pmatrix} 0 & n_x & n_y \\ c^2 n_x - u\mathbf{u}.\vec{n} & \mathbf{u}.\vec{n} + un_x & un_y \\ c^2 n_y - v\mathbf{u}.\vec{n} & vn_x & \mathbf{u}.\vec{n} + vn_y \end{pmatrix}\,.$$

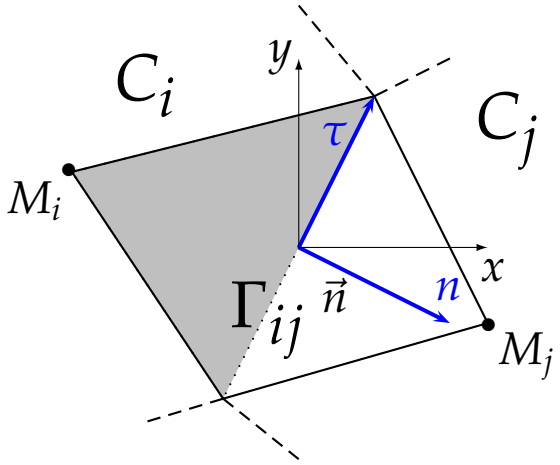

Figure I .3: Numerical flux in the (n, τ) coordinates.

Lastly, the change of variables $U \begin{pmatrix} h \\ hu \\ hv \end{pmatrix} \to \mathfrak{U} \begin{pmatrix} h \\ h\mathfrak{u} \\ h\mathfrak{v} \end{pmatrix}$, where $\mathfrak{u} = un_x + vn_y$ and $\mathfrak{v} = -vn_x + un_y$ enables to express (I .9) in terms of normal and tangential velocities in the (n, τ) reference :

$$\frac{\partial \mathfrak{U}}{\partial t} + \mathfrak{A}_n(U)\frac{\partial \mathfrak{U}}{\partial n} = 0\,, \tag{I .10}$$

where :

$$\mathfrak{A}_n(\mathfrak{U}) := \begin{pmatrix} 0 & 1 & 0 \\ c^2 - \mathfrak{u}^2 & 2\mathfrak{u} & 0 \\ -\mathfrak{u}\mathfrak{v} & \mathfrak{v} & \mathfrak{u} \end{pmatrix}\,. \tag{I .11}$$

In consequence, the interface fluxes approximation in (I .7) rests upon the resolution of 1d Riemann problems associated with equations under the form (I .10).

Another way to formulate this is to say that the system is invariant by rotation. Hence, without loss of generality, one can be exempted from studies in general directions, focusing on the particular 1d case arising from the projection of (I .8) onto the x-coordinates :

$$\frac{\partial U}{\partial t} + A_x(U)\frac{\partial U}{\partial x} = 0\,. \tag{I .12}$$

Regarding the structure of this system, the Jacobian matrix $A_x(U) := \dfrac{\partial(G^1(U))}{\partial U}$ admits $\lambda_1(U) = u - c\,, \lambda_2(U) = u\,,$ and $\lambda_3(U) = u + c$ as eigenvalues, all distinct if $h \neq 0$, in which case the system is strictly hyperbolic. The corresponding eigenvectors are :

$$r_1(U) = \begin{pmatrix} 1 \\ u - 2c \\ v \end{pmatrix} \quad , \quad r_2(U) = \begin{pmatrix} 0 \\ 0 \\ 1 \end{pmatrix} \quad , \quad r_3(U) = \begin{pmatrix} 1 \\ u + 2c \\ v \end{pmatrix}\,. \tag{I .13}$$

These quantities define three characteristics fields, corresponding to non linear waves travelling at speeds $\lambda_1, \lambda_2, \lambda_3$, generally called k-*fields*, $k = 1, 2, 3$ (the terminology *-waves* or *-characteristics* is also employed). We can easily verify that the 1 and 3 - *fields* are *genuinely non-linear*, that is :

$$\nabla_U \lambda_1(U).r_1(U) \neq 0 \quad , \quad \nabla_U \lambda_3(U).r_3(U) \neq 0\,,$$

while the 2-*field* is *linearly degenerate* :

$$\nabla_U \lambda_2(U).r_2(U) = 0\,,$$

meaning that $\lambda_2(U) = u$ is constant along the 2-*wave*, which corresponds to a contact discontinuity. By the way, one can also establish that this is also the case for h, so that the 2-*wave* only involves variations of the tangential velocity. As for the 1-*wave* and the 3-*wave*, looking for quantities $\beta(U)$ satisfying $\nabla_U \beta(U).r(U)$, we obtain :

$$\begin{array}{llll} u + 2c = cte & \text{and} & hv = cte & \text{through the } 1-wave\,. \\ u - 2c = cte & \text{and} & hv = cte & \text{through the } 3-wave\,. \end{array} \tag{I .14}$$

We effectively recover the Riemann invariants $\beta^- := u - 2c$ and $\beta^+ := u + 2c$ of the 1d case.

Remark I.2 .1. *The sign of λ_1 and λ_3 is closely linked to the Froude number :*

$$F_r = \frac{|u|}{c}\,, \tag{I .15}$$

and we refer to Section §I.4 for applications of this ratio as regards the implementation of boundary conditions.

I.2.2 The Riemann problem

We restate here some fundamental results concerning the solution of Riemann problems. Only the case of flat bottoms is investigated, the extension to varying bottoms following the same lines. Actually, the goal of the coming section is to get a better picture on the general structure of the system's solutions in the particular case of interface Riemann problems, and serves as support for the introduction of Riemann solvers. The reader is referred to [39, 118, 138, 267, 209] for some works introducing piecewise constant topography. The crucial issue of inclusion of source terms is postponed to §I.5.3 and numerical methods are presented in the next chapters.

According to the previous results, the computation of the exchanging fluxes (I .7) at each boundary interface comes down to the analysis of "pseudo" 1d Riemann problems of the form :

$$\begin{cases} \dfrac{\partial U}{\partial t} + \dfrac{\partial G^1(U)}{\partial x} = 0\,, \\ U(x,0) = \begin{cases} U^- = (h^-, hu^-, hv^-) & \text{if} \quad x < 0\,, \\ U^+ = (h^+, hu^+, hv^+) & \text{if} \quad x > 0\,, \end{cases} \end{cases} \tag{I .16}$$

where we recall that G^1 stands for the first component of the flux function G (I .2). According to the structure of the system, the solution of (I .16) consists of four constant states, separated by three non linear characteristic waves. As the *2-wave* only concerns variations on the tangential velocity, the connexion between the states U^- and U^+ can be deduced from the 1d case. To connect a given intermediate state (h, hu, hv) to the "left" state U^- we thus have :

$$u = \begin{cases} u^- + 2(\sqrt{gh^-} - \sqrt{gh}) & \text{if} \quad h < h^-\,, \\ u^- + (h - h^-)\sqrt{\dfrac{g}{2}\left(\dfrac{1}{h} + \dfrac{1}{h^-}\right)} & \text{otherwise}\,. \end{cases} \tag{I .17}$$

Similarly, an intermediate state (h, hu, hv) is linked to U^+ through the 3-*wave* via :

$$u = \begin{cases} u^+ - 2(\sqrt{gh^+} - \sqrt{gh}) & \text{if} \quad h < h^+\,, \\ u^+ - (h - h^+)\sqrt{\dfrac{g}{2}\left(\dfrac{1}{h} + \dfrac{1}{h^+}\right)} & \text{otherwise}\,. \end{cases} \tag{I .18}$$

In the resolution of (I .16), the value of h in the intermediate state is enforced by compatibility conditions issuing from (I .17) and (I .18). Numerically, it can be approached having recourse to iterative methods. As regards the 1-*wave*, the case $h < h^-$ leads to a rarefaction wave, and the expression of u is furnished by the 1-Riemann invariant β^-. On the other hand, increasing values of h will favour appearance of shock waves. When $h > h^-$, a shock occurs and u is given by the so called *Rankine-Hugoniot* relations (Fig. I .4) :

$$\begin{aligned} s(h_r - h_l) &= (hu)_r - (hu)_l\,, \\ s\left((hu)_r - (hu)_l\right) &= \left(hu^2 + g\frac{h^2}{2}\right)_r - \left(hu^2 + g\frac{h^2}{2}\right)_l\,, \end{aligned} \tag{I .19}$$

where s is the shock speed and the subscripts l, r denote the variable values at each side of the discontinuity. Similar observations can be made on the $u + c -$ *wave*, which gives rise to a rarefaction or a shock wave, depending on the value of h.

Remark I.2 .2. *In the sequel, in order to make easier jump manipulations, we will adopt the standard notation* $[[w]]$ *to refer to the difference between "exterior" and "interior" values of the variable* w*. The Rankine Hugoniot conditions (I .19) hence simply take the form :*

$$\begin{aligned} s[[h]] &= [[hu]] \,, \\ s[[hu]] &= [[hu^2 + g\frac{h^2}{2}]] \,. \end{aligned} \tag{I .20}$$

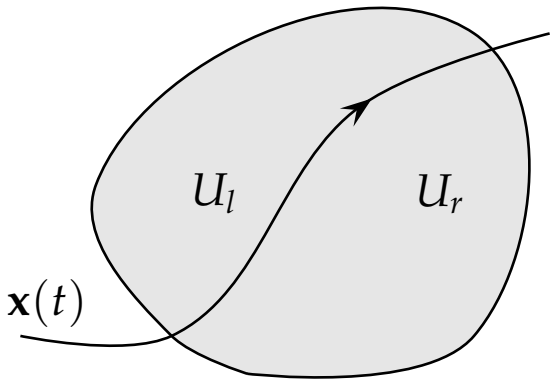

Figure I .4: Rankine-Hugoniot conditions : Jump along the discontinuity $\mathbf{x}(t)$.

Variations on the tangential velocity v are exclusively handled by the 2-*wave*, behaving exactly as in the case of a passive tracer [188]. The jump from v^- to v^+ hence occurs through the contact discontinuity, while h and u remains constant as 2 - Riemann invariants. To summarize, the possibilities for the state connexions involved in the Riemann problem are illustrated by Fig. I .5, the *1-wave* and *3-wave* being shocks or rarefaction waves.

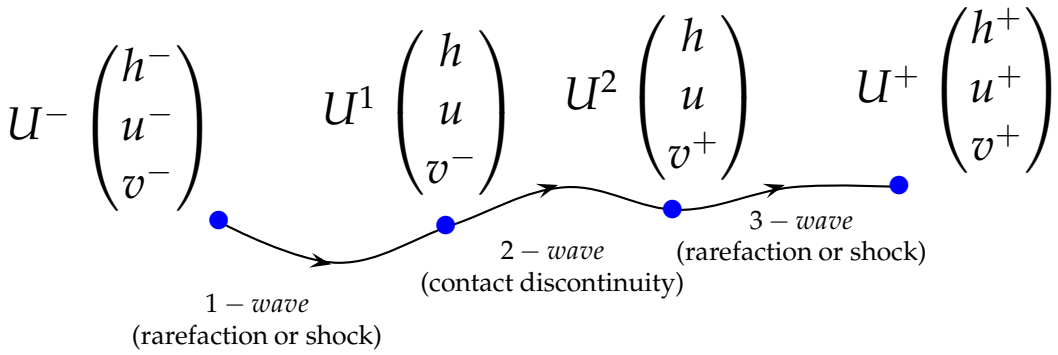

Figure I .5: Connecting U^- to U^+.

I.3 Exchanging fluxes computation

It is commonly agreed that one of the first approaches that has been developed to deal with Riemann problems in the context of Finite Volumes is due to Godunov [129], in 1959. Without going into the technicalities, the method consists of computing the exact solutions at each interface, and subsequently inject them in the numerical fluxes. It's worthwhile to mention that the resolution of such problems is computationally demanding. Indeed, as mentioned previously, and excepted from comfortable particular cases, the research of exact solutions for systems (I .17 - I .18) requires the implementation of iterative root finders. Even if the limitations in terms of computational cost are always being advanced, it turns out to be a major constraint, especially in the case of large scale 2d simulations or complex applications requiring a very high level of refinement in some area of interest. Since this pioneering work, lots of numerical models have been proposed to cure such a problem, and dramatic advances have been achieved.

Nowadays, a classical solution to overcome this drawback is to employ *approximate Riemann* solvers. The main idea is to consider a simplified problem at each interface, which resolution is far less costly. Obviously, as it may not always lead to the exact solution of the Riemann problem, the question arises of finding a good compromise between accuracy and computational constraints. In this section, we draw up a non exhaustive list of possible choice for the numerical fluxes. All the following solvers have been employed in our numerical simulations, and some of their properties will be further investigated in the next chapters.

I.3.1 Lax-Friedrichs fluxes

A very simple way to approximate the interface contributions is to employ the well-known *Lax - Friedrichs* fluxes. The method is based on the average flux at the

boundary, supplemented as follows by an upwind term :

$$\mathcal{G}(U^-, U^+, \vec{n}) = \frac{G(U^-).\vec{n} + G(U^+).\vec{n}}{2} - a\frac{U^+ - U^-}{2}, \tag{I .21}$$

where a stands for a positive parameter. A possible choice, usually encountered in the literature, is to take $a = \max\Big(|\lambda_1(U)|, |\lambda_3(U)|\Big)$, the maximum being taken on the whole domain. This leads to the so called *Global Lax Fredrichs* (GLF) fluxes. The value of a can also be locally optimized taking the maximum between U^- and U^+ only, to obtain the *Rusanov* fluxes ([39]).

The additional term $a\frac{U^+ - U^-}{2}$ is introduced to bring some numerical diffusion in order to stabilize the method. The counterpart is that the resulting diffusive losses may slightly distort the structure of the flow, entailing occasionally under estimations of the water height for instance. Nevertheless, this drawback is not systematically considered as a discriminating criterion: this scheme is usually chosen for its simplicity and generally provides quite satisfying results. In addition, it's worthwhile to note that the simple formulation (I .21) enables the establishment of some fundamental properties at the discrete level. As for the Shallow Water numerical models developed in this work, these fluxes are systematically shown to preserve the positivity of the water height, and play a central role as regards the inclusion of friction source terms. These points will be discussed in the next chapters. Lastly, it should be mentioned that this flux function is Lipschitz continuous, monotone increasing with respect to U^-, monotone decreasing with respect to U^+, consistent with the exact flux in the following sense :

$$\mathcal{G}(U, U, \vec{n}) = G(U).\vec{n}\,, \ \forall\, U \in \Theta\,, \tag{I .22}$$

and satisfies the following conservation property :

$$\mathcal{G}(U^-, U^+, -\vec{n}) = -\mathcal{G}(U^+, U^-, \vec{n})\,, \forall (U^-, U^+, -\vec{n}) \in \Theta^2\,. \tag{I .23}$$

I.3.2 HLL and HLLC solvers

I.3.2.a HLL Solver

A classical example of approximate Riemann solver is supplied by the HLL solver, introduced by Harten, Lax, Van Leer in 1983 [143] in the context of gas dynamics. Consider again the Riemann problem (I .16) in the x-direction, with the same notations as previously :

$$\begin{cases} \dfrac{\partial U}{\partial t} + \dfrac{\partial G^1(U)}{\partial x} = 0\,, \\ U(x,0) = \begin{cases} U^- & \text{if} \quad x < 0\,, \\ U^+ & \text{if} \quad x > 0\,. \end{cases} \end{cases}$$

The method aims at introducing an intermediate state U_* expected to establish a relevant connexion between the *interior* and *exterior* states. For that purpose, a two-waves configuration is assumed to separate the constant states U^-, U_*, U^+. The corresponding wave speeds s^- and s^+ can be defined as follows ([39, 89]) :

$$s^- = \min(u^- - c^-, u^+ - c^+), \quad s^+ = \max(u^- + c^-, u^+ + c^+), \tag{I .24}$$

where we have set $c^\pm = \sqrt{gh^\pm}$. Then, involving the Rankine Hugoniot relations (I .19) through these two waves :

$$\begin{aligned} s^-(U_* - U^-) &= G^1(U_*) - G^1(U^-), \\ s^+(U^+ - U_*) &= G^1(U^+) - G^1(U_*), \end{aligned}$$

we can easily determine U_* :

$$U_* = \frac{s^+U^+ - s^-U^- - (G^1(U^+) - G^1(U^-))}{s^+ - s^-}, \tag{I .25}$$

as well as the numerical flux :

$$G^1(U_*) = G^1(U^-) + s^-(U_* - U^-) = \frac{s^+G^1(U^-) - s^-G^1(U^+) + s^-s^+(U^+ - U^-)}{s^+ - s^-}. \tag{I .26}$$

In summary, the HLL flux is defined as :

$$\mathcal{G}(U^-, U^+) := \begin{cases} G^1(U^-) & \text{if} \quad s^- > 0, \\ G^1(U_*) & \text{if} \quad s^- < 0 < s^+, \\ G^1(U^+) & \text{if} \quad s^+ < 0. \end{cases} \tag{I .27}$$

.

Remark I.3 .1. *For an arbitrary direction $\vec{n}$, (I .27) is expressed as :*

$$\mathcal{G}(U^-, U^+, \vec{n}) := \begin{cases} G(U^-).\vec{n} & \textit{if} \quad s^- > 0, \\ \dfrac{s^+G(U^-).\vec{n} - s^-G(U^+).\vec{n} + s^-s^+(U^+ - U^-)}{s^+ - s^-} & \\ & \textit{if} \quad s^- < 0 < s^+, \\ G(U^+).\vec{n} & \textit{if} \quad s^+ < 0. \end{cases} \tag{I .28}$$

From this, we can easily verify that the resulting flux function can be seen as a generalization of the Lax Friedrichs fluxes, obtained setting $s^+ = -s^- = a$. Also notice that this solver enjoys the consistency and conservativity properties (I .22 - I .23) previously discussed. Although offering a better level of accuracy, we point out that the construction (I .27) infringes the general structure of the exact Riemann problem, which solution depends on three characteristic waves. To enhance the solver's accuracy, an intermediate wave speed can be introduced to handle the contact discontinuity and overcome the limitations entailed by a two wave assumption. The strategy is discussed the next section.

Remark I.3 .2. *It should be stressed that finest choice are possible for the wave speed estimates s^+ and s^-. A first important result can be found in the works of Vila [279]. In the context of gas dynamics, the author derives rigorous upper and lower bounds that ensure the consistency with entropy condition (see I.5.2) and the L^∞ stability. When applied to the NSW equations, this gives :*

$$s^- = \min(u^- - c^-, u^+ - c^+ + 2c^-)\,, \quad s^+ = \min(u^+ + c^+, u^- + c^- - 2c^+)\,, \tag{I .29}$$

which guarantees the production of admissible solutions, both in the sense of entropy conditions and positivity of the water height. One can also mention the so called HLLE variant proposed by Einfeldt [102] for instance, where the definition of the wave speeds is based on the Roe average states (see [121, 188]). This choice allows slight gains in accuracy and a better stability when dealing with wet/dry transitions ([89]). The reader is referred to [84, 250] for another example and Toro [272] for further details.

I.3.2.b HLLC solver

A possible improvement of the HLL solver has been proposed by Toro, Spruce and Spears [273], leading to the so called HLLC scheme (where C stands for Contact). Without getting into the specifics, let mention that the restoration of the contact discontinuity in the HLL solver generates two intermediate states, that will be denoted U_*^- and U_*^+. Then, imposing the standard requirements :

$$h_*^- = h_*^+ \quad , \quad u_*^- = u_*^+ = s_*\,,$$

issuing from investigations carried on in §I.2.1 , algebraic manipulations based on Rankine-Hugoniot jump conditions lead to the third wave speed (see also [100]) :

$$s_* = \frac{s^- h^+(u^+ - s^+) - s^+ h^-(u^- - s^-)}{h^+(u^+ - s^+) - h^-(u^- - s^-)}\,,$$

and the following values for the intermediate states :

$$U_*^\pm = h_\pm \left(\frac{s^\pm - u^\pm}{s^\pm - s_*}\right) \begin{pmatrix} 1 \\ s_* \\ v_\pm \end{pmatrix}\,.$$

At last, the HLLC flux is given by :

$$\mathcal{G}(U^-, U^+, \vec{n}) := \begin{cases} G(U^-).\vec{n} & \text{if} \quad s^- > 0\,, \\ G(U^-).\vec{n} + s^-(U_*^- - U^-) & \text{if} \quad s^- < 0 < s_*\,, \\ G(U^+).\vec{n} + s^+(U_*^+ - U^+) & \text{if} \quad s_* < 0 < s^+\,, \\ G(U^+).\vec{n} & \text{if} \quad s^+ < 0\,. \end{cases} \tag{I .30}$$

This definition of the numerical fluxes induces a dependency cone similar to the one resulting from the structure of the exact problem. In 1d, a summary of the situation is given through the classical illustration proposed in Fig. I .6 :

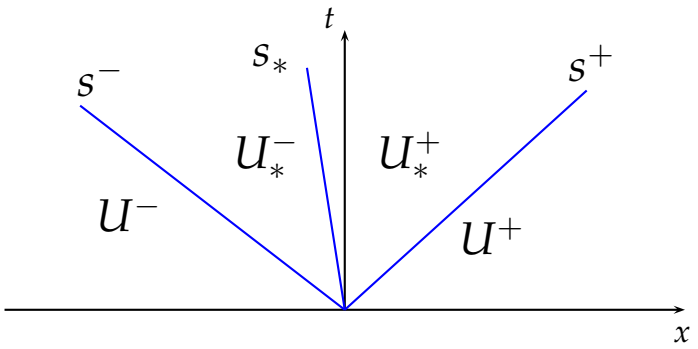

Figure I .6: Riemann fan for the HLLC solver.

I.3.3 VFRoe-ncv solver

The VFroe-ncv scheme has been introduced in the early 2000s, and is an example of linearised Riemann solver. The VFroe-ncv formalism has been developed by Gallouet and collaborators in the context of Shallow Water equations [50, 118], in parallel with applications to gas dynamics [51, 212]. The class of VRoe-ncv schemes is a derivation of the VFroe scheme, introduced in [119] as well as an alternative for the Roe solver [245]. Indeed, although being quite commonly used, the Roe solver is not well suited for such environmental applications since it is notably not positive-preserving, which becomes a huge inconvenience when low water depths are involved.

The method is based on the exact resolution of a linearised Riemann problem, together with the introduction of a non conservative (*ncv*) change of variables. As previously, we explore the case of a flat bottom, and refer to the corresponding references for extensions to varying topography. The strategy starts with the introduction of an arbitrary change of variables $W = \phi(U)$, followed by the linearisation of the system (I .12) around the average value $\overline{W} = \frac{1}{2}(W^- + W^+)$:

$$\begin{cases} \dfrac{\partial W}{\partial t} + B_x(\overline{W})\dfrac{\partial W}{\partial x} = 0\,, \\ W(x,0) = \begin{cases} W^- & \text{if} \quad x < 0\,, \\ W^+ & \text{if} \quad x > 0\,, \end{cases} \end{cases} \tag{I .31}$$

where

$$B_x(W) = JA_x(W)J^{-1} \quad \text{and} \quad J = \frac{\partial W}{\partial U}\,.$$

Among the possibilities for ϕ, we suggest to consider $W = \phi(U) = (2c, u, v)$, known to provide a symmetric convection matrix and preserve the water depth positivity ([117]). After straightforward computations, we indeed obtain :

$$B_x(\overline{W}) = \begin{pmatrix} \overline{u} & \overline{c} & 0 \\ \overline{c} & \overline{u} & 0 \\ 0 & 0 & \overline{u} \end{pmatrix}\,, \tag{I .32}$$

from which we easily extract the following eigenvalues :

$$\overline{\lambda}_1 = \overline{u} - \overline{c} \quad , \quad \overline{\lambda}_2 = \overline{u} \quad , \quad \overline{\lambda}_3 = \overline{u} + \overline{c} \, .$$

Afterwards, denoting $W_*(\frac{x}{t}, W^-, W^+)$ the exact solution of the linear Riemann problem (I .31), we call the general result :

$$\begin{aligned} W_*^- \left((\frac{x}{t})^-, W^-, W^+ \right) &= W^- + \sum_{\frac{x}{t} > \overline{\lambda}_k} ({}^t\overline{l}_k . [[W]]) \overline{r}_k \, , \\ W_*^+ \left((\frac{x}{t})^+, W^-, W^+ \right) &= W^+ - \sum_{\frac{x}{t} < \overline{\lambda}_k} ({}^t\overline{l}_k . [[W]]) \overline{r}_k \, , \end{aligned}$$

to compute the left and right intermediate states. In the relations mentioned hereinabove, $\overline{l}_k$ and $\overline{r}_k$ are respectively the left and right eigenvectors of the jacobian matrix (I .32). In the current context, these vectors can be basically determined, which leads to :

$$W_*^- = W^- + ([[c]] - \frac{1}{2}[[u]]) \begin{pmatrix} 1 \\ -1 \\ 0 \end{pmatrix} \text{ , through the } (\overline{u} - \overline{c}) - \textit{wave} \, .$$

$$W_*^+ = W^+ - ([[c]] + \frac{1}{2}[[u]]) \begin{pmatrix} 1 \\ 1 \\ 0 \end{pmatrix} \text{ , through the } (\overline{u} + \overline{c}) - \textit{wave} \, .$$

We deduce from the previous relations the following formula for each of the transitory states :

$$\begin{aligned} c_*^- &= \overline{c} - \frac{1}{4}[[u]] \, , & c_*^+ &= \overline{c} - \frac{1}{4}[[u]] \, , \\ u_*^- &= \overline{u} - [[c]] \, , & u_*^+ &= \overline{u} - [[c]] \, , \\ v_*^- &= v^- \, . & v_*^+ &= v^+ \, . \end{aligned} \tag{I .34}$$

This time, we are in the presence of three waves propagating at speeds $\overline{u} - \overline{c}, \overline{u}, \overline{u} + \overline{c}$, separating four constant states. The nature of the solution is the same as in the HLLC case (Fig. I .6) :

$$U^*(0, U^-, U^+) = \begin{cases} U^- & \text{if} \quad \overline{\lambda}_1 > 0 \, , \\ U_*^- & \text{if} \quad \overline{\lambda}_1 < 0 < \overline{\lambda}_2 \, , \\ U_*^+ & \text{if} \quad \overline{\lambda}_2 < 0 < \overline{\lambda}_3 \, , \\ U^+ & \text{if} \quad \overline{\lambda}_3 < 0 \, . \end{cases} \tag{I .35}$$

For a given direction $\vec{n}$, the resulting numerical fluxes can be written as :

$$\mathcal{G}(U^-, U^+, \vec{n}) = G\left(U^*(0, U^-, U^+)\right) . \vec{n} \, . \tag{I .36}$$

I.3.4 Some complements

Another popular approach for the resolution of non linear systems is to employ *relaxation* schemes [162]. This class of solvers is based on rescaled (*relaxed*) equations and some analysis around appropriate equilibrium functions. As stated in [39, 189] for instance, Lax Friedrichs, HLL and Roe schemes can be derived from a such a viewpoint. In [26], authors shown that the VFRoe-ncv scheme previously introduced also admits an interpretation in terms of relaxation approach. Other schemes of this nature can be encountered in the literature, among which [93, 160]. For further details on this topic, one can also refer to the works carried out in [38, 80, 185, 197, 262, 263] for instance.

A second important class of methods deserving mention is obtained from a kinetic interpretation of the Shallow Water system. We refer to the reference works of Perthame [231, 232] for a detailed presentation of kinetic solvers and attached formalism. In addition of their entropy satisfying features, kinetic schemes offer interesting possibilities regarding water height positivity preservation and inclusion of bottom source term, and also appear as a reasonable compromise between accuracy and efficiency. Notably due to this, they have been widely validated as an efficient tool in the framework of NSW equations since the past decade ([101, 11, 235, 265]).

I.4 Boundary conditions

I.4.1 Classical methods

The problem of boundary conditions stands for a fundamental issue when setting up a numerical model for unsteady processes, since they principally dictate the evolution of the solution. Their enforcement is generally governed by the flow regime at the level of each boundary interface, relying on the Froude number $Fr = \dfrac{|u|}{c}$ (I .15). This ratio evaluates the magnitude of the velocity u with respect to the speed of gravity waves, and its physical interpretation determines the flow regime :

- $Fr \leq 1$: *subcritical flow*. This is the case corresponding to a *fluvial* regime. The flow is dominated by gravitational forces, and controlled from downstream regions.

- $Fr \geq 1$: *supercritical flow*. The flow is dominated by inertial forces, and controlled from upstream. Such a regime is also referred to as *torrential* regime.

If $Fr = 1$, the flow is called *critical flow*. This state is unstable, and corresponds to a transitory case in which flows are moving from subcritical to critical, or vice-versa. For instance we usually say that a *hydraulic jump* occurs in the

particular case of a transition from an unstable flow (supercritical) to a stable flow (subcritical). Actually, through these physical considerations, the problem of boundary conditions can be simply interpreted in terms of information exchanges with the exterior domain. In the following lines we propose some examples of classical methods devoted to boundary conditions.

Taking this into account, numerical methods based on the characteristic theory and the conservation of Riemann invariants are often proposed to determine the variable value at the boundary (see [5, 89, 194, 227, 247], and Bristeau *et al* [43] in the particular case of kinetic schemes). The resulting state is subsequently employed in the physical fluxes, which gives the desired contribution. Several cases have to be distinguished, depending if the flow is torrential or fluvial. Consider a boundary cell C_i, with a boundary edge Γ and its corresponding outward normal vector $\vec{n}$ (see Fig. (I .7)). We denote $\lambda_1 = \lambda_1(U_i) = u - c$, $\lambda_3 = \lambda_3(U_i) = u + c$ the minimum and maximum velocity waves.

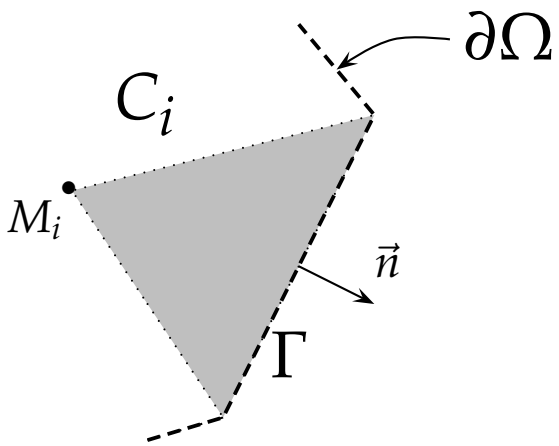

Figure I .7: Boundary fluxes computation.

If $\lambda_3 < 0$, we are in the case of a supercritical inflow boundary condition. Informations are coming from outside, and the value of the approximated vector solution at the boundary (denoted U_Γ) is prescribed by the physical constraints relative to the exterior of the domain. The case $\lambda_1 > 0$ corresponds to the supercritical outflow case, and we have $U_\Gamma = U_i$. In all remaining situations, the flow is subcritical : one or two informations may come from outside, according to the sign of u. The Riemann invariant $\beta^+ = u - 2c$ is constant through the outgoing characteristic, allowing to prescribe the water depth or normal discharge. These cases are gathered in the drawing I .8.

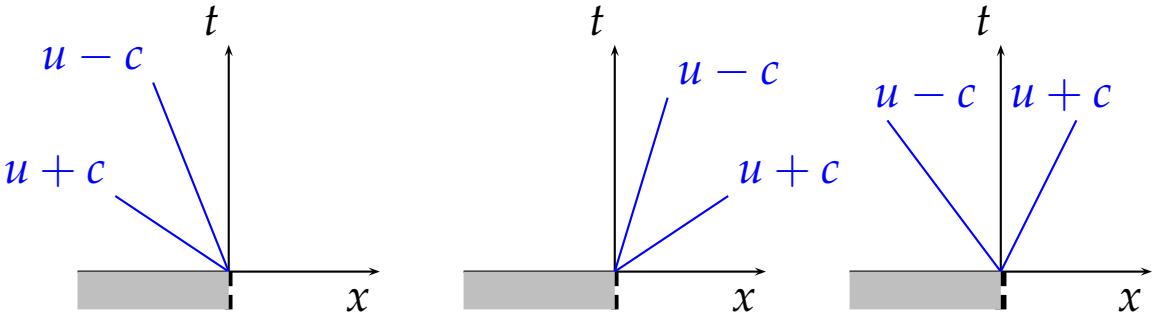

Supercritical inflow Supercritical outflow Subcritical flow

Figure I .8: Possibilities for the flow regime at the boundary interface Γ.

As regards Dirichlet conditions for instance, where the water depth is imposed: $h_\Gamma = h_0 > 0$, the normal velocity is given by :

$$u_\Gamma = u_i - 2(\sqrt{gh_i} - \sqrt{gh_0})\,. \tag{I .37}$$

Similarly, solid wall boundary conditions are obtained setting $u_\Gamma = 0$, and extracting the water height from the following relation :

$$2\sqrt{gh_\Gamma} = u_i - 2\sqrt{gh_i}\,. \tag{I .38}$$

In the case of a shock, the Hankine Hugoniot relations (I .19) are used to determine the unknowns, returning to (I .18). Other classical boundary conditions can be addressed that way.

A second efficient method is inspired from the works of Ghidaglia and Pascal [123, 124], where authors propose a general method aiming to directly compute the numerical fluxes at the boundaries. We start with the following system :

$$\frac{\partial G^1(U)}{\partial t} + A_x(U)\frac{\partial G^1(U)}{\partial x} = 0\,, \tag{I .39}$$

obtained using (I .12) and the relation $A_x(U) = \dfrac{\partial G^1(U)}{\partial U}$. The key ideas are, in a first time, to rewrite the system (I .39) employing the boundary cell value in the convection matrix. Adopting the same notations as previously, let's note that by mean of an appropriate change of variables, (I .39) becomes a system of uncoupled advection equations :

$$\frac{\partial W_k}{\partial t} + \lambda_k \frac{\partial W_k}{\partial x} = 0 \quad k = 1, 2, 3\,, \tag{I .40}$$

where $W = \begin{pmatrix} W_1 \\ W_2 \\ W_3 \end{pmatrix} = P^{-1}G^1(U)$, and P is the matrix formed by the right eigenvectors of $A_x(U_i)$ (see I .13). Subsequently, authors suggest to exploit the transport relations arising from the linearised system, with the goal of providing direct

informations on the boundary fluxes. If $\lambda_3 < 0$, all informations transit from the *exterior* to the *interior*, and we recover the supercritical inflow case previously discussed. Similarly $\lambda_1 > 0$ gives $G^1(U_\Gamma) = G^1(U_i)$.

To further understand the procedure, let's now analyse what happens with a reflective-type condition ($u_\Gamma = 0$) in the subcritical case. As we have $\lambda_3 > 0$, the third transport equation of (I .40) allows to impose a numerical boundary condition accounting for informations originating from Ω. In the current context, we hence have $W_3(U_\Gamma) = W_3(U_i)$, or under an equivalent form :

$$l_3(U_i).\Big(G^1(U_\Gamma) - G^1(U_i)\Big) = 0\,, \tag{I .41}$$

where $l_3(U_i)$ is the third left eigenvector of $A_x(U_i)$. After straightforward computations, (I .41) gives:

$$\frac{g}{2}h_\Gamma^2 = c_i h_i u_i + \frac{g}{2}h_i^2\,, \tag{I .42}$$

from which, taking $u_\Gamma = 0$ into account, we deduce the numerical flux :

$$G^1(U_\Gamma) = \begin{pmatrix} 0 \\ \frac{g}{2}h_\Gamma^2 \\ 0 \end{pmatrix}\,. \tag{I .43}$$

Note that this method is successfully applied in [100] in the Shallow Water framework. Our numerical investigations confirmed that such a strategy may also turn out to be a wise option in general, since the two methods discussed so far share the same level of accuracy and are both quite easy to implement.

A very simple way to proceed when seeking to minimize efforts to handle standard boundary conditions is to have recourse to ghost cells. This technique is certainly the most economic in terms of implementation efforts, and has been widely employed in the framework of NSW equations ([42, 151, 187, 209, 252, 305]). Dirichlet, Neumann and solid wall conditions for instance can easily be enforced attributing appropriate values at the unknowns in a fictitious cell C_g at the external boundary, according to the type of the flow. Periodic boundary conditions can also be handled that way. Concerning solid wall conditions for instance, a *mirror state* is generally imposed, that is :

$$U_g = \begin{pmatrix} h_i \\ -hu_i \\ hv_i \end{pmatrix}\,, \tag{I .44}$$

to account for the reflection on the wall. Note that this case is particularly interesting since it allow to establish connexions with the three methods discussed in this section. For instance, we easily verify that the boundary values (I .42 - I .43) can be recovered employing (I .44) in the Rusanov fluxes (I .21) in the case where $a = u_i - c_i$. Also note that injecting (I .44) in the VFRoe-ncv solver yields identical results to those obtained with the Riemann invariants (I .38).

It's important to notice that accounting for the presence of varying topography at the boundaries is a complicated task. The subject is far from being totally understood and still subject to intensive research. That being so, in the set of numerical validations presented in this work, it has been systematically possible to enforce proper conditions assuming a flat bottom (that is neglecting the corresponding source term). All of the above methods have been implemented and validated during our experimentations. Even if they have not been extensively compared, they quite clearly demonstrated equivalent capacities in terms of accuracy and had a very limited impact on the overall computational cost.

I.4.2 Open sea boundary conditions

In the perspective of real-life simulations, we are in the necessity of implementing boundary conditions able to reproduce possibly complex situations. As for the description of nearshore hydrodynamics processes, where the computational domain has generally to be limited to capture at best water motions in some regions of interest, the consideration of open sea boundary conditions is particularly important. It is useful to note that the generation of incident waves is often accompanied with the production of outgoing waves issuing from reflection at the shoreline. These reflected waves may interfere with the generation process, and potentially bring some instabilities if they are unable to exit correctly the domain. Thus, the complex mechanism of coming and going water waves is rather difficult to reproduce, and implies a time evolving inflow boundary which is locally able to demonstrate proper generating/absorbing abilities. In the Shallow Water frame, some interesting ideas can be encountered in [209], where the issues of generating and generating/absorbing boundary conditions are addressed, with the use of fictitious cells. These ideas are inspired from Kobayashi *et al* [218], and Cienfuegos *et al* [75] in the context of Boussinesq equations, principally relying on the characteristic theory and Riemann invariants conservation. We refer to these references for more details.

When dealing with absorbing/generating boundary conditions, the use of relaxation techniques may stand as an efficient alternative to handle regular waves. In the last part of this work, devoted to a numerical discretization of a new Green Naghdi model, such tools are required to properly trig the generation mechanism in deep waters, and handle absorption of outgoing waves. The basic principle consists of extending the computational domain with relaxation zones at the inflow (and sometimes outflow) boundaries, allowing to progressively transit from a theoretical solution imposed at the boundary to the numerical solution. Such a strategy enables to initiate the flow motion and capture reflected waves in a very stable way, and is frequently involved in numerical simulations within dispersive models [70, 103, 184, 205]. In this work, following [155], the relaxed solution along the domain will take the form :

$$U_{relax} = F_a U_{num} + (1 - F_a) F_g R(t) U_{theo} \, , \tag{I .45}$$

where F_a , F_g stand for the absorption and generation profiles and R governs the time evolution of the generation process. U_{num} and U_{theo} naturally stand for the numerical and theoretical solutions. Among the quantity of different relaxation functions available, we follow [283], taking the exponential forms :

$$F_a(x) = 1 - \frac{exp\left((x_r)^n - 1\right))}{exp(1) - 1} \quad , \quad F_g(x) = 1 - \frac{exp\left((1 - x_r)^n - 1\right))}{exp(1) - 1} \, ,$$

where $x_r = \dfrac{x - x_R}{\Delta_R}$, n is a positive parameter, and x_R, Δ_R are respectively the beginning and the width of the relaxation zone. Of course, lots of combinations are possible when defining the set of parameters, leading to various behaviours. In conformity with other works, it appears from our numerical investigations that a reasonable initialization is given by Δ_R equal to 2 wave lengths and $n = 3$. The reader is referred to [155] for complementary studies on these relaxation profiles.

I.5 Numerical constraints

I.5.1 Stability issues

As far as time discretization is concerned, a first order explicit Euler scheme will be employed to illustrate the construction process of our numerical approaches. In this work, only fully explicit methods will be experimented. Unlike implicit methods, it's not useless to recall that the use of explicit schemes naturally induces stability conditions. Full consideration has to be given to the way time step is selected, to avoid production of numerical noise resulting from interacting waves or very low water depths. This is a very important concern, since these instabilities can evolve as a function of time and rapidly deteriorate the quality of the numerical approximation. In what follows, the classical Euler scheme will be used for the sake of simplicity.

Following the lines of [21], first note that the homogeneous scheme (I .6) can be recast under the following standard convex combination, provided the use of a consistent flux function :

$$U_i^{n+1} = \sum_{k=1}^{\Lambda(i)} \frac{|T_{ij(k)}|}{|C_i|} U_{ij(k)}^{n+1} \, , \tag{I .46}$$

with

$$U_{ij(k)}^{n+1} = U_i^n - \frac{\Delta t}{\delta_{ij(k)}} \left(\mathcal{G}_{ij(k)} - \mathcal{G}_{ij(k)}^c \right) , \tag{I .47}$$

where we have set $\delta_{ij(k)} = |T_{ij(k)}| / \ell_{ij(k)}$ and $\mathcal{G}_{ij(k)}^c = \mathcal{G}(U_i, U_i, \vec{n}_{ij(k)})$ stand for "ghost" fluxes, which are counterbalancing according to the discrete Green formula. Considering this rewriting, in order to rule out some instabilities and based on the classical stability analysis of the 1d schemes, the homogeneous scheme is

endowed with a CFL condition given by :

$$a_i \frac{\Delta t}{\delta_{ij(k)}} \leq \tau_{CFL}\,, \quad \forall C_i\,,\, k = 1, \cdots, \Lambda(i)\,, \tag{I .48}$$

where $\tau_{CFL} \leq 1$, and

$$a_i = \max_{k=1,\cdots,\Lambda(i)} \left(|\lambda^-(U_i, U_{j(k)}, \vec{n}_{ij(k)})|\,,\, |\lambda^+(U_i, U_{j(k)}, \vec{n}_{ij(k)})| \right), \tag{I .49}$$

$\lambda^{\pm}(U_i, U_{j(k)}, \vec{n}_{ij(k)})$ being the minimum and maximum velocity waves involved in the Riemann solver at the edge $\Gamma_{ij(k)}$. In what follows, and when no confusion is possible, these values will be noted $\lambda_k^{\pm}$ for simplification purposes. Later, this time constraint will have to be strengthened to ensure the stability of the method in the case of high order reconstructions.

Of course, while being the most fast and simple method, the use of a basic first order explicit time scheme entails important limitations in practice. It is indeed preferable to use more accurate supports for the advance in time, especially not to spoil the possible gains brought by high order methods in space. Thus, high order explicit Runge-Kutta algorithms are used in our numerical examples. Bearing in mind that such time marching methods can be viewed as combinations of Euler schemes, the time step (I .48) has to be evaluated accordingly. Nevertheless, note that the second order Heun scheme [39] does not imply any modification of the CFL (I .48). This is the choice made to validate the future Finite Volume approaches. Denoting formally $\frac{d}{dt}U^n + \mathcal{A}(U^n) = 0$ the semi-discrete equations at time t^n, the evolution to the next time level is given by the following steps :

$$\begin{cases} U^{n+1/2} = U^n - \Delta t \mathcal{A}(U^n)\,, \\ U^{n+1} = U^n - \dfrac{\Delta t}{2}\left[\mathcal{A}(U^n) + \mathcal{A}(U^{n+1/2})\right]\,. \end{cases} \tag{I .50}$$

Actually, this scheme belongs to the general class of *Strong Stability Preserving Runge-Kutta* (SSP-RK) schemes. They were introduced by Shu and Tadmor in [256],[255], with the objective of preserving the TVD (*Total Variation Diminishing*) property while seeking for more accurate time discretizations (see also the collaborations with Gottlieb [135] on this topic). As a matter of fact, these schemes can be interpreted as convex combinations of first order explicit Euler schemes, which allows to simply deduce stability conditions, depending on the involved coefficients. In particular, the second order scheme (I .50) can be written as a two-stage SSP-RK scheme, subject to the same CFL :

$$\begin{cases} U^{n,1} = U^n - \Delta t \mathcal{A}(U^n)\,, \\ U^{n,2} = U^{n,1} - \Delta t \mathcal{A}(U^{n,1})\,, \\ U^{n+1} = \dfrac{1}{2}U^n + \dfrac{1}{2}U^{n,2}\,. \end{cases} \tag{I .51}$$

Higher order methods will be discussed during our investigations on dG approaches, together with their corresponding CFL.

I.5.2 Entropy relations

Another difficulty generally linked to the concept of stability comes from the non-uniqueness of weak solutions for the non-linear shallow water equations. This implies the introduction of another criteria, allowing to select the solution of the system that is physically admissible, and brings us to the notion of entropy and admissibility conditions. In 1d, we first specify that the existence of an *entropy function* $\mathfrak{n}$ is linked to the existence of an *entropy flux* $\mathfrak{G}$ via the relation :

$$\partial_x(\mathfrak{n}(U))A_x(U) = \partial_x(\mathfrak{G}(U))\,. \tag{I .52}$$

The entropy $\mathfrak{n}$ is generally asked to be a convex function of U, and it should be noted that the existence of a strictly convex entropy is also linked to the notion of hyperbolicity ([39]). An entropic solution U should satisfy the following inequality ([186, 188]) :

$$\partial_t(\mathfrak{n}(U)) + \partial_x(\mathfrak{G}(U)) \leq 0\,, \tag{I .53}$$

which can be interpreted by the fact that we force the total entropy to be non-increasing with time. Note that for smooth solutions (I .53) actually comes down to an equality. Based on (I .53), and under several regularity hypothesis on the fluxes, existence and uniqueness results are provided by Kružkov's theory [175]. Thus, admissible solutions of the NSW system are those who satisfy (I .53), and usually called *entropy satisfying*.

In the case of the shallow water equations, and accounting for the bottom elevation, a couple entropy/flux is given by :

$$\begin{aligned} \mathfrak{n}(U,z) &= h\frac{|u|}{2} + \frac{gh^2}{2} + ghz\,, \\ \mathfrak{G}(U,z) &= u(\mathfrak{n}(U,z) + \frac{gh^2}{2})\,. \end{aligned} \tag{I .54}$$

At the numerical level, we work with the discrete equivalent of (I .53). Thus, we usually say that a numerical scheme satisfies a *discrete entropy inequality* associated with an entropy $\mathfrak{n}$ if, under an appropriate CFL, we have :

$$\mathfrak{n}(U_i^{n+1}, z_i) - \mathfrak{n}(U_i^n, z_i) + \frac{\Delta t}{\Delta x}\left(\mathfrak{G}_{i+1/2} - \mathfrak{G}_{i-1/2}\right) \leq 0\,, \tag{I .55}$$

$\mathfrak{G}_{i+1/2} = \mathfrak{G}(U_i^n, U_{i+1}^n, z_i, z_{i+1})$ being a numerical entropy flux function. As stated in [188], and under some suitable assumptions, the condition (I .55) is sufficient to guarantee that the weak solution obtained as the limit when the space step tends to zero is entropy satisfying in the sense of (I .53).

In the context of NSW equations, only a few schemes take this notion of stability under consideration. The kinetic approaches presented in [101, 240, 235] are part of them. Also note that, if a fully discrete entropy inequality is not verified, a semi-discrete inequality can be obtained with the hydrostatic reconstruction scheme (see [10, 39] for details). Let us finally remark that, though

generally hidden by other constraints in practically all the numerical works, the problem of preserving entropy inequalities when implementing boundary conditions should ideally be investigated. Some developments on this topic are available in [14]. The issue of entropy inequalities is left out in this work.

I.5.3 Steady states and survey on well balanced methods

In the following part we give a particular focus on the class of time independant solutions of Shallow Water equations . The solutions we are interested in obey to the following balance law :

$$\nabla.G(U) = B(U,z)\,. \tag{I .56}$$

In one dimension, seeking for smooth solutions on wet beds ($h > 0$) satisfying this relation, one finds the following family of steady states :

$$hu = cst \quad , \quad \frac{u^2}{2} + g(h+z) = cst\,. \tag{I .57}$$

Les us note in passing that based on these assumptions, one easily remarks that an equality is satisfied in (I .53) with the couple enotropy/flux given by (I .54). In many ways, the role played by these equilibrium states is fundamental, since they actually correspond to long time solutions of the system and govern the asymptotic behaviour of the flow. The inability in restoring such steady states may have dramatic repercussions regarding the convergence of the numerical solution, with appearance of noise and instabilities that can critically degrade the approximation, even after a few iterations. It should be clarified that in (I .56) the friction source term contribution is neglected. The long time behaviour of solutions subjected to resistance laws will be discussed in Chapter III . Also point out that a focus on the one dimensional case is sufficient to give a general overview of the problematic. An extensive study of the 2d case would only bring unnecessary complexity. For the sake of completeness, we refer to [242] for a derivation of steady states in two space dimensions.

On these aspects, research on numerical methods for the solutions of the Shallow Water system has attracted tremendous attention in the past years. The Finite Volume numerical discretization of the convective flux in the NSW equations has been extensively studied in many recent works. A useful result in computing such solutions is proposed in [20] with the C-property, referring to the ability of the scheme to exactly preserve the motionless steady state solution (also called *lake at rest* solution) :

$$\mathbf{u} = 0 \quad , \quad \eta = cte\,. \tag{I .58}$$

which alone already represents a complex issue. After the works of Greenberg and Leroux [138], such numerical methods are often called *well-balanced* methods. It is worthwhile to underline that generally, a basic approach does not lead to a well balanced scheme, and the discretization of both fluxes and source terms has

to be submitted to suitable adaptations in order to achieve this property. Indeed, going back to (I .56), we need an appropriate discretization of the bed slope source term, which exactly counteracts with the contribution of the numerical fluxes. Note that the capability to preserve *lake at rest*-type configurations is essential to obtain resolutions that make sense physically, in that it prevents from perturbations that would inexorably initiate incoherent motion and propagate along the domain. This phenomena can constitute a significant inconvenience in situations bringing into play flows evolving around their rest states, or expected to converge toward steady solutions.

Since the pioneering work of Bermudez and Vazquez [20], this need of an adequate discretization of the topography source term in the Shallow Water equations has been raised, and many researchers have developed well-balanced methods for the Shallow Water equations. These first results were based on the Q-schemes of Roe and Van Leer, with the introduction of appropriate upwind of the source, evaluated in the same way as the fluxes. Such a strategy, also encountered in the works of Glaister [126], is notably applied in [120]. Shortly thereafter, Greenberg and Leroux [138] and Gosse and Leroux [132] resolved this issue investigating the idea of accounting for the topography through the Riemann problem. This approach raised great popularity since the past years, and is used by Gallouët *et al* [118] for instance to include a varying topography in the general class of VFRoe-ncv schemes introduced earlier. In this connexion, one can also refer to the works of Bouchut [39], and complementary studies of Gosse [130, 131] and Greenberg *et al* [139]. Another principle of resolution is supplied by the so called Quasi-Steady Wave-Propagation algorithm introduced by Leveque [187], with the use of an enhanced Godunov type Finite Volume scheme allowing a simple centred discretization of the source. Mention can be made of the centred approach proposed by Russo [248], and the *interface method* of Jin [159], able to restore steady states in motion with second order accuracy in the scalar case. Concerning kinetic approaches, Perthame and Simeoni [235] suggested to reformulate their microscopic scheme taking into consideration possible reflections on bottom jumps (see also Botchorishvili *et al* [240] for works of a more general scope and convergence results).

Among the quantity of recent available techniques, one can mention the *hydrostatic reconstruction* proposed by Audusse *et al* [10]. The method involves the reconstruction of the bathymetry at the boundary interface, yielding a common value for the left and right states. Afterwards, water depth and discharge are re-evaluated accordingly and employed in the solver as new Riemann states. This modification allows the restoration of the C-property provided an appropriate discretization of the source. While initially employed in a kinetic scheme, such a method can be applied with any conservative solver for the homogeneous Shallow Water system. Together with an easy implementation and interesting positive preserving features, this partly explains its popularity, and distinguishes from aforementioned works, most of them being solver dependent. This method inspired many authors in a large variety of different contexts (see

[26, 60, 91] for some 1d applications, and [211, 222, 288, 182] for 2d applications on cartesian grids).

Of course, lots of other works are still regularly published to cure the problem of steady states preservation, with the progressive willingness to achieve better level of accuracy and handle more complex situations, while seeking for simplicity. Some interesting ideas can be found in [116], with the so called Modified Roe scheme (MRoe), allowing to handle wet/dry transitions. As for the two dimensional case, it's worthwhile to note that all the previous approaches admit natural extensions on cartesian grids. Concerning the 2d unstructured frame, the preservation of the lake at rest still stands for an ambitious challenge, around which the community remains very active. The hydrostatic reconstruction has been extended on unstructured triangulations [12], and has a large range of applications. Among them, we can mention the recent work of Dutykh *et al* [100] devoted to tsunami modelling for example, or the discontinuous Galerkin schemes proposed by Ern *et al* [96, 108]. Otherwise, various alternatives have been validated. In [200], a suitable balance with the source is reached by the mean of well balanced approximate evolution operators in the context of Finite Volume Evolution Galerkin (FVEG) method. Another procedure is adopted by Benkhaldoun *et al* [19], relying on an appropriate reconstruction of the source with respect a relevant sub grid. We finally underline some adaptations of the results of Bermudez and collaborators [20] available in [152, 151, 221]: the steady states are preserved through the projection of the source term integral onto the eigenvectors of the flux Jacobian, in the philosophy of the original work.

Remark I.5 .1. *We notice that all the aforementioned schemes have in common the set of equations (I .1) as starting point. There are, however, other convenient ways to formulate these equations, offering interesting perspectives with the view to treat the well balanced property. Two of these methods have been used in this work and will be described later on.*

Remark I.5 .2. *So far, we just have partially mentioned the preservation of the lake at rest in the framework of discontinuous Galerkin schemes. Even if some numerical techniques can be borrowed from Finite Volume Methods, this problem is far from being obvious, as both approximate vector solution and topography are no longer assumed as piecewise constant within the domain. This concern, especially pronounced when using unstructured meshes, will be further examined in next chapters.*

Although settling the problem of steady states preservation, we emphasize that the use of well balanced methods is not sufficient to guarantee stable and relevant approximations of Shallow Water flows. Indeed, the implementation of a suitable numerical model for the NSW equations involves additional constraints such as the capacity of maintaining positive water heights, and handling correctly dry interfaces. These points call for a deeper analysis of the schemes under consideration, or at least compatibility conditions with other techniques able to satisfy these supplementary requirements. The key ideas are restated in what follows.

I.5.4 Robustness and dry cells

A recurring problem in the numerical approximations of the NSW equations concerns the so called *robustness property*, which signify that the approximate solution stays in the set of admissible states (I .4) at each time step. The capacity of preserving the positivity of the water height is fundamental to avoid again the possible appearance of spurious oscillations or unbounded computations entailed by the production of non physical solutions. A scheme enjoying this property will be referred to as Θ - *preserving* in the next sections.

Another notable difficulty, closely related to robustness, is the ability to guarantee stable computations in the vicinity of dry areas, especially if the model pretends to deal with classical friction laws. Indeed, many Shallow Water applications involve rapidly moving interfaces between wet and dry areas, including dam break problems, flood waves and run-up phenomena at a coast with tsunamis for instance. When vanishing water depths are involved, the system losses hyperbolicity, and the classical methods based on characteristics decomposition of the fluxes and source terms such as those based on Roe's scheme may demonstrate some weaknesses. More generally, these situations require special attention, if only for the vector field reconstruction or the gravity waves speed evaluation. Thus, an inappropriate evaluation of low water depths states is very likely to cause instabilities, mostly characterized by spontaneous apparitions of undesirable perturbations in the neighbourhood of the water front. When attempting to remedy this problem, the most common practice is to force these quantities to zero as soon as the water height falls under a certain tolerance value ϵ, but this is generally not sufficient to provide totally satisfying results.

As a whole, the difficulty stands in the dual objective of accounting for these aspects within a well balanced approach. Shortly after the first propositions of well balanced schemes, this challenge has given one of the major research guidelines in the construction of NSW approximations. Among the successful attempts in the Finite Volume frame, the hydrostatic reconstruction method [10] and the kinetic scheme introduced in [235] have been shown to offer this possibility, as well as the central upwind scheme of Kurganov and Levy [181]. As for the Roe solver, we stress out the improvements brought by Castro *et al* [59] concerning robustness property and the capture of wet/dry fronts (see also [97] on these questions). In recent years, Berthon and Marche [26] proposed a novel advancement, establishing the robustness of VFRoe-ncv schemes. The problem of vanishing water height is addressed in Bollerman *et al* [34] who furnished an enhanced version of the FVEG evolution operator technique [200] accounting for dry cells. The success of the method lies in a particular reconstruction of the vector field whenever h is lower than a threshold value. The problem of lake at rest preservation in dry bed situations is also addressed. Also note that some additional techniques are employed in [92] or [221] to deal specifically with partly dry domains. This last work couples a traditional cut off technique to a casual re-evaluation of the source term whose role is to preserve flows at rest in

wet/dry configurations.

More elaborated works have been developed with a particular orientation toward nearshore hydrodynamics, to capture accurately more severe run up phenomena or any other complex evolution problem in the vicinity of coasts. An accurate description of moving shorelines is fundamental in practice since most of simulations involving real life processes aim at evaluating their impact on populations or targeted infrastructures. Among the class of approaches available, Eulerian methods with fixed grids are commonly employed [198], as well as Lagrangian and Eulerian methods with deformed grids whose role is to track the position of the shoreline (see [145, 202, 227, 297] for some reference works). Although being unavoidable in some cases, these methods have not been required in our numerical simulations. Hence, we do not give supplementary details, and refer to [209] for a more complete review.

Remark I.5 .3. *It should be stressed that the problem of vanishing water heights is even more present when the inclusion of friction terms is planned. According to the law under consideration, divisions by h can be involved and threaten the stability of the model. This issue is addressed in Chapter III .*
Let us also mention that the problem of robustness is not addressed here for discontinuous Galerkin schemes, and is postponed to Chapter IV .

I.6 Conclusion

In this chapter we proposed a succinct presentation of the 2d Shallow Water system, in the perspective of future resolutions in the context of unstructured meshes. On the basis of general Finite Volume methods, some Riemann solvers are introduced and the problem of boundary conditions is addressed. The model analysis also enables to broach some of the specific problems that are regularly encountered while focusing on these equations, allowing to anticipate and identify some of the future numerical difficulties.

Thus, this introductory part lays the groundwork for the construction of an appropriate numerical model. To summarize, an efficient and modern scheme for the NSW equations has to satisfy the following properties :

♯ 1 allow a simple and consistent discretization of the topography source term;

♯ 2 preserve the motionless steady states;

♯ 3 preserve the water height positivity;

♯ 4 allow the occurrence of dry states.

Taken together, these general conditions are undeniably a key issue, and should be kept in mind as far as possible. They appear indeed as the common feature on which is based the set of methods that will be presented.

Chapter II

Finite Volume discretization of the *Pre Balanced* system

II.1 Introduction

An interesting idea to minimize efforts in obtaining well-balanced and robustness properties, not mentioned so far, consists of considering the total free surface η instead of h as a flow variable. This method finds certainly its roots in the works of Zhou [302] with the so called Surface Gradient Methods, in which the free surface is preferred to the water height in the evaluation of the fluxes contributions within a Godunov type second order scheme. The strategy provides a balanced scheme by mean of a simple centred approach of the source. With the aim of preserving quiescent flows, the idea of exploiting the invariance of η during lake at rest situations has been subsequently followed by several authors, notably Xing and Shu [286] which suggested a modification of the Lax Friedrichs flux splitting to eliminate the viscosity term, thus reaching the C-property. In a 2d context, this substitution is performed by Bradford [42] for the evaluation of surface integrals in some correction terms. Meanwhile, an alternate formulation of NSW equations, using the free surface elevation ξ above the still water depth, was introduced by Rogers *et al* [247] with the objective of obtaining telescoping effects between fluxes and source contributions employing a Roe solver. In a similar way, Kurganov and Levy [179] and Russo [248] advanced the idea to directly replace h by $\eta - z$ in the set of primitive equations.

Nowadays, in view of the efficiency of the approach, and based on these pioneering works, many improvements and derivations have been proposed. Kurganov and Petrova [181] improved the original scheme [179] enforcing simultaneously well balancing and robustness, and Bryson *et al* [46] worked on an extension to unstructured triangulations. We also refer to [257] for another using on 2d cartesian grids, and [44] for an implementation on GPU and additional highlight of performances.

Contribution and objectives

In this work, we hence seek a discretization of the NSW model from such a point of view, working with the so called *pre-balanced* formulation presented by Liang and Borthwick in [194] to resolve the 1d equations. Following the authors, we remark that :

$$-\frac{g}{2}\nabla h^2 - gh\nabla z = -\frac{g}{2}\nabla(\eta^2 - 2\eta z) - g\eta\nabla z\,,$$

and reformulate the NSW equations in an alternative way :

$$\frac{\partial V}{\partial t} + \nabla \cdot H(V,z) = S(V,z)\,, \tag{II .1}$$

where

$$V = \begin{pmatrix} \eta \\ q_x \\ q_y \end{pmatrix}\ ,\ H(V,z) = \begin{pmatrix} q_x & q_y \\ uq_x + \frac{1}{2}g(\eta^2 - 2\eta z) & vq_x \\ uq_y & vq_y + \frac{1}{2}g(\eta^2 - 2\eta z) \end{pmatrix}\,, \tag{II .2}$$

and the underlying relation $\mathbf{u} = \dfrac{\mathbf{q}}{\eta - z}$ is kept in the writing of the equations for the sake of simplicity. The bed slope source term is given by :

$$S(V,z) = \begin{pmatrix} 0 \\ -g\eta\partial_x z \\ -g\eta\partial_y z \end{pmatrix}, \tag{II .3}$$

We have to specify that (II .1) is valid in the weak sense for continuous topographies, allowing to consider as well discontinuous solutions for the flow variable. Also, this system is still hyperbolic, and has the same eigenstructure as (I .1). The main advantage of (II .1) is that a very simple well-balanced scheme can be built from any numerical flux and a trivial discretization of the bed-slope source term. It should be noticed that the convenient aspects of this formulation have been successfully exploited in several efficient well-balanced and robust FVM (for example [195, 282] in 1d and 2d cartesian grids respectively). We aim at extending these properties in the frame of unstructured meshes, preserving as much as possible a reasonable level of complexity. In the sequel, the acronym PBSW (standing for *Pre Balanced Shallow Water*) will be used to refer to these equations.

Keeping in mind the objectives previously mentioned, one of the main features of the approach is its great simplicity and unified formulation, for both first order scheme and its MUSCL extensions: there is no need to introduce some additional source terms discretizations to ensure the well-balancing and consistency properties. Additionally, the C-property can be established independently from the numerical flux used for the homogeneous equations. We also investigate several ways to ensure the preservation of the positivity of the water depth, with a particular focus on the HLL scheme. Provided the first order scheme is $\Theta-$preserving, the preservation of admissible states is equally ensured for the MUSCL reconstructions. The development of the resulting code lead to the publication [-1-].

This work is structured around the following points : after having resettled some 1d results, we propose in a first time an extension of the *pre balanced* Finite Volume approach on unstructured meshes, that naturally preserves the well balanced and robustness properties of the original scheme. Some results are given concerning the preservation of admissible states. The second component is devoted to high order extensions of the model, presented in Section §II.3 . They help maintaining an interesting degree of simplicity and respect the properties stated in the first order case as well. The scheme's abilities are finally solicited during a fairly complete set of challenging applications, including dry cells, irregular bottom variations, non trivial geometries with eventually local mesh refinement.

II.2 Finite Volume approach

II.2.1 The 1d case

In a first time we need to remember a possible approach of the 1d *pre-balanced* system related to (II .1). Let's consider a regular partition of the computational domain with a space step Δx. In the present Godunov-type Finite Volume framework, using a Euler scheme in time for the sake of simplicity, and denoting V_i the flow variable approximation on the i^{th} cell, the flow update from time t^n to time $t^{n+1} = t^n + \Delta t$ is governed by the classical relation :

$$V_i^{n+1} = V_i^n - \frac{\Delta t}{\Delta x}(\mathcal{H}_{i+\frac{1}{2}} - \mathcal{H}_{i-\frac{1}{2}}) + \Delta t S_i \,, \tag{II .4}$$

where $\mathcal{H}_{i-\frac{1}{2}}$ are $\mathcal{H}_{i+\frac{1}{2}}$ are the numerical fluxes and S_i stands for a discretization of the bed slope. The evaluation of the exchanging fluxes $\mathcal{H}_{i-\frac{1}{2}}$ and $\mathcal{H}_{i+\frac{1}{2}}$ is based on the resolution of a local Riemann problem involving reconstructed states at each side of the interfaces $i-1/2$ and $i+1/2$. They take the form :

$$\mathcal{H}_{i-\frac{1}{2}} = \mathcal{H}(\check{V}^-_{i-\frac{1}{2}}, \check{V}^+_{i-\frac{1}{2}}, \check{z}_{i-\frac{1}{2}}, \check{z}_{i-\frac{1}{2}}) \quad , \quad \mathcal{H}_{i+\frac{1}{2}} = \mathcal{H}(\check{V}^-_{i+\frac{1}{2}}, \check{V}^+_{i+\frac{1}{2}}, \check{z}_{i+\frac{1}{2}}, \check{z}_{i+\frac{1}{2}}) \,, \tag{II .5}$$

where a double dependency with z is introduced, to account for the presence of the topography in the convective fluxes. The evaluation of these intermediate states is explained in the following lines.

Borrowing the pioneering ideas of [10], the reconstruction process starts by the introduction of a new interface value for the bed elevation :

$$\tilde{z} = \max(z^-, z^+) \,, \tag{II .6}$$

and the following positive reconstruction of the water depth component (see [195]) :

$$\check{h}^\pm = \max(0, \eta^\pm - \tilde{z}) \,. \tag{II .7}$$

In the lines above, and in the sequel, the superscripts "$-,+$" will stand for the *interior* and *exterior* values, to be consistent with the previous notations. In the present first order context, and at the interface $i+1/2$, they explicitly correspond to the variable value on the cells i and $i+1$ respectively. On this basis, new interface values for the free surface and discharge are defined by :

$$\begin{aligned} \check{\eta}^- &= \check{h}^- + \tilde{z} \quad , \quad \check{q}^- = \frac{\check{h}^-}{h^-} q^- \,. \\ \check{\eta}^+ &= \check{h}^+ + \tilde{z} \quad , \quad \check{q}^+ = \frac{\check{h}^+}{h^+} q^+ \,. \end{aligned} \tag{II .8}$$

Remark II.2 .1. *In (II .8) , we implicitly assumed that we have $h^\pm > 0$ in the evaluation of the discharge. The case $h^\pm = 0$ (or numerically $h^\pm < \epsilon$) is classically handled by setting the corresponding values of $q^\pm$ (and $u^\pm$ if needed) to 0.*

We follow the procedure at each interface problem involved in (II .4). As stated in [195], these new values can be directly injected in the numerical fluxes, leading to a well-balanced scheme that also ensures non-negative water depths, provided the use of an appropriate Riemann solver. However, this strategy requires the introduction of additional source terms in order to ensure the preservation of motionless steady states (I .58) in wet/dry contexts. To avoid this, one can consider the following parameter :

$$\Delta z^- = \max(0, \tilde{z} - \eta^-)\,, \tag{II .9}$$

specifically introduced to account for such particular configurations (see Fig. II .1). Finally, a new intermediate state for the topography is defined as :

$$\breve{z} = \tilde{z} - \Delta z^-, \tag{II .10}$$

and the free surface is obtained after subtraction from the original value :

$$\breve{\eta}^{\pm} = \breve{h}^{\pm} + \tilde{z} - \Delta z^- \tag{II .11}$$

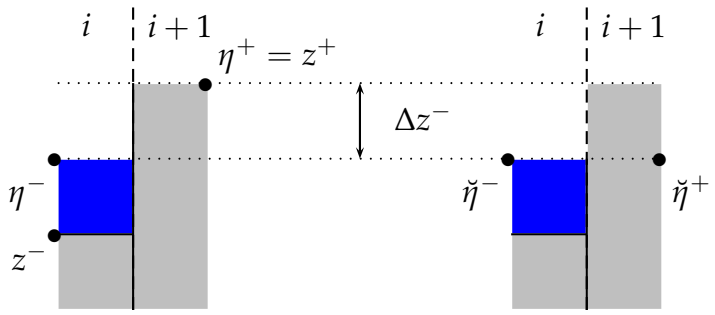

Figure II .1: Non-negative reconstruction : Case of a wet/dry interface.

Obviously, this additional step does not affect the flow variables in wet bed applications. To obtain the C-property, this reconstruction step can be combined with this simple centred discretization of the source :

$$S_i = \begin{pmatrix} 0 \\ -g\hat{\eta}_i \left(\dfrac{\breve{z}_{i+\frac{1}{2}} - \breve{z}_{i-\frac{1}{2}}}{\Delta x} \right) \end{pmatrix}, \tag{II .12}$$

where :

$$\hat{\eta}_i = \frac{\breve{\eta}^+_{i-\frac{1}{2}} + \breve{\eta}^-_{i+\frac{1}{2}}}{2}, \tag{II .13}$$

and the subscripts $i \pm 1/2$ indicate the interface on which the reconstruction is performed.

We give now a rapid recall concerning the C-property.

Consider first the case of a "wet/wet" steady state, that is $u = 0, \eta = \eta_c = cte$ on the cell i and its neighbours. Involving steps (II .6 - II .11) and assuming the consistency of the numerical fluxes (II .5) (in the sense of (I .22)), it's straightforward to verify that :

$$\frac{1}{\Delta x}\left(\mathcal{H}_{i+\frac{1}{2}} - \mathcal{H}_{i-\frac{1}{2}}\right) = \frac{1}{\Delta x}\left(\begin{pmatrix} 0 \\ \frac{1}{2}g(\eta_c^2 - 2\eta_c \check{z}_{i+\frac{1}{2}}) \end{pmatrix} - \begin{pmatrix} 0 \\ \frac{1}{2}g(\eta_c^2 - 2\eta_c \check{z}_{i-\frac{1}{2}}) \end{pmatrix}\right) = S_i\,, \tag{II .14}$$

so that (II .4) gives $V_i^{n+1} = V_i^n$.

In the situation where the interface $i + 1/2$ is supposed to be of type "wet/dry" (Fig. II .1), the reconstruction also yields $\check{V}_{i\pm\frac{1}{2}} = (\eta_c, 0)$ and $\hat{\eta}_i = \eta_c$, allowing to recover the wet case. The cases "dry/wet" and "dry/dry" can also be easily treated (we refer to [282] for more details). A more detailed proof is available in Proposition 3 in a purely 2d context to treat both first order scheme and its high order extensions. We now actually intend to propose an extension of this scheme in 2d and on unstructured meshes.

Remark II.2 .2. *So far we did not evoked the robustness property. The problem of preservation of water depth positivity will be simultaneously addressed for the 1d and 2d schemes in the next section.*

II.2.2 Extension to the unstructured case

Let's move on to the two dimensional case. Still working in a Godunov type Finite Volume framework, we suggest to advance in time with the usual formula (see §I.2 and Fig. I .2 for notations) :

$$V_i^{n+1} = V_i^n - \frac{\Delta t}{|C_i|}\sum_{k=1}^{\Lambda(i)} \ell_{ij(k)}\mathcal{H}_{ij(k)} + \Delta t S_i\,, \tag{II .15}$$

where $\mathcal{H}_{ij(k)}$, $k = 1, \cdots, \Lambda(i)$ are the exchanging fluxes between the cell C_i and its neighbours $C_{j(k)}$, and S_i denotes the bottom source term discretization. Following the 1d procedure, we write :

$$\mathcal{H}_{ij(k)} = \mathcal{H}(\check{V}_k^-, \check{V}_k^+, \check{z}_k, \check{z}_k, \vec{n}_{ij(k)})\,, \tag{II .16}$$

and aim at proposing a non-negative reconstruction for the Riemann states that allow the restoration of the well-balanced property, even if dry zones are involved. Therefore, for a given interface $\Gamma_{ij(k)}$, we define a single valued term for the topography :

$$\tilde{z}_k = \max(z_k^-, z_k^+)\,, \tag{II .17}$$

where z_k^-, z_k^+ refer to the *interior* and *exterior* values at the interface $\Gamma_{ij(k)}$. Using similar notations for the other variables of interest, the water depth reconstruction is given by :

$$\check{h}_k^- = \max(0, \eta_k^- - \tilde{z}_k)\,,\ \check{h}_k^+ = \max(0, \eta_k^+ - \tilde{z}_k)\,, \tag{II .18}$$

and, gathering steps (II .8 - II .11), we naturally set :

$$\begin{aligned} \check{z}_k &= \tilde{z}_k - \max(0, \tilde{z}_k - \eta_k^-)\,, \\ \check{\eta}_k^- &= \check{h}_k^- + \check{z}_k \quad , \quad \check{\mathbf{q}}_k^- = \frac{\check{h}_k^-}{h_k^-}\mathbf{q}_k^-\,, \\ \check{\eta}_k^+ &= \check{h}_k^+ + \check{z}_k \quad , \quad \check{\mathbf{q}}_k^+ = \frac{\check{h}_k^+}{h_k^+}\mathbf{q}_k^+\,, \end{aligned} \tag{II .19}$$

with the necessary caution mentioned in Remark II.2 .1 for the treatment of vanishing water depths. To complete the numerical scheme, we introduce the following discretization of the bottom source term :

$$S_i = \frac{1}{|C_i|}\sum_{k=1}^{\Lambda(i)} \ell_{ij(k)} S_{ij(k)} = \frac{1}{|C_i|}\sum_{k=1}^{\Lambda(i)} \ell_{ij(k)} \begin{pmatrix} 0 \\ g\hat{\eta}_k(z_i - \check{z}_k)\vec{n}_{ij(k)} \end{pmatrix}\,, \tag{II .20}$$

where

$$\hat{\eta}_k = \frac{\eta_i + \check{\eta}_k^-}{2}\,. \tag{II .21}$$

The motivations for this choice of $\hat{\eta}_k$ are twofold. The first point is linked to the general problem of consistency, meaning that the set of contributions $S_{ij(k)}$ actually has to provide a correct approximation of the physical source term issuing from the continuous equations. This property will be further discussed in Proposition 3. The second, more specific, concerns the structure of the scheme. Indeed, from such a point of view, this particular choice for $\hat{\eta}_k$ has important consequences, since the numerical approach can actually be seen as convex combinations of 1d schemes of the form (II .4). In the following lines, this feature is detailed and exploited to obtain a proof of the robustness and C-properties in a considerably simple way, with a straightforward stability criteria :

Proposition 1. *We assume known a consistent numerical flux function for the 1d scheme (II .4) associated with the reconstruction (II .6 - II .11), allowing to preserve the water height positivity under a time constraint of the form :*

$$a\frac{\Delta t}{\Delta x} \leq \tau_{CFL}\,, \tag{II .22}$$

where $a = \max_{i\in\mathbb{Z}}\left(|\lambda^-_{i+\frac{1}{2}}|, |\lambda^+_{i+\frac{1}{2}}|\right)$ *and* $\lambda^\pm_{i+\frac{1}{2}}$ *are the maximum and minimum velocity waves employed in the Riemann solver at the interface* $i+1/2$*. Then, the scheme (II .15 - II .19, II .20) preserves the water height positivity under the CFL condition (I .48), that is :*

$$\begin{aligned} a_i\frac{\Delta t}{\delta_{ij(k)}} &\leq \tau_{CFL}\,, \quad \forall C_i\,,\, k = 1, \cdots, \Lambda(i)\,, \\ a_i &= \max_{k=1,\cdots,\Lambda(i)}\left(|\lambda_k^-|\,,\, |\lambda_k^+|\right)\,, \end{aligned} \tag{II .23}$$

and satisfies the C-property.

Proof. The key idea is to rewrite (II .15) as a convex combination of 1d schemes. To this end, we use the set of sub-triangles $(T_{ij(k)})_{k=1,\cdots,\Lambda(i)}$ introduced in the previous Chapter (Fig. I .2). In the spirit of [24], the current scheme is recast under the following form :

$$V_i^{n+1} = \sum_{k=1}^{\Lambda(i)} \frac{|T_{ij(k)}|}{|C_i|} V_{ij(k)}^{n+1}, \tag{II .24}$$

where each convex component is defined as :

$$V_{ij(k)}^{n+1} = V_i^n - \frac{\Delta t}{\delta_{ij(k)}} \left(\mathcal{H}_{ij(k)} - \mathcal{H}_{ij(k)}^c \right) + \frac{\Delta t}{\delta_{ij(k)}} S_{ij(k)}, \tag{II .25}$$

and we have set $\mathcal{H}_{ij(k)}^c = H(V_i^n, z_i).\vec{n}_{ij(k)}$. We also recall that $\delta_{ij(k)} = |T_{ij(k)}|/\ell_{ij(k)}$. Involving the solver's consistency and the steps (II .17, II .18, II .19), one can easily verify that $\mathcal{H}_{ij(k)}^c$ corresponds to the numerical flux in the direction $\vec{n}_{ij(k)}$ evaluated with V_i^n as "left" and "right" Riemann states. It follows that relation (II .25) is nothing but the 1d scheme (II .4) applied to the states $V_i^n, V_i^n, V_{j(k)}^n$ in the direction $\vec{n}_{ij(k)}$, and with a space step $\delta_{ij(k)}$ (Fig. II .2). Consequently, according to (II .24), the preservation of the water height positivity is directly inherited from the 1d numerical model, leading to the criteria (II .23).

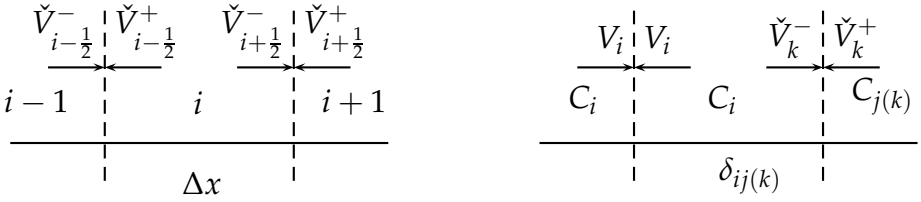

Figure II .2: Left and right Riemann states for the 1d and 2d schemes.

The C-property can also be straightforwardly deduced from this construction, arguing that formula (II .24) preserves the motionless steady states as soon as (II .25) does. This also stands for the consistency with the Saint-Venant equations with source term (II .3). □

We now show that this general result of robustness can be applied to the Lax-Friedrichs and HLL schemes. As a matter of fact, the proof can be straightforwardly derived from a strictly 2d analysis which itself provides a very close time step limitation. As this more general result will be useful in the sequel, we propose to detail the 2d case, and subsequently establish the links with the 1d scheme.

Proposition 2. *We consider the following first order scheme for the free surface :*

$$\eta_i^{n+1} = \eta_i^n - \frac{\Delta t}{|C_i|} \sum_{k=1}^{\Lambda(i)} \ell_{ij(k)} \mathcal{H}_{ij(k)}^{\eta}, \tag{II .26}$$

where the numerical fluxes $\mathcal{H}^{\eta}_{ij(k)} = \mathcal{H}^{\eta}(\check{V}_k^-, \check{V}_k^+, \check{z}_k, \check{z}_k, \vec{n}_{ij(k)})$ *are computed with the HLL solver, and* $\check{V}_k^-, \check{V}_k^+, \check{z}_k$ *are given by the reconstruction steps (II .17,II .18,II .19). Assume that* h_i^n *and* $h_{j(k)}^n$, $k = 1, \cdots, \Lambda(i)$ *are positive. Then, under the CFL condition :*

$$\max_{i\in\mathbb{Z}} a_i \frac{\Delta t}{|C_i|}\mathfrak{p}_i \leq 1\,, \tag{II .27}$$

where

$$\begin{aligned} a_i &= \max_{k=1,\cdots,\Lambda(i)} \lambda_k\,, \\ \lambda_k &= \max\left(|\mathbf{u}_k^-.\vec{n}_{ij(k)}| + \sqrt{gh_k^-}\,,\, |\mathbf{u}_k^+.\vec{n}_{ij(k)}| + \sqrt{gh_k^+}\right), \end{aligned} \tag{II .28}$$

we have $h_i^{n+1} \geq 0$.

Proof. For a given interface $\Gamma_{ij(k)}$, let's first denote the normal velocities as $\mathfrak{u}_k^{\pm} = \mathbf{u}_k^{\pm}.\vec{n}_{ij(k)}$, and introduce the following notations for the HLL wave speeds (I .24) :

$$\begin{aligned} s_k^- &= \min(\mathfrak{u}_k^- - c_k^-, \mathfrak{u}_k^+ - c_k^+)\,, \\ s_k^+ &= \max(\mathfrak{u}_k^- + c_k^-, \mathfrak{u}_k^+ + c_k^+)\,, \\ \Delta s_k &= s_k^+ - s_k^-\,. \end{aligned}$$

We now introduce the following notations :

$$\mathfrak{s}_k^+ = \max(0, s_k^+)\,,\ \mathfrak{s}_k^- = \min(0, s_k^-)\,,\ \Delta\mathfrak{s}_k = \mathfrak{s}_k^+ - \mathfrak{s}_k^-\,,$$

so that the HLL flux (I .28) can be recast into :

$$\mathcal{H}^{\eta}_{ij(k)} = \frac{\mathfrak{s}_k^+\check{h}_k^-\mathfrak{u}_k^- - \mathfrak{s}_k^-\check{h}_k^+\mathfrak{u}_k^+ + \mathfrak{s}_k^+\mathfrak{s}_k^-(\check{\eta}_k^+ - \check{\eta}_k^-)}{\Delta\mathfrak{s}_k}\,.$$

According to (II .19), we have $\check{\eta}_k^+ - \check{\eta}_k^- = \check{h}_k^+ - \check{h}_k^-$, leading to :

$$\mathcal{H}^{\eta}_{ij(k)} = \frac{\mathfrak{s}_k^+\check{h}_k^-(\mathfrak{u}_k^- - \mathfrak{s}_k^-)}{\Delta\mathfrak{s}_k} + \frac{\mathfrak{s}_k^-\check{h}_k^+(\mathfrak{s}_k^+ - \mathfrak{u}_k^+)}{\Delta\mathfrak{s}_k}\,.$$

Then, subtracting z_i on both sides of (II .26) :

$$h_i^{n+1} = h_i^n\left(1 - \frac{\Delta t}{|C_i|}\sum_{k=1}^{\Lambda(i)}\ell_{ij(k)}\frac{\check{h}_k^-}{h_i^n}\frac{\mathfrak{s}_k^+(\mathfrak{u}_k^- - \mathfrak{s}_k^-)}{\Delta\mathfrak{s}_k}\right) - \frac{\Delta t}{|C_i|}\sum_{k=1}^{\Lambda(i)}\ell_{ij(k)}\frac{\mathfrak{s}_k^-\check{h}_k^+(\mathfrak{s}_k^+ - \mathfrak{u}_k^+)}{\Delta\mathfrak{s}_k}\,. \tag{II .29}$$

Finally, arguing that $\dfrac{\check{h}_k^-}{h_i^n} \in [0,1]$, we have :

$$\frac{\check{h}_k^-}{h_i^n}\frac{\mathfrak{s}_k^+(\mathfrak{u}_k^- - \mathfrak{s}_k^-)}{\Delta\mathfrak{s}_k} \leq \frac{\mathfrak{s}_k^+(\mathfrak{u}_k^- - \mathfrak{s}_k^-)}{\Delta\mathfrak{s}_k} \leq \frac{\mathfrak{s}_k^+\Delta\mathfrak{s}_k}{\Delta\mathfrak{s}_k} \leq a_i.$$

As a consequence, under (II .27), the second member in equality (II .29) is the sum of two positive values. The proof is complete. □

Remark II.2 .3. *This results also stands for the Lax - Friedrichs fluxes, as it can be seen as a particular case of the HLL fluxes (see I.3.2.a).*

Remark II.2 .4. *This proof can be straightforwardly adapted to the 1d case, giving a time step constraint of the form :*

$$a\frac{\Delta t}{\Delta x} \leq \tau_{CFL}\,, \tag{II .30}$$

where $a = \max_{i\in\mathbb{Z}}(|u_i \pm c_i|)$*, with a CFL equal to* $\tau_{CFL} = \frac{1}{2}$*, and the relaxed condition* $\tau_{CFL} = 1$ *when using the Global Lax Friedrichs scheme (see [291] for instance). Note that the resulting time constraint (II .23) is almost equivalent to (II .27) in practice, though being slightly more stringent. This can be seen as the counterpart of the method based on 1d schemes for having a more general applicability.*

II.3 Formal "Second order" reconstruction

From a general point of view, the diffusive losses entailed by the consideration of first order schemes generally require the implementation of numerical techniques devoted to increase the space accuracy. This problem arises notably in the context of FVM with the use of cell-averaged approximations. To overcome these limitations, lots of numerical methods have been developed within the Computational Fluid Dynamics (CFD) community. In the spirit of the MUSCL method of Van Leer [276], the desired gain in space accuracy can be reached by a preliminary reconstruction of the flow variable at each interface, supplemented by a limiting strategy, to avoid oscillations in the vicinity of discontinuities. In this connexion, Harten [143] later introduced the concept of Total Variation Diminishing (TVD) schemes, that preserves monotonicity and consequently prevents from appearance of local extrema, to obtain approximations free from unrealistic oscillations. Such class of schemes are robust, but only first order accurate in the neighbourhood of discontinuities. This entails truncation errors that may bring excessive numerical dissipation. To limit these disadvantages, some alternatives were later proposed, with the apparition of Essentially Non Oscillatory (ENO) schemes [142, 256], followed by the so called Weighted Essentially Non Oscillatory WENO schemes [156, 199].

These pioneering works paved the way for amounts of complementary studies, extensions or attempts of improvements, and multiple applications to NSW equations have been proposed. It should be stressed that one of the main difficulties often encountered when seeking high order resolutions of NSW equations is not to break the well-balanced and robustness properties of the first order scheme. This is a serious threat when reconstructed values are proposed at each interface. In [10] for instance, the topography also needs to be modified and an additional source term has to be introduced to preserve the C-property. On that subject, we refer to [222] for higher order extensions of the hydrostatic reconstruction, and to [54, 56, 163, 280, 286, 288] for other examples of well-balanced high order schemes devoted to NSW equations. Also require

emphasis the general success of high order central schemes [30, 178, 284, 236], and attached applications to multidimensional problems [157, 180, 190]. These approaches are also extended to the 2d NSW system in [179, 248], by mean of cartesian grids. Let us finally mention the difficult issue of well-balancing for general moving water steady states. Very few high-order accuracy methods are able to maintain such general steady steady states, see for instance the recent works [61, 223]. However, it is shown in [289] that moving-water well-balanced schemes exhibit some advantages when compared to motionless steady states preserving methods.

Naturally, carrying out high order methods on unstructured grids require supplementary effort. Amongst many others, some notable advances in CFD concerning high order extensions on general meshes were proposed by Abgrall [1], Barth and Jespersen [16], Barth and Frederickssson [15], Friedrich [115], Ollivier-Gooch [225], Perthame and Qiu [233] and others. We can also mention Arminjon *et al* [8] for an unstructured extension of the central scheme proposed by Nessyahu and Tadmor [220], and Venkatakrishnan [278], where the issue of convergence toward steady states is addressed. Nowadays, numbers of efficient approaches issuing from CFD are available, based on least squares methods, centred or upwind gradients, linear gradient approximations, and combined with low diffusive limiting strategies. Based on these ideas, there are many ways to increase the accuracy of the proposed first order scheme, keeping in mind that careful attention has to be paid to the preservation of the properties originally established. Note that in the context of unstructured meshes, in addition of concerns around steady states, the question of preservation of water height positivity is also far from trivial, see [21, 234].

We present here two possible strategies inspired from MUSCL methods. Both have in common the double objective of improving the order of space accuracy, while maintaining the features of the first order scheme. This is achieved by substituting the primitive values in the numerical flux function with better interpolations at the interface, and an additional coupling with appropriate limiting procedures. We actually aim at providing piecewise linear approximations of the variables $V = (\eta, q_x, q_y)$ at each cell face. In the sequel, it will be useful to work with an augmented vector variable that also includes the water height $\hat{V} = (h, \eta, q_x, q_y)$. Indeed, reconstructions on water depth are also necessary in the perspective of well-balanced issues. As previously mentioned, it actually allows to re-evaluate the topography appropriately so as to recover the balance between fluxes and source terms provided by the first order scheme. As regards robustness, we adapt the general strategy introduced in [21].

The two methods involve gradients obtained from $\mathbb{P}^1$ (continuous and linear) interpolations of the solution on relevant triangular sub-grids. For a fixed triangle T, such an approximation will be denoted $\nabla \hat{V}_T$ in the next sections. It can be directly determined having knowledge of the approximate solution at each of the three nodes. For a given element T, denoting $(A_i)_{i=1,\cdots,3}$ the nodes

and $(\vec{n}_i)_{i=1,\cdots,3}$ the corresponding outward normals (see Fig. II .3), the linear approximation of the variable on T can be written as :

$$\hat{V}_T = \sum_{i=1}^{3} \hat{V}_{T,i} l_i \,, \tag{II .31}$$

where $(l_i)_{i=1,\cdots,3}$ refers to the Lagrangian basis associated to T. More explicitly, one has, for a given point $M(x,y)$ in T :

$$l_i(M) = 1 - \frac{\overrightarrow{A_i M}.\vec{n}_i}{\|\overrightarrow{A_i A_j}\|} \,, \quad i = 1,2,3 \,, \quad j \neq i \,, \tag{II .32}$$

so that we have :

$$\nabla \hat{V}_T = -\sum_{i=1}^{3} \hat{V}_{T,i} \frac{\vec{n}_i}{\|\overrightarrow{A_i A_j}\|} \,. \tag{II .33}$$

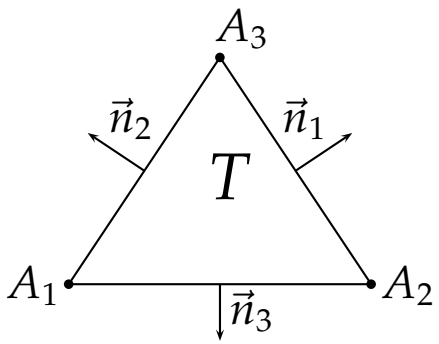

Figure II .3: $\mathbb{P}_1$ gradient approximation for a given element T.

II.3.1 A first example

We present and adapt here the MUSCL method described in [12]. The carrying out requires some manipulations involving the set of sub cells $T_{ij(k)}$ introduced in the previous chapter (see Fig. II .4). We consider now the problem at an edge $\Gamma_{ij(k)}$. Denoting its midpoint P_k, the piecewise linear reconstruction is expressed as follows :

$$\hat{V}^*_{(1)} = \hat{V}_i + \overrightarrow{M_i P_k}.\nabla \hat{V}_k \,, \tag{II .34}$$

where $\nabla \hat{V}_k$ denotes an appropriate limited gradient. The evaluation of $\nabla \hat{V}_k$ is based on a gradient approximation on C_i, computed by the following weighted average :

$$\nabla \hat{V}_i = \frac{\sum_{k=1}^{\Lambda(i)} |C_k| \nabla \hat{V}_{T_{ij(k)}}}{\sum_{k=1}^{\Lambda(i)} |C_k|} \,,$$

and a second quantity, accounting for the variations of $\hat{V}$ at the corresponding edge :

$$\nabla \hat{V}_\beta = (1+\beta)\nabla \hat{V}_i - \beta \nabla \hat{V}_{T_{ij(k)}} \qquad 0 \leq \beta \leq 1 \,.$$

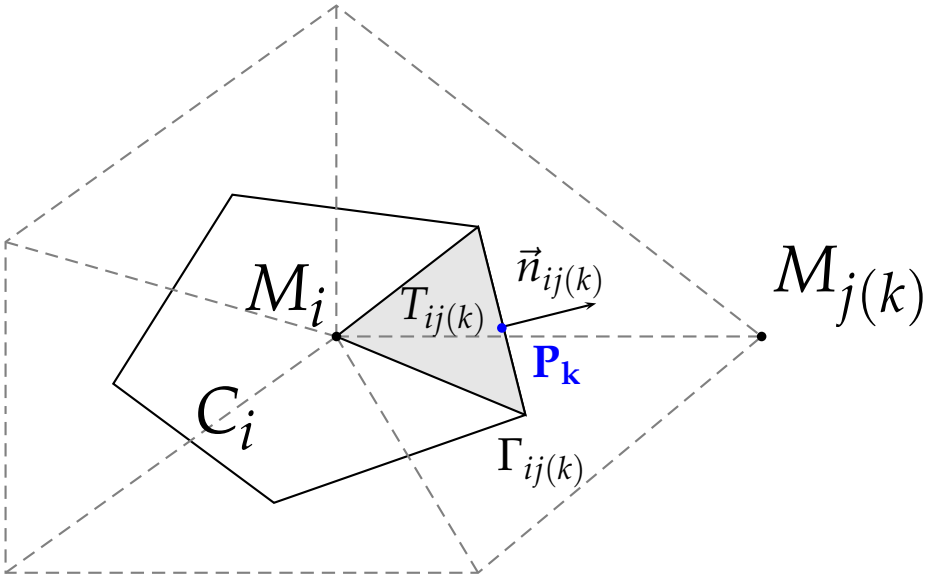

Figure II .4: Second order reconstruction : Focus on the interface $\Gamma_{ij(k)}$.

These approximate gradients are then involved in a classical limitation step :

$$\nabla \hat{V}_k = \text{minmod}(\nabla \hat{V}_{T_{ij(k)}}, \nabla \hat{V}_\beta)\,, \tag{II .35}$$

where the *minmod* limiter is defined as :

$$\text{minmod}(a,b) = \begin{cases} s\min(|a|,|b|) & \text{if} \quad s = sgn(a) = sgn(b)\,, \\ 0 \quad \text{otherwise}\,. \end{cases} \tag{II .36}$$

Of course, concerning the limiter, many other choice are possible to enhance the diffusive properties of the reconstruction. To finalize the procedure, a last step is applied on the water height obtained from (II .34) to provide a conservative reconstruction (see [12, 233]) :

$$h^* = h_i + \beta^+ (h^*_{(1)} - h_i)_+ - \beta^- (h^*_{(1)} - h_i)_-\,, \tag{II .37}$$

where

$$\beta^\pm = \min\left(1, \frac{\sum_{k=1}^{\Lambda(i)} |T_{ij(k)}| (h^*_{(1)} - h_i)_\mp}{\sum_{k=1}^{\Lambda(i)} |T_{ij(k)}| (h^*_{(1)} - h_i)_\pm}\right)\,,$$

and with the standard notations $x_- = \max(0,-x)$, $x_+ = \max(0,x)$.

At each interface $\Gamma_{ij(k)}$, we deduce from (II .34, II .37) piecewise linear reconstructed variable vectors $V_k^{*,\pm} = {}^t(\eta_k^{*,\pm}, \mathbf{q}_k^{*,\pm})$ for the conservative variables, together with new edges values for the topography :

$$z_k^{*,\pm} = \eta_k^{*,\pm} - h_k^{*,\pm}\,. \tag{II .38}$$

From this, the new Riemann states are now defined as follows :

$$\tilde{z}_k^* = \max(z_k^{*,-}, z_k^{*,+})\,, \quad \breve{z}_k^* = \tilde{z}_k^* - \max(0, \tilde{z}_k^* - \eta_k^{*,-})\,, \tag{II .39}$$

and

$$\check{h}_k^{*,-} = \max(0, \eta_k^{*,-} - \tilde{z}_k^*) \quad , \quad \check{\eta}_k^{*,-} = \check{h}_k^{*,-} + \tilde{z}_k^* \quad , \quad \check{\mathbf{q}}_k^{*,-} = \frac{\check{h}_k^{*,-}}{h_k^{*,-}} \mathbf{q}_k^{*,-} , \tag{II .40}$$

$$\check{h}_k^{*,+} = \max(0, \eta_k^{*,+} - \tilde{z}_k^*) \quad , \quad \check{\eta}_k^{*,+} = \check{h}_k^{*,+} + \tilde{z}_k^* \quad , \quad \check{\mathbf{q}}_k^{*,+} = \frac{\check{h}_k^{*,+}}{h_k^{*,+}} \mathbf{q}_k^{*,+} , \tag{II .41}$$

leading to the new face values :

$$\check{V}_k^{*,-} = (\check{\eta}_k^{*,-}, \check{\mathbf{q}}_k^{*,-}), \quad \check{V}_k^{*,+} = (\check{\eta}_k^{*,+}, \check{\mathbf{q}}_k^{*,+}) . \tag{II .42}$$

At this point, only remains to be proposed an appropriate discretization of the source term. Actually, as it will be established in the next lines, we can keep the original formulation, without losing the properties of the first order scheme. We thus take :

$$S_i = \frac{1}{|C_i|} \sum_{k=1}^{\Lambda(i)} \ell_{ij(k)} S_{ij(k)} = \frac{1}{|C_i|} \sum_{k=1}^{\Lambda(i)} \ell_{ij(k)} \begin{pmatrix} 0 \\ g\hat{\eta}_k (z_i - \tilde{z}_k^*) \vec{n}_{ij(k)} \end{pmatrix} , \tag{II .43}$$

where

$$\hat{\eta}_k = \frac{\eta_i + \check{\eta}_k^{*,+}}{2} , \tag{II .44}$$

and the MUSCL Finite Volume scheme becomes :

$$V_i^{n+1} = V_i^n - \frac{\Delta t}{|C_i|} \sum_{k=1}^{\Lambda(i)} \ell_{ij(k)} \mathcal{H}(\check{V}_k^{*,-}, \check{V}_k^{*,+}, \tilde{z}_k^*, \tilde{z}_k^*, \vec{n}_{ij(k)}) + \Delta t S_i . \tag{II .45}$$

We now establish the consistency and well-balancing properties satisfied by the current MUSCL scheme, summarized within the following result :

Proposition 3. *We consider a numerical flux function $\mathcal{H}$ for the scheme (II .42, II .43, II .45), consistent with the exact flux in the sense of (I .22) and high order MUSCL reconstructions (II .34) for the face values. Then, the scheme satisfies the following properties :*

1. *well-balancing: the motionless steady states are preserved.*
2. *consistency with the Saint-Venant equations with source term (II .3).*

Proof. The first part of the proof revolves around two typical cases :

i) We consider the classical situation where C_i and all the neighbouring cells are wet, and suppose an initial static equilibrium, formulated as :

$$\eta_{j(k)} = \eta_i = \eta_c \quad , \quad \mathbf{u}_i = \mathbf{u}_{j(k)} = 0 \quad , \ \forall k = 1, \cdots, \Lambda(i) .$$

The piecewise linear reconstruction (II .34) directly gives $\eta_k^{*,\pm} = \eta_c$, and consequently :

$$\tilde{z}_k^* = \max(\eta_c - h_k^{*,-}, \eta_c - h_k^{*,+}) \leq \eta_c .$$

We deduce from this :

$$\check{h}_k^{*,-} = \check{h}_k^{*,+} = \eta_c - \tilde{z}_k^* \quad \text{and} \quad \check{z}_k^* = \tilde{z}_k^* \,,$$

which leads to :

$$\check{V}_k^{*,\pm} = V := {}^t(\eta_c, 0, 0) \quad , \quad \hat{\eta}_k = \eta_c \,. \tag{II .46}$$

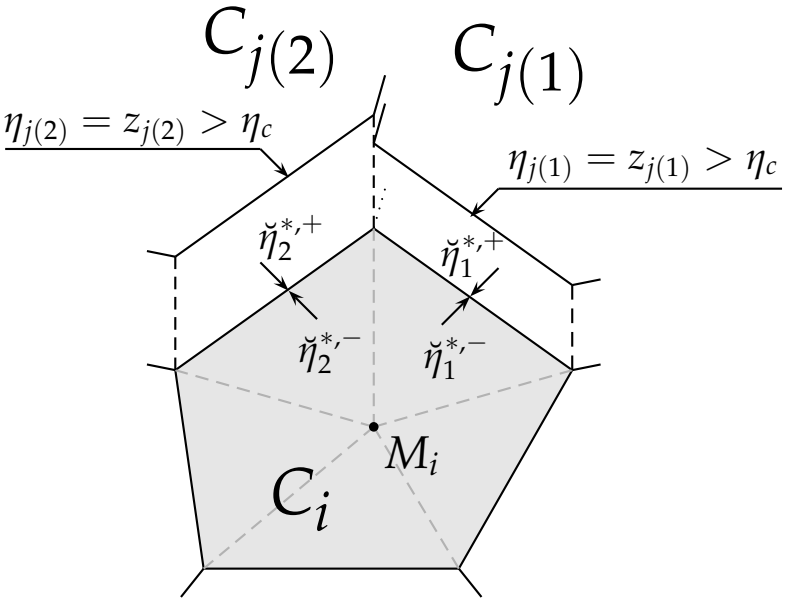

Figure II .5: Steady state with $C_{j(1)}$ and $C_{j(2)}$ as dry cells.

ii) Let's now consider the case of a motionless steady state involving a wet/dry interface. As a first remark, we can notice that, for a each surrounding cell $C_{j(k)}$, we have $\eta_{j(k)} \geq \eta_c$, independently from whether the cell is wet or not. As a result, the $\mathbb{P}_1$ approximation $V_{T_{ij(k)}}$ of V on $T_{ij(k)}$ satisfies $\eta_{T_{ij(k)}} \geq \eta_c$ on the edge $\Gamma_{ij(k)}$, and we necessarily have $\overrightarrow{M_i P_k}.\nabla \hat{V}^{\eta}_{T_{ij(k)}} \geq 0$. The limitation process (II .35) subsequently gives $\eta^*_{(1)} \geq \eta_c$, for all $k = 1, \cdots, \Lambda(i)$.

Consider now a k for which $C_{j(k)}$ is a dry cell. At the discrete level, the situation comes down to :

$$\eta_i = \eta_c \quad , \quad \eta_{j(k)} = z_{j(k)} > \eta_i \quad , \quad \mathbf{u}_i = \mathbf{u}_{j(k)} = 0 \,.$$

If we now give a focus on the dry cell $C_{j(k)}$, we can follow the previous lines to obtain $h^*_{(1)} \geq 0$ for each surrounding cell, arguing that $h_{j(k)} = 0$ and that the water height is positive for all the neighbours of $C_{j(k)}$. Keeping this in mind, we can easily verify that the correction step (II .37) yields $h_k^{*,+} = 0$. At this stage, we also need to apply this reconstruction for the free surface, to obtain $\eta_k^{*,-} = \eta_c$, according to the preliminary remark. We then write :

$$\tilde{z}_k^* = \max(\eta_c - h_k^{*,-}, \eta_k^{*,+}) = \eta_k^{*,+} \,,$$

from which we deduce :

$$\begin{aligned} \check{z}_k^* &= \eta_k^{*,-} = \eta_c \,, \\ \check{h}_k^{*,-} &= \check{h}_k^{*,+} = 0 \,. \end{aligned}$$

At last, we have :

$$\check{V}_k^{*,\pm} = V = {}^t(\eta_c, 0, 0) \quad , \quad \hat{\eta}_k = \eta_c \,. \tag{II .47}$$

Gathering (II .46) and (II .47) we obtain for all $k \in K(i)$, in the appropriate interface reference :

$$\begin{aligned} \mathcal{H}(\check{V}_k^{*,-}, \check{V}_k^{*,+}, \check{z}_k^*, \check{z}_k^*, \vec{n}_{ij(k)}) &= H(V, \check{z}_k^*) \cdot \vec{n}_{ij(k)} \\ &= \begin{pmatrix} 0 & 0 \\ \frac{1}{2} g(\eta_c^2 - 2\eta_c \check{z}_k^*) & 0 \\ 0 & \frac{1}{2} g(\eta_c^2 - 2\eta_c \check{z}_k^*) \end{pmatrix} \cdot \vec{n}_{ij(k)}. \end{aligned}$$

As Green's formula gives :

$$\sum_{k=1}^{\Lambda(i)} \ell_{ij(k)} \vec{n}_{ij(k)} = 0 \,,$$

we have :

$$\sum_{k=1}^{\Lambda(i)} \ell_{ij(k)} \mathcal{H}(V, V, \check{z}_k^*, \check{z}_k^*, \vec{n}_{ij(k)}) = -g\eta_c \sum_{k=1}^{\Lambda(i)} \ell_{ij(k)} \check{z}_k^* \begin{pmatrix} 0 \\ \vec{n}_{ij(k)} \end{pmatrix}.$$

In the same way (II .43) gives :

$$\sum_{k=1}^{\Lambda(i)} \ell_{ij(k)} S_{ij(k)} = -g\eta_c \sum_{k=1}^{\Lambda(i)} \ell_{ij(k)} \check{z}_k^* \begin{pmatrix} 0 \\ \vec{n}_{ij(k)} \end{pmatrix},$$

and consequently, $V_i^{n+1} = V_i^n$.

Note that here C_i is supposed to be a wet cell. However, the opposite situation is trivial, since we just have to consider the set of well neighboring cells. If C_i only admits dry neighbours, then nothing happens and C_i remains dry. If there exists $k \in K(i)$ such that $h_{j(k)} > 0$, then we are in the wet/dry case of Fig. II .5, inverting the subscripts " $-$ " and " $+$ ".

For the consistency with the source, we adopt the notation :

$$\mathcal{H}_s(V_i, V_{j(k)}, z_i, z_{j(k)}, \vec{n}_{ij(k)}) = \mathcal{H}(\check{V}_k^{*,-}, \check{V}_k^{*,+}, \check{z}_k^*, \check{z}_k^*, \vec{n}_{ij(k)}) - S_{ij(k)}.\vec{n}_{ij(k)} \,.$$

We thus have :

$$\begin{aligned} \mathcal{H}_s(V_i, V_{j(k)}, z_i, z_{j(k)}, \vec{n}_{ij(k)}) + \mathcal{H}_s(V_{j(k)}, V_i, z_{j(k)}, z_i, -\vec{n}_{ij(k)}) \\ = (S_{j(k)i} - S_{ij(k)}).\vec{n}_{ij(k)} \,, \end{aligned}$$

and therefore :

$$\mathcal{H}_s(V_i, V_{j(k)}, z_i, z_{j(k)}, \vec{n}_{ij(k)}) + \mathcal{H}_s(V_{j(k)}, V_i, z_{j(k)}, z_i, -\vec{n}_{ij(k)})$$
$$= -\begin{pmatrix} 0 \\ g\eta\,\vec{n}_{ij(k)} \end{pmatrix}(z_{j(k)} - z_i) + (z_{j(k)} - z_i)\epsilon(\hat{\eta}_k - \eta)$$
$$\text{as} \quad V_i, V_{j(k)} \longrightarrow V = \begin{pmatrix} \eta \\ q_x \\ q_y \end{pmatrix} \quad \text{and} \quad z_i, z_{j(k)} \longrightarrow z.$$

□

Remark II.3 .1. *Obviously, this proof can be reproduced for the first order scheme. We also emphasize that, as it does not involve a rewriting in terms of convex combinations, it allows a larger latitude regarding the choice of $\hat{\eta}_k$ (II .21) in the discretization of the source (II .20), and this is also the case for the present MUSCL reconstructions.*

For instance, by setting $\hat{\eta}_k = \bar{\eta}_i$, where $\bar{\eta}_i$ is an average of $\check{\eta}_k^-$ for $k \in K(i)$, one has the following formulation of the source term :

$$S_i = \frac{1}{|C_i|}\sum_{k=1}^{\Lambda(i)} g\bar{\eta}_i \ell_{ij(k)} \begin{pmatrix} 0 \\ (z_i - \check{z}_k)\vec{n}_{ij(k)} \end{pmatrix} = -g\bar{\eta}_i \sum_{k=1}^{\Lambda(i)} \frac{\ell_{ij(k)}}{|C_i|}\check{z}_k \begin{pmatrix} 0 \\ \vec{n}_{ij(k)} \end{pmatrix},$$

using Green's formula. This last formulation can be regarded as an extension of the source term discretization in the 1d case (II .12), in accordance with the original proposition [195] :

$$-g\eta\frac{\partial z}{\partial x} \approx -g\hat{\eta}_i \frac{(\check{z}_{i+\frac{1}{2}} - \check{z}_{i-\frac{1}{2}})}{\Delta x}, \text{ with } \hat{\eta}_i = \frac{\check{\eta}^+_{i-\frac{1}{2}} + \check{\eta}^-_{i+\frac{1}{2}}}{2}. \qquad \text{(II .48)}$$

It should be stressed that many other relevant approximations have been tested, such as $\hat{\eta}_k = \frac{1}{2}(\check{\eta}_k^- + \check{\eta}_k^+)$, which appeared as the most natural choice at the beginning of our numerical investigations. They all lead to very close results. In particular, our simulations shown that they provide the same level of accuracy and convergence rates, even when MUSCL reconstructions are involved.

Finally, as regards the present space accuracy improvement, it is worth mentioning that the source term discretization (II .20) does not need to be modified to preserve well-balancing and consistency, unlike [12] or [221] in which additional quadrature terms are needed. Similar observation can be made for the next MUSCL reconstruction, attesting of the practical aspects of the approach.

II.3.2 A second example

The method comes from multidimensional CFD problems and the accuracy is improved following the ideas of [57] (see also [81, 172]). Again, both reconstruction on h and η are necessary with the view of well-balanced issues. Following [57], let us introduce the following notations :

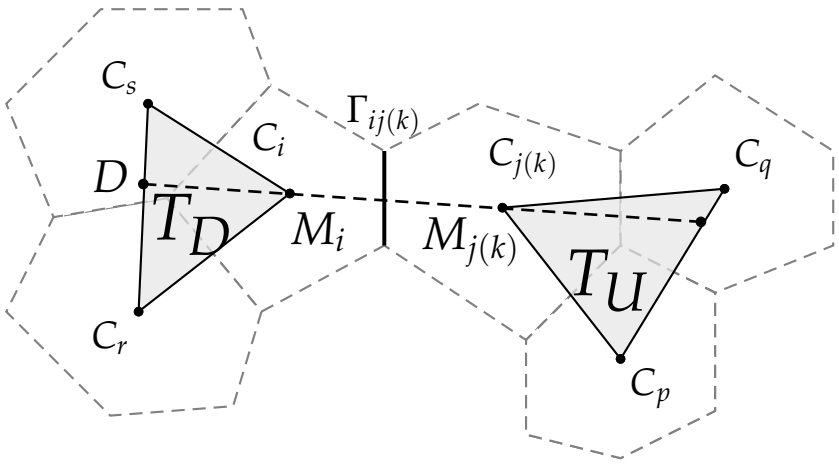

Figure II .6: Upstream and Downstream triangles T_U and T_D.

- T_U and T_D are, respectively, the upstream and downstream triangles, from the initial triangulation $\mathcal{T}$, with respect to the edge $\Gamma_{ij(k)}$ (triangles having respectively M_i and $M_{j(k)}$ as a vertex and such that edge $\Gamma_{ij(k)}$ intersects the opposite edge, see Fig. II .6),
- $\nabla \hat{V}_T$ is the gradient obtained from a $\mathbb{P}^1$ interpolation of $\hat{V}$ on the triangle T,
- $\nabla \hat{V}_k^- = \nabla \hat{V}_{T_D} \cdot \overrightarrow{M_i M_{j(k)}}$, $\nabla \hat{V}_k^+ = \nabla \hat{V}_{T_U} \cdot \overrightarrow{M_i M_{j(k)}}$,
- $\nabla \hat{V}_k^c = \hat{V}_{j(k)} - \hat{V}_i$ is a centred gradient ,
- $\nabla \hat{V}_k^{ho,\pm} = \frac{1}{3}\nabla \hat{V}_k^{\pm} + \frac{2}{3}\nabla \hat{V}_k^c$ is another way of evaluating the variation of $\hat{V}$ on both sides of the edge $\Gamma_{ij(k)}$, to increase the accuracy of the resulting scheme ,
- $\mathcal{L}$ is a three entries continuous limiter, defined as follows :

$$\mathcal{L}(a,b,c) = \begin{cases} 0 \quad \text{if} \quad sgn(a) \neq sgn(b) , \\ sgn(a)\min(|2a|,|2b|,|c|) \quad \text{otherwise} , \end{cases} \tag{II .49}$$

- $\mathcal{L}_k^-(\hat{V}) = \mathcal{L}(\nabla \hat{V}_k^-, \nabla \hat{V}_k^c, \nabla \hat{V}_k^{ho,-})$, $\mathcal{L}_k^+(\hat{V}) = \mathcal{L}(\nabla \hat{V}_k^+, \nabla \hat{V}_k^c, \nabla \hat{V}_k^{ho,+})$.

Thus, better interpolated values $\hat{V}_k^{*,-}$ and $\hat{V}_k^{*,+}$ at the edge $\Gamma_{ij(k)}$ are defined by :

$$\hat{V}_k^{*,-} = \hat{V}_i + \frac{1}{2}\mathcal{L}_k^-(\hat{V}), \quad \hat{V}_k^{*,+} = \hat{V}_{j(k)} - \frac{1}{2}\mathcal{L}_k^+(\hat{V}) . \tag{II .50}$$

As previously, we extract from (II .50) new face values at the corresponding edge, and follow the reconstruction steps (II .38 - II .41) as in the previous method. The source term has exactly the same form :

$$S_i = \sum_{k=1}^{\Lambda(i)} \ell_{ij(k)} S_{ij(k)} = \sum_{k=1}^{\Lambda(i)} \ell_{ij(k)} \begin{pmatrix} 0 \\ g\hat{\eta}_k(z_i - z_k^*)\vec{n}_{ij(k)} \end{pmatrix} , \tag{II .51}$$

and the MUSCL scheme is still given by (II .45).

Remark II.3 .2. *As stated in [81, 154], the gradient approximations $\nabla\hat{V}_k^-$ and $\nabla\hat{V}_k^+$ can be computed with :*

$$\nabla\hat{V}_k^- = \epsilon_{si}(\hat{V}_i - \hat{V}_s) + \epsilon_{ri}(\hat{V}_i - \hat{V}_r), \tag{II .52}$$

$$\nabla\hat{V}_k^+ = \epsilon_{jp}(\hat{V}_p - \hat{V}_j) + \epsilon_{jq}(\hat{V}_q - \hat{V}_j), \tag{II .53}$$

where $\overrightarrow{M_{j(k)}M_i} = \epsilon_{si}\overrightarrow{M_iM_s} + \epsilon_{ri}\overrightarrow{M_iM_r}$, and $\overrightarrow{M_iM_{j(k)}} = \epsilon_{jp}\overrightarrow{M_{j(k)}M_p} + \epsilon_{jq}\overrightarrow{M_{j(k)}M_q}$ (see Fig.II .6).

Basic computations yields (see Fig. II .7) :

$$\epsilon_{si} = \frac{l_{ij(k)}}{l_{is}}\frac{sin(\theta_r)}{sin(\theta)}\ ,\ \epsilon_{ri} = \frac{l_{ij(k)}}{l_{ir}}\frac{sin(\theta_s)}{sin(\theta)}\ ,$$

with the notation $l_{ij(k)} = \|\overrightarrow{M_iM_{j(k)}}\|$. Additionally, using these classical relations :

$$sin(\theta) = \frac{2|T_D|}{l_{is}l_{ir}}\ ,\ sin(\theta_s) = \frac{2|T_s|}{l_{is}l_{id}}\ ,\ sin(\theta_r) = \frac{2|T_r|}{l_{ir}l_{id}}\ ,$$

where D is the intersection of line $M_iM_{j(k)}$ with the opposite edge of T_D, it may be useful to remark that (II.3 .2) can alternatively be expressed in terms of area ratios :

$$\epsilon_{si} = \frac{l_{ij(k)}}{l_{id}}\frac{|T_r|}{|T_D|}\ ,\ \epsilon_{si} = \frac{l_{ij(k)}}{l_{id}}\frac{|T_s|}{|T_D|}\ , \tag{II .54}$$

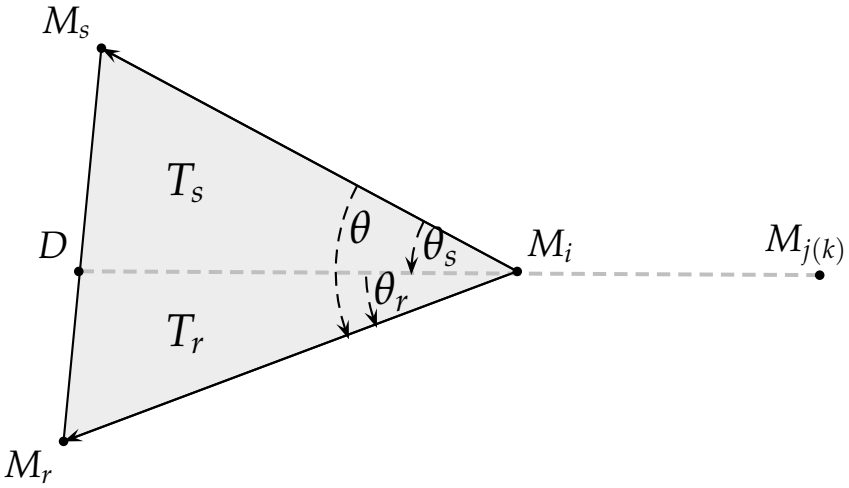

Figure II .7: Evaluation of downstream coefficients.

Remark II.3 .3. *Note that $\nabla\hat{V}_k^{ho,-} = \frac{1}{3}\nabla\hat{V}_k^- + \nabla\frac{2}{3}\hat{V}_k^c$ gives a third-order space-accurate scheme for linear advection on cartesian triangular meshes. More generally, the high-order gradient $\nabla\hat{V}_k^{ho,-}$ evaluation can involve extra data to increase accuracy.*

For instance, one can consider the following gradient, which gives a numerical dissipation built as a sixth-order spatial derivative for linear advection, introduced in [57] :

$$\nabla \hat{V}_{ij}^{ho,-} = \frac{1}{3}\nabla \hat{V}_k^- + \frac{2}{3}\nabla \hat{V}_k^c - \frac{1}{30}(\nabla \hat{V}_k^- - 2\nabla \hat{V}_k^c + \nabla \hat{V}_k^-) - \frac{2}{15}(\nabla \hat{V}_D \cdot \overrightarrow{M_i M_{j(k)}} - 2\nabla \hat{V}_i \cdot \overrightarrow{M_i M_{j(k)}} + \nabla \hat{V}_{j(k)} \cdot \overrightarrow{M_i M_{j(k)}}), \tag{II .55}$$

where $\nabla \hat{V}_i$ is an average of the $\mathbb{P}_1$ gradients on triangles having the node i as vertex, and $\nabla \hat{V}_D$ is the gradient at point D, interpolated between $\nabla \hat{V}_s$ and $\nabla \hat{V}_r$ (see Fig. II .6).
In our numerical investigations, we observe that although this modification does not increase the rate of convergence for our test cases, it helps to reduce the numerical error.

Again, one can establish that the source term discretization (II .51) is able to preserve the C-property. More precisely :

Proposition 4. *We consider a numerical flux function $\mathcal{H}$ for the scheme (II .42, II .43, II .45), consistent with the exact flux in the sense of (I .22) and high order MUSCL reconstructions (II .50) for the face values. Then, the motionless steady states are preserved.*

Proof. Again, we consider two cases :

i) We begin by the wet case. Consider a cell C_i and one of its neighbours $C_{j(k)}$, and assume $\eta_{j(k)} = \eta_i = \eta_c$, $\mathbf{u}_i = \mathbf{u}_{j(k)} = 0$. The η-component of the centred gradient $\nabla \hat{V}_k^c$ is zero, which immediately implies $\mathcal{L}_k^{\pm}(\hat{V})^{\eta} = 0$, and (II .50) gives $\eta_k^{*,-} = \eta_k^{*,+} = \eta_c$. We consequently have :

$$\tilde{z}_k^* = \max(\eta_c - h_k^{*,-}, \eta_c - h_k^{*,+}) \leq \eta_c \,, \tag{II .56}$$

leading to $\check{z}_k^* = \tilde{z}_k^*$. We subsequently deduce the reconstructed values for the water height and free surface:

$$\check{h}_k^{*,-} = \check{h}_k^{*,+} = \eta_c - \tilde{z}_k^* \quad , \quad \check{\eta}_k^{*,-} = \check{\eta}_k^{*,+} = \eta_c \,. \tag{II .57}$$

This allows to conclude as in Proposition 3.

ii) Let's now consider $C_{j(k)}$ as a dry cell. In a motionless steady state configuration, it is useful to underline that :

$$\begin{aligned} &\forall p = 1, \cdots, \Lambda(i) \,, \quad \eta_{j(p)} \geq \eta_i = \eta_c \,, \\ &\forall p = 1, \cdots, \Lambda(j(k)) \,, \quad h_{i(p)} \geq h_{j(k)} = 0 \,. \end{aligned} \tag{II .58}$$

According to (II .52), we have $\mathrm{sgn}(\nabla \hat{V}_k^-) \neq \mathrm{sgn}(\nabla \hat{V}_k^{c,-})$ on the η-component. Likewise, (II .53) entails $\mathrm{sgn}(\nabla \hat{V}_k^+) \neq \mathrm{sgn}(\nabla \hat{V}_k^{c,+})$ on the h-component. Note that these arguments are quite similar to those advanced in the dry case of Proposition 3.
Consequently, the limitation step provides $h_k^{*,+} = h_{j(k)} = 0$ and $\eta_k^{*,-} = \eta_c$, so that :

$$z_k^{*,-} = \eta_c - h_k^{*,-} \quad \text{and} \quad z_k^{*,+} = \eta_k^{*,+} \,. \tag{II .59}$$

Thus, since we have $\check{z}_k^* = \eta_k^{*,+} \geq \eta_c$, we obtain the following intermediate states :

$$\check{z}_k^* = \eta_k^{*,-} = \eta_c \quad , \quad \check{h}_k^{*,-} = \check{h}_k^{*,+} = 0 \quad , \quad \check{\eta}_k^{*,-} = \check{\eta}_k^{*,+} = \eta_c \, , \tag{II .60}$$

and conclude as previously.

□

We now show that the Θ-preserving property is preserved by these two MUSCL schemes.

II.3.3 Robustness issues

The following developments concern the class of solvers able to preserve the positivity of the first order scheme for the free surface :

$$\eta_i^{n+1} = \eta_i^n - \frac{\Delta t}{|C_i|} \sum_{k=1}^{\Lambda(i)} \ell_{ij(k)} \mathcal{H}^\eta(\check{V}_k^-, \check{V}_k^+, \check{z}_k, \check{z}_k, \vec{n}_{ij(k)}) \, , \tag{II .61}$$

under a CFL condition of the form (II .23), that is :

$$\begin{aligned} & a_i \frac{\Delta t}{\delta_{ij(k)}} \leq \tau_{CFL} \, , \quad \forall C_i \, , \, k = 1, \cdots, \Lambda(i) \, , \\ & a_i = \max_{k=1,\cdots,\Lambda(i)} \left(|\lambda_k^-| \, , \, |\lambda_k^+| \right) . \end{aligned} \tag{II .62}$$

To study the robustness of the MUSCL scheme (II .42, II .43, II .45), let us first introduce a relevant sub-grid. Considering a dual cell C_i and $k = 1, \cdots, \Lambda(i)$, we denote $R_{ij(k)j(k+1)}$ the mass center of the triangle $M_i M_{j(k)} M_{j(k+1)}$ and $m_{ij(k)j(k+1)}$ the middle of the edge $M_i R_{j(k)j(k+1)}$ (see Fig. II .8). Joining the vertexes $m_{i\,j(k)\,j(k+1)}$, we split the dual cell C_i into a sub-cell C_i' and $\Lambda(i)$ sub-cells $Q_{ij(k)}$ obtained with joining the vertexes $R_{ij(k-1)j(k)}$, $R_{ij(k)j(k+1)}$, $m_{ij(k)j(k+1)}$ and $m_{ij(k-1)j(k)}$ (Fig. II .8), leading to :

$$C_i = C_i' \cup \left(\bigcup_{k=1}^{\Lambda(i)} Q_{ij(k)} \right) .$$

Let us also denote (see Fig. II .9) :

- $\Gamma'_{ij(k)}$ the segment separating C_i' and $Q_{ij(k)}$,
- $\ell'_{ij(k)}$ the length of $\Gamma'_{ij(k)}$
- $\vec{n}'_{ij(k)}$ the outer unit normal to $\Gamma'_{ij(k)}$,
- $\Gamma^p_{ij(k)}$, for $p \in \{1, \ldots, 4\}$, the boundaries of $Q_{ij(k)}$ (so that $\bigcup_{p=1}^{4} \Gamma^p_{ij(k)} = \partial Q_{ij(k)}$),
- $\ell^p_{ij(k)}$ the length of $\Gamma^p_{ij(k)}$,

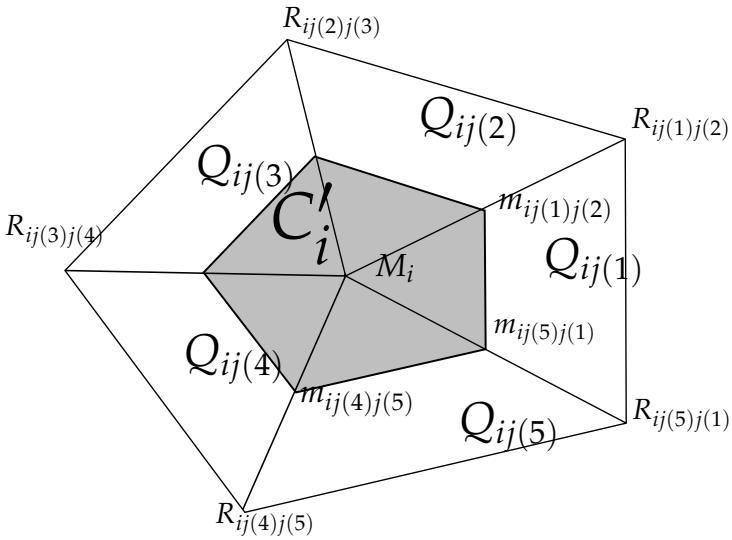

Figure II .8: Sub-cell decomposition of the dual cell C_i

- $\vec{n}^p_{ij(k)}$ the outer unit normal to $\Gamma^p_{ij(k)}$,
- V^p_k, for $p \in \{1, \dots, 4\}$, the value of V in the neighboring cells of $Q_{ij(k)}$.

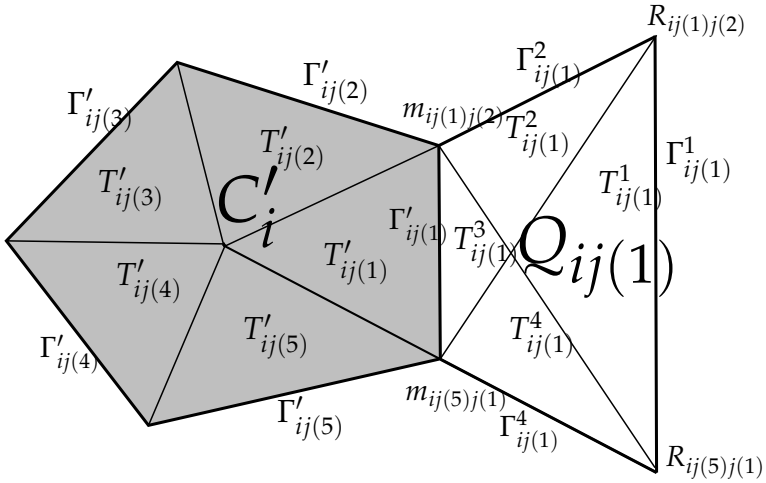

Figure II .9: Sub-grid as a disjoint union of triangles.

Let us finally assume that all the sub-cells described above are the disjoint union of triangles (see Fig. II .9) :

$$Q_{ij(k)} = \bigcup_{p=1}^{4} T^p_{ij(k)} \quad \text{and} \quad C_i' = \bigcup_{k=1}^{\Lambda(i)} T'_{ij(k)} \,. \tag{II .63}$$

Proposition 5. *We consider a numerical flux function $\mathcal{H}$ consistent with the exact flux in the sense of (I .22), verifying the conservation property (I .23) and such that the associated first order scheme (II .61) is Θ-preserving. We assume that $(h_i^n)_{i\in\mathbb{Z}}$ and $(h_i')_{i\in\mathbb{Z}}$*

(defined above by II .66) are positive and we consider the updated states $(V_i^{n+1})_{i\in\mathbb{Z}}$ *obtained with the scheme (II .42, II .43, II .45). Then, under the following CFL condition :*

$$\Delta t \frac{\ell^p_{ij(k)}}{|T^p_{ij(k)}|} \max \left| \lambda^{\pm}(V_k^{*,-}, V_k^p, \vec{n}^p_{ij(k)}) \right| \leq \tau_{CFL}, \, \forall\, C_{ij(k)}, \, T^p_{ij(k)}, \, 1 \leq p \leq 4\,, \quad \text{(II .64)}$$

$$\Delta t \frac{\ell'_{ij(k)}}{|T'_{ij(k)}|} \max \left| \lambda^{\pm}(V_i', V_k^{*,-}, \vec{n}'_{ij(k)}) \right| \leq \tau_{CFL}, \, \forall C'_i, \, T'_{ij(k)}, \, 1 \leq k \leq \Lambda(i)\,, \quad \text{(II .65)}$$

we have $h_i^{n+1} \geq 0$*, for all* $i \in \mathbb{Z}$*.*

Proof. Considering the cell C_i, let us associate the inner reconstructed vector state $V_k^{*,-}$ to the cell $Q_{ij(k)}$. Following [21], we introduce a new intermediate state V_i', associated with the sub-cell C_i', deduced from a water height defined as follows :

$$\frac{|C_i'|}{|C_i|} h_i' + \sum_{k=1}^{\Lambda(i)} \frac{|Q_{ij(k)}|}{|C_i|} h_k^{*,-} = h_i^n\,, \quad \text{(II .66)}$$

and the same relations for both discharge and topography. Now, considering the interpolated values of the water height h on the split-grid, let us evolve in time these intermediate states using the scheme (II .61), to obtain :

$$(h_i')^{n+1} = h_i' - \frac{\Delta t}{|C_i'|} \sum_{k=1}^{\Lambda(i)} \ell'_{ij(k)} \mathcal{H}^{\eta}(\check{V}_i', \check{V}_k^{*,-}, \vec{n}'_{ij(k)})\,, \quad \text{(II .67)}$$

$$(h_k^{*,-})^{n+1} = h_k^{*,-} - \frac{\Delta t}{|Q_{ij(k)}|} \sum_{p=1}^{4} \ell^p_{ij(k)} \mathcal{H}^{\eta}(\check{V}_k^{*,-}, \check{V}_k^p, \vec{n}_k^p)\,, \quad \text{(II .68)}$$

where the subscript "ˇ" refers to the reconstruction (II .17,II .18,II .19). Above we did not specify the reconstructed values for the topography in the writing of the fluxes for the sake of simplicity. As the additional source terms (II .43) have no contribution to the first component and using the conservativity property (I .23), we obtain that h_i^{n+1}, computed with the scheme (II .42, II .43, II .45), can be regarded as the following convex combination :

$$h_i^{n+1} = \frac{|C_i'|}{|C_i|} (h_i')^{n+1} + \sum_{k=1}^{\Lambda(i)} \frac{|Q_{ij(k)}|}{|C_i|} (h_k^{*,-})^{n+1}\,. \quad \text{(II .69)}$$

Note that when the initial states on C_i and its neighbours admit positive water depths, the two MUSCL reconstructions automatically give $h_k^{*,-} \geq 0$. Consequently, considering a sub-cell $Q_{ij(k)}$, recalling that $h_k^{*,-}$ is evolved by (II .68), and that the scheme (II .61) preserves the positivity of h, then the CFL condition (II .64) ensures that $(h_k^{*,-})^{n+1}$ is positive, for all $k \in \{1, \ldots, \Lambda(i)\}$. In the same way, if we are able to enforce $h_i' \geq 0$, the criterion (II .65) will guarantee that the evolved state $(h_i')^{n+1}$ given by (II .67) is positive, allowing to conclude, using (II .69).

We thus have to ensure that $h_i' \geq 0$. Using (II .66) we have :

$$h_i' = \frac{|C_i|}{|C_i'|} h_i^n - \sum_{k=1}^{\Lambda(i)} \frac{|Q_{ij(k)}|}{|C_i'|} h_k^{*,-}. \tag{II .70}$$

Therefore, we only have to enforce :

$$h_i^n - \sum_{k=1}^{\Lambda(i)} \frac{|Q_{ij(k)}|}{|C_i|} h_k^{*,-} \geq 0\,.$$

This can be achieved with the linear approach suggested in [21]. Considering the better interpolated value $h_k^{*,-}$ issued from either of the MUSCL reconstructions, we define the corresponding reconstruction increment δh_k with:

$$h_k^{*,-} = h_i^n + \delta h_k.$$

We now modify this increment, considering a coefficient α and the modified value of $h_k^{*,-}$:

$$h_k^{*,-} = h_i^n + \alpha \delta h_k.$$

where α must satisfy :

$$h_i^n - \sum_{k=1}^{\Lambda(i)} \frac{|Q_{ij(k)}|}{|C_i|} \alpha \delta h_k \geq 0\,.$$

□

Remark II.3 .4. *We recall that, following Section I.5.1 , as the finite volume scheme (II .61) can be regarded as a convex combination of one-dimensional schemes on the subgrid, it preserves the positivity of the water height as soon as the 1d associated scheme does. An direct example of application is supplied by the HLL scheme previously discussed.*

II.4 Numerical Validations

This last section is devoted to the numerical validation of the scheme and its successive improvements. In the tests presented here we employed the HLL scheme for the evaluation of the numerical fluxes. In addition of providing robustness, it exhibited interesting implementation amenities and offered a good overall precision. Though this work is not devoted to an extensive comparative study of different numerical solvers, we specify here that HLLC and VFRoe schemes have also been tested. Although being slightly more precise, they provided very similar results in the vast majority of cases. The high order schemes (II .42, II .43, II .45) obtained from reconstructions (II .34) and (II .50) will be referred to as M1-scheme and M2-scheme respectively. The time discretization relies on the second-order Runge-Kutta scheme (I .50).

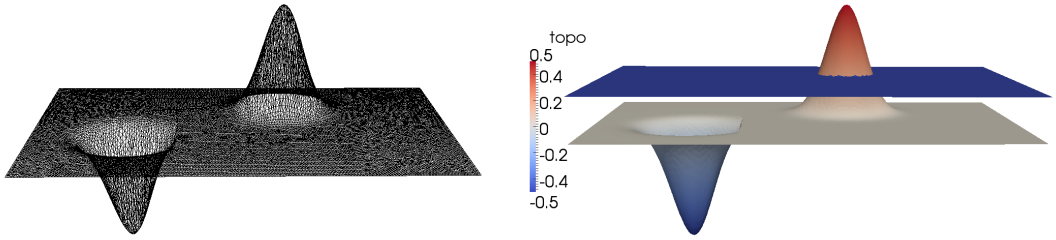

Figure II .10: Well balancing validation : Meshed topography (*left*) and free surface after 1000 iterations (*right*).

	L^1			L^2			L^∞		
	h	q_x	q_y	h	q_x	q_y	h	q_x	q_y
1^{st} order	1.1E-16	3.4E-16	4.5E-16	1.1E-16	4.4E-16	1.8E-16	1.1E-16	2.4E-16	2.1E-16
M1	4.9E-18	3.8E-17	3.6E-17	4.3E-18	3.9E-17	2.3E-17	4.5E-18	2.2E-17	2.2E-17
M2	3.7E-17	5.8E-17	5.2E-17	3.6E-17	6.1E-17	3.2E-17	3.6E-17	3.2E-17	3.2E-17

Table II .1: Well balancing validation : Evaluation of the numerical error for the conservative variables for several norms of interest.

II.4.1 Well balancing validation

The initial condition of this test is a flow at rest, with a varying topography, and a dry area. We consider a rectangular domain $[0,2] \times [0,1]$, with the following topography :

$$z(x,y) = \begin{cases} 0.5 \exp\left(-(25(x-1.2)^2 + 50(y-0.7)^2)\right) & \text{if } x > 0.68\,, \\ -0.5 \exp\left(-(50(x-0.45)^2 + 100(y-0.4)^2)\right) & \text{elsewhere}\,. \end{cases}$$

The domain is meshed with 13 000 nodes (see Fig. II .10 left) and we impose at $t = 0$ $\eta = \max(z, 0.2)$ and $\mathbf{q} = 0$ on the whole domain (see Fig. II .10 right). For the sake of completeness, errors on the total free surface, normal and tangential discharge have been computed after 1 000 time iterations, for the L^1, L^2 and L^∞ norms. Results are reported in Tab. II .1. As expected, the first order scheme (II .15 - II .19, II .20), as well as its high order extensions preserve the steady state up to round-off error.

II.4.2 Subcritical flow over a bump

In this test, we study the ability in converging toward stationary steady states and we perform some convergence studies. The computational domain consists of a 20m $\times$ 5m channel, and the topography is defined as follows :

$$z(x,y) = \begin{cases} 0.2 - 0.05(x-10) & \text{if} \quad 8 \leq x \leq 12\,, \\ 0 \quad \text{otherwise}\,. \end{cases}$$

Three main classes of solutions are available, namely the sub-critical case and the transcritical cases (with or without shock), as described in [136]. Due to

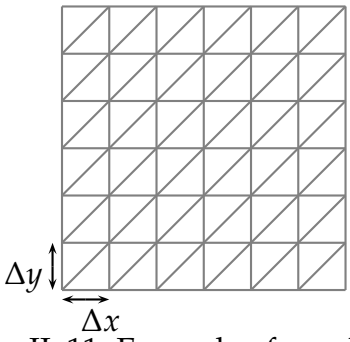

Figure II .11: Example of regular mesh.

the relative rarity of analytical solutions involving converging flows, these tests are widely used in the literature (see [12, 24, 65, 108, 179, 243, 288, 302] and the recent compilation [90] for further details). We consider here the subcritical case. Hence, we enforce the inflow discharge at the left boundary with $q_x = 4,42\, m/s$, $q_y = 0\, m/s$ and we impose $\eta = h = 2\, m$ at the outflow boundary. A 3d view of the initial configuration and topography is given in Fig. II .12 (top). We first employ the high order M2 scheme and a regular mesh with space step $\Delta x = \Delta y = 0.1$ (see Fig. II .11). We rapidly obtain a stationary flow for which a classical analytical solution is available. The convergence phenomena is properly described here : the steady state clearly appears around $t = 80s$ (Fig. II .12 (bottom)), with a strong alignment with the analytical solution (Fig. II .13).

We now consider several regular meshes, with a discretization step $\Delta x = 20/n$ and an increasing level of refinement: $n = 20, 40, 80, 160$. We compare both first order and high order schemes with this exact solution, at time $t = 80\, s$ and Fig. II .14 shows the L^1-error versus Δx in logarithm scale. Convergence rate of 0.86 and 2.03 are obtained for η, respectively for the first order and M2 schemes. Similar values are observed for the normal discharge. When comparing the two high order reconstructions we remark that the M2 approach (II .50) provides slightly better results. Though moderate, this superiority has been confirmed throughout the other tests, and we consequently choose to pursue our validations with the M2 scheme.

II.4.3 Flows over steps

It is well known that the NSW model is not theoretically valid in the frame of discontinuous bottoms. The modelization problem posed by water waves over irregular topographies is anything but simple, and is still subject to intensive research (see the works of Cathala and Lannes [62, 182] for recent investigations on this topic). Nevertheless, several authors proposed numerical models to account for vertical steps in the classical context of NSW equations. As an example, shortly thereafter the so called Surface Gradient Method, Zhou *et al* [301] extended this approach to account for possible occurrence of discontinuities in the topography. The method is based on an appropriate re-calculation of the water height at each side of an interface having a discontinuity, together

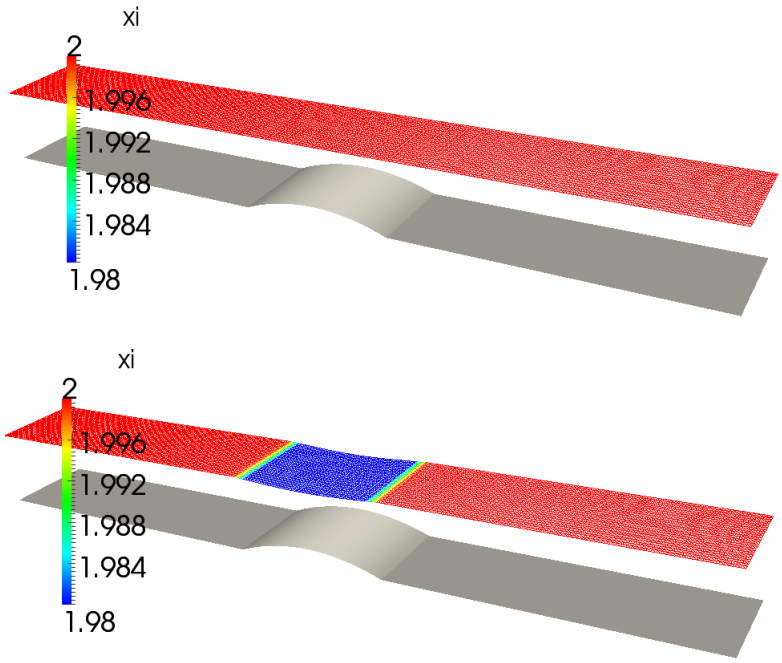

Figure II .12: Subcritical flow over a bump : Initial condition and topography (*top*) and free surface profile at $t = 80s$ (*bottom*).

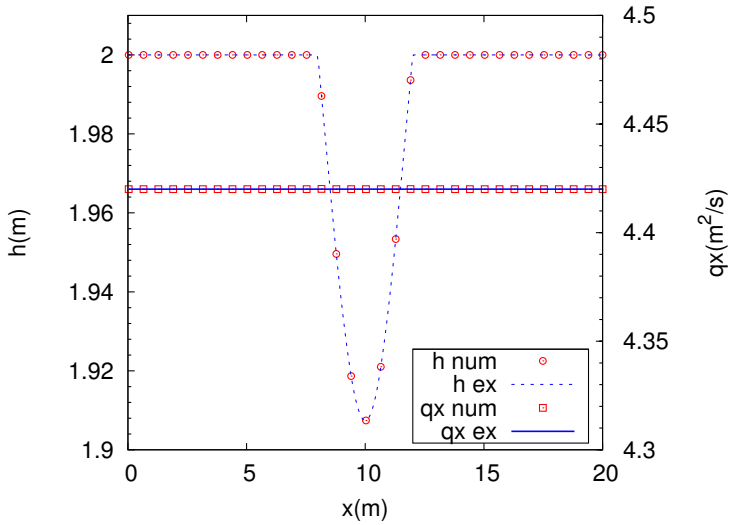

Figure II .13: Subcritical flow over a bump : Steady state : values of the free surface and the normal discharge along the middle section. Analytic vs numeric.

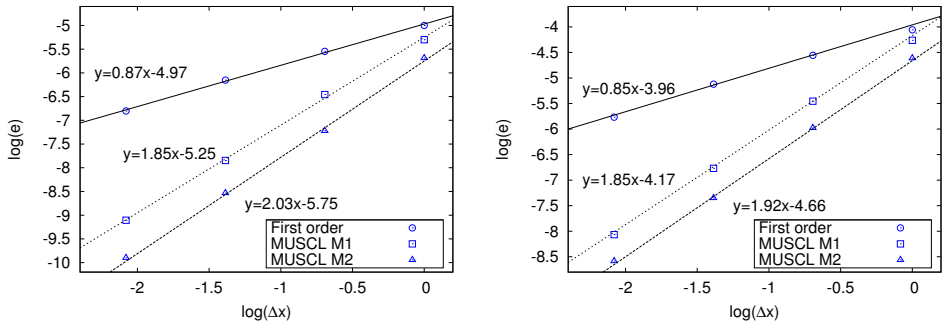

Figure II .14: Subcritical flow over a bump : Convergence curves in logarithm scale, for the free surface η (*left*), and the normal discharge q_x (*right*).

with the inclusion of a resistance term to account for a relevant head loss due to the bottom jump. As done in [150], one can also plan to regard these jumps as very steep gradients, provided the use of refined grids in the vicinity of the discontinuities. Another strategy, less costly, consists of considering a continuous piecewise bilinear reconstruction of the bottom in a pre-processing step [181].

Using the bed profile proposed by the *working group on dam-break modelling* [136], the following tests involve a rectangular $1\,500m$ long flume with a central step characterized by :

$$z(x,y) = \begin{cases} 8 & \text{if } |x-750| < 187.5\,, \\ 0 & \text{otherwise}\,, \end{cases}$$

available in Fig. II .15. We actually aim at showing that the current scheme is able to ensure stable computations in the case of irregular bottoms. No specific treatment is required to handle vertical jumps: as in [195], they are simply approximated by very steep slopes defined by the ratio between the jump height and the mesh size.

II.4.3.a Tidal wave over steps

For this simulation, the width of the channel is set to $150m$, and an unstructured mesh of 3 721 elements is used. Our assessments are based on the 1d asymptotic analytical solution provided by Bermudez et Vazquez [20] :

$$\begin{cases} h(x,y,t) = 20 - z(x,y) - 4\,sin\left[\pi\left(\dfrac{4t}{86\,400} + \dfrac{1}{2}\right)\right]\,, \\ u(x,y,t) = \dfrac{(x-L)\pi}{5\,400\,h(x,y,t)}\,cos\left[\pi\left(\dfrac{4t}{86\,400} + \dfrac{1}{2}\right)\right]\,. \end{cases} \tag{II .71}$$

The initial condition is supplied by the analytical solution at $t = 0$. The flow evolution is mainly dictated by the inflow boundary condition, where $h(0,0,t)$ is enforced, while solid wall is assumed at the other surrounding boundaries. Comparisons are performed at several time intervals throughout the simulation,

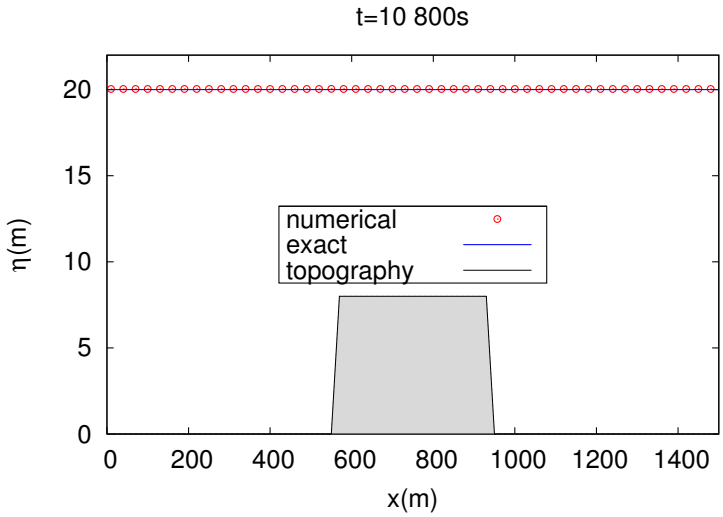

Figure II .15: Tidal wave over steps : Water depth profile at t=10 800s along the x-direction centreline. Comparison with analytical water depth.

until $T = 35\,000s$. On Fig. II .15 we propose a snapshot of the water height at $t = 10\,800s$. At this time, according to (II .71) the flow is expected to be planar. Such a situation is perfectly replicated at the discrete level, and this in spite of the presence of the bottom jump. We can observe on Fig. II .16 the x-velocity profiles at two reference times, corresponding to the maximum and minimum values reached by the flow. They exhibit a very good agreement with the analytical solution.

II.4.3.b Dam break problem

To further investigate this issue, one can consider a dam breaking problem over the current topography, as proposed in [280]. To capture at best the characteristics of the flow, the M2 scheme is used on a regular mesh of 20 000 elements, corresponding to a $3m$ space step. Solid wall boundary conditions are considered at each side of the domain. The initial condition is now given by :

$$h(x,y,t) = \begin{cases} 20 & \text{if } x < 750\,, \\ 15 & \text{otherwise}\,. \end{cases}$$

The resulting solution is free from oscillations, and, in a first time, is able to correctly reproduce the classical rarefaction/shock configuration of which are submitted classical dam break problems (see Fig. II .17). The situation becomes more complicated once the front wave reaches the limits of the bed step. Note that, at both sides, water height and bed slope are discontinuous while the free surface elevation is smooth. Thus, the loss of energy due to the passing of the bottom jump gives rise to a rapidly varying flow with complex characteristics, quite difficult to restore. To illustrate this, an insight of the wave evolution at $t = 60s$ is

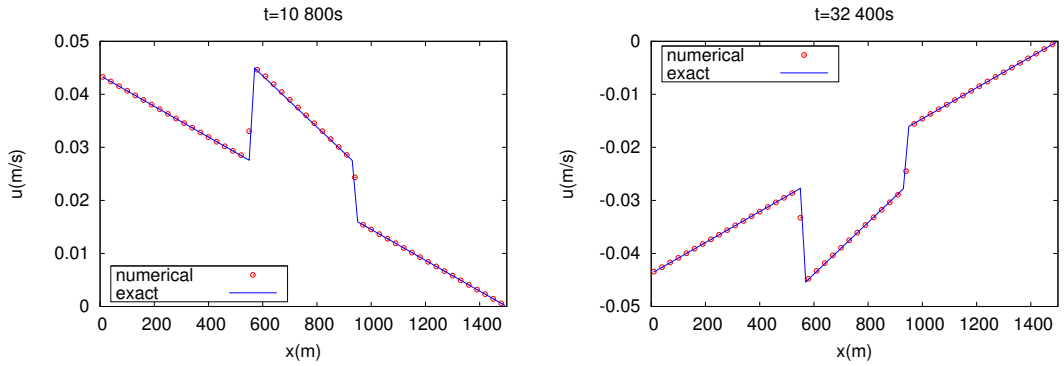

Figure II .16: Tidal wave over steps : x-component of the velocity along the x-direction centreline at t=10 800s and t=32 400s. Comparison with analytical velocity.

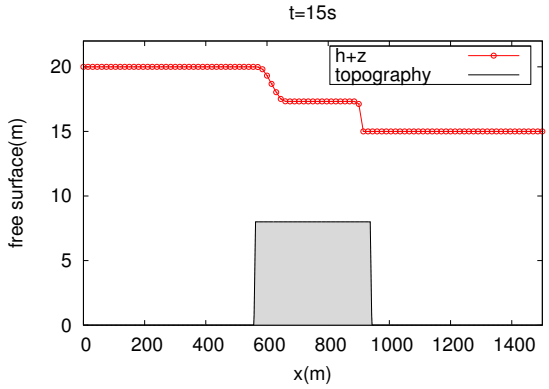

Figure II .17: Dam break over steps : Free surface profile at t=15s.

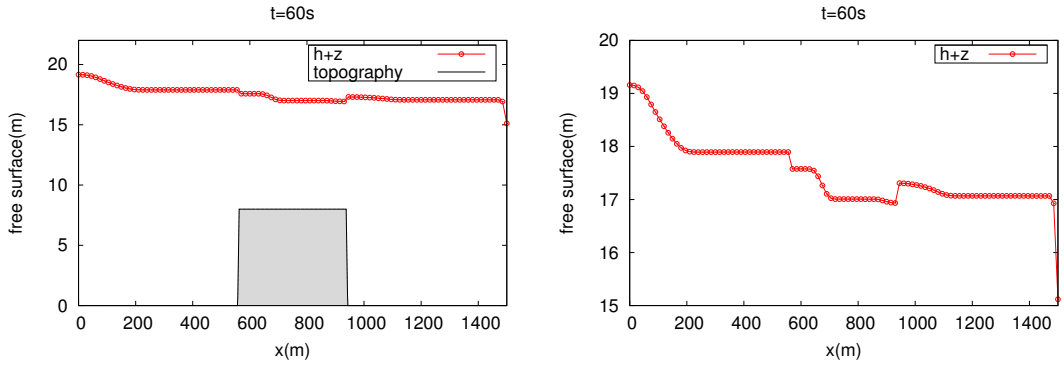

Figure II .18: Dam break over steps : Free surface profile at t=60s.

proposed on Fig. II .18. The results are in good agreement with those obtained with high order ENO and WENO balanced schemes available in [280, 286]. It should be mentioned that, as underlined in [6], concerns related to the treatment of the bottom source term are primordial for this test. Resolutions issuing from an unbalanced scheme for instance may entail important disturbances spreading around each ends of the bottom step. Thus, as a whole, these observations tends to confirm the ability of our numerical scheme to deal with critical slope values, without implementing some additional algorithms.

II.4.4 Oscillatory flow in a parabolic basin

We consider a $r = 4\,300$ m radius circular domain and we compute the periodic fluid evolution described in [266]. In this test case, we want to assess the accuracy of our scheme in a rather severe two dimensional framework, with an unstructured mesh, involving dry cells and varying topography. Two classes of exact solutions are available, namely the "planar" and "curved" cases, run for example in [34, 116, 171, 221, 243] and [34, 108, 243] respectively. We consider here the planar case, and use a 24 000 nodes unstructured triangulation. The bed profile is defined as follows :

$$z(x,y) = \frac{h_0}{L^2}(x^2+y^2),$$

and the exact solution is :

$$\begin{cases} \eta(x,y,t) = h_0 - \dfrac{B^2}{2g} - \dfrac{B}{g}s\,x\cos(s\,t) + \dfrac{B}{g}s\,y\sin(s\,t), \\ u(x,y,t) = B\sin(s\,t), \\ v(x,y,t) = -B\cos(s\,t), \end{cases} \tag{II .72}$$

with

$$h_0 = 10, \quad L = 3\,000, \quad p = \sqrt{\frac{8gh_0}{L^2}}, \quad s = \sqrt{\frac{p^2}{2}} \quad \text{and} \quad B = 5.$$

The initial condition is defined by evaluating (II .72) at $t = 0$. It provides a planar flow put in motion in the tangential direction. The corresponding profile is given in Fig. II .19, with an insight of the mesh and topography. The problem of boundary conditions is anecdotal for this case since the flow in not expected to reach the limits of the domain. When friction effects are neglected, the exact solution describes an oscillatory flow with an half-period of 672s. Fig. II .20 shows free surface profiles at times $t = 672$, 1 344, and 2 688 s, across the section $y = 0$. We observe a good agreement between numerical results and analytic solution, even after a long simulation time. The flow stays planar and the moving shoreline is properly described. The point (-1000 , 0) is selected to follow the evolution of the normal velocity (Fig. II .21). Here again, results attest of an appropriate treatment of the bed slope and wet/dry transitions. No losses of amplitude are observed. Similar conclusions can be derived from Fig. II .22, where we analyse the moving

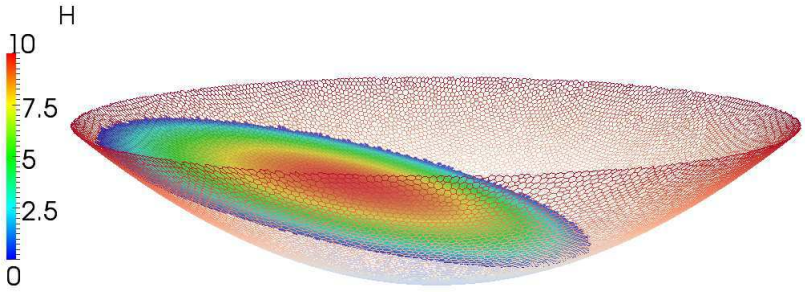

Figure II .19: Oscillatory flow in a parabolic basin : Mesh, geometry and initial condition.

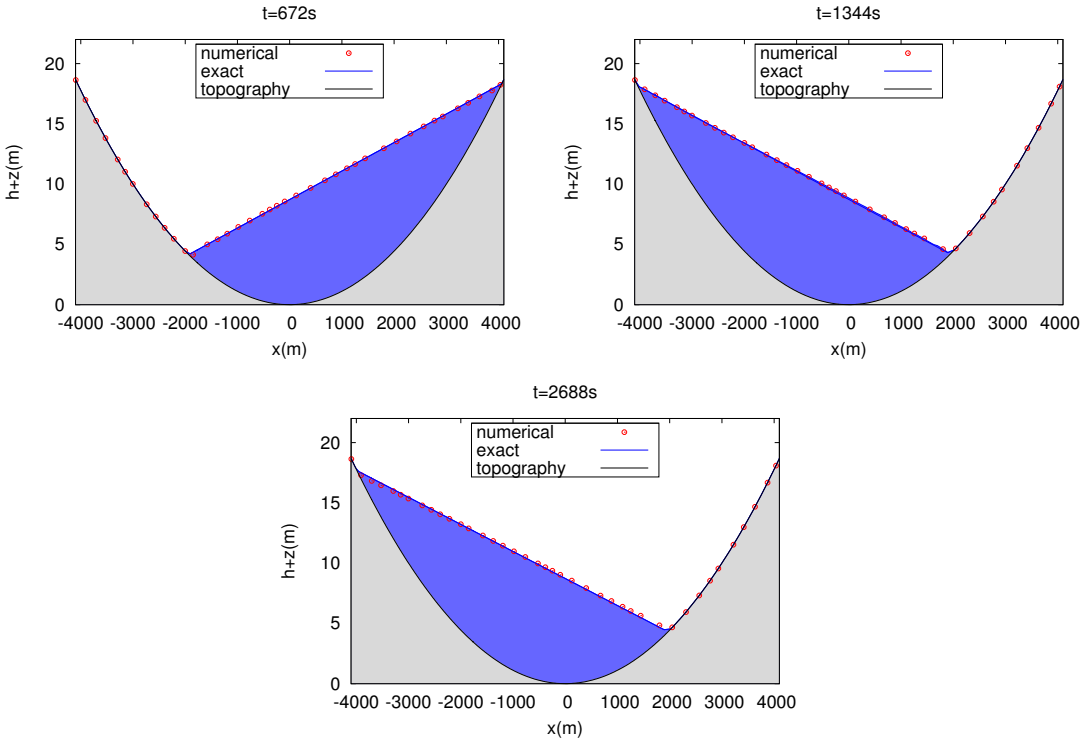

Figure II .20: Oscillatory flow in a parabolic basin : Free surface profiles at several times during the revolution process, and comparison with the analytic solution.

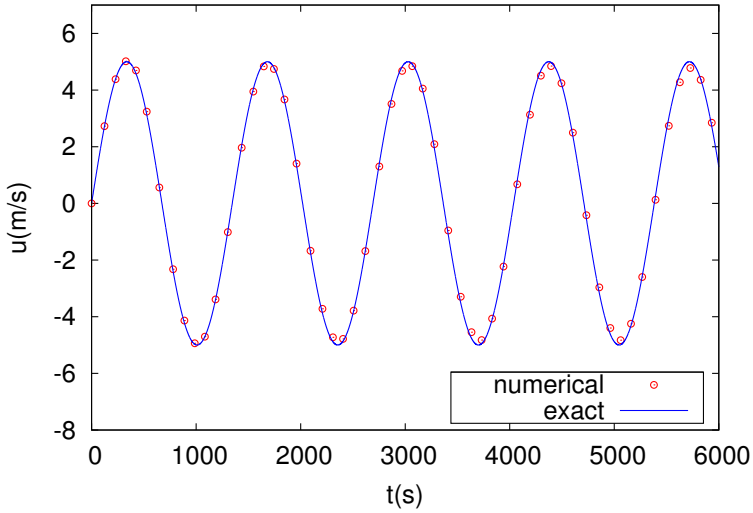

Figure II .21: Oscillatory flow in a parabolic basin : Time evolution of the x-direction velocity; analytic vs numeric.

shoreline location along the x-direction, the analytical solution being given by :

$$x(t) = \frac{a^2}{2gh_0}\big(-Bs\,cos(st)\big) \pm a\,.$$

II.4.5 Small perturbation of a lake at rest

We investigate a flow propagation around a stationary steady state, based on the test case proposed by LeVeque [187]. This test and several variants are widely used to exhibit the efficiency of 2d well-balanced methods in the vicinity of steady states, see for instance [152, 179, 194, 200, 243, 288]. This simulation involves a rectangular channel of $2\,m \times 1\,m$, and the topography variations are given by :

$$z(x,y) = 0.8e^{-5(x-0.9)^2-50(y-0.5)^2}\,.$$

The domain is discretized with an unstructured triangulation involving 11 476 nodes. The initial steady state is perturbed with the following initial free surface :

$$\eta(x,y,t=0) = \begin{cases} 1.01 & \text{if } 0.05 < x < 0.15, \\ 1 & \text{elsewhere.} \end{cases}$$

We can observe on Fig. II .23 some snapshots of the solutions obtained at times $t = 0.12\,s$, $t = 0.24\,s$, $t = 0.36\,s$ and $t = 0.48\,s$, with 3d free surface (left) and vertical section profiles along the line $y = 0.5$ (right). The M2 high order reconstruction employed in the computations is able to correctly reproduce the expected behaviour of the flow. High gradients are not excessively smoothed, but sufficiently controlled yet to avoid appearance of spurious oscillations. We obtain

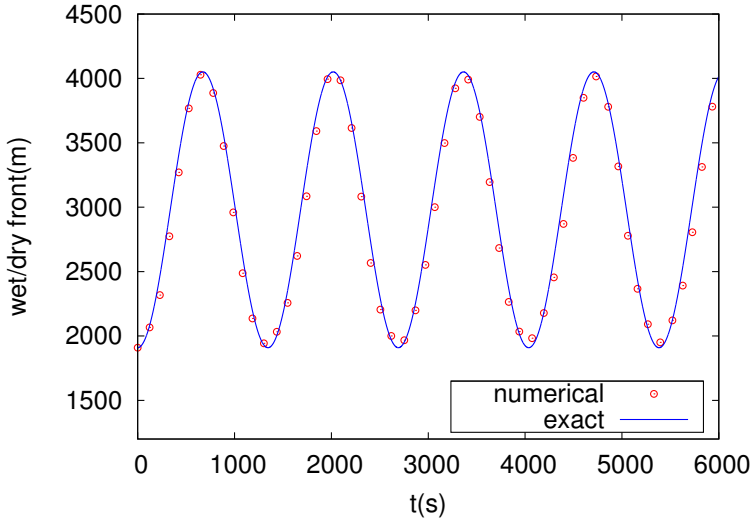

Figure II .22: Oscillatory flow in a parabolic basin : Time history of the wet/dry interface.

comparable results to those obtained in the literature with high order schemes ([46, 194, 243, 286, 291]), indicating a good resolution. The small perturbation seems to be accurately followed and the free surface profiles highlight the real efficiency of the low diffusion "second order" reconstruction (II .50).

II.4.6 Dam break problems

II.4.6.a 1d dam break

We further investigate the stability of the scheme in the key sector of dry domains through a series of dam break problems. Let's first analyse an archetypal example of 1d Riemann problem, with initial condition :

$$h(x) = \begin{cases} h_0 \text{ if } x < 0\,, \\ 0 \text{ otherwise}\,. \end{cases} \quad , \quad u(x) = 0\,.$$

The simulation involves a $20m$ long rectangular channel, centred in $x = 0$. A regular mesh is used with a space step $\Delta x = 0.05$ and we enforce $h_0 = 1m$ as upstream water height. Setting $c_0 = \sqrt{g h_0}$, the analytical solution is (see [33] for instance) :

$$\begin{aligned} h(x,t) &= \begin{cases} 1 & \text{if } x < -c_0 t\,, \\ \dfrac{1}{9g}\left(2c_0 - \dfrac{x}{t}\right)^2 & \text{if } -c_0 t < x < 2c_0 t\,, \\ 0 & \text{otherwise}\,. \end{cases} \\ u(x,t) &= \begin{cases} 0 & \text{if } x < -c_0 t\,, \\ \dfrac{2}{3}\left(c_0 + \dfrac{x}{t}\right) & \text{if } -c_0 t < x < 2c_0 t\,, \\ 0 & \text{otherwise}\,. \end{cases} \end{aligned} \tag{II .73}$$

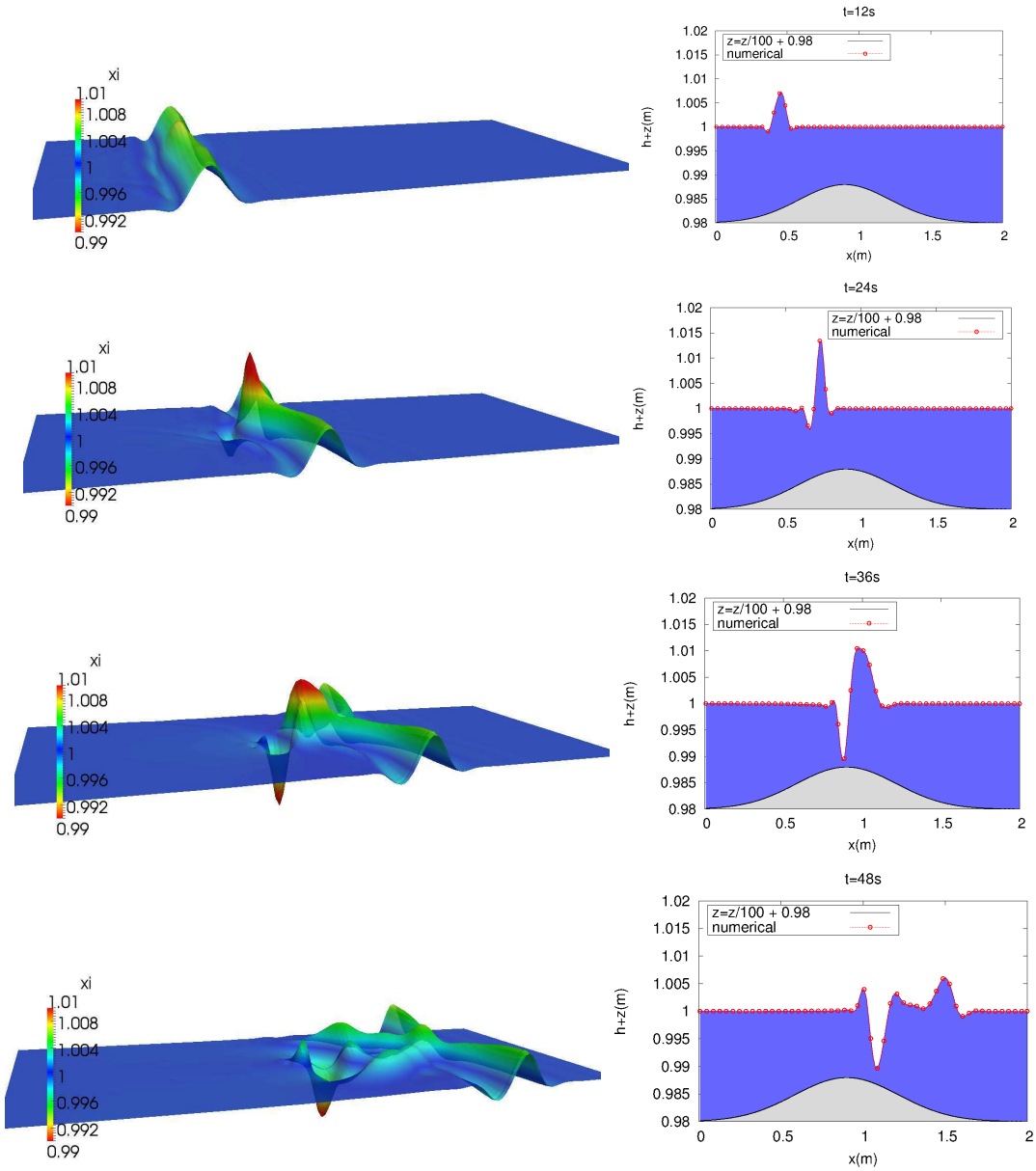

Figure II .23: Perturbation of a steady state at rest : Free surface elevation at several reference times: 3d surface and vertical section at $y = 0.5\,m$.

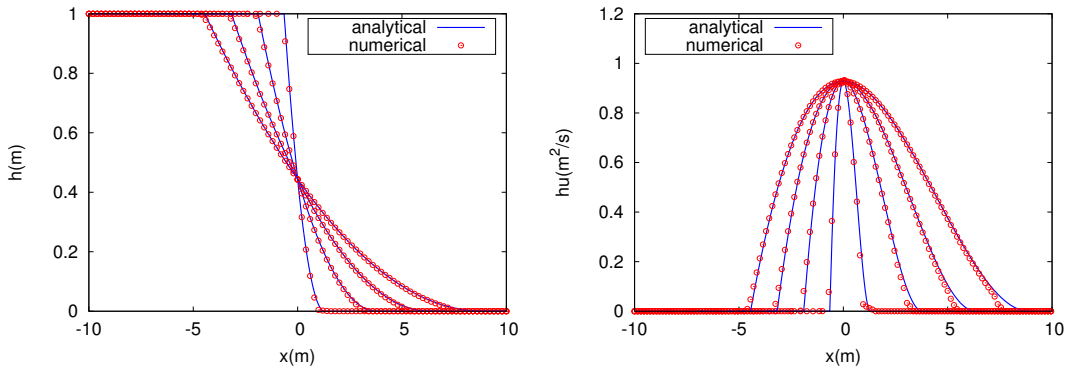

Figure II .24: 1d dam break : Water height (*left*) and discharge (*right*) profiles at $t = 0.2, 0.4, 0.6$ and $0.8s$.

Computations are run with the M2 scheme, and the numerical data on water height and discharge are stored for comparison at regular time intervals, up to $t = 1s$. This idealized situation leads to a solution composed of a rarefaction wave, propagating upstream and a travelling wet/dry front directed downstream. We can observe on Fig. II .24 that the numerical results follow closely the analytical solution. In particular, a closer look on the water depth profiles confirms that the initial discontinuity is correctly handled, with no excessive diffusive losses. The advancing water front is also accurately described, validating the stability of our numerical model when dealing with dry zones. In this connexion, also note that we effectively validated the positivity of the water height at each time step, in conformity with our theoretical expectations. As stated in [93, 170] for instance, when focusing on the discharge, one can assess the difficulties induced by the transition point of the water front. Note that comparable results are also obtained with the recent high order scheme [291] on cartesian grids. Naturally, as highlighted in [101], the space step can be decreased to reduce these discrepancies. As a whole, these results appear as totally satisfying, and form a solid basis for assessing the current scheme's accuracy during applications involving dry domains.

II.4.6.b Dam break over three mounds

This problem was initially proposed by Kawahara and Umetsu [164]. It involves a rectangular domain with dimensions $[0,75] \times [0,30]$. The bottom is composed of three circular domes with constant slopes, which shape and emplacement are given by (see [221]) :

$$\begin{aligned} z(x,y) = \max \Big(0 \,,\, & 1 - 0.1\sqrt{(x-30)^2 + (y-22.5)^2}, \\ & 1 - 0.1\sqrt{(x-30)^2 + (y-7.5)^2}, \\ & 2.8 - 0.28\sqrt{(x-47.5)^2 + (y-15)^2} \Big) \,. \end{aligned} \tag{II .74}$$

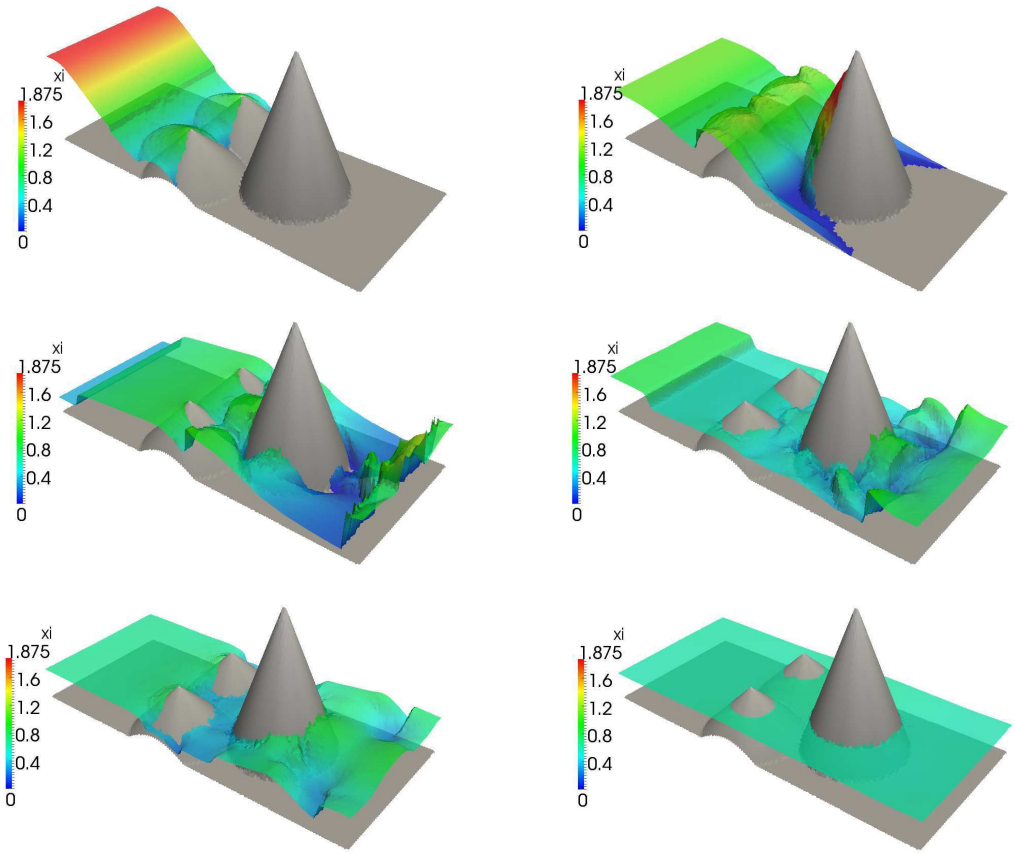

Figure II .25: Dam break over three mounds : 3d view of the flow at times t=2.5s, 5.5s, 16s, 23s, 30s up to the rest state (t=300s).

The dam is situated at $x = 16m$, all along the y-direction. An upstream free surface of $1.875m$ is prescribed, while the rest of the channel is supposed dry. We consider a closed basin, enforcing solid wall conditions at the surrounding boundaries. We lastly inform that the first order scheme has been employed, on an unstructured mesh of 19 142 elements. According to the boundary conditions, the quantity of water initially released has to be conserved throughout the simulation, and one can reasonably expect that the flow evolution leads to a motionless steady state. The main steps of the flow propagation can be assessed on Fig. II .25. The initial flood wave submerges the small mounds and propagates towards the central dome, channelled by the intermediate slopes. Two reflected waves are also generated and propagate in the opposite direction. Once the flow reached the principal mount, the advancing front separates in two surrounding waves. While following their progression downstream, we observe the apparition of a second second series of reflections around the central dome, with more complex features. This complicated behaviour results from multiple interactions induced by the slide walls and the combination of various contributions supplied by the successive passing of the three obstacles. After a certain time of evolution, the motion progressively attenuates, and we finally reach the quiescent state illustrated in the last picture. When compared against other results reported in

the literature [19, 45, 116, 169, 194, 221], our approximation seems to correctly describe the dynamics of the flow. All the steps previously mentioned are well reproduced by the numerical solution, which is also able to respect the symmetry of the problem. Again, robust computations are observed, without requiring particular treatment of dry zones. Also note that the final steady state is perfectly maintained at the discrete level, as we could expect.

II.4.7 Carrier and Greenspan transient solution

In this test case, we compare numerical results with one of the analytical solutions provided in [58]. The initial water surface elevation is assumed to be depressed near the frontier between the fluid domain and the dry area, and the fluid held motionless. Then, the fluid is released at $t = 0$ and we mainly focus on the interface evolution. During the evolution, the wet/dry interface rises above the mean fluid level and then the water surface elevation asymptotically settles back to it. The computational domain is a rectangular channel $[-20, 6] \times [0, 10]$, which is discretized with a regular triangulation, denoted $\Delta x = \dfrac{26}{n}$ for the x direction, and $\Delta y = \dfrac{10}{m}$ for the y direction, with $n = 100$ and $m = 30$. The topography is given by :

$$z(x, y) = s\, x \quad \text{with} \quad s = \frac{1}{50}, \tag{II .75}$$

and we denote V_{ex} the analytic solution introduced in [58]. The initial condition shown on Fig. II .27 (top) is defined with $V(x, y, t = 0) = V_{ex}(x, y, t = 0)$ and the time-evolving boundary condition on the left side of the domain is enforced with $V(x = -20, y, t) = V_{ex}(x = -20, y, t)$. Solid-wall boundary conditions are set elsewhere. Reader is referred to [209] for practical issues regarding the computation of the analytic solution. Fig. II .26 shows a comparison between numerical results obtained with the M2 scheme and the exact solution for the fluid free surface at several times, across the section $y = 5\, m$. Numerical results are accurate: the whole run up mechanism is very well reproduced, up to the steady state. The moving shoreline is properly described, as illustrate the 3d snapshots available in Fig. II .27. Fig. II .28 provides an overall appreciation of an additional convergence rate study, obtained with increasingly refined meshes ($\Delta x = \dfrac{26}{10 \times 2^n}$, $n = 1, \cdots, 4$), for the L^1-error for both first and formal second order schemes, in logarithmic scale. We can again point out the benefits conferred by the MUSCL reconstruction, in terms of accuracy and convergence rate.

II.5 Conclusion

In this chapter we have introduced a new two-dimensional well-balanced scheme on unstructured meshes for the NSW equations with topography source term, inspired from previous works in the 1d and 2d cartesian case. The construction of this scheme relies on a modified set of equations, in which the

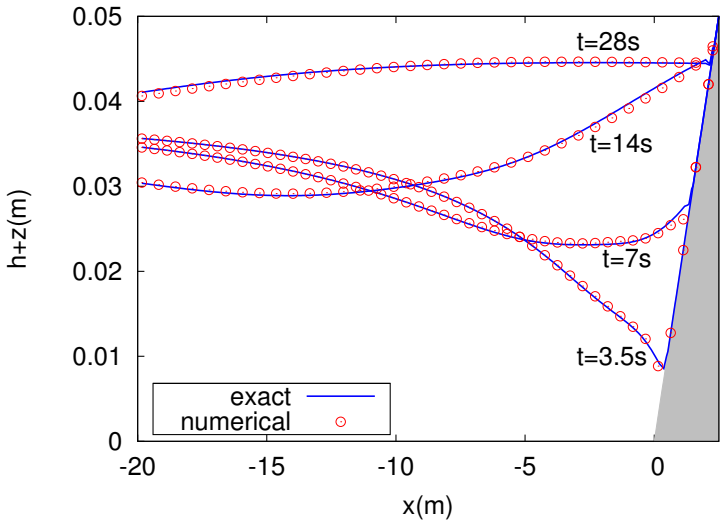

Figure II .26: Carrier and Greenspan transient solution : Evolution of the water free surface at several times during the evolution, and comparison with the analytic solution.

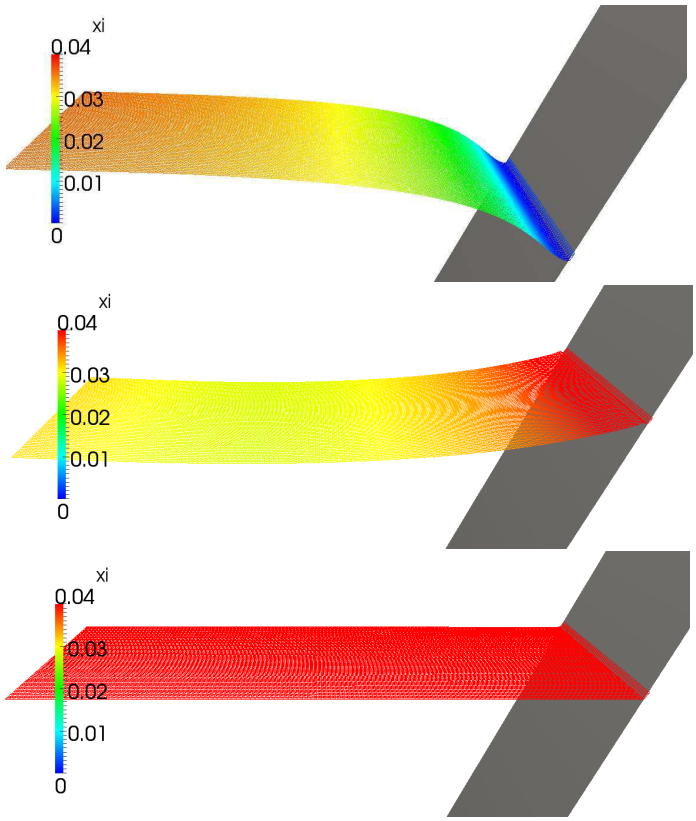

Figure II .27: Carrier and Greenspan transient solution : 3d views of the free surface. Initial condition, intermediate time t=15s, and final steady state.

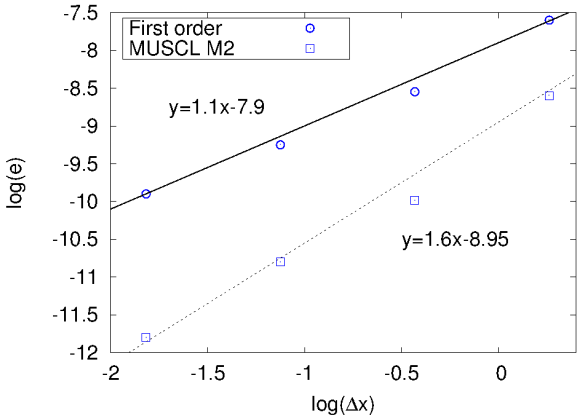

Δx	1^{st} order	MUSCL M2
1.3	5.00e-4	1.84e-4
0.65	1.94e-4	4.61e-5
0.325	9.61e-5	2.04e-5
0.1625	5.02e-5	7.50e-6

Figure II .28: Carrier and Greenspan transient solution : Convergence rate study for increasingly refined regular meshes.

free surface is used as a conservative variable instead of the water height. The discretization of the topography is shown to be consistent with the source term of the continuous equations, and provides a well-balanced scheme provided the choice of consistent numerical fluxes. In addition, whenever the initial one-dimensional solver satisfies some classical stability properties, we obtain a simple two-dimensional scheme that preserves the positivity of the water height. Two MUSCL reconstructions are proposed, allowing to significantly increase accuracy and convergence rate. Without requiring the introduction of some correction terms, they are theoretically and numerically shown to preserve the features of the original scheme.

An extensive series of benchmark experiments has been proposed, attesting of the efficiency of the numerical model in a wide variety of different contexts. The model is tested against some severe test cases, involving complex geometry, irregular topographies and dry cells. Strong stabilities properties are exhibited. The scheme is naturally able to deal with vertical bottom steps and dry areas without implementing additional algorithms. Well-balanced and robustness properties have been validated throughout the numerical validations, for both first order and MUSCL schemes, and the preservation of static equilibriums is still observed in the presence of emerging slopes.

To summarize, the present Finite Volume scheme fulfils the standard numerical requirements of a modern and efficient approach of the Shallow Water system. The first order scheme and its high order extensions share a unified formulation, with a basic discretization of the source. Moreover, in the absence of supplementary treatment for bottom jumps or dry cells, one of its main features is its great simplicity, together with an easy implementation. As a consequence, it appears as a solid basis in view of realistic applications. This brings us to the central question of the inclusion of resistance effects, that account for some physical and mechanical specificities of the domain, and may play an important role in many situations. In this perspective, an efficient way to treat these

additional source terms remains to be proposed, and is discussed in the coming chapter.

Chapter III

Friction treatment

III.1 Introduction

The orientation of numerical codes devoted to water waves toward realistic situations requires the introduction of some additional source terms able to account for various physical phenomena, neglected so far. One of the most recurring problems, because not straightforwardly handled via most of classical techniques, concerns the treatment of resistance terms. The general objective of this chapter is to propose some modern FVM which are able to correctly deal with friction. To get a more practical idea of the difficulty, let's first complete the current PBSW system with a second source term :

$$\frac{\partial V}{\partial t} + \nabla \cdot H(V,z) = S(V,z) + F(V,z)\,. \tag{III .1}$$

Friction laws being traditionally expressed in terms of water height and discharge, this friction term is first rewritten as: $F(V,z) = E(U)$, using the relation $h = \eta - z$. For the sake of generality, the present work will involve the three laws most commonly used :

$$\text{Manning} : E(U) = -\begin{pmatrix} 0 \\ n^2 \dfrac{\|\mathbf{q}\|}{h^{10/3}}\, q_x \\ n^2 \dfrac{\|\mathbf{q}\|}{h^{10/3}}\, q_y \end{pmatrix}, \tag{III .2a}$$

$$\text{Darcy} : E(U) = -\begin{pmatrix} 0 \\ \dfrac{d}{8}\dfrac{\|\mathbf{q}\|}{h^2} q_x \\ \dfrac{d}{8}\dfrac{\|\mathbf{q}\|}{h^2} q_y \end{pmatrix}, \tag{III .2b}$$

$$\text{Linear} : E(U) = -\begin{pmatrix} 0 \\ \kappa q_x \\ k q_y \end{pmatrix}, \tag{III .2c}$$

where n, d and κ are positive parameters.

Among the quantity of available works on Shallow Water equations, the problem of a suitable approach for the bed friction source term may deserve investigations yet. The main reason stands in the fact that divisions by h can be involved (III .2a, III .2b), and possibly generate instabilities in low water depths areas. To circumvent this difficulty, in some appropriate circumstances, linear terms [5, 302] or simplified friction laws [46, 181] may appear relevant as a first approximation. However, this solution cannot be considered as totally satisfactory since it does not allow to describe a large range of realistic situations. More severe laws may be accounted for through straightforward pointwize methods [151, 280, 293], provided again that the resistance parameters are moderate enough. Such an explicit method is suggested in [221] in a 2d node-centred unstructured FVM. In more general contexts, when attempting to reach better level of stability, semi implicit or fully implicit treatments are often employed

[43, 54, 92]. This is also the case in [63], with a supplementary effort concerning the balance between source and friction terms to exactly restore uniform channel flows equilibriums.

However, calculations issuing from these methods are generally not exempted from divisions by h either, and underlying stability issues still holds. As stated in [42], numerical models turns out to be very sensitive to the calibration of the tolerance value used to define the wet/dry transitions when friction terms are included. This threshold has sometimes to be considerably increased to avoid the perturbation mechanisms that threaten to be activated in very shallow waters, which becomes a dilemma if an accurate description of moving interfaces is simultaneously desired.

Although being generally overshadowed by other concerns in many works, several propositions driven by this problematic started to emerge since the last decade. Motivated by the necessity to have some control on these potential instabilities, Liang and Marche [194] proposed to add an additional *a posteriori* limiting stage to prevent an eventual reversing of the flow, which is evidence that the resistance effects have been locally overestimated. This method is successfully reused in [282] on cartesian grids, and more recently in the frame of unstructured grids [147, 148]. Note that similar stability arguments were also advanced by Murillo *et al* in the context of triangular meshes [217]. The method ensures that the sign of the discharge remains unchanged under a suitable time step condition. Thereafter, some improvements have been proposed by the authors in order to relax this time constraint [216], with the use of an upwind explicit well-balanced method, combined with an implicit discretization of the friction source term, specifically employed in critical areas to prevent from instabilities. Based on these ideas, another strategy consists in directly limiting the friction force to ensure relevant and stable computations [55].

Another way to proceed is borrowed from the recent headways made in the context of Asymptotic Preserving schemes [28]. The key idea consists of accounting for the source through a modified Riemann solver. The strategy is successfully employed in 1d for the NSW equations [27], leading to a stable, robust and well-balanced second order scheme. It should be stressed that similar ideas can be encountered in [215], where the authors include the bed slope and bottom friction terms within an augmented version of the HLL solver.

Contribution and objectives

The use of unstructured triangulations makes potentially complicated the implementation of direct extensions of 1d approaches. However, keeping in mind the first order scheme's structure of the previous chapter, such an objective is completely possible here. We hence first propose the extension of the 1d scheme [27]. More precisely, inspired from this work, we give a 1d discretization of the *pre-balanced* equations, allowing to deal with friction, and then re-valuate each convex component of the 2d scheme accordingly. The strategy naturally

extends the benefits of the method on unstructured meshes, and also preserves the original features of the frictionless scheme previously proposed. These improvements are detailed in the recent work [-3-].

Exploiting the practical aspects for which have been conceived these methods (see [28]), some modification can be introduced to preserve the asymptotic regime satisfied by the NSW equations, as done in [25] in the homogeneous 1d frame. Still in the context of unstructured meshes, and in the presence of varying topography, we propose a numerical scheme able to restore the diffusive limit of the continuous equations perturbed by strong friction effects. This work is intended to provide some initial responses about the conception and usefulness of AP schemes in such a context. This is illustrated within another Finite Volume approach, subject to an article under evaluation to date ([-4-]).

In point of fact, this analysis is organized on the basis of two numerical schemes. The first section will complement the construction of our Finite Volume *pre balanced* model. The strategy leading to the inclusion of friction is detailed in 1d first, and then straightforwardly extended on vertex-based geometries. The properties of the enhanced scheme are illustrated in a series of numerical validations. In the second part the approach is implemented within another recent FVM [24], with the objective of achieving some Asymptotic Preserving property. A novel series of experiments is proposed, partly intended to show the impact of such a property over several types of flows. According to the previous remarks, a focus on stability issues will also be of interest throughout the experimental parts.

III.2 *Pre Balanced* friction scheme

III.2.1 The 1d case

We first see how to integrate friction in the 1d *pre balanced* scheme. To address the problem, let's first assume that the friction law has the following form :

$$E(U) = -\kappa \frac{|q|}{h^\gamma} \begin{pmatrix} 0 \\ q \end{pmatrix}, \tag{III .3}$$

with κ, γ two positive constants. Note that Manning and Darcy friction laws (III .2a, III .2b) falls within such a formalism, with $\kappa = n^2, \gamma = 10/3$ and $\sigma = d/8, \gamma = 2$ respectively. Following the general ideas introduced in [28] for such class of source terms, the method relies on the use of a modified HLL scheme. In this section, for the sake of simplicity, we indistinctly denote H the exact flux function of the 1d or 2d continuous equations (III .1). Denoting $s^\pm$ the minimum and maximum velocity waves involved in the approximate Riemann solver, the inclusion of friction is accounted for through the following corrected states :

$$\tilde{V}_{\mathcal{R}}(\frac{x}{t}, V^-, V^+) = \begin{cases} V^- \quad \text{if} \quad \frac{x}{t} \leq s^-, \\ \alpha V_* + (1-\alpha) R(V^-) \quad \text{if} \quad \min(0, s^-) < \frac{x}{t} \leq \min(0, s^+), \\ \alpha V_* + (1-\alpha) R(V^+) \quad \text{if} \quad \max(0, s^-) < \frac{x}{t} \leq \max(0, s^+), \\ V^+ \quad \text{if} \quad \frac{x}{t} \geq s^+. \end{cases} \tag{III .4}$$

where V_* is the classical HLL intermediate state (I .25) :

$$V_* = \frac{s^+ V^+ - s^- V^- - \big(H(V^+) - H(V^-)\big)}{s^+ - s^-}, \tag{III .5}$$

and we adopted the simplified notation :

$$R(V) = \begin{pmatrix} R^\eta(V) \\ R^q(V) \end{pmatrix} = \begin{pmatrix} \eta^* \\ q - |q|q \end{pmatrix}. \tag{III .6}$$

Remark III.2 .1. *As concerns the expression of R given just above, the choice of the first component appears as natural, considering that, at the continuous level, the friction term does not impact the mass equation. Thus, if we denote $V_{\mathcal{R}}$ the usual HLL Riemann solver, we have $V^\eta_{\mathcal{R}} = \tilde{V}^\eta_{\mathcal{R}}$, and we consequently have to focus on the evolution of the discharge only.*
Considering now the discharge, we first remark that the corresponding component of the friction source term can be recast under the form:

$$E^q(U) = \sigma(h)\Big(R^q(V) - q\Big), \text{ with } \sigma(h) = \frac{\kappa}{h^\gamma}. \tag{III .7}$$

Historically, in the pioneering works mentioned above, modified HLL solvers are precisely introduced to handle source terms under the general form (III .7). In several

physical situations of interest indeed, the presence of a convex combination linking V^* to R (appearing here in the intermediate waves (III.3.2)) allows both to recover the classical solver in absence of source terms, and supplies a technical support for the restoration of particular limit regimes at the discrete level (corresponding to the situation where α tends to zero). Obviously, it requires a consistent calibration of α, offering relevant approximations in both limits. In this work, and based on these objectives, we actually show that this modification allows a proper evaluation of the friction source term, able to cover very low resistance values and extremely rough coefficients.

Before going further, some complements on the HLL solver might be useful. Primarily, let's remark that defining an approximate solution at time $t^{n+1} = t^n + \Delta t$ as :

$$V_{\mathfrak{h}}(x) = V_{\mathcal{R}}\Big(\frac{x - x_{i+1/2}}{t^{n+1}}, V_i, V_{i+1}\Big)\,, \quad \text{if} \quad x \in [x_i, x_{i+1}]\,, \tag{III .8}$$

the HLL fluxes (I .27) can be rewritten under the classical form :

$$\begin{aligned}
\mathcal{H}_{i-\frac{1}{2}} &= \mathcal{H}(V_{i-1}, V_i, z_{i-i}, z_i) = \frac{1}{\Delta t}\int_{x_{i-1/2}}^{x_i} V_{\mathfrak{h}}(x)\,dx - \frac{\Delta x}{2\Delta t}V_i + H(V_i, z_i)\,,\\
\mathcal{H}_{i+\frac{1}{2}} &= \mathcal{H}(V_i, V_{i+1}, z_i, z_{i+1}) = -\frac{1}{\Delta t}\int_{x_i}^{x_{i+1/2}} V_{\mathfrak{h}}(x)\,dx + \frac{\Delta x}{2\Delta t}V_i + H(V_i, z_i)\,.
\end{aligned} \tag{III .9}$$

It directly results that the 1d Finite Volume homogeneous HLL scheme :

$$V_i^{n+1} = V_i^n - \frac{\Delta t}{\Delta x}\big(\mathcal{H}_{i+\frac{1}{2}} - \mathcal{H}_{i-\frac{1}{2}}\big)\,, \tag{III .10}$$

can be expressed in terms on projection of the approximate solution (III .8) onto the piecewise constant functions :

$$V_i^{n+1} = \frac{1}{\Delta x}\int_{x_{i-1/2}}^{x_{i+1/2}} V_{\mathfrak{h}}(x)\,dx\,. \tag{III .11}$$

In the current context, we can straightforwardly reproduce the analysis performed in [28] for the present solver. For purposes of clarifications, we exhibit the main steps of the reasoning. Invoking the modified solver (III .4) in (III .8), we set :

$$\tilde{V}_{\mathfrak{h}}(x) = \tilde{V}_{\mathcal{R}}\Big(\frac{x - x_{i+1/2}}{t^{n+1}}, V_i, V_{i+1}\Big)\,, \quad \text{if} \quad x \in [x_i, x_{i+1}]\,,$$

and propose to advance to the next time level via :

$$V_i^{n+1} = \frac{1}{\Delta x}\int_{x_{i-1/2}}^{x_{i+1/2}} \tilde{V}_{\mathfrak{h}}(x)\,dx\,. \tag{III .12}$$

This integral is subsequently decomposed in two contributions. Setting $x_{i-1/2}^{\pm} =$

$x_{i-1/2} + \Delta t \max(0, s^{\pm}_{i-1/2})$, the first one is expanded as :

$$\begin{aligned}\frac{1}{\Delta x}\int_{x_{i-1/2}}^{x_i} \tilde{V}_{\mathfrak{h}}(x)\,dx &= \frac{\alpha_{i-1/2}}{\Delta x}\int_{x_{i-1/2}}^{x_i} V_{\mathfrak{h}}(x)\,dx + \\ &\quad \frac{1-\alpha_{i-1/2}}{\Delta x}\left(\int_{x_{i-1/2}}^{x^-_{i-1/2}} V_{i-1}\,dx + \int_{x^-_{i-1/2}}^{x^+_{i-1/2}} R(V_i)\,dx + \int_{x^+_{i-1/2}}^{x_i} V_i\,dx\right) \\ &= \frac{\alpha_{i-1/2}}{\Delta x}\int_{x_{i-1/2}}^{x_i} V_{\mathfrak{h}}(x)\,dx + \frac{1-\alpha_{i-1/2}}{2}V_i + \\ &\quad \frac{\Delta t}{\Delta x}(1-\alpha_{i-1/2})\left(\max(0,s^-_{i-1/2})(V_{i-1}-R(V_i)) + \max(0,s^+_{i-1/2})(R(V_i)-V_i)\right).\end{aligned}$$

Then, calling (III .9), one obtains :

$$\frac{1}{\Delta x}\int_{x_{i-1/2}}^{x_i} \tilde{V}_{\mathfrak{h}}(x)\,dx = \frac{1}{2}V_i + \frac{\Delta t}{\Delta x}\alpha_{i-1/2}\mathcal{H}_{i-1/2} - \frac{\Delta t}{\Delta x}H(V_i) + \frac{\Delta t}{\Delta x}(1-\alpha_{i-1/2})F^+_{i-1/2}, \tag{III .13}$$

where

$$F^+_{i-1/2} = \max(0,s^-_{i-1/2})(V_{i-1}-R(V_i)) + \max(0,s^+_{i-1/2})(R(V_i)-V_i) + H(V_i,z_i).$$

In a similar way, we also have :

$$\frac{1}{\Delta x}\int_{x_i}^{x_{i+1/2}} \tilde{V}_{\mathfrak{h}}(x)\,dx = \frac{1}{2}V_i - \frac{\Delta t}{\Delta x}\alpha_{i+1/2}\mathcal{H}_{i+1/2} + \frac{\Delta t}{\Delta x}H(V_i) + \frac{\Delta t}{\Delta x}(1-\alpha_{i+1/2})F^-_{i+1/2}, \tag{III .14}$$

with

$$F^-_{i+1/2} = \min(0,s^-_{i+1/2})(V_i-R(V_i)) + \min(0,s^+_{i+1/2})(R(V_i)-V_{i+1}) - H(V_i,z_i).$$

At last, gathering (III .12, III .13, III .14), and proceeding to the reconstruction steps (II .6 - II .11) before evaluating the numerical fluxes $\mathcal{H}_{i\pm1/2}$, we reach the following formula for the update of the discharge :

$$q_i^{n+1} = q_i^n - \frac{\Delta t}{\Delta x}\left(\alpha_{i+\frac{1}{2}}\mathcal{H}^q_{i+\frac{1}{2}} - \alpha_{i-\frac{1}{2}}\mathcal{H}^q_{i-\frac{1}{2}}\right) + \frac{\Delta t}{\Delta x}\left((1-\alpha_{i-\frac{1}{2}})F^{+,q}_{i-\frac{1}{2}} + (1-\alpha_{i+\frac{1}{2}})F^{-,q}_{i+\frac{1}{2}}\right). \tag{III .15}$$

The consideration of the modified solver hence induces the presence of weighted fluxes and generates a numerical source term, designed to approximate the friction forces. In the above formula, the fluxes $\mathcal{H}_{i\pm\frac{1}{2}}$ are provided by the usual HLL scheme, applied to the reconstructed states (II .6,II .7,II .9,II .11) to guarantee robustness and well-balancing properties.

We come now to the evaluation of the quantities $\alpha_{i\pm\frac{1}{2}}$, which are the discrete equivalents of the parameter $\alpha \in [0,1]$ introduced in (III .4). As stated in Remark III.2 .1, this coefficient mainly controls friction and has to be appropriately defined. One of the first requirements is driven by the fact that we ask the modified solver to degenerate toward the usual HLL solver when the resistance

effects tends to zero. On the other hand, the case of dominant friction terms will correspond to the situation where α tends to zero. Another fundamental requirement is related to consistency aspects, since we actually have to ensure that the contribution:

$$F_i := \Big(\frac{1-\alpha_{i-\frac{1}{2}}}{\Delta x}\Big) F^{+,q}_{i-\frac{1}{2}} + \Big(\frac{1-\alpha_{i+\frac{1}{2}}}{\Delta x}\Big) F^{-,q}_{i+\frac{1}{2}} \tag{III .16}$$

furnishes a correct approximation of the corresponding term $E^q(U)$ appearing in the continuous equations. Lastly, keeping in mind the willingness to prevent from computational difficulties in situations of vanishing water depths, the expression of α should ideally remain relevant whenever h tends to (or even reaches) zero. To summarize, the criteria that have to be satisfied are:

- $\alpha \in [0,1]$.
- $\lim\limits_{\sigma\to\infty} \alpha = 0$.
- $\alpha = 1$ in absence of friction.
- α is defined on dry cells.
- Consistency with the friction source term of the continuous equations.

Among the possible choices satisfying these properties, one can consider (see also [27]) :

$$\alpha = \frac{\overline{h}^{\gamma}\big(s^+ - s^-\big)}{\overline{h}^{\gamma}\big(s^+ - s^-\big) + \kappa\Delta x} \ , \ \text{where } \overline{h} = \frac{h^- + h^+}{2} , \tag{III .17}$$

from which are extracted the coefficients $\alpha_{i\pm\frac{1}{2}}$ involved in (III .15), using the *exterior* and *interior* values at the interfaces $i \pm 1/2$.

Remark III.2 .2. *Thus, with this choice, it's worth mentioning that the friction source term discretization F_i proposed in (III .16) makes it possible to avoid divisions by h, which traditionally threaten the stability of numerical models dealing with laws based on (III .3). In this work, the consistency of F_i with the continuous equations will be established in the 2d frame, in the simplified case $s^+ = -s^-$. We refer to [28] for more general consistency results in the 1d case.*

III.2.2 The 2d case

Now, let us take advantage of the formulation (II .24 - II .25) to include the friction source term. We propose to carry out the update of each convex component

by the mean of (III .15). For any edge $\Gamma_{ij(k)}$, we consequently set :

$$\begin{aligned} hu_{ij(k)}^{n+1} &= hu_i^n - \Delta t \frac{\ell_{ij(k)}}{|T_{ij(k)}|}\Big(\alpha_k \mathcal{H}_{ij(k)}^{hu} - \alpha_k^c \mathcal{H}_{ij(k)}^{c,hu}\Big) + \\ &\qquad \Delta t \frac{\ell_{ij(k)}}{|T_{ij(k)}|}\Big((1-\alpha_k^c)F_k^{c,hu} + (1-\alpha_k)F_k^{hu}\Big)\,, \\ hv_{ij(k)}^{n+1} &= hv_i^n - \Delta t \frac{\ell_{ij(k)}}{|T_{ij(k)}|}\Big(\alpha_k \mathcal{H}_{ij(k)}^{hv} - \alpha_k^c \mathcal{H}_{ij(k)}^{c,hv}\Big) + \\ &\qquad \Delta t \frac{\ell_{ij(k)}}{|T_{ij(k)}|}\Big((1-\alpha_k^c)F_k^{c,hv} + (1-\alpha_k)F_k^{hv}\Big)\,, \end{aligned} \tag{III .18}$$

where the friction parameters are straightly derived from those given in the 1d formulation. In the sequel, we denote $R^{\mathbf{q}}(V) = {}^t\big(R^{hu}(V), R^{hv}(V)\big) = \mathbf{q} - \|\mathbf{q}\|\mathbf{q}$, and employ similar notations to gather the discharge components of the friction terms $F_k^{\mathbf{q}}$, $F_k^{c,\mathbf{q}}$ involved in (III .18). In the continuity of the previous developments, let us employ the notations $s_k^{c,\pm}$, $s_k^{\pm}$ for the velocity waves involved in the computation of $\mathcal{H}_{ij(k)}^c$ and $\mathcal{H}_{ij(k)}$ respectively, and set $\overline{h}_k = (h_i + h_{j(k)})/2$. Thus, in the reference associated with $\vec{n}_{ij(k)}$, each contribution relative to friction is evaluated that way :

$$\begin{aligned} &\alpha_k^c = \frac{h_i^\gamma\big(s_k^{c,+} - s_k^{c,-}\big)}{h_i^\gamma\big(s_k^{c,+} - s_k^{c,-}\big) + \kappa\delta_{ij(k)}} \quad , \quad \alpha_k = \frac{\overline{h}_k^\gamma\big(s_k^{+} - s_k^{-}\big)}{\overline{h}_k^\gamma\big(s_k^{+} - s_k^{-}\big) + \kappa\delta_{ij(k)}}\,, \\ &F_k^{c,\mathbf{q}} = \max(0, s_k^{c,-})\big(\mathbf{q}_i - R^{\mathbf{q}}(V_i)\big) + \max(0, s_k^{c,+})\big(R^{\mathbf{q}}(V_i) - \mathbf{q}_i\big) + H^{\mathbf{q}}(V_i, z_i).\vec{n}_{ij(k)}\,, \\ &F_k^{\mathbf{q}} = \min(0, s_k^{-})\big(\mathbf{q}_i - R^{\mathbf{q}}(V_i)\big) + \min(0, s_k^{+})\big(R^{\mathbf{q}}(V_i) - \mathbf{q}_{j(k)}\big) - H^{\mathbf{q}}(V_i, z_i).\vec{n}_{ij(k)}\,, \end{aligned} \tag{III .19}$$

Now, keeping in mind that the evolution of the free surface is still governed by the original scheme, and including the bed slope source term introduced in (II .20), formula (II .24 - II .25) gives, integrating modifications (III .18) :

$$\begin{aligned} \eta_i^{n+1} &= \eta_i^n - \frac{\Delta t}{|C_i|}\sum_{k=1}^{\Lambda(i)} \ell_{ij(k)} \mathcal{H}_{ij(k)}^{\eta}\,, \\ hu_i^{n+1} &= hu_i^n - \frac{\Delta t}{|C_i|}\sum_{k=1}^{\Lambda(i)} \ell_{ij(k)}\big(\alpha_k \mathcal{H}_{ij(k)}^{hu} - \alpha_k^c \mathcal{H}_{ij(k)}^{c,hu}\big) + \frac{\Delta t}{|C_i|}\sum_{k=1}^{\Lambda(i)} \ell_{ij(k)} \mathcal{F}_k^{hu} + \Delta t S_i^{hu}\,, \\ hv_i^{n+1} &= hv_i^n - \frac{\Delta t}{|C_i|}\sum_{k=1}^{\Lambda(i)} \ell_{ij(k)}\big(\alpha_k \mathcal{H}_{ij(k)}^{hv} - \alpha_k^c \mathcal{H}_{ij(k)}^{c,hv}\big) + \frac{\Delta t}{|C_i|}\sum_{k=1}^{\Lambda(i)} \ell_{ij(k)} \mathcal{F}_k^{hv} + \Delta t S_i^{hv}\,, \end{aligned} \tag{III .20}$$

where

$$\mathcal{F}_k^{\mathbf{q}} = {}^t(\mathcal{F}_k^{hu}, \mathcal{F}_k^{hv}) = (1-\alpha_k^c)F_k^{c,\mathbf{q}} + (1-\alpha_k)F_k^{\mathbf{q}}\,. \tag{III .21}$$

It is useful to note that, invoking the consistency relation $\mathcal{H}_{ij(k)}^c = H(V_i, z_i).\vec{n}_{ij(k)}$, the discharge evolution in the previous set of equations can

equally be written as :

$$\begin{aligned} hu_i^{n+1} &= hu_i^n - \frac{\Delta t}{|C_i|}\sum_{k=1}^{\Lambda(i)} \ell_{ij(k)}\big(\alpha_k \mathcal{H}_{ij(k)}^{hu} - \alpha_k \mathcal{H}_{ij(k)}^{c,hu}\big) + \frac{\Delta t}{|C_i|}\sum_{k=1}^{\Lambda(i)} \ell_{ij(k)}\mathcal{E}_k^{hu} + \Delta t S_i^{hu}\,, \\ hv_i^{n+1} &= hv_i^n - \frac{\Delta t}{|C_i|}\sum_{k=1}^{\Lambda(i)} \ell_{ij(k)}\big(\alpha_k \mathcal{H}_{ij(k)}^{hv} - \alpha_k \mathcal{H}_{ij(k)}^{c,hv}\big) + \frac{\Delta t}{|C_i|}\sum_{k=1}^{\Lambda(i)} \ell_{ij(k)}\mathcal{E}_k^{hv} + \Delta t S_i^{hv}\,, \end{aligned} \tag{III .22}$$

where

$$\begin{aligned} \mathcal{E}_k^{\mathbf{q}} &= {}^t(\mathcal{E}_k^{hu}, \mathcal{E}_k^{hv}) = (1-\alpha_k^c)E_k^{c,\mathbf{q}} + (1-\alpha_k)E_k^{\mathbf{q}}\,, \\ E_k^{c,\mathbf{q}} &= \max(0, s_k^{c,-})\big(\mathbf{q}_i - R^{\mathbf{q}}(V_i)\big) + \max(0, s_k^{c,+})\big(R^{\mathbf{q}}(V_i) - \mathbf{q}_i\big)\,, \\ E_k^{\mathbf{q}} &= \min(0, s_k^{-})\big(\mathbf{q}_i - R^{\mathbf{q}}(V_i)\big) + \min(0, s_k^{+})\big(R^{\mathbf{q}}(V_i) - \mathbf{q}_{j(k)}\big)\,. \end{aligned} \tag{III .23}$$

Thanks to the use of convex combinations, the consistency results issuing from the 1d analysis ensure a relevant estimation of the source term appearing in the continuous equations. More precisely, we have the following result :

Proposition 6. *Assume that the numerical fluxes are computed using the Rusanov fluxes (I.3.1). In other words, we define the maximum and minimum characteristic speeds in the HLL Riemann solver as :*

$$s_k^{\pm} = \pm a_k \quad , \quad a_k = \max\left(|\mathbf{u}_i.\vec{n}_{ij(k)}| + \sqrt{g h_i}, |\mathbf{u}_{j(k)}.\vec{n}_{ij(k)}| + \sqrt{g h_{j(k)}}\right)\,. \tag{III .24}$$

Then, the contribution $\dfrac{\Delta t}{|C_i|}\sum_{k=1}^{\Lambda(i)} \ell_{ij(k)}\mathcal{E}_k^{\mathbf{q}}$ *is consistent with the friction source term present in the momentum equations of (III .1).*

Proof. We first notice that in these conditions, (III .23) becomes :

$$\mathcal{E}_k^{\mathbf{q}} = a_k^c(1-\alpha_k^c)(R^{\mathbf{q}}(V_i) - \mathbf{q}_i) + a_k(1-\alpha_k)(R^{\mathbf{q}}(V_i) - \mathbf{q}_i)\,.$$

We then write :

$$\begin{aligned} \frac{\ell_{ij(k)}}{|C_i|}(1-\alpha_k^c) &= \frac{|T_{ij(k)}|}{|C_i|}\frac{\kappa}{2a_k^c h_i^{\gamma} + \kappa\delta_{ij(k)}}\,, \\ \frac{\ell_{ij(k)}}{|C_i|}(1-\alpha_k) &= \frac{|T_{ij(k)}|}{|C_i|}\frac{\kappa}{2a_k \overline{h}_k^{\gamma} + \kappa\delta_{ij(k)}}\,, \end{aligned}$$

and study the behaviour of the source term $\sum_{k=1}^{\Lambda(i)} \dfrac{\ell_{ij(k)}}{|C_i|}\mathcal{E}_k^{\mathbf{q}}$ as $\mathfrak{d}_i = diam(C_i)$ tends to zero. We can easily check that we have :

$$\begin{aligned} \lim_{\mathfrak{d}_i\to 0} \frac{\ell_{ij(k)}}{|C_i|}a_k^c(1-\alpha_k^c)(R^{\mathbf{q}}(V_i) - \mathbf{q}_i) &= \lim_{\mathfrak{d}_i\to 0} \frac{\ell_{ij(k)}}{|C_i|}a_k(1-\alpha_k)(R^{\mathbf{q}}(V_i) - \mathbf{q}_i) \\ &= \frac{|T_{ij(k)}|}{|C_i|}\frac{\kappa}{2h_i^{\gamma}}(R^{\mathbf{q}}(V_i) - \mathbf{q}_i)\,. \end{aligned}$$

Consequently :

$$\lim_{\mathfrak{d}_i \to 0} \frac{1}{|C_i|} \sum_{k=1}^{\Lambda(i)} \ell_{ij(k)} \mathcal{E}_k^{\mathbf{q}} = \sum_{k=1}^{\Lambda(i)} \frac{|T_{ij(k)}|}{|C_i|} \frac{\kappa}{h_i^{\gamma}} (R^{\mathbf{q}}(V_i) - \mathbf{q}_i) . \\ = E^{\mathbf{q}}(U_i) .$$

□

Remark III.2 .3. *This strategy can be adapted to other resistance laws. In the context of linear friction (III .2c) for example, an appropriate discretization of the source can be deduced from :*

$$\alpha = \frac{s^+ - s^-}{s^+ - s^- + k\Delta x} , \ R(V) = \begin{pmatrix} \eta^* \\ 0 \end{pmatrix} .$$

Remark III.2 .4. *Recalling that no additional time constraint has been introduced, that the evolution of the total free surface is not modified, and that the friction terms vanish in absence of motion, robustness and C-property results still holds, even when applying the MUSCL extensions previously introduced.*
Again, note that the friction terms evaluation (III .19) is not problematic when the water depth tends to zero.

III.2.3 Numerical validations

III.2.3.a Dam break with friction

We consider a classical 1d dam break problem with friction on a flat bottom, and focus on the treatment of dominant resistance effects in the neighbourhood of the wet/dry front. In a 2d framework, the test involves a rectangular flume with dimensions $[-10, 10] \times [0, 4]$. The initial water depth is set to $1m$ at the left of the dam $(x \leq 0)$, and 0 elsewhere. For this test, we employ a Darcy friction law (III .2b) with $d = 0.05$, and use a 8 241 nodes regular grid, with $\Delta x = \Delta y = 0.1m$.

One can build a relevant approximation of the exact solution decomposing the domain in two regions behind the wave front location : in the first area, friction effects are neglected and the analytical solution is provided by an ideal fluid flow model, while in the wave tip region bed the resistance phenomena are considered as dominant compared to acceleration and inertial effects. Physical and mathematical aspects of such construction are detailed in [68]. Fig. III .1 (top) shows some profiles of the water depth along the x-direction centreline, until $t = 2.4s$. We can observe a good agreement with the analytical solution, for both first order and MUSCL schemes. If the benefits of the MUSCL reconstruction principally appear during the handling of the shock for the water depth, we also remark a more accurate evaluation of the front speed on Fig. III .1 (bottom). The flood wave front location seems to be accurately computed, which tends to validate the ability of the current scheme to deal with friction when vanishing water heights and dry cells are involved. We can also point out the good concordance with the predictions provided by the approach of Céa *et al* in [63] for the water depth.

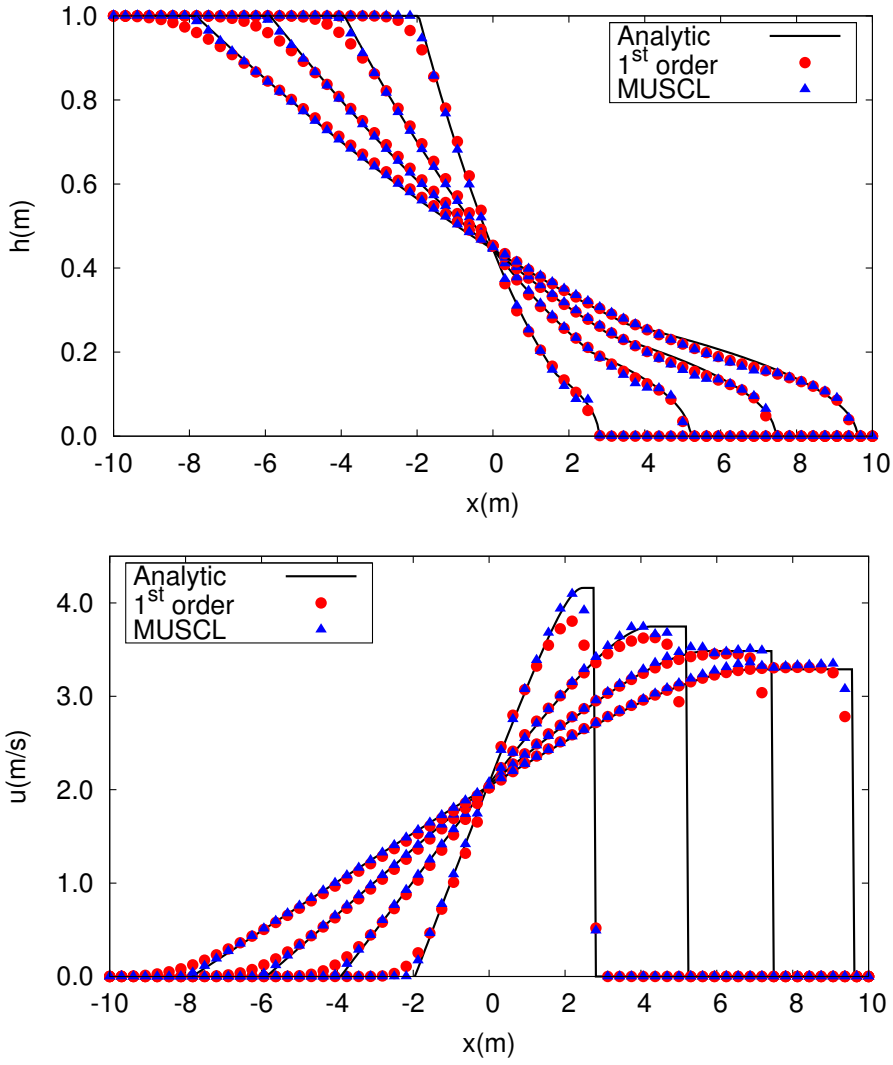

Figure III .1: Dam break with friction : Water depth (*top*) and velocity (*bottom*) profiles at t=0.6, 1.2, 1.8 and 2.4s. Analytical solution compared with first order and MUSCL approximations.

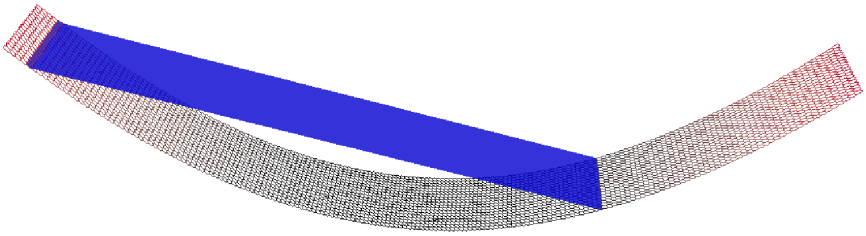

Figure III .2: Moving boundary over a parabolic bottom : Initial condition.

III.2.3.b Moving boundary over a parabolic bottom

The following test is adapted from a 1d version [195] of the experiments initially set up by Thacker [266]. Recently, several authors proposed some enhancements on the family of Thacker's test cases, introducing some friction terms in the exact solutions. Sampson *et al* [249] proposed a first advancing for the planar case over a parabolic bottom in 1d, considering a linear friction law (III .2c). Since then, this test is regularly employed [170, 171, 195], and more recently, a 2d extrapolation has been proposed by Wang *et al* [282]. We refer to test case (III.3.4.d) for a complete 2d simulation with friction. Here, computations are run on a $8\,640m \times 500m$ channel, regularly meshed with a discretisation step $\Delta x = \Delta y = 24m$, until $T = 10\,000s$. The topography is the following :

$$z(x,y) = h_0\big((\frac{x}{a})^2 - 1\big)\,.$$

We are accordingly working with a bed friction source term of the form (III .2c), setting $\kappa = 0.001$. Enforcing the y-component of the velocity to zero for the 2d derivation, we consider the following exact solution of the NSW equations :

$$\begin{aligned} \eta(x,y,t) &= h_0 + \frac{a^2B^2e^{-\kappa t}}{8g^2h_0}\Big(-s\kappa\, sin(2st) + (\frac{\kappa^2}{4} - s^2)cos(2st)\Big) \\ &\quad -\frac{B^2e^{-\kappa t}}{4g} - \frac{e^{-\kappa t/2}}{g}\Big(Bs\, cos(st) + \frac{\kappa B}{2}sin(st)\Big)x\,, \\ u(t) &= Be^{-\kappa t/2}sin(st), \end{aligned} \tag{III .25}$$

where $s = \sqrt{p^2 - \kappa^2}$ and $p = \sqrt{8gh_0/a^2}$. The coefficients are $a = 3\,000$, $B = 5$ and the still water level h_0 is fixed to $10m$. Straightforward computations give $\partial_x\eta(0,x,y) = cte$ and $\mathbf{q}(0,x,y) = 0$, so that the initial condition consists of a motionless planar flow (Fig. III .2). According to the exact solution, the free surface is supposed to remain planar along the channel, and oscillate with a decreasing amplitude, under the effects of the resistance. As $t \to \infty$, the velocity vanishes and the free surface asymptotically settles back to the water level at rest h_0. Considering the relative poor number of analytical solutions involving friction flows, we dispose of an interesting test case to assess the capacity of dealing simultaneously with complex topography, friction and dry states. We first focus on the evolution of the water height during a half period (Fig. III .3), and observe a very good agreement with the exact solution. Having knowledge of the

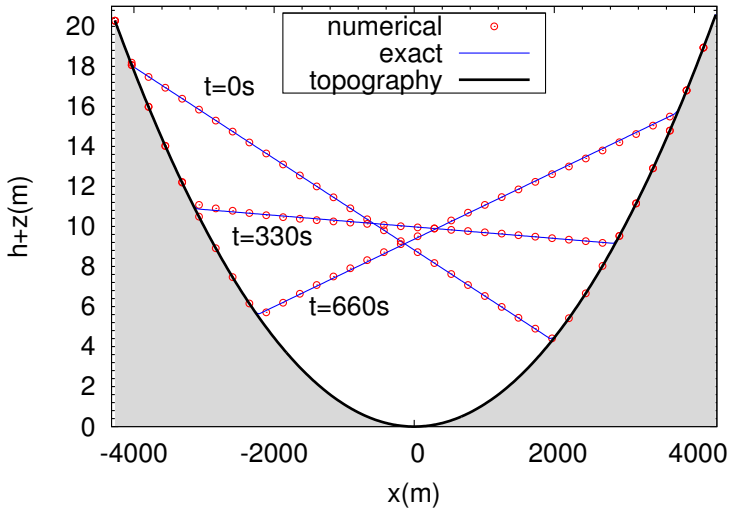

Figure III .3: Moving boundary over a parabolic bottom : Time history of the water height during a half period : analytical vs numerical.

theoretical location of the moving water interface :

$$x = \frac{a^2 e^{-\kappa t/2}}{2gh_0}\Big(- Bs\,cos(st) - \frac{\kappa B}{2}\,sin(st)\Big) \pm a\,,$$

comparisons are also run on the time history of the wet/dry front evolution (Fig. III .4), and exhibit the capacity in correctly handling flooding and drying. In conformity with theoretical predictions, the numerical approximation is progressively damped by friction up to the apparition of the motionless steady state. As far as accuracy is concerned, we proceed to quantifications of the L^1 error in a series of simulations involving coarser regular triangulations ($\Delta x = 24, 48, 96, 192$). We can observe the significant improvements provided by the MUSCL M2 scheme in terms of convergence rate on Fig. III .5. The numerical error is plotted with respect to Δx, in a log-log scale for both water height and normal discharge hu. Slopes around 1 and 1.55 are respectively observed for the first order and MUSCL schemes. Numerical results are available in Tab. III .6, and clearly confirm the efficiency of the MUSCL reconstruction discussed in §II.3.2 , even when combined with the friction approach.

III.2.3.c Periodic subcritical flow

An important step in the validation of a numerical model for shallow water flows is to confirm the ability to converge toward steady states. Some classical test cases involving converging frictionless flows can be found in the literature (see for instance [12, 195] and test cases II.4.2 II.4.6.b II.4.7 of the previous chapter), but far less involving resistance. In [91], in a one dimensional framework, an approach able to generate new steady states solutions for a Shallow Water model with viscous and friction terms is developed. Returning to a Manning formulation (III .2a), we choose to derive one of them for a 2d experiment, considering a

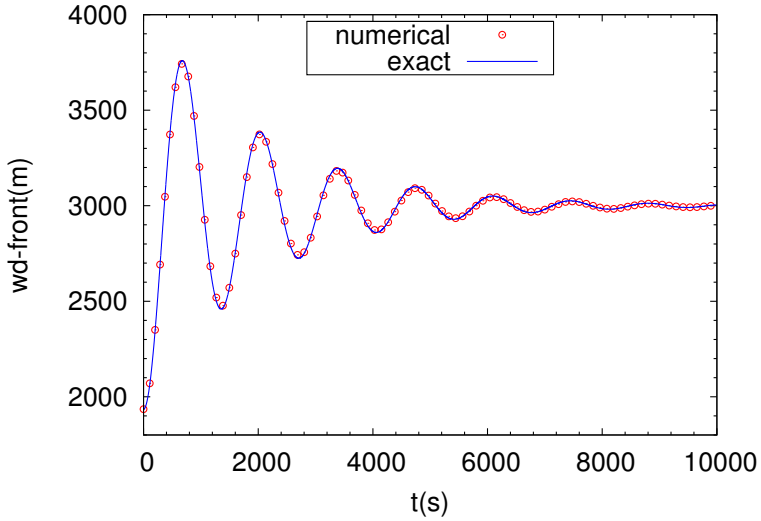

Figure III .4: Moving boundary over a parabolic bottom : Time history of the wet/dry interface.

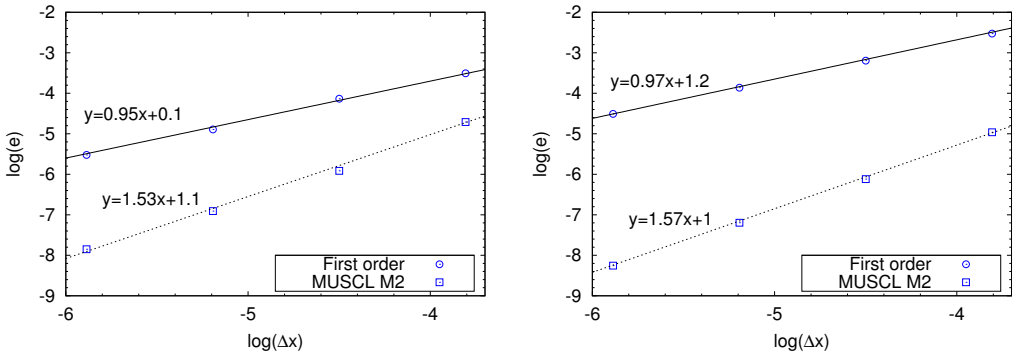

Figure III .5: Moving boundary over a parabolic bottom : Convergence rate analysis for the water height and the discharge.

	h		hu	
Δx	1^{st} order	MUSCL M2	1^{st} order	MUSCL M2
192	3.0e-2	9.0e-3	8.0e-2	7.0e-3
96	1.6e-2	2.7e-3	4.1e-2	2.2e-3
48	7.5e-3	1.0e-3	2.1e-2	7.5e-3
24	4.0e-3	3.9e-4	1.1e-2	2.6e-4

Figure III .6: Moving boundary over a parabolic bottom : Convergence analysis - L^1 numerical error quantification.

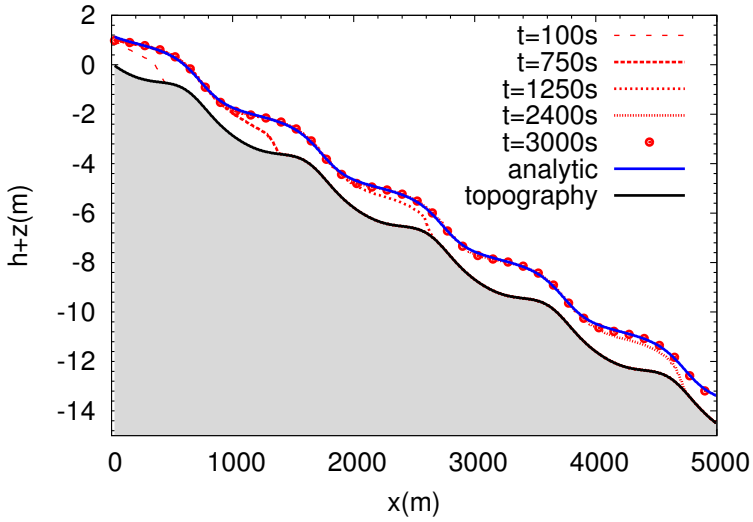

Figure III .7: Periodic subcritical flow : Free surface profile evolution - Convergence toward h_{ref}.

$5\,000m \times 500m$ channel, in which we study a converging subsonic flow. Numerical predictions are compared to the reference solution provided by the steady state for the free surface :

$$h_{ref}(x) = \frac{9}{8} + \frac{1}{4} sin(\frac{\pi x}{500}) \,. \tag{III .26}$$

The topography computation is run following the 1d iterative method described in [91]. The discharge is enforced at the left boundary, prescribing $2m.s^{-1}$, as well as the water height, set to $h_{ref}(0)$. Neumann conditions are set a the outflow boundary. The Manning coefficient set to $n = 0.03$, and we run computations on a regular mesh with a space step $\Delta x = \Delta y = 100/3$. Fig. III .7 shows the evolution of the total water height at several times during the transient part; the convergence toward the steady state is clear. The absence of instabilities despite the possible hazards resulting from dry areas and resistance terms confirms the efficiency of the friction approach. The results are very close to the ones provided by the 1d scheme [27]. Note that when equilibrium is reached, the flow is not static and friction effects are still present. As a consequence, these results are of interest since they actually show that the current scheme may be able to restore a larger class of steady states than those involved by the C-property.

III.2.4 Two dimensional steady flow with friction

In this test, extracted from [217], we study now the convergence toward a truly 2d steady state in the presence of non trivial topography and friction effects. The computational domain is the square $[0, 10] \times [0, 10]$, and we use an unstructured mesh made of 3054 vertices. A constant discharge is assumed on the whole domain :

$$q_x = q_y = 0.1 \,,$$

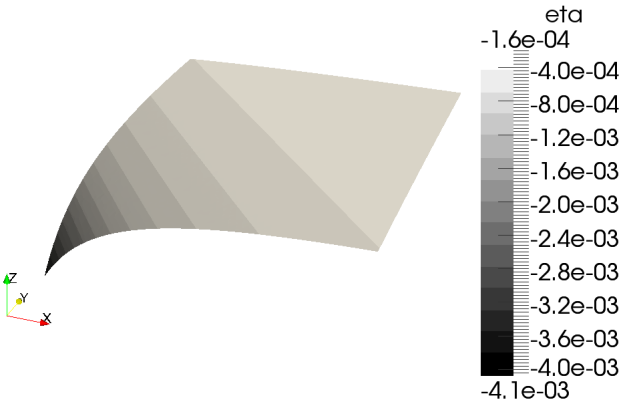

Figure III .8: Two dimensional steady flow with friction : 3d view of the exact free surface for $n = 0.03$.

and the water height at steady state is defined as follows :

$$h(x,y) = d + q_x x + q_y y\,,$$

with $d = 0.5$. The analytical function for the associated topography can be written as :

$$z(x,y) = -\frac{1}{2g}\frac{\left(q_x^2 + q_y^2\right)}{h^2} - h + \frac{3}{7}\frac{q_x n^2\sqrt{2}}{h^{7/3}}\,.$$

The total free surface elevation is set to zero at the beginning of the simulation, the final time being t=300s.
In a first time the case of a Manning roughness coefficient $n = 0.03$ is investigated. This leads to the configuration available on Fig. III .8, toward which is expected to converge the solution. A comparison between the first order approximation and the analytical solution is available on Fig. III .9 at the end of the simulation, exhibiting a good correspondence. Similar results are obtained with the MUSCL extension of the scheme. As done in [217], we propose to focus on the evolution of the L^1 numerical error to evaluate the relative performances of the first order and MUSCL approaches. In accordance with the observations made by the authors, Fig III .10 shows that in the presence of slight perturbations induced by friction, the high order scheme fails in reaching a perfect equilibrium, while the first order solution is able to restore the steady state with a better level of precision.

We consider now the case where the flow is strongly dominated by the resistance terms, taking $n = 0.3$. A 3d view of the corresponding steady state is proposed in Fig. III .11. Again, we initially consider a still water configuration, and run the simulation until t=300s. An overview of the free surface extracted from the first order solution is proposed on Fig III .12, together with the exact profile. In spite of the steepness of the friction effects, particularly pronounced in this case, the scheme is able to give stable and accurate results. Note here that, probably tempered by friction, the behaviour of the numerical error rapidly

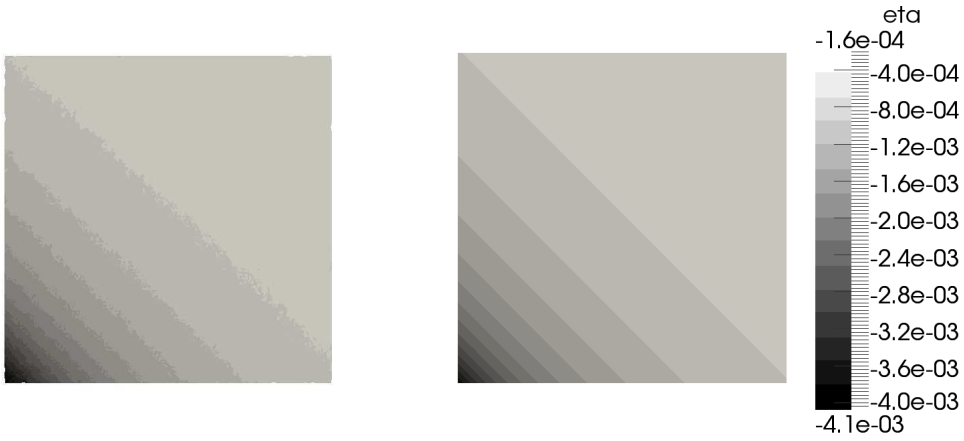

Figure III .9: Two dimensional steady flow with friction : Predicted (*left*) and exact (*right*) free surface for $n = 0.03$.

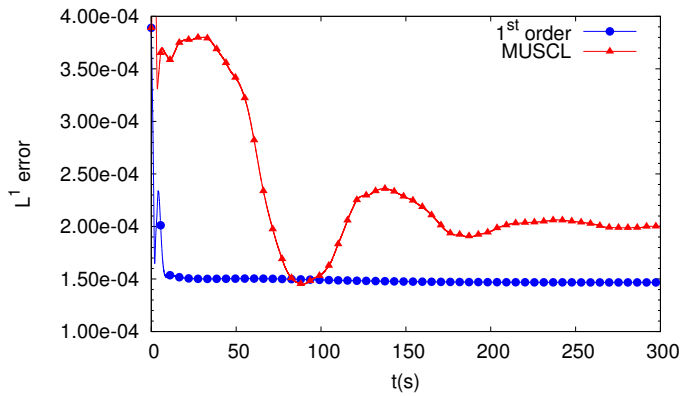

Figure III .10: Two dimensional steady flow with friction : Evolution of the numerical error for first order and MUSCL schemes for $n = 0.03$.

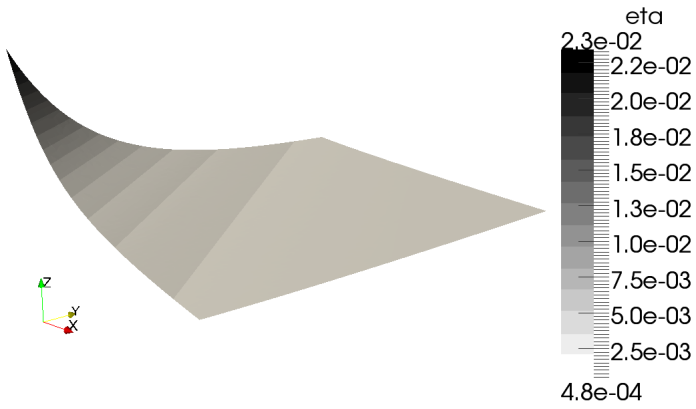

Figure III .11: Two dimensional steady flow with friction : 3d view of the exact free surface for $n = 0.3$.

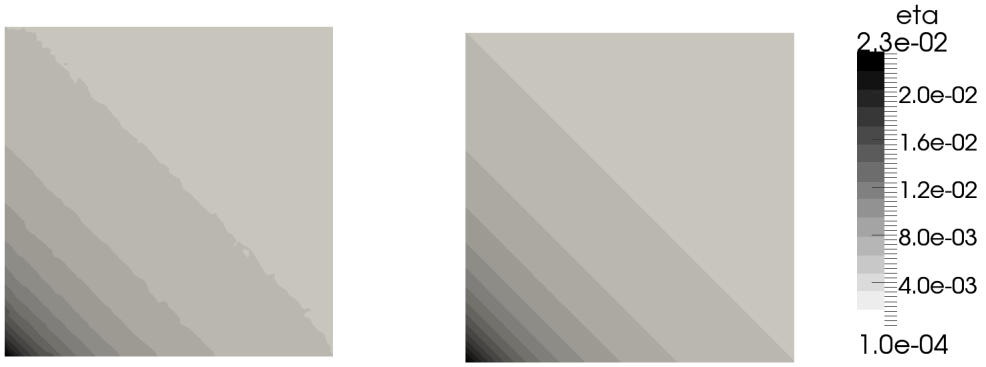

Figure III .12: Two dimensional steady flow with friction : Predicted (*left*) and exact (*right*) free surface for $n = 0.3$.

tends to stabilize, even for the MUSCL scheme, still slightly less accurate in this case (see Fig. III .13).

III.2.4.a Tsunami wave on a sloping beach

Now, let us focus on a 2d case, with the study of a wave surge over a beach with complex topography. This test has initially been performed by Zelt to validate a Lagrangian model for shallow flows [295]. The dimensions of the coastal area are set to $[-10, 15] \times [-10, 10]$. The computational domain is meshed with a 8 413 nodes unstructured triangulation, deliberately refined in the neighbourhood of threatened dry areas (Fig. III .14). The high order MUSCL M2 reconstruction is chosen here. Denoting L the half-width of the bay, the bed slope source term is

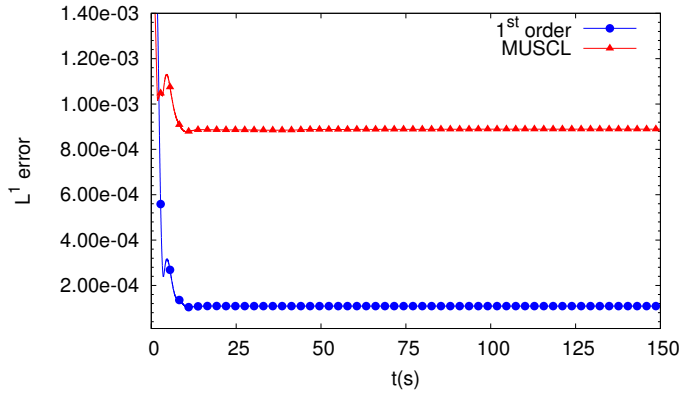

Figure III .13: Two dimensional steady flow with friction : Evolution of the numerical error for first order and MUSCL schemes for $n = 0.3$.

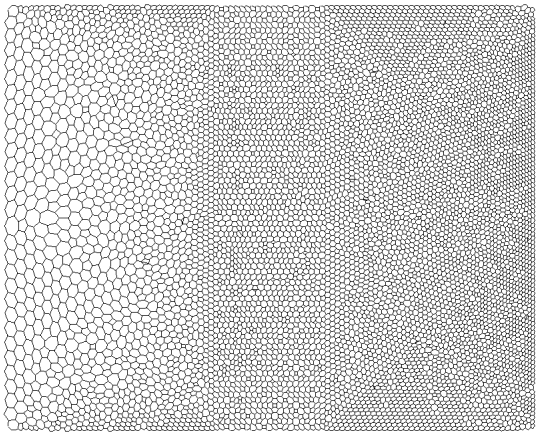

Figure III .14: Tsunami wave on a sloping beach : Mesh of the computational domain.

expressed as follows :

$$z(x,y) = \begin{cases} H\Big(1 + \dfrac{x - x_p}{L\,cos(\pi y/L)/\pi + x_p}\Big) & \text{if} \quad x \geq x_p\,, \\ 1 \quad \text{elsewhere.} \end{cases} \tag{III .27}$$

Considering a cross-shore section, we observe that the slope of the topography slowly decreases from the lateral boundaries to the x-direction centreline. The water depth at rest is initially set to $H = 1.273m$, and we set $x_p = 3\,L/\pi$. At the left side of the domain, an impulse for the generation of the wave is furnished by the following offshore boundary condition :

$$h(t) = H + \alpha H sech^2\Big(\{\frac{\sqrt{gH}}{L}\chi\, t\}\Big), \tag{III .28}$$

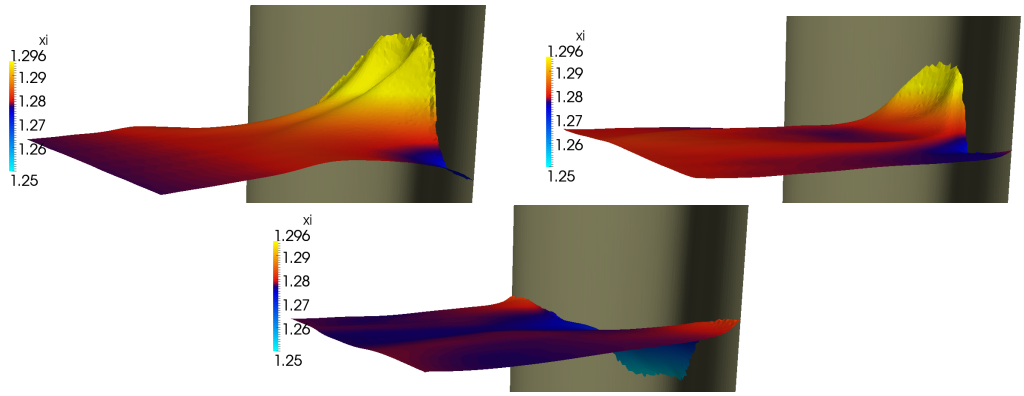

Figure III .15: Tsunami wave on a sloping beach : 3d surface profiles at t=11, 14 and 17s (frictionless flow).

where $\chi = \sqrt{\frac{3\alpha}{4\beta}(1+\alpha)}$, $\beta = (H/L)^2$ and $\alpha = 0.02$. We can observe on Fig. III .15 some 3d snapshots of the propagation wave after the arrival time at the initial shoreline. According to the bottom profile, steeper at the upper and lower boundaries, part of the energy is gradually transferred into the center of the basin. This preferential direction of the propagation is also supplemented by a precocious run-down issuing from the reflection at the lateral emerging boundaries. Our numerical model is able to correctly describe the flooding phenomena involved in this test, as well as the entire development of the reflected wave until it goes down to the open sea. To illustrate this, we propose on Fig. III .16 the time series of the run up along five cross sections, until $T = 60s$. These results can be compared with other observations available in the literature, as [151, 209, 227] for instance. We do not notice any significant discrepancies with these works, or even when compared against the model of Zelt, which attests of a good reproduction of the two-dimensional process.

Now, we study the impact of a supplemented physical resistance over the evolution of the water front. To do so, we observe the results obtained with a Manning friction law (III .2a) for increasing values of $\kappa = n^2$. Middle sections of the total free surface along the x-direction are available at several stages of the propagation on Fig. III .17, for increasing friction coefficients ($\kappa = 0, 0.1, 0.25, 0.5$ and 1), and clearly highlight the loss of amplitude resulting from the consideration of friction. The reduction of the flooded area can be observed on Fig. III .18, offering an overview of the rectangular domain and pointing all the wet cells at the level of the beach for the different values of κ involved in the simulations. It is noteworthy that the same CFL has been used for all these computations, with the same tolerance value as in the frictionless case to identify dry areas, precisely $\epsilon = 1.e-7$. In all cases, in accordance with the objectives sought, we did not have to face any instability problem.

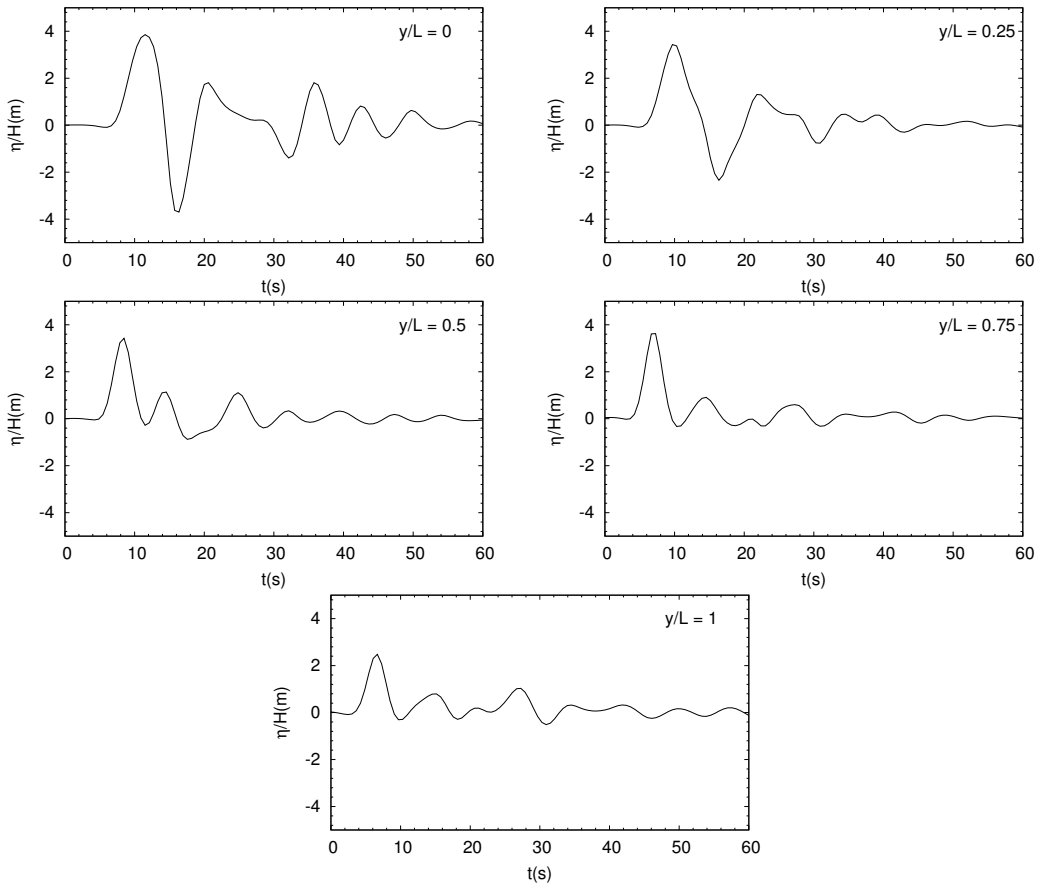

Figure III .16: Tsunami wave on a sloping beach : Time series of the run up along several cross sections.

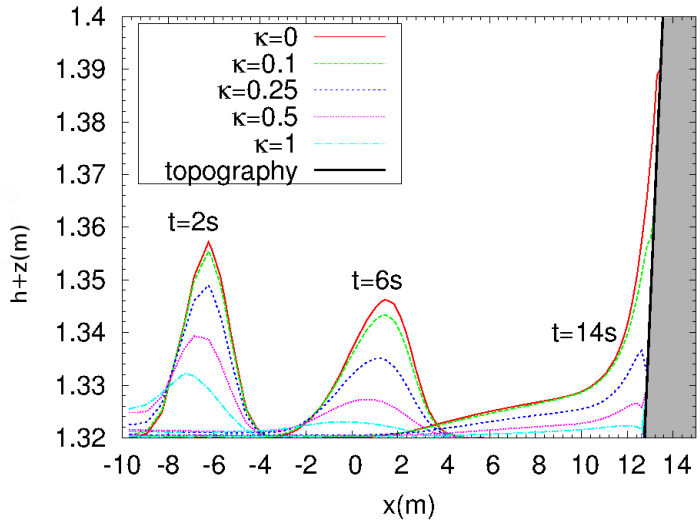

Figure III .17: Tsunami wave on a sloping beach : Water depth profiles at t=2, 6 and 14s for increasing Manning coefficients.

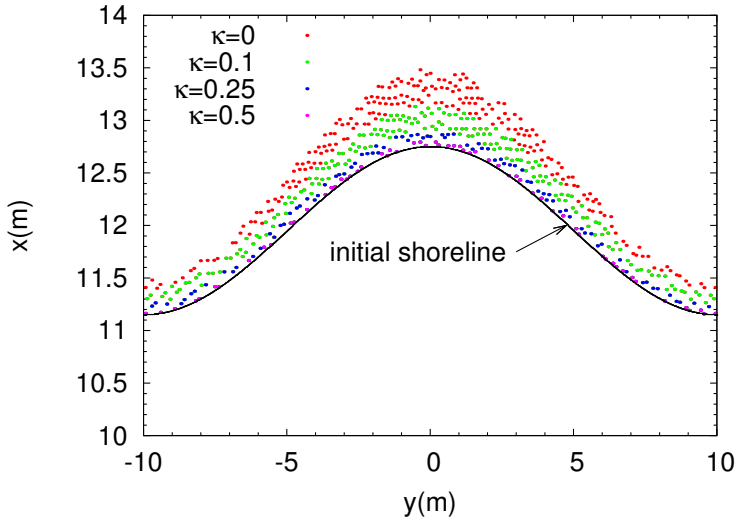

Figure III .18: Tsunami wave on a sloping beach : Sketch of flooded areas.

III.2.5 Malpasset dam break

As a final experiment, we perform the classical simulation of the Malpasset dam break. A 3d view of the narrow gorge of the Reyran River Valley (South of France) is available in Fig. III .19, locating the dam and its upstream and downstream regions. In December 1 959, the left side of the dam collapsed under the effects of pressure, after a heavy rain fall; more than 55 000m^3 of water started to pour in the valley, and the generated flood wave reached the city of Frejus, located 12km downstream. The context of this benchmark test for dam break models involves complex bathymetry and geometry, and is de facto supplemented by occurrence of dry areas. As we also have to consider friction effects, this real life application is particularly appropriate to assess the performances of the current scheme. Reconstruction of the disaster during laboratory studies furnished reference data for the arrival time of the water front at several gauges located in the floodplain. Concerning the implementation, we set an upstream total water height of 100m, and assume the bed river initially dry. We make use of the first order scheme on a vertex-centred mesh of 13 541 nodes, and the Manning roughness coefficient is fixed to $n = 0.03$. We follow the evolution of the flood wave on Fig. III .20, where snapshots of the free surface are available as the flood wave reaches gauges 8, 10 and 14. Numerical results are compared with some data issuing from the experiment on Fig. III .21a and III .21b, where the arrival time of the flood wave is available at gauges 6 to 14, as well as the maximum elevation. We also propose a comparison on the maximum elevation with the police measurements at some survey points on Fig. III .21c, that also exhibits a good agreement. Note that significant discrepancies are observed on Fig. III .21a in absence of friction, highlighting the important role played by these terms in this test. From a qualitative point of view, numerical predictions are in the same order of precision than other studies reported in the literature (see [44, 257, 282]). Again we can conclude on the good accuracy and stability properties provided

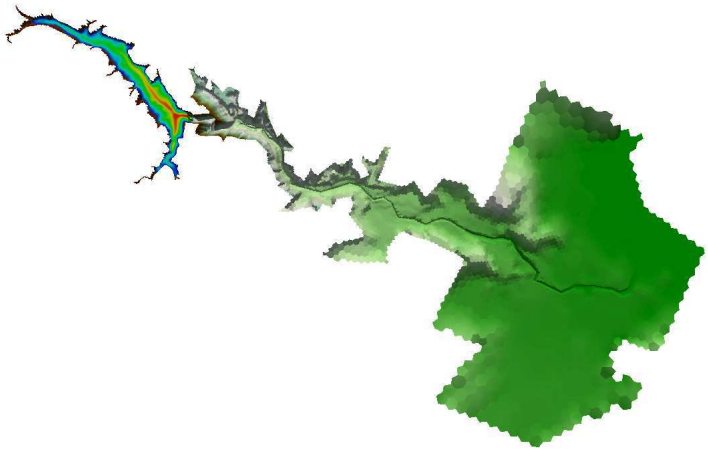

Figure III .19: Malpasset dam break : Initial configuration.

by our friction approach in the context of real life applications.

III.3 Asymptotic Preserving scheme

It results from the previous investigations a simple and well-balanced scheme, able to account for general friction laws and guarantee stable computations in the context of dry terrains. The time step limitation ensuring the water depth positivity preservation is not impacted. It has to be specified here that in practice, even in the more severe real life applications that have been performed, the consideration of strong friction laws such as Manning or Darcy did not entail a significant decrease of the time step, while we used the same threshold value as in the frictionless case to differentiate wet cells from dry cells. Remembering the efforts needed to achieve proper resolutions of the NSW system on unstructured meshes, these strong stability properties, readily obtained, may prove to be interesting for a large range of practical applications. This being so, the inclusion of friction can be subject to a deeper analysis, in relation to the long time behaviour of the scheme. This leads to the concept of Asymptotic Preserving property, referring to the capacity to restore the late-time regime satisfied by the continuous equations. In a variety of physical domains, this property may be of major importance, notably to recover particular equilibriums or handle multiscale problems.

Indeed, many theoretical and numerical studies devoted to the asymptotic behaviour of 1d conservation laws appeared in the last decades. A lot of numerical schemes are now designed to restore the asymptotic regime of the corresponding equations. Such numerical methods are commonly called "Asymptotic Preserving" (AP). We can mention for instance the works of Berthon *et al* [22, 23, 25] and Buet *et al* [48, 47] on the M1 model for radiative transfer, or the schemes developed by Bouchut *et al* [40], Chalons *et al* [66], or Marcati

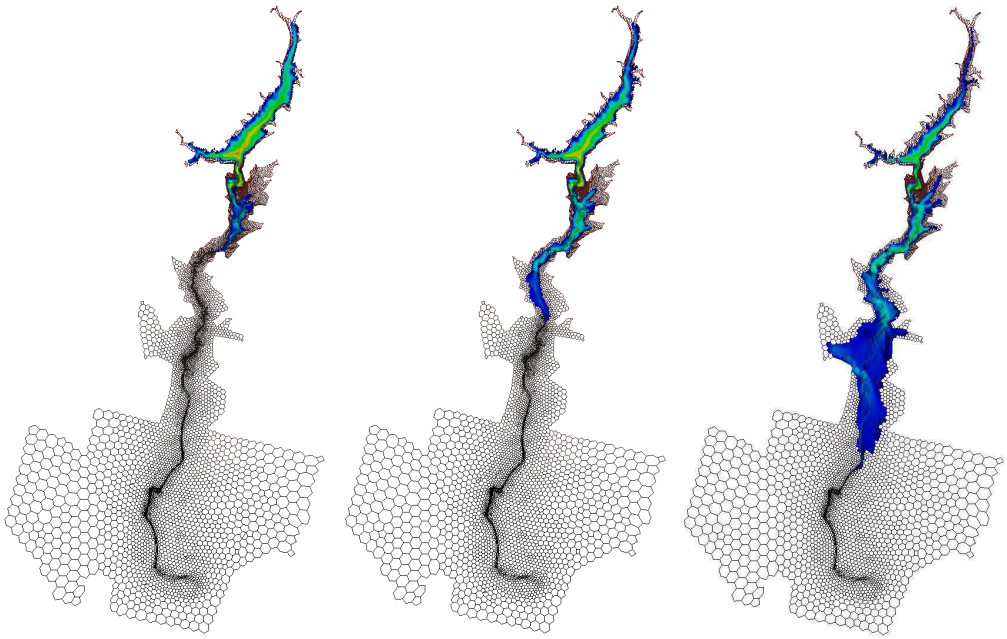

Figure III .20: Malpasset dam break : Mesh and evolution of the flow at gauges 8, 10 and 14.

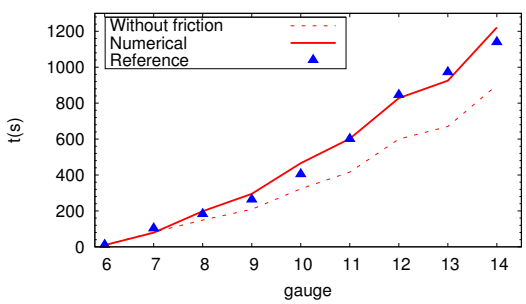

(a) Arrival time at gauges 6 to 14.

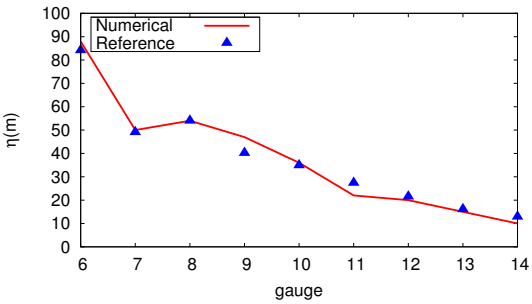

(b) Maximum elevation at gauges 6 to 14.

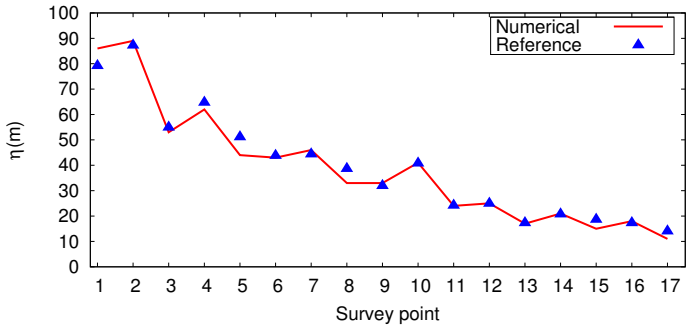

(c) Maximum elevation at survey points.

Figure III .21: Malpasset dam break : Comparison with experimental data.

et al [208] for the discretization of Euler equations. Several other systems have been treated, such as the Boltzmann kinetic model [133, 196], or Euler-Poisson system [83, 158] for instance. The reader is also referred to [7, 29, 80, 134, 158] for additional studies. In the 2d case, the quantity of published results is definitively less abundant. On cartesian grids, in addition of [23], we can highlight the scheme introduced by Degond *et al* [88] for the Euler-Lorentz system. In an unstructured context, the extrapolation technique developed by Franck for the Friedrichs systems [114] is, to our knowledge, the only method available to date (see also [49]). In this connexion, although the issue of the 1d NSW equations has been considered is some studies [25, 71, 161, 158], no Asymptotic Preserving scheme has already been developed in the framework of unstructured meshes.

Thus, in what follows, we propose the construction and validation of an Asymptotic Preserving numerical scheme for the 2d Shallow Water model, accounting for topography and friction source terms. To achieve this, following the lines of [28] for the Telegraph Equations, Euler equations with high friction, or the M1 model developed by Dubroca *et al* ([98]), we introduce a relevant correction of some friction parameters in order to recover a discrete version of the diffusive limit observed by the governing equations. The efficiency of Asymptotic Preserving schemes has been highly pointed out in the above references and we also aim at highlighting its benefits for the NSW equations.

We first approximate solutions of frictionless flows considering a suitable formulation of the conservation laws, involving the water free surface and some fractions of water to integrate topography variations [24]. As previously, the discretization of the friction term relies on the use of a modified Riemann solver used for the flux computation. The resulting scheme is then corrected to preserve the late-time regime derived from the continuous equations. The numerical approach is shown to be consistent, Θ-preserving, satisfies the C-property and tolerates dry areas well. Additionally, the MUSCL reconstructions introduced in II.3 can be easily adapted. These results are widely assessed with several benchmark tests appropriately selected. In the presence of dry areas, special attention will be paid to the wave front computation to evaluate the relevancy and stability of the asymptotic preserving correction.

III.3.1 Frictionless scheme

In this section, for the sake of completeness, we expose the broad lines of the well-balanced *hydrostatic upwind scheme* developed in [24] that will constitute the basis of our future developments. Let us introduce the new variable $W = (\eta, \eta u, \eta v)$ and the following formulation of the NSW equations :

$$\frac{\partial U}{\partial t} + \nabla . \left(\chi G(W) - \begin{pmatrix} 0 & 0 \\ \frac{ghz}{2} & 0 \\ 0 & \frac{ghz}{2} \end{pmatrix} \right) = -gh \begin{pmatrix} 0 \\ \partial_x z \\ \partial_y z \end{pmatrix} , \qquad \text{(III .29)}$$

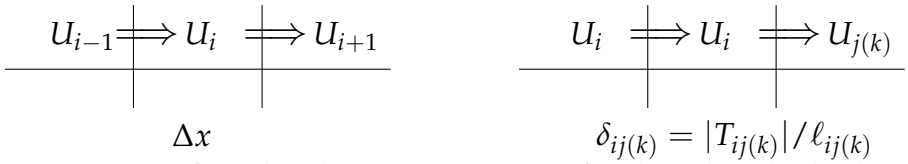

Figure III .22: Left and right Riemann states for the 1d and 2d schemes.

where $\chi = \dfrac{h}{\eta}$ and G, U are given by the set of primitive equations (I .1, I .2). We consider again the dual mesh issuing from a triangulation $\mathcal{T}$ of the computational domain. Same geometry and notations are used (Fig. I .2). As was the case for its predecessor, the scheme's conception relies on the use of a convex combination :

$$U_i^{n+1} = \sum_{k=1}^{\Lambda(i)} \frac{|T_{ij(k)}|}{|C_i|} U_{ij(k)}^{n+1}\,, \tag{III .30}$$

where each contribution can be interpreted as coming from a 1d-like scheme (see Fig. III .22) :

$$U_{ij(k)}^{n+1} = U_i^n - \Delta t \frac{\ell_{ij(k)}}{|T_{ij(k)}|}\left[\phi(U_i, U_{j(k)}, \vec{n}_{ij(k)}) - \phi(U_i, U_i, \vec{n}_{ij(k)})\right] + \Delta t \frac{\ell_{ij(k)}}{|T_{ij(k)}|} B_{ij(k)}\,, \tag{III .31}$$

where:

- $\phi(U_i, U_{j(k)}, \vec{n}_{ij(k)}) = X_{ij(k)} \mathcal{G}(W_i, W_{j(k)}, \vec{n}_{ij(k)})$.
- $\mathcal{G} = \mathcal{G}(U^-, U^+, \vec{n})$ denotes a numerical flux function for the approximation of $G.\vec{n}$.
- $B_{ij(k)}$ is the discretization of the bed slope :

$$B_{ij(k)} = \frac{g}{2}\begin{pmatrix} 0 \\ H_{ii} H_{ij(k)} (X_{ij(k)} - X_{ii})\, \vec{n}_{ij(k)} \end{pmatrix}\,. \tag{III .32}$$

- X_{ij} and H_{ij} are given by the following transport relations :

$$X_{ij} = \begin{cases} \chi_i^n & \text{if} \quad \mathcal{G}^h(W_i, W_j, \vec{n}_{ij}) \geq 0\,, \\ \chi_j^n & \text{otherwise.} \end{cases} \tag{III .33}$$

$$H_{ij} = \begin{cases} \eta_i & \text{if} \quad \mathcal{G}^h(W_i, W_j, \vec{n}_{ij}) \geq 0\,, \\ \eta_j & \text{otherwise.} \end{cases} \tag{III .34}$$

Remark III.3 .1. *We recall that, as highlighted in [24], the NSW system (I .1) only involves variations of the bed slope. The ground level can consequently be defined from any reasonable reference. Thus, we suppose that the minimum value of z is positive within the computational domain, giving sense to the definition of χ. For this we may be compelled to introduce some vertical bottom translation in the experimental part.*

Remark III.3 .2. *The evaluation of the numerical flux function $\mathcal{G}$ is classically based on the use of an approximate Riemann solver in the normal reference associated with the interface. Still observing the classical principles, such a function is supposed to be consistent with the exact flux $\mathcal{H}$ and satisfy the conservativity property in the sense of (I .22), (I .23). To be consistent with the precedent study, we will also denote $\lambda_k^{\pm}$ the maximum and minimum wave speeds involved in the Riemann solver during the evaluation of the exchanging fluxes $\mathcal{G}(U_i, U_{j(k)}, \vec{n}_{ij(k)})$.*

Using formula (III .30), we obtain, after straightforward computations involving discrete Green formula :

$$U_i^{n+1} = U_i^n - \frac{\Delta t}{|C_i|} \sum_{k=1}^{\Lambda(i)} \ell_{ij(k)} \phi(U_i, U_{j(k)}, \vec{n}_{ij(k)}) + \Delta t B_i \,, \tag{III .35}$$

where

$$B_i = \sum_{k=1}^{\Lambda(i)} \frac{\ell_{ij(k)}}{|C_i|} B_{ij(k)} \,. \tag{III .36}$$

We can already emphasize that robustness and well-balancing properties are straightly inherited from the 1d scheme. More precisely :

Proposition 7. *We consider a numerical flux function $\mathcal{G}$ consistent with the exact flux in the sense of (I .22), verifying the conservativity property (I .23). Assume that $(U_i^n)_{i\in\mathbb{Z}}$ belongs to Θ. We consider the updated states $(U_i^{n+1})_{i\in\mathbb{Z}}$ obtained with the scheme (III .35). The following properties holds :*

1 *Robustness : under the following CFL condition :*

$$\Delta t \max_{i\in\mathbb{Z}, k\in K_i} \frac{\ell_{ij(k)}}{|T_{ij(k)}|} |\lambda_k^{\pm}| \leq \frac{1}{2} \,, \tag{III .37}$$

supplemented by the following CFL restriction :

$$\Delta t \max_{i\in\mathbb{Z}, k\in K_i} \left[\frac{\ell_{ij(k)}}{|T_{ij(k)}|} \Big(\max\left(0, \mathcal{G}^h(W_i, W_{j(k)}, \vec{n}_{ij(k)})\right) - \min\left(0, \mathcal{G}^h(W_i).\vec{n}_{ij(k)}\right) \Big) \right] < \eta_i \,, \tag{III .38}$$

we have $h_i^{n+1} \geq 0$, for all $i \in \mathbb{Z}$.

2 *Well Balancing : assume $u_i^n = u_{j(k)}^n = 0$ and $\eta_i^n = \eta_{j(k)}^n = \eta_c$ for all $k \in K_i$. Then $u_i^{n+1} = 0$ and $\eta_i^{n+1} = \eta_c$.*

Proof. We consider the formulation (III .30, III .31), together with the robustness and well balancing properties of the 1d scheme. See [24] for details. A complete analysis will be conducted later, with the inclusion of friction. □

Remark III.3 .3. *Note that the time step limitation (III .38) can be interpreted as resulting from an analysis of the outflow and inflow parts of the numerical fluxes appearing in the 1D scheme. Such a separation between outflow and inflow contributions is also performed in [34], allowing to obtain the preservation of the water height positivity under the so called "draining time" CFL.*

III.3.2 Friction scheme

We presently face the question of friction treatment. For the sake of clarity, we consider the Manning formulation (III .2a), while making clear that the other ones can be addressed that way. We consequently enrich the set of equations (III .29) with the corresponding source term, recast under the following form :

$$E(U) = \sigma(R(U) - U)\,, \tag{III .39}$$

where :

$$\sigma = \sigma(h) = \frac{n^2}{h^\gamma} \quad , \quad R(U) = {}^t(h, q_x - \|\mathbf{q}\|q_x, q_y - \|\mathbf{q}\|q_y)\,. \tag{III .40}$$

We follow again the ideas introduced in [28], modifying the wave structure of the HLL Riemann solver, now expressed as follows :

$$\tilde{U}_{\mathcal{R}}(\frac{x}{t}, U^-, U^+) = \begin{cases} U^- \quad \text{if} \quad \dfrac{x}{t} \leq s^-\,, \\ \alpha U_* + (1-\alpha)R(U^-) \quad \text{if} \quad \min(0, s^-) \leq \dfrac{x}{t} \leq \min(0, s^+)\,, \\ \alpha U_* + (1-\alpha)R(U^+) \quad \text{if} \quad \max(0, s^-) \leq \dfrac{x}{t} \leq \max(0, s^+)\,, \\ U^+ \quad \text{if} \quad \dfrac{x}{t} \geq s^+\,, \end{cases}$$

Here too, U_* and $s^\pm$ stand respectively for the intermediate state and upper and lower extremities of the dependency cone involved by the approximate Riemann solver. Directly inspired from the strategy previously described, each convex component (III .31) is now updated as follows :

$$\begin{aligned} U_{ij(k)}^{n+1} = U_i^n \quad & - \Delta t \frac{\ell_{ij(k)}}{|T_{ij(k)}|}\Big(\alpha_k \phi(U_i, U_{j(k)}, \vec{n}_{ij(k)}) - \alpha_k^c \phi(U_i, U_i, \vec{n}_{ij(k)})\Big) \\ & + \Delta t \frac{\ell_{ij(k)}}{|T_{ij(k)}|}\Big((1-\alpha_k^c)F_k^c + (1-\alpha_k)F_k\Big) + \Delta t \frac{\ell_{ij(k)}}{|T_{ij(k)}|} B_{ij(k)}\,, \end{aligned} \tag{III .41}$$

where we have set :

$$\begin{aligned} F_k^c &= \max(0, s_k^{c,-})\big(U_i - R(U_i)\big) + \max(0, s_k^{c,+})\big(R(U_i) - U_i\big) + \phi(U_i, U_i, \vec{n}_{ij(k)})\,, \\ F_k &= \min(0, s_k^-)\big(U_i - R(U_i)\big) + \min(0, s_k^+)\big(R(U_i) - U_{j(k)}\big) - \phi(U_i, U_i, \vec{n}_{ij(k)})\,, \end{aligned} \tag{III .42}$$

Then, getting back to the convex combination (III .30), and gathering the bed slope contributions (III .36), we obtain :

$$\begin{aligned} U_i^{n+1} = U_i^n & - \frac{\Delta t}{|C_i|} \sum_{k=1}^{\Lambda(i)} \ell_{ij(k)} \Big(\alpha_k \phi(U_i, U_{j(k)}, \vec{n}_{ij(k)}) - \alpha_k^c \phi(U_i, U_i, \vec{n}_{ij(k)})\Big) \\ & + \frac{\Delta t}{|C_i|} \sum_{k=1}^{\Lambda(i)} \ell_{ij(k)} \mathcal{F}_k + \Delta t B_i\,, \end{aligned} \tag{III .43}$$

with

$$\mathcal{F}_k = (1-\alpha_k^c)F_k^c + (1-\alpha_k)F_k\,. \tag{III .44}$$

Equivalently, for consistency reasons we have the alternate writing of (III .41) :

$$\begin{aligned} U_{ij(k)}^{n+1} = U_i^n \quad & - \Delta t \frac{\ell_{ij(k)}}{|T_{ij(k)}|}\Big(\alpha_k \phi(U_i, U_{j(k)}, \vec{n}_{ij(k)}) - \alpha_k \phi(U_i, U_i, \vec{n}_{ij(k)})\Big) \\ & + \Delta t \frac{\ell_{ij(k)}}{|T_{ij(k)}|}\Big((1-\alpha_k^c)E_k^c + (1-\alpha_k)E_k\Big) + \Delta t \frac{\ell_{ij(k)}}{|T_{ij(k)}|} B_{ij(k)}\,, \end{aligned} \tag{III .45}$$

with

$$\begin{aligned} E_k^c &= \max(0, s_k^{c,-})\big(U_i - R(U_i)\big) + \max(0, s_k^{c,+})\big(R(U_i) - U_i\big)\,, \\ E_k &= \min(0, s_k^{-})\big(U_i - R(U_i)\big) + \min(0, s_k^{+})\big(R(U_i) - U_{j(k)}\big)\,, \end{aligned} \tag{III .46}$$

leading to :

$$\begin{aligned} U_i^{n+1} = U_i^n & - \frac{\Delta t}{|C_i|}\sum_{k=1}^{\Lambda(i)} \ell_{ij(k)}\Big(\alpha_k \phi(U_i, U_{j(k)}, \vec{n}_{ij(k)}) - \alpha_k \phi(U_i, U_i, \vec{n}_{ij(k)})\Big) \\ & + \frac{\Delta t}{|C_i|}\sum_{k=1}^{\Lambda(i)} \ell_{ij(k)}\mathcal{E}_k + \Delta t B_i\,, \end{aligned} \tag{III .47}$$

where we have set :

$$\mathcal{E}_k = (1-\alpha_k^c)E_k^c + (1-\alpha_k)E_k\,.$$

Note that formulations (III .43) and (III .47) may both be useful in practice. Schemes of the form (III .43) are in general designed for asymptotic preserving methods [22, 28, 48, 47]. Its features will be effectively exploited later to derive matching conditions with regard to the diffusive limit of the NSW equations. On the other hand, (III .47) is more easy to implement and is intended to serve as a simple support to illustrate the main properties.

We now state that this use of weighted fluxes does not compromise the properties previously established :

Proposition 8. *We consider a numerical flux function $\mathcal{G}$ consistent with the exact flux in the sense of (I .22), verifying the conservativity property (I .23). Assume that $(U_i^n)_{i\in\mathbb{Z}}$ belongs to Θ. We consider the updated states $(U_i^{n+1})_{i\in\mathbb{Z}}$ obtained with the scheme (III .47).*

1 *Under the CFL condition (III .37), supplemented by the following CFL restriction :*

$$\Delta t \max_{i\in\mathbb{Z}, k\in K_i}\Big[\frac{\ell_{ij(k)}\alpha_k}{|T_{ij(k)}|}\Big(\max\big(0, \mathcal{G}^h(W_i, W_{j(k)}, \vec{n}_{ij(k)})\big) - \min\big(0, \mathcal{G}^h(W_i).\vec{n}_{ij(k)}\big)\Big)\Big] < \eta_i\,, \tag{III .48}$$

we have $h_i^{n+1} \geq 0$, for all $i \in \mathbb{Z}$.

2 *Well Balancing : assume* $\mathbf{u}_i^n = \mathbf{u}_{j(k)}^n = 0$ *and* $\eta_i^n = \eta_{j(k)}^n = \eta_c$ *for all* $k \in K_i$. *Then* $\mathbf{u}_i^{n+1} = 0$ *and* $\eta_i^{n+1} = \eta_c$.

Proof. Concerning the well balancedness result, starting from $W_i = W_{j(k)} = {}^t(\eta_c, 0, 0)$, it can be readily appreciated that $\phi(U_i, U_i, \vec{n}_{ij(k)}) = \phi(U_i, U_{j(k)}, \vec{n}_{ij(k)})$ and $B_{ij(k)} = 0$ for all $k = 1, \cdots, \Lambda(i)$, returning to formulation (III .30, III .45). It results $U_{ij(k)}^{n+1} = U_i^n$ for all k and at last the preservation of the initial static state.

Let's now focus on the robustness property. For the sake of simplicity, we denote $\mathcal{G}_k^h := \mathcal{G}^h(W_i, W_{j(k)}, \vec{n}_{ij(k)})$. According to the definition (III .33) and the consistency relation (I .22), we write :

$$\begin{aligned}
\phi_k^h := \phi^h(U_i, U_{j(k)}, \vec{n}_{ij(k)}) = X_{ij(k)}\mathcal{G}_k^h &= \frac{1}{2}(\chi_i + \chi_{j(k)})\mathcal{G}_k^h - \frac{1}{2}(\chi_{j(k)} - \chi_i)|\mathcal{G}_k^h| \\
&= \chi_i \frac{1}{2}(\mathcal{G}_k^h + |\mathcal{G}_k^h|) + \chi_{j(k)} \frac{1}{2}(\mathcal{G}_k^h - |\mathcal{G}_k^h|)\,, \\
\phi_k^{c,h} := \phi^h(U_i, U_i, \vec{n}_{ij(k)}) = X_{ii}\eta_i \mathrm{u}_i &= h\mathrm{u}_i\,.
\end{aligned}$$

Thereafter, remembering that the current scheme is built on formulas (III .30, III .45) :

$$\begin{aligned}
h_{ij(k)}^{n+1} &= h_i^n - \frac{\Delta t}{\delta_{ij(k)}}\left[\alpha_k \phi_k^h - \alpha_k \phi_k^{c,h}\right] \\
&= \chi_{j(k)} \frac{\Delta t \alpha_k}{2\delta_{ij(k)}}(|\mathcal{G}_k^h| - \mathcal{G}_k^h) + \left[h_i^n - \chi_i \frac{\Delta t \alpha_k}{2\delta_{ij(k)}}(\mathcal{G}_k^h + |\mathcal{G}_k^h|) + \frac{\Delta t \alpha_k}{\delta_{ij(k)}} h\mathrm{u}_i\right].
\end{aligned}$$

The first term of the right member being positive, we focus on the positivity of the second one, equivalent to the following condition, after factorization by $\chi_i = h_i^n / \eta_i^n \geq 0$:

$$\eta_i^n - \frac{\Delta t \alpha_k}{\delta_{ij(k)}}\left(\frac{1}{2}(\mathcal{G}_k^h + |\mathcal{G}_k^h|) - \eta_i \mathrm{u}_i\right) \geq 0\,. \tag{III .49}$$

Under (III .48), we have (III .49). The proof is complete.

□

We investigate now the question of a relevant choice for the parameters α_k, α_k^c. As previously it is mainly governed by consistency relations. From this perspective, and to simplify the subsequent developments, we consider once again the Rusanov approximate flux function (I.3.1), that can be written, for the primal variables :

$$\begin{aligned}
&\mathcal{G}(U_i, U_{j(k)}, \vec{n}_{ij(k)}) = \frac{1}{2}\left(G(U_i).\vec{n}_{ij(k)} + G(U_{j(k)}).\vec{n}_{ij(k)}\right) - \frac{a_k}{2}\left(U_{j(k)} - U_i\right), \\
&\text{where} \quad a_k = \max\left(|\mathbf{u}_i.\vec{n}_{ij(k)}| + \sqrt{gh_i}, |\mathbf{u}_{j(k)}.\vec{n}_{ij(k)}| + \sqrt{gh_{j(k)}}\right).
\end{aligned} \tag{III .50}$$

Since from now on $s_k^+ = -s_k^- = a_k$, we have the following simplifications in (III .42, III .46) :

$$\left\{\begin{array}{l} F_k^c = a_k^c\big(R(U_i) - U_i\big) + \phi(U_i, U_i, \vec{n}_{ij(k)}) \\ F_k = a_k\big(R(U_i) - U_i\big)\big) - \phi(U_i, U_i, \vec{n}_{ij(k)}) \end{array}\right. , \quad \left\{\begin{array}{l} E_k^c = a_k^c\big(R(U_i) - U_i\big) \\ E_k = a_k\big(R(U_i) - U_i\big) \end{array}\right. . \tag{III .51}$$

As stated in the following lines, a possible choice for the friction parameters is then given by :

$$\begin{aligned} \alpha_k^c &= \frac{2\Lambda(i)a_k^c}{2\Lambda(i)a_k^c + \sigma_k^c \dfrac{|C_i|}{\ell_{ij(k)}}} , \; \sigma_k^c = \sigma(U_i) , \\ \alpha_k &= \frac{2\Lambda(i)a_k}{2\Lambda(i)a_k + \sigma_k \dfrac{|C_i|}{\ell_{ij(k)}}} , \; \sigma_k = \frac{n^2}{(h_i^\gamma + h_{j(k)}^\gamma)/2} . \end{aligned} \tag{III .52}$$

Proposition 9. *The term* $\dfrac{1}{|C_i|}\sum_{k=1}^{\Lambda(i)} \ell_{ij(k)}\mathcal{E}_k$ *appearing in the scheme (III .47) is consistent with the exact friction source term* $\sigma(R(U) - U)$.

Proof. Thee proof is almost the same as in Proposition 6. Basic calculations yield :

$$\begin{aligned} \frac{\ell_{ij(k)}}{|C_i|}(1 - \alpha_k^c) &= \frac{\sigma_k^c}{2\Lambda(i)a_k^c + \sigma_k^c \dfrac{|C_i|}{\ell_{ij(k)}}} , \\ \frac{\ell_{ij(k)}}{|C_i|}(1 - \alpha_k) &= \frac{\sigma_k}{2\Lambda(i)a_k + \sigma_k \dfrac{|C_i|}{\ell_{ij(k)}}} . \end{aligned}$$

According to (III .51), we hence have :

$$\lim_{\mathfrak{d}_i \to 0} \frac{\ell_{ij(k)}}{|C_i|}(1 - \alpha_k^c)E_k^c = \lim_{\mathfrak{d}_i \to 0} \frac{\ell_{ij(k)}}{|C_i|}(1 - \alpha_k)E_k = \frac{\sigma(U_i)}{2\Lambda(i)}(R(U_i) - U_i) ,$$

to finally obtain :

$$\begin{aligned} \lim_{\mathfrak{d}_i \to 0} \frac{1}{|C_i|}\sum_{k=1}^{\Lambda(i)} \ell_{ij(k)}\mathcal{E}_k &= \sum_{k=1}^{\Lambda(i)} \Big[\frac{\sigma(U_i)}{2\Lambda(i)}(R(U_i) - U_i) + \frac{\sigma(U_i)}{2\Lambda(i)}(R(U_i) - U_i)\Big] \\ &= \sigma(U_i)(R(U_i) - U_i) . \end{aligned}$$

Let us remark that this consistency result also stands for $\dfrac{1}{|C_i|}\sum_{k=1}^{\Lambda(i)} \ell_{ij(k)}\mathcal{F}_k$ in (III .43). We also point out that the numerical constraints entailed by the possible divisions by h brought by friction can be avoided in the scheme (III .43) (or equivalently (III .47)) provided an appropriate rewriting of (III .52). □

III.3.3 Asymptotic Preserving issues

In this section we bring the asymptotic preserving correction announced in the introduction. It should be useful to note that most of theoretical and numerical studies have been developed in a 1d framework and marginal consideration has been given to the particular context of unstructured triangulations. For that purpose, the novelty lies in the construction of a numerical scheme which is able to degenerate toward an appropriate discrete version of the diffusive regime satisfied by the late-time solutions of the 2d Shallow Water system. We highlight that numerical schemes taking these aspects under consideration can possibly demonstrate very different behaviours compared to traditional approaches. In the current context, this may take an important dimension in several contexts of interest, notably when dry areas are involved, in which case the asymptotic regime is immediately reached. Such particular situations will be explored in the experimental part (Section III.3.4).

III.3.3.a Asymptotic regime for NSW

Firstly, we identify the late-time behaviour satisfied by the solutions of the NSW equations. Formally, we introduce a rescaling parameter ϵ, intended to vanish, in the set of equations (I .1), leading to the following set of relaxed equations (see also [28, 25]) :

$$\epsilon\partial_t h^\epsilon + \partial_x q_x^\epsilon + \partial_y q_y^\epsilon = 0\,, \tag{III .53}$$

$$\epsilon\partial_t q_x^\epsilon + \partial_x\left((q_x^\epsilon)^2/h^\epsilon + \frac{1}{2}g(h^\epsilon)^2\right) + \partial_y\left(q_x^\epsilon q_y^\epsilon/h^\epsilon\right) = -gh^\epsilon\partial_x z - g\frac{\varrho^2(h^\epsilon)}{\epsilon^2}\|\mathbf{q}\|q_x^\epsilon\,, \tag{III .54}$$

$$\epsilon\partial_t q_y^\epsilon + \partial_x\left(q_x^\epsilon q_y^\epsilon/h^\epsilon\right) + \partial_y\left((q_y^\epsilon)^2/h^\epsilon + \frac{1}{2}g(h^\epsilon)^2\right) = -gh^\epsilon\partial_y z - g\frac{\varrho^2(h^\epsilon)}{\epsilon^2}\|\mathbf{q}\|q_y^\epsilon\,. \tag{III .55}$$

Herein, we rewrite the friction term setting $g\varrho^2(h) = \dfrac{n^2}{h^\gamma}$. We highlight that the stiff relaxation source term involved in (III .54)-(III .55) introduces an additional scale in the problem, defined in accordance with the specific nonlinearity of the friction source term (quadratic function of $\mathbf{q}$). This system enters the framework of the generalized analysis proposed in [25], that encompasses models with strong nonlinearities in the relaxation and in the following, we focus on its asymptotic behavior in the singular regime $\epsilon \to 0$. In the spirit of Chapman-Enskog expansions of the kinetic theory [64], we perform a formal expansion of each component of the variable vector :

$$U^\epsilon = U^0 + \epsilon U^1 + \mathcal{O}(\epsilon^2)\,. \tag{III .56}$$

Considering that equations (III .54) and (III .55) have to be relevant whenever ϵ tends to zero, we necessarily have $q_x^0 = q_y^0 = 0$, and the following relations

satisfied by the discharge components :

$$gh^0\partial_x(h^0+z) = -g\varrho^2(h^\epsilon)\|\mathbf{q}\|q_x^1\,,$$
$$gh^0\partial_y(h^0+z) = -g\varrho^2(h^\epsilon)\|\mathbf{q}\|q_y^1\,.$$

After some algebraic manipulations, we obtain :

$$q_x^1 = -\frac{\sqrt{h^0}}{\varrho(h^\epsilon)}\frac{\partial_x(h^0+z)}{\sqrt{\|\nabla(h^0+z)\|}}\,,$$
$$q_y^1 = -\frac{\sqrt{h^0}}{\varrho(h^\epsilon)}\frac{\partial_y(h^0+z)}{\sqrt{\|\nabla(h^0+z)\|}}\,,$$

so that the Chapman-Enskog expansion in (III .53) yields the following diffusive regime :

$$\partial_t h - \mathrm{div}\Big(\frac{\sqrt{h}}{\varrho(h)\sqrt{\|\nabla\eta\|}}\nabla\eta\Big) = 0\,, \tag{III .57}$$

which is nothing but the 2d version of the equations obtained in [25], including bathymetry.

III.3.3.b Asymptotic Preserving Correction

We recall that we aim at building a friction scheme designed to restore the asymptotic diffusive regime satisfied by the system (III .1,III .2a), that is (III .57). To access such an issue, we slightly modify the formulation of the source proposed in (III .39), writing :

$$E(U) = \hat{\sigma}(\overline{R}(U) - U)\,, \tag{III .58}$$

where

$$\hat{\sigma} = \sigma + \overline{\sigma} \quad , \quad \overline{R}(U) = \left(\frac{\sigma}{\hat{\sigma}}R(U) + \frac{\overline{\sigma}}{\hat{\sigma}}U\right)\,, \tag{III .59}$$

and σ, R are given by (III .40). The free parameter $\overline{\sigma}$ is introduced to reach the desired asymptotic property, and its choice will be discussed later on. Still employing the fluxes (III .50), the friction parameters in the scheme (III .43) are this time expressed as follows :

$$\alpha_k^c = \frac{2\Lambda(i)a_k^c}{2\Lambda(i)a_k^c + \hat{\sigma}_k^c\dfrac{|C_i|}{\ell_{ij(k)}}} \quad , \quad \alpha_k = \frac{2\Lambda(i)a_k}{2\Lambda(i)a_k + \hat{\sigma}_k\dfrac{|C_i|}{\ell_{ij(k)}}}\,, \tag{III .60}$$

and

$$F_k^c = a_k^c\big(\overline{R}(U_i) - U_i\big) + \phi(U_i, U_i, \vec{n}_{ij(k)})\ ,\ F_k = a_k\big(\overline{R}(U_i) - U_i\big)\big) - \phi(U_i, U_i, \vec{n}_{ij(k)})\,. \tag{III .61}$$

Noting that we have $\overline{R}(U) - U = \begin{pmatrix} 0 \\ -\frac{\sigma}{\hat{\sigma}}\|\mathbf{q}\|\mathbf{q} \end{pmatrix}$, we obtain from (III .44) the following expression for the components of $\mathcal{F}_k = {}^t(\mathcal{F}_k^h, \mathcal{F}_k^{\mathbf{q}})$:

$$\mathcal{F}_k^h = (\alpha_k - \alpha_k^c)\phi^h(U_i, U_i, \vec{n}_{ij(k)}), \tag{III .62}$$

$$\mathcal{F}_k^{\mathbf{q}} = -\frac{|C_i|}{\ell_{ij(k)}}\left[\frac{a_k^c\,\sigma_k^c}{2\,\Lambda(i)\,a_k^c + \hat{\sigma}_k^c|C_i|/\ell_{ij(k)}} + \frac{a_k\,\sigma_k}{2\,\Lambda(i)\,a_k + \hat{\sigma}_k|C_i|/\ell_{ij(k)}}\right]\|\mathbf{q}_i\|\mathbf{q}_i + (\alpha_k - \alpha_k^c)\,\phi^{\mathbf{q}}(U_i, U_i, \vec{n}_{ij(k)}). \tag{III .63}$$

Considering the rescaling $\Delta t \longleftarrow \Delta t/\epsilon$, $\sigma_k \longleftarrow \sigma_k/\epsilon$, $\overline{\sigma}_k \longleftarrow \overline{\sigma}_k/\epsilon$, where ϵ is devoted to tend to zero, a brief study of the term (III .63) gives $\mathbf{q}_i = 0$. Denoting α_k^ϵ the corresponding rescaled friction parameters (III .60), we also have :

$$\frac{\Delta t}{\epsilon}\alpha_k^\epsilon \underset{\epsilon\to 0}{\longrightarrow} \Delta t\frac{2\,\Lambda(i)\,a_k}{\hat{\sigma}_k|C_i|/\ell_{ij(k)}}.$$

Consequently, at the fully discrete level, the asymptotic behaviour of the water height issuing from (III .41) reads :

$$h_{ij(k)}^{n+1} = h_i^n - \frac{\Delta t}{\delta_{ij(k)}}\frac{\ell_{ij(k)}}{|C_i|}\left[\frac{2\,\Lambda(i)\,a_k}{\hat{\sigma}_k}\phi^h(U_i, U_{j(k)}, \vec{n}_{ij(k)}) - \frac{2\,\Lambda(i)\,a_k^c}{\hat{\sigma}_k^c}\phi^h(U_i, U_i, \vec{n}_{ij(k)})\right]_{|\mathbf{q}=0}. \tag{III .64}$$

We point out that this formula also holds for varying bathymetry profiles. Since the discharge vanishes as ϵ tends to zero (and so does the velocity), the choice of Lax Friedrichs-type fluxes yields :

$$\phi^h(U_i, U_{j(k)}, \vec{n}_{ij(k)})_{|\mathbf{u}=0} = X_{ij(k)}\mathcal{G}^h(W_i, W_{j(k)}, \vec{n}_{ij(k)})_{|\mathbf{u}=0} = -\frac{a_k}{2}X_{ij(k)}(\eta_{j(k)} - \eta_i),$$
$$\phi^h(U_i, U_i, \vec{n}_{ij(k)})_{|\mathbf{u}=0} = 0,$$

and we reach the following limit equation satisfied by the water height :

$$h_i^{n+1} = \sum_{k=1}^{\Lambda(i)}\frac{|T_{ij(k)}|}{|C_i|}h_{ij(k)}^{n+1},$$
$$h_{ij(k)}^{n+1} = h_i^n + \frac{\Delta t}{\delta_{ij(k)}}\frac{\ell_{ij(k)}}{|C_i|}\frac{X_{ij(k)}\,\Lambda(i)\,(a_k)^2}{\hat{\sigma}_k}(\eta_{j(k)} - \eta_i),$$

that is :

$$h_i^{n+1} = h_i^n + \frac{\Delta t}{|C_i|}\sum_{k=1}^{\Lambda(i)}\frac{(\ell_{ij(k)})^2}{|C_i|}\frac{X_{ij(k)}\,\Lambda(i)\,(a_k)^2}{\hat{\sigma}_k}(\eta_{j(k)} - \eta_i). \tag{III .65}$$

Now, given an appropriate scheme for the diffusive limit (III .57), one can extract from (III .65) matching conditions on $\hat{\sigma}_k$ so that the current approach degenerates toward a discrete version of the asymptotic regime.

Remark III.3 .4. *Provided the modifications (III .60, III .61), the new friction scheme with asymptotic preserving abilities is still given by (III .43).*

From now, the crucial underlying matter concerns the Finite Volume discretization of the diffusive limit (III .57). Given the complex nature of the continuous equations, many numerical constraints have to be taken into account, and the design of a suitable approximation appears as a complex problem. Amongst others, this discretization should yield $\hat{\sigma}_k > 0$ to give sense to the previous lines, satisfy the maximum principle, and fulfil the requirements attached to the definition of α (see III .17). This is indeed an important and rather difficult problematic, deviating from the original purposes and competences mobilized in the present study. In this work, though such an objective has not been rigorously achieved, we made our possible to make this approximation relevant, with the use of an upwind scheme enabling to deduce from (III .65) positive values for $\hat{\sigma}_k$ in practice. Our first numerical results seems to fit well with the observations arising from the 1d AP numerical studies.

Remark III.3 .5. *The MUSCL extensions exposed earlier can equally be employed here to reach better level accuracy. For any edge $\Gamma_{ij(k)}$, the preliminary reconstruction is performed between the states U_i and $U_{j(k)}$, providing new values for water height, free surface and discharge. They are subsequently used for the evaluation of the additional variables $X_{ij(k)}$, $H_{ij(k)}$ and injected in the convective fluxes and source terms. The arguments put forward to conclude on the C-property of the pre-balanced FVM can easily be reused in this context. As far as the the preservation of the water height positivity is concerned, note that the technique introduced by Berthon in [21] and used in the previous part can successfully be applied in the frictionless case. Again, the technical aspects are very similar and we do not give further details. We acknowledge here that the presence of friction makes difficult the proof of robustness for MUSCL schemes, since the water height is also affected here. This points may probably be technic-dependant and require further investigations. They are left for future works.*

III.3.4 Numerical validations

In this section we present some numerical benchmark tests expected to show the abilities of this new friction scheme. Keeping in mind one of the objectives for which it has been originally designed, full consideration will be given to the stability performances, particularly in the neighbourhood of dry cells. Also we will pay special attention to applications involving dominant resistance effects, considering run-up on dry beds and/or strong friction laws with high roughness parameter for instance. In these contexts, the scheme tends to reach its limit behaviour, and the characteristics of the asymptotic correction are expected to emerge over time. All the computations are performed using an explicit RK2 scheme for the time discretization (I .50). We distinguish corrected and uncorrected schemes by *U-HY AP scheme* and *U-HY NAP scheme* respectively (U-HY standing for Upwind Hydrostatic, in reference to the original work [24]). Finally, when nothing else is mentioned, we consider a Manning formulation for the resistance term.

Concerning comparisons against the *pre balanced* friction scheme (simply

Gauge	Ref	PB	U-HY AP	U-HY NAP
6	10	10	11	10
7	102	80	91	90
8	182	192	188	184
9	263	260	279	274
10	404	428	440	436
11	600	578	608	602
12	845	847	810	806
13	972	969	928	924
14	1139	1174	1176	1167

Table III .1: Malpasset dam break : Arrival time of the flood wave front at gauges 6 to 14 for our different friction schemes.

denoted PB in what follows), all the tests previously run have been performed again. The schemes appears are very close, regardless of whether it is assessed in terms of computational cost, accuracy or even implementation efforts. We consequently do not reproduce the whole set of experiments. We just stress out that the most significant discrepancies appeared throughout the Malpasset test case, for which we have reported some numerical results in Tab. III .1. That said, these data can be considered as satisfying when compared with other numerical predictions that can be found in the literature. Note that while the differences are small on the total time scale, we observe that carrying out the AP correction tends to slow down the evolution of the wave front in the floodplain. This typical behaviour will be clearly confirmed throughout a relevant selection of numerical tests.

As the previous tests were not intended to exhibit the possible advantages of the asymptotic preserving property, part of the following validations are built in this perspective. We also propose another series of numerical experiments to validate the general features of the hydrostatic upwind friction scheme.

III.3.4.a Accuracy validation

We perform this test to study the accuracy of the first and MUSCL M2 schemes, as well as their behaviour for increasing values of n. Initially, 1d and 2d versions have been proposed by Xing *et al* [286]. This test case has also been adapted to evaluate the scheme developed in [27] for flows with friction, and we choose a 2d extrapolation. The channel dimensions are fixed to 1×0.2, and we use a regular mesh with $\Delta x = \Delta y = (1/60)m$. Periodic boundary conditions are set both on left and right side regions. The topography is defined by the following function :

$$z(x, y) = sin^2(\pi x),$$

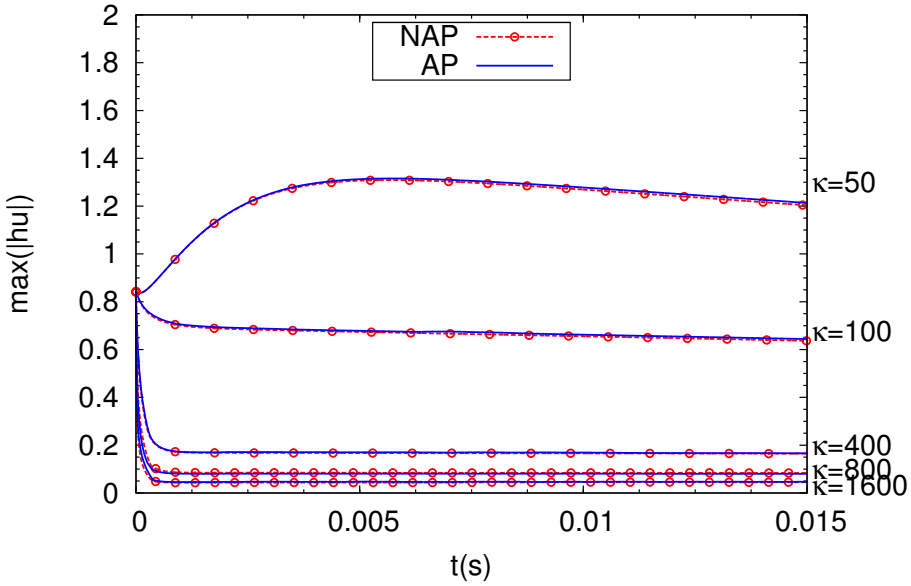

Figure III .23: Accuracy validation : Time series of the L^∞ norm of the discharge for increasing values of $\kappa = n^2$. AP scheme (*blue*) and NAP scheme (*red*).

and the initial flow vector is :

$$\begin{aligned} h(x,y,0) &= 5 + exp(cos(2\pi x))\,, \\ q_x(x,y,0) &= sin(cos(2\pi x))\,, \\ q_y(x,y,0) &= 0\,. \end{aligned}$$

The time evolution of the L^∞ norm of the x-direction discharge for several values of n is shown in Fig. III .23. We can note a very good agreement with the numerical predictions provided by the 1d scheme [27] for both AP and NAP scheme, even considering high values of n. The current friction approach exhibits good stability properties and, in particular, is able to account for varying bottoms whenever the friction terms are dominant.

As for the convergence rate analysis, several tests are performed with different values of the roughness coefficient. For a given n, a reference solution is computed with the MUSCL scheme on a 20 865 nodes regular mesh until t=0.1s, avoiding this way appearance of shocks, and then run simulations on a mesh series with increasingly refined triangulations: $\Delta x = \Delta y = 1/20, 1/40, 1/80, 1/160$ and $1/320m$. Our numerical results are compared with the reference, which stands for an exact solution. Fig. III .24 shows the evolution of the L^1 error on h and normal discharge q_x with respect to the mesh refinement for first and high order approaches in the case n=1, in a log-log scale. As shown in Tab. III .2, slopes of 0.9 and 2 are respectively reached up to n=10, which is very respectable for the description of a flow mainly controlled by friction effects, notably on unstructured grids (see [34, 91]). Note that similar convergence rates can also be observed in [181] in the frictionless case. If the order of convergence is significantly improved up to n=50 here, we observe that the benefits of the

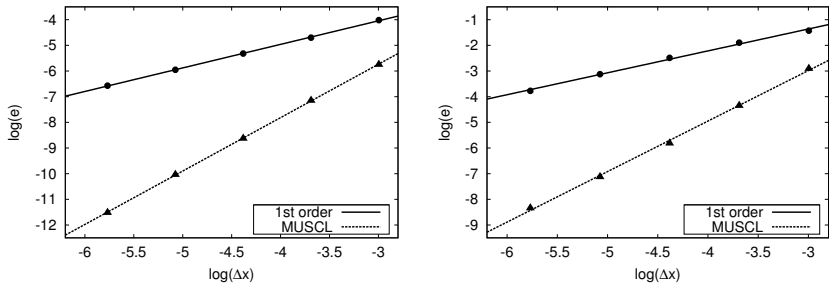

Figure III .24: Accuracy validation : L^1 error for h (*left*) and q_x (*right*) for increasing values of Δx (log-log scale).

MUSCL reconstruction tend to attenuate with very stiff perturbations.

III.3.4.b Dam break with friction

This test is destined to highlight the possible influence of the asymptotic correction as the effects of the physical resistance becomes dominant. We proceed to a series of simulations of dam break problems in a rectangular channel $\Omega = [-10, 10] \times [-2, 2]$, on a flat bottom. The computational domain is initially meshed with a regular triangulation of 5 884 nodes. The dam is supposed to be located at x=0 along the y direction. the initial condition is :

$$h(x) = \begin{cases} h_g & \text{if} \quad x < 0\,, \\ h_d & \text{otherwise}\,, \end{cases} \qquad \text{with} \qquad h_g > h_d\,. \tag{III .66}$$

The first test consists of a non physical case : we deliberately choose an excessive friction parameter n, and study the results given by the AP and NAP schemes. As the AP scheme is precisely designed to degenerate toward the discrete version of the asymptotic regime (III .57), the corresponding approximations should get closer as the time and the friction parameter increase. We set $n = 25$, $h_g = 2m$, $h_d = 1m$, and study the evolution of the flow until $t = 9s$. Fig. III .25 shows a middle section of the water height for both corrected and uncorrected schemes at the end of the simulation, put in comparison with the scheme used for the diffusive limit. We can clearly observe the impact of the modification on the limit behavior. Taking the limit regime as a reference, L^1 and L^∞ errors are quantified and plotted in Fig. III .26. The trends emerging from this complementary error study clearly corresponds to the intended outcomes, confirming the pertinence of the correction.

We consider now more moderate values of the friction parameter, with the intention to identify the AP scheme's specificities in contexts more in line with real situations. First, we enforce the same left and right initial values for the water elevation, with this time $n = 0.1$. Considering the downstream water depth involved in this test, the asymptotic regime is far from being reached during the simulation, and the effects of the asymptotic correction are expected to be insignificant. Sections of the water surface profile along the x-direction are

	Δx	1/20	1/40	1/80	1/160	1/320	order
n=0	**1^{st} order**						
	h	1.9e-2	9.7e-3	5.3e-3	2.8e-3	1.5e-3	**0.9**
	q	2.6e-1	1.5e-1	8.8e-2	4.7e-2	2.4e-2	**0.9**
	MUSCL						
	h	3.5e-3	8.7e-4	1.9e-4	4.6e-5	1.0e-5	**2.1**
	q	5.9e-2	1.4e-2	3.2e-3	8.2e-4	2.3e-4	**2.0**
n=1	**1^{st} order**						
	h	1.9e-2	9.7e-3	5.3e-3	2.8e-3	1.5e-3	**0.9**
	q	2.6e-1	1.5e-1	8.8e-2	4.7e-2	2.4e-2	**0.9**
	MUSCL						
	h	3.5e-3	8.7e-4	1.9e-4	4.6e-5	1.0e-5	**2.1**
	q	5.9e-2	1.4e-2	3.2e-3	8.2e-4	2.3e-4	**2.0**
n=10	**1^{st} order**						
	h	1.8e-2	9.1e-3	4.9e-3	2.6e-3	1.4e-3	**0.9**
	q	2.4e-1	1.5e-1	8.3e-2	4.4e-2	2.3e-2	**0.8**
	MUSCL						
	h	3.2e-3	7.9e-4	1.8e-4	4.4e-5	1.0e-5	**2.1**
	q	5.5e-2	1.3e-2	3.0e-3	8.1e-4	2.4e-4	**2.0**
n=25	**1^{st} order**						
	h	1.3e-2	7.0e-3	3.6e-3	1.9e-3	9.8e-4	**0.9**
	q	2.1e-1	1.3e-1	6.8e-2	3.6e-2	1.9e-2	**0.9**
	MUSCL						
	h	1.9e-3	6.3e-4	1.9e-4	6.0e-5	1.7e-5	**1.7**
	q	4.1e-2	1.1e-2	3.9e-3	1.3e-3	3.6e-4	**1.7**
n=50	**1^{st} order**						
	h	7.9e-3	4.8e-3	2.4e-3	1.2e-3	6.5e-4	**0.9**
	q	1.6e-1	1.0e-1	5.5e-2	3.0e-2	1.6e-2	**0.8**
	MUSCL						
	h	1.4e-3	6.4e-4	2.7e-4	1.1e-4	3.7e-5	**1.3**
	q	3.7e-2	1.6e-2	7.4e-3	2.8e-3	8.9e-4	**1.4**
n=100	**1^{st} order**						
	h	6.7e-3	4.6e-3	2.8e-3	1.5e-3	8.3e-4	**0.8**
	q	1.2e-1	1.0e-1	5.5e-2	3.1e-2	1.7e-2	**0.7**
	MUSCL						
	h	2.1e-3	9.8e-4	5.3e-4	2.4e-4	8.3e-5	**1.2**
	q	1.0e-1	3.9e-2	1.8e-2	7.5e-3	2.5e-3	**1.3**

Table III .2: Accuracy validation : Convergence analysis - L^1 numerical error quantification and corresponding convergence rates for increasing Manning coefficients.

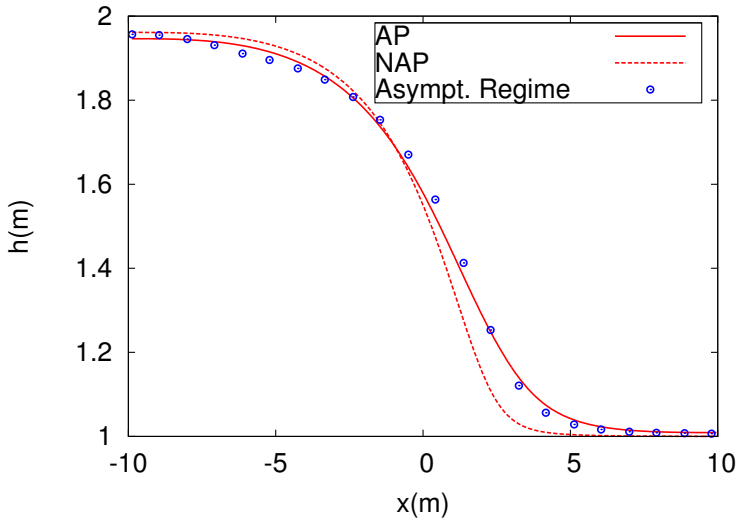

Figure III .25: Dam break with friction - test 1 : $n = 25$, $h_g = 2m$, $h_d = 1m$. Middle section of the water depth profiles at t=9s - Comparison with the asymptotic regime.

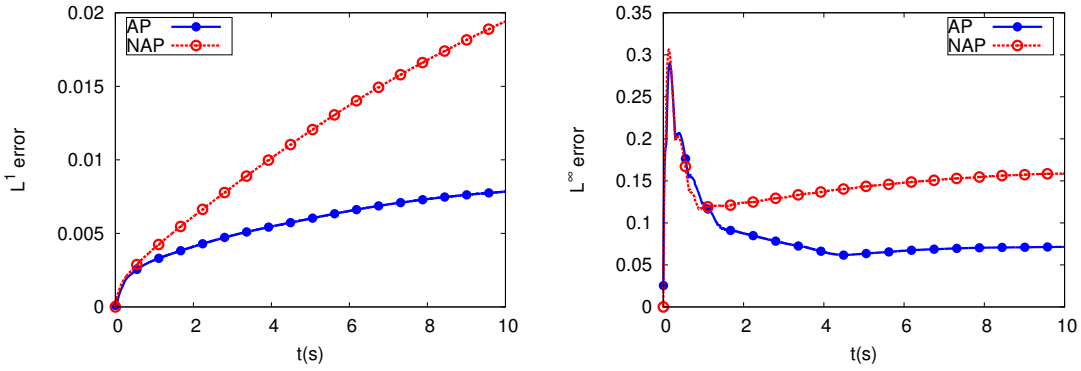

Figure III .26: Dam break with friction - test 1 : L^1 (*left*) and L^∞ (*right*) error evolution.

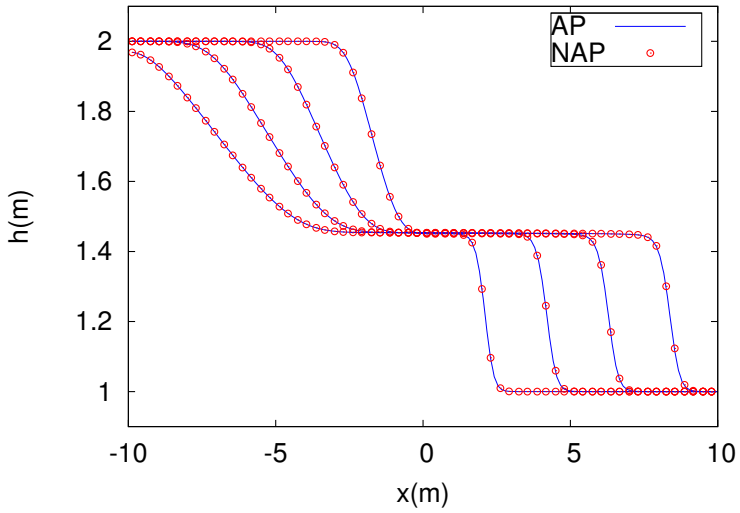

Figure III .27: Dam break with friction - test 2 : $n = 0.1, h_g = 2m, h_d = 1m$. Middle section of the water depth profiles for both AP and NAP schemes at times t=0.5, 1, 1.5 and 2 s.

available on Fig. III .27 at several times of the simulation. And indeed, AP and NAP schemes provide very close results. The curves are almost undistinguishable at this level of zoom. These observations tend to confirm the worthlessness of the correction when the water height levels involved in the simulation are relatively high, or when the friction term is not particularly stiff.

Before observing the impact in a dry bed context, we suggest an intermediate test, keeping $h_g = 2m$ and $n = 0.1$, and enforcing $h_d = 0.1m$. As previously, we follow the evolution of the predicted flood wave elevation given by the two schemes. Results are plotted in Fig. III .28, highlighting some discrepancies. We reach a difference of $15cm$ between the two predicted fronts at time $t = 2s$. This time, considering the low value of h_d, both schemes get closer to their asymptotic behaviour in the vicinity of the front location : the use of an asymptotic preserving scheme seems to be necessary to have a better evaluation of the flood wave velocity.

For the last configuration, we set $h_d = 0m$. In this dry context, the asymptotic regime is immediately reached in the right side of the domain. We observe similar results than those provided by test 3 (Fig. III .29), with a stronger impact of the correction : the location of the two fronts differs this time from almost $Dx = 30cm$ at the end of the simulation.

We finally study the behaviour of the AP and NAP schemes for different values of h_g : $1, 2, 3, 4$ and $5m$. We also improve the quality of the mesh, working with a 20 890 nodes regular triangulation. On Fig. III .30 we can follow the evolution of the wet/dry interface location (left) for both AP and NAP schemes,

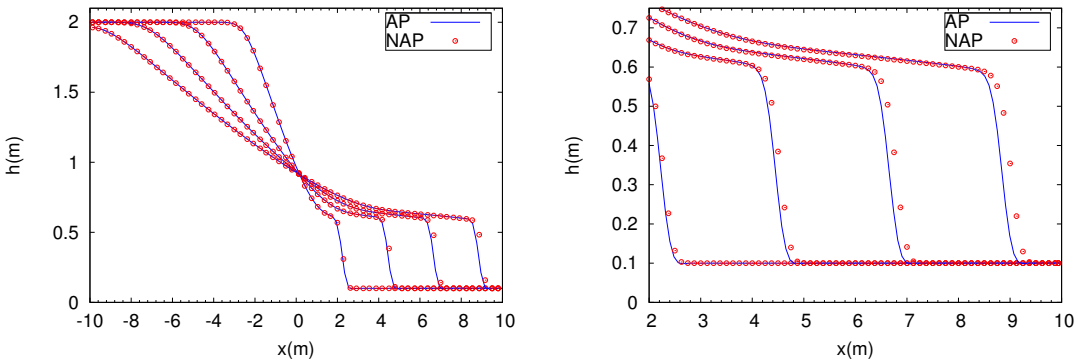

Figure III .28: Dam break with friction - test 3 : $n = 0.1$, $h_g = 2m$, $h_d = 0.1m$. Middle section of the water depth profiles for AP and NAP schemes at times t=0.5, 1, 1.5 and 2 s.

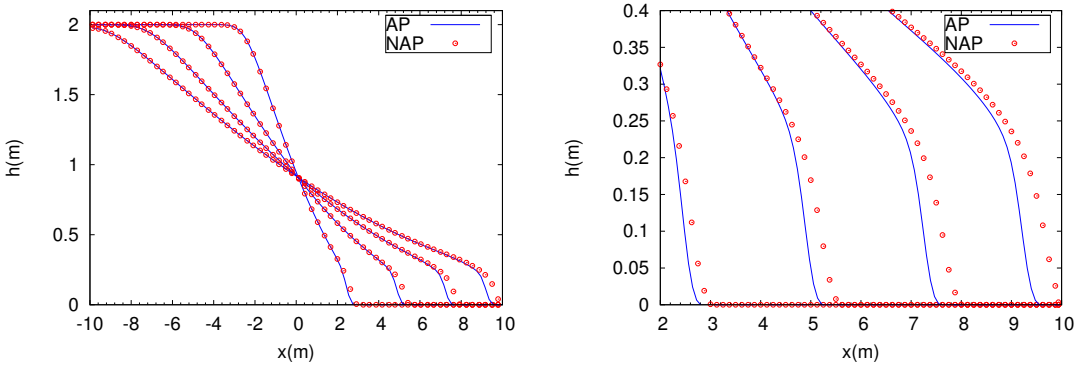

Figure III .29: Dam break with friction - test 4 : $n = 0.1$, $h_g = 2m$, $h_d = 0m$. Middle section of the water depth profiles for AP and NAP schemes at times t=0.5, 1, 1.5 and 2 s.

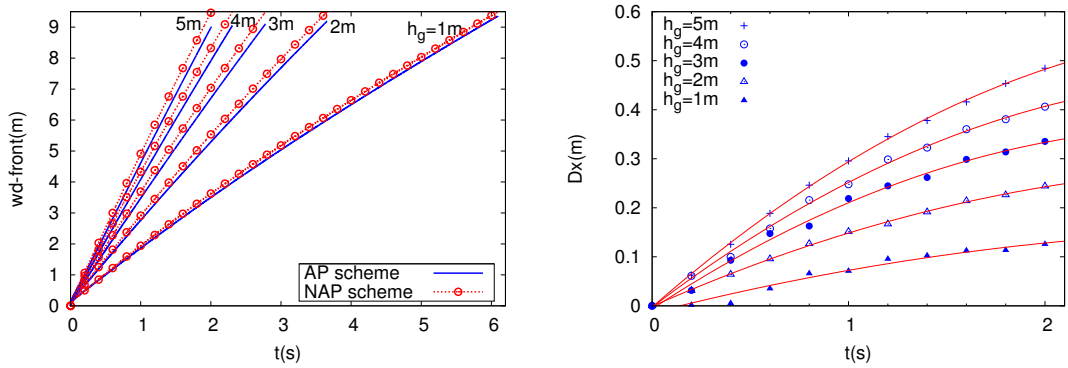

Figure III .30: Dam break with friction - test 5 : Location of the shoreline for the AP and NAP schemes (*left*) and flood wave gap Dx (*right*) for increasing values of h_g.

supplemented by a visualization of the resulting gap Dx with respect to time (right) until $t = 2s$. Numerical results clearly show that the impact of the correction is all the more pronounced since the initial jump is important. We also emphasize that the amplitude of the gap Dx does not decrease as the mesh is refined : the loss of accuracy related to the non consideration of the limit regime restoration can definitively not be offset by an increase of the number of nodes. Note that employing the *pre balanced* friction scheme instead of the NAP approach we obtained similar observations. The use of an asymptotic preserving scheme seems to describe slightly different behaviours when compared to traditional approaches in such a context.

III.3.4.c Dam break in a double-slope basin

In the subsequent application we consider a domain with closed boundaries formed by a rectangular retention basin and two parallel sloping channels, separated by a central ridge line, as represented on Fig. III .31. The topography is given by the following formula :

$$z(x,y) = \begin{cases} c(x,y) + 0.5\, exp\Big(-9\ \big((x-x_A)^2 + (y-y_A)^2\big)\Big) & \text{if} \quad x < x_A\,, \\ c(x,y) + 0.5\, exp\Big(-9\ \big((y-y_A)^2\big)\Big) & \text{otherwise}\,, \end{cases}$$

where

$$\begin{aligned} &c(x,y) = c_m(x) + 0.5\,(c_M(x) - c_m(x))\,\Big(\tanh\left(5(y-y_A)\right) + 1\Big)\,, \\ &c_m(x) = \min(z_0,\, z_0 - s\,(x-d)) \quad , \quad c_M(x) = \max(z_0, z_0 + s\,(x-d))\,. \end{aligned} \tag{III .67}$$

The constants are taken to $z_0 = 0.5$, $d = 1.5m$, the slope s is fixed to $1/20$, and the critical point A announcing the channels separation is located at $(x_A, y_A) = (2.5, 1.5)$. This test is conceived to express the possible nuances that might be brought by the AP correction in a more difficult context, introducing

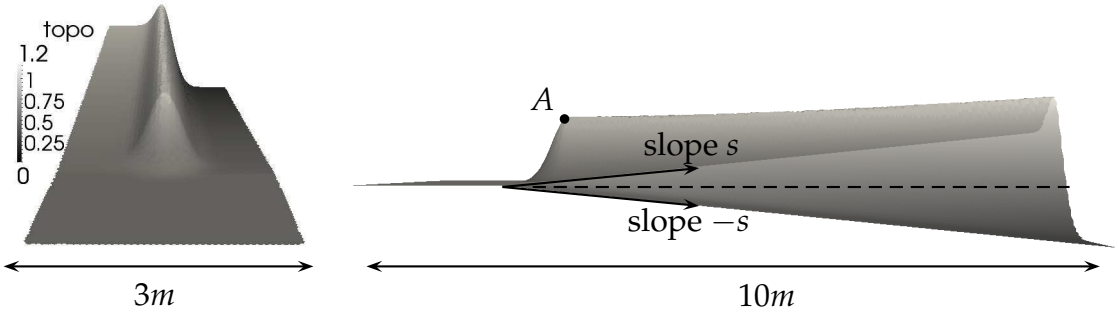

Figure III .31: Dam break in a double-slope basin : Details on the topography and dimensions of the computational domain.

rapidly varying bottom in a 2d frame. We hence consider a water retention of $0.5m$ total height on the platform $0 \leq x \leq 1.5$, and assume dry the rest of the basin. We then imagine a sudden failure in the dam structure, modelized by an initial discontinuity along the cross section $y = 1.5m$. We make consecutive uses of the PB scheme, Upwind Hydrostatic AP and NAP approaches, for different values of Manning roughness parameter n. An unstructured triangulation composed of 15 120 elements is used. We underscore that the access to pertinent comparisons for our friction approaches is a very challenging objective here, conditioned by the capacity to describe the whole complexity of the propagation. The flow definitely mobilises all the typical difficulties encountered in the description of hydrodynamic processes, with dry areas, presence of sophisticated mechanisms such as hydraulic jumps or multiple reflections of different origins, stiff source terms and at last convergence toward a motionless steady state with emerging slopes. For the first simulation we are opting for a moderate perturbation, taking $n = 0.002$.

We can observe on Fig. III .32 some free surface profiles taken at regular time intervals along the two cross sections $y = 0.75$ and $y = 2.25$ (left), as well as the corresponding 3d views (right). The initial discontinuity is correctly captured on the platform. The resulting advancing front of water subsequently splits itself in two parts after reaching the separating point (t=0.5s), giving rise to a circular reflected wave, observable on the second picture (t=1s), and swiftly partially returned by the lateral walls. As a result, the evolution on the upward and downward dry slopes is perturbed by secondary waves that significantly enrich the flow structure, and give an additional impulse to the motion. In spite of this tricky context, no spurious oscillations and instabilities were identified throughout the simulation. As expected according to the timid calibration of the friction terms, the three schemes under consideration provide very similar results, particularly as far as concerns the advancing water front position. These numerical data validate a good overall reproduction of the flow structure, and strongly value the general capacities of the different approaches that are implicated. After reaching the external boundaries, the two wave fronts are abruptly pushed in the opposite direction, and it follows a staggered arrival of the water fronts at the platform, due to the opposite slopes. The flow acquires then even more complicated characteristics. During all the simulation, we

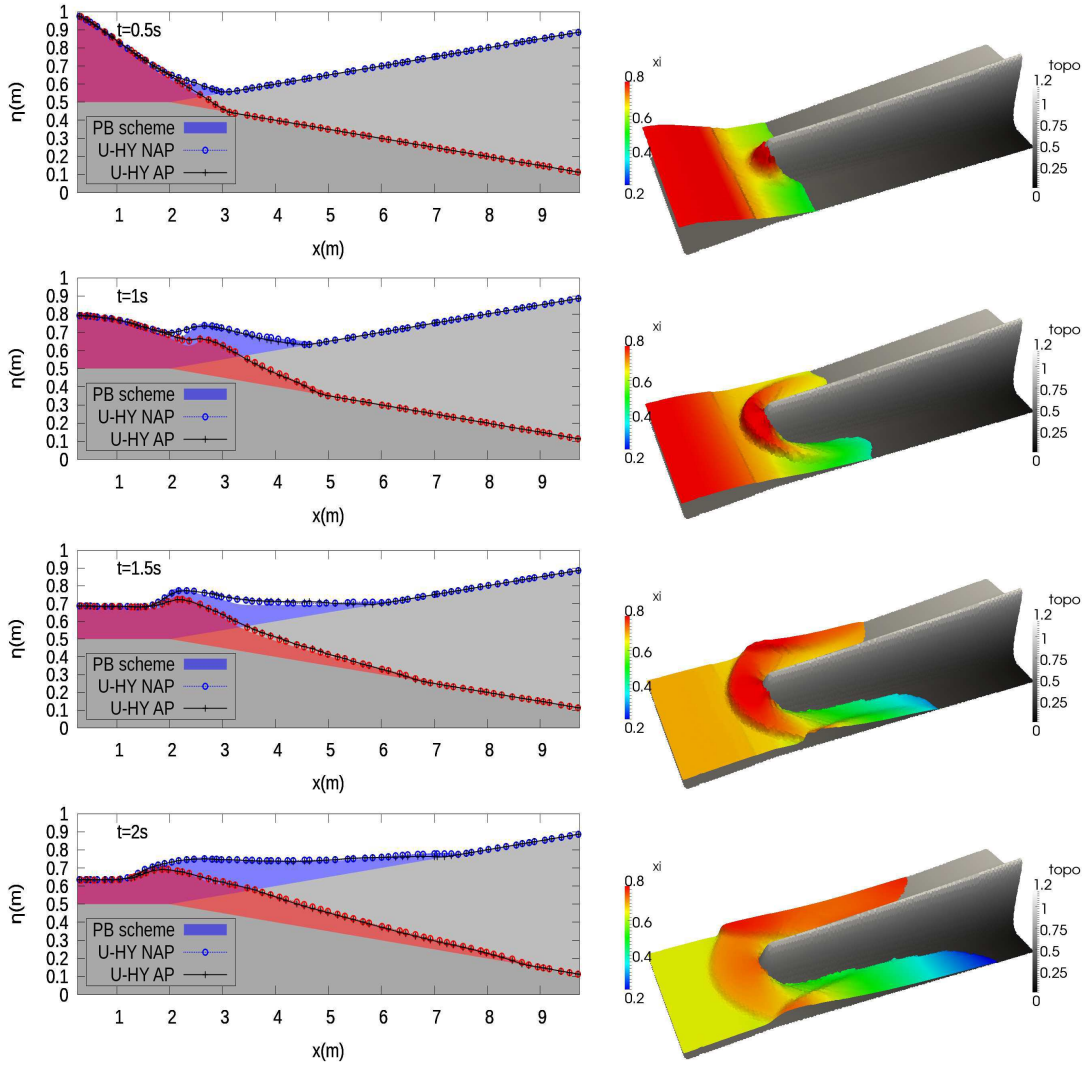

Figure III .32: Dam break in a double-slope basin : Free surface profiles at several times for $n = 0.002$. Blue profiles correspond to the positive slope (section y =2.25m), and red ones to the negative slope (section y=0.75).

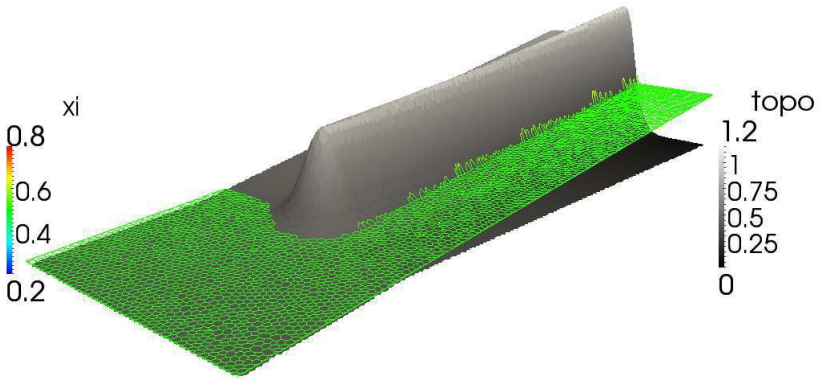

Figure III .33: Dam break in a double-slope basin. Motionless steady state.

hence are in presence of convoluted processes, made of multiple interactions with the slopes, complex exchanges on the left sector, and reflections on the walls. Therefore, damped by friction, the motion progressively decays up to the apparition of a rest state. This equilibrium, depicted in Fig. III .33 has always been numerically restored, confirming that the presence of friction in now way alters the C-property. Using the same mesh and CFL, we now increase the roughness coefficient, setting $n = 0.02$, corresponding to the order of magnitude of realistic applications. Here, friction terms tend to take a pronounced role in the flow behaviour. Thus, more noticeable divergences between corrected and uncorrected approaches are expected. These discrepancies indeed principally appear on the moving boundary interface for both up and down slopes, after a sufficient time of observation (Fig. III .34). While the other schemes produce again very similar approximations, the asymptotic correction inhibits somewhat more the flow progression. These results are in good accordance with those previously obtained for the other dam break problems on flat bottom. If we now double the roughness coefficient, one can note that the impact of the AP correction may not only provide a re-adjustment of the water front location, but also possibly entail light modifications on the overall flow structure (Fig. III .35). Again, the numerical approaches demonstrate strong stability abilities, and the convergence toward the static equilibrium is observed.

III.3.4.d Oscillatory flow with friction in a parabolic basin

We propose now to work on the 2d extrapolation of Thacker's parabolic test case introduced in [282]. There are very few analytic solutions for 2d friction flows in the literature and for this, since their enhancements mentioned in §III.2.3.b , the Thacker's cases are attracting even higher interest. As a matter of fact, we can assess the capacity of our scheme in describing perturbed flows in a real two dimensional framework, involving at the same time unstructured mesh,

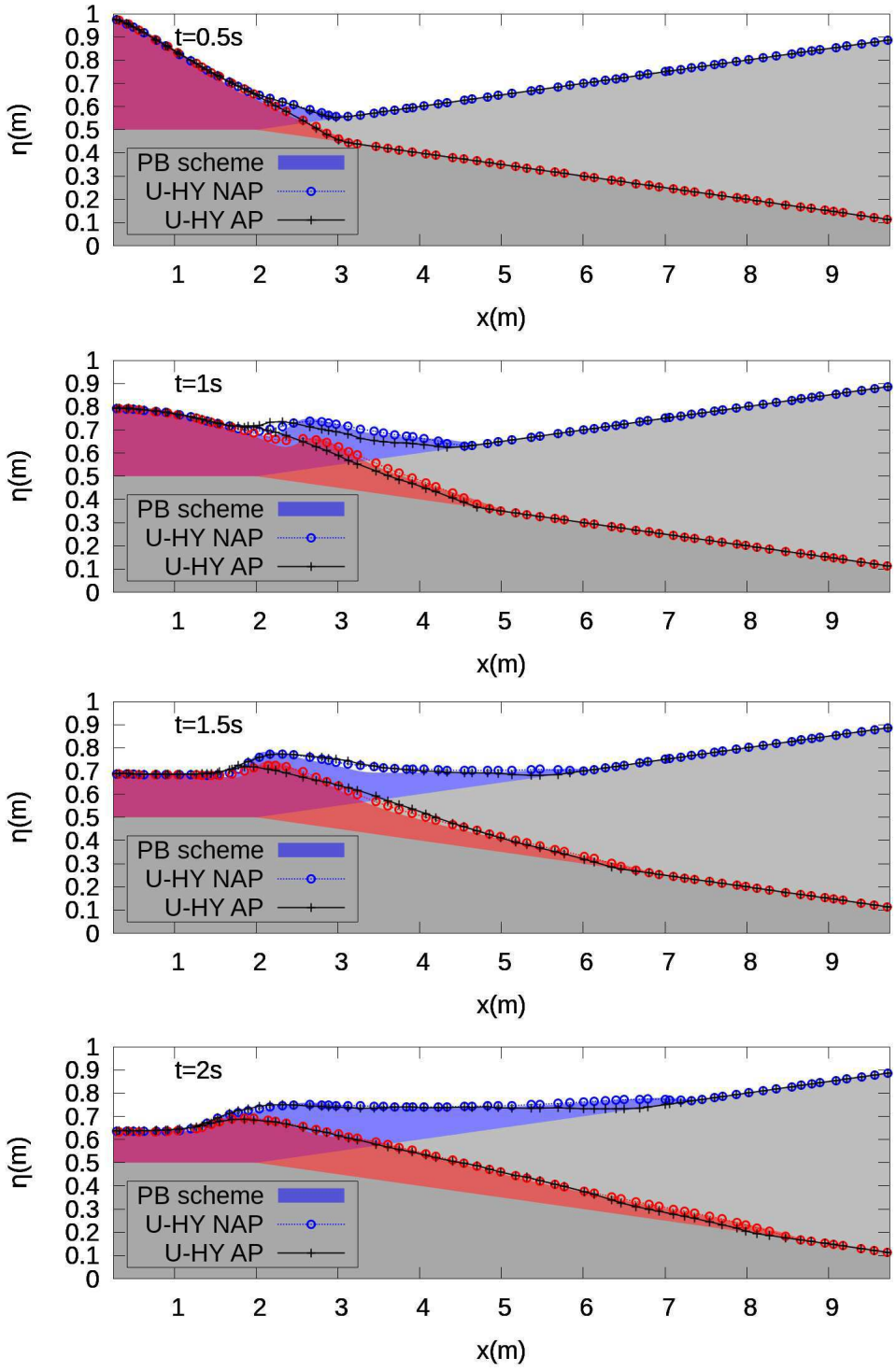

Figure III .34: Dam break in a double-slope basin. Free surface profiles at several times for $n = 0.02$.

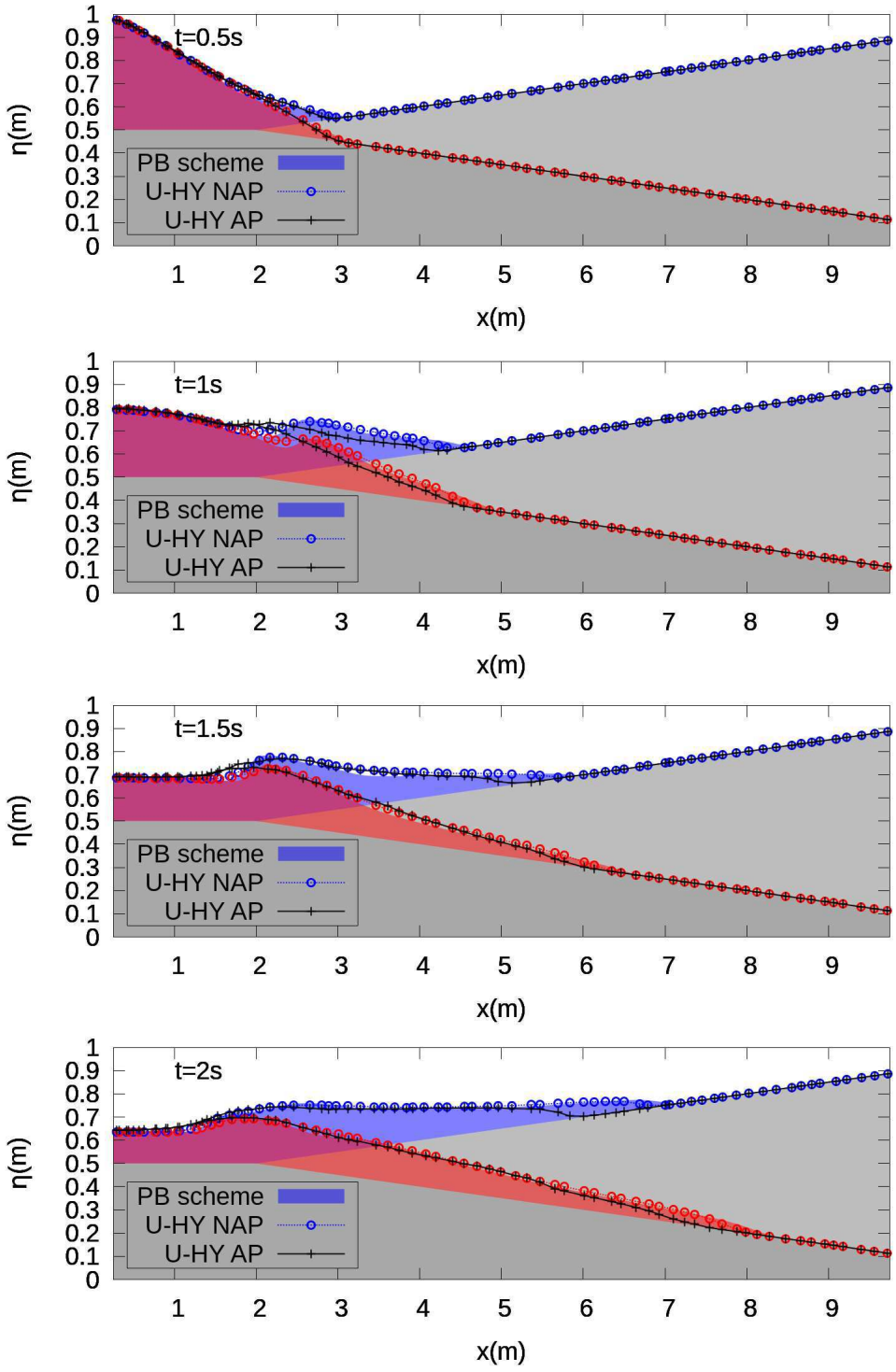

Figure III .35: Dam break in a double-slope basin. Free surface profiles at several times for $n = 0.04$.

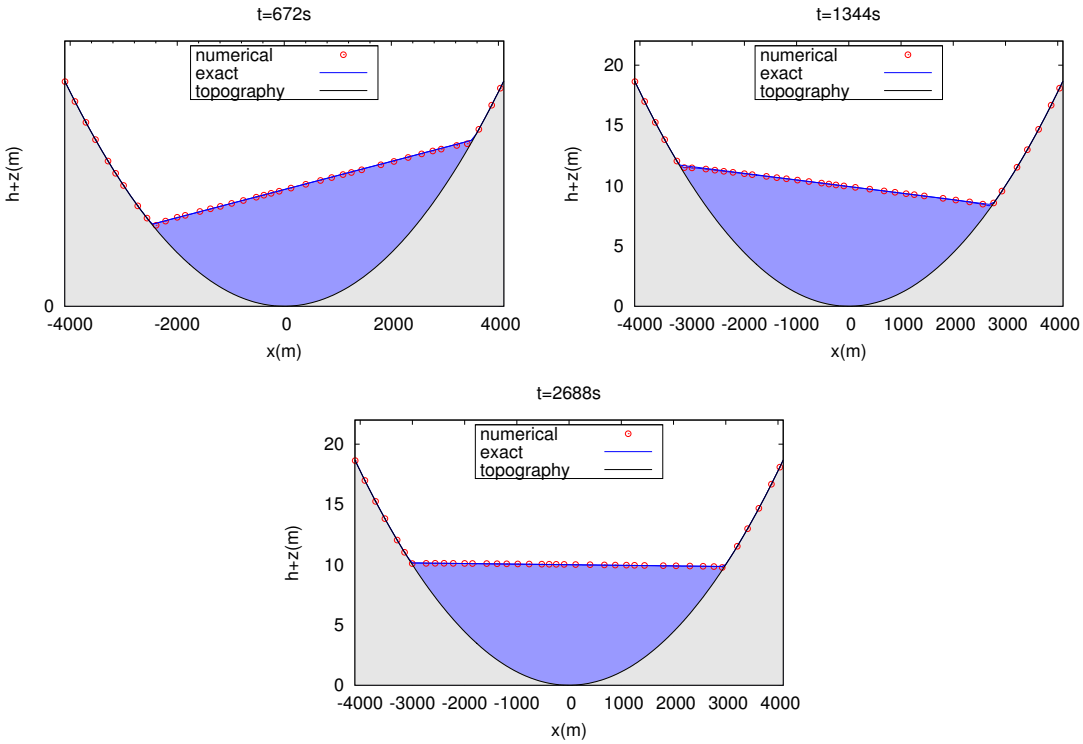

Figure III .36: Oscillatory flow with friction in a parabolic basin : Free surface profiles at several times during the revolution process, and comparison with the analytic solution.

dry cells and non trivial topography. The extended solutions are :

$$\begin{cases} \eta(x,y,t) = h_0 - \dfrac{B^2}{2g}e^{-\kappa t} - \dfrac{B}{g}e^{-\kappa t/2}\Big(\dfrac{\kappa}{2}sin(st) + s\,cos(st)\Big)x \\ \qquad\qquad -\dfrac{B}{g}e^{-\kappa t/2}\Big(\dfrac{\kappa}{2}cos(st) - s\,sin(st)\Big)y\,, \\ u(t) = Be^{-\kappa t/2}sin(st)\,, \\ v(t) = -Be^{-\kappa t/2}cos(st)\,, \end{cases} \tag{III .68}$$

and the shoreline location is :

$$x(t) = \frac{a^2}{2gh_0}e^{-\kappa t/2}\Big(-B\,s\,cos(s\,t) - \frac{1}{2}\kappa B sin(s\,t)\Big) \pm a\,. \tag{III .69}$$

In this test, the constants are the same as in the frictionless case (see test II.4.4), for which we recall that the solution consists of a planar free surface revolving within the basin with an half-period of 672s. The linear friction coefficient is set to $\kappa = 0.002$. Considering here resistance effects, the energy dissipation is obviously expected to have an impact on the amplitude of the periodic regime. We show on Fig. III .36 some 2d views of the free surface along the middle section at half, one an two periods, supplemented by a comparison with the exact solution. We can

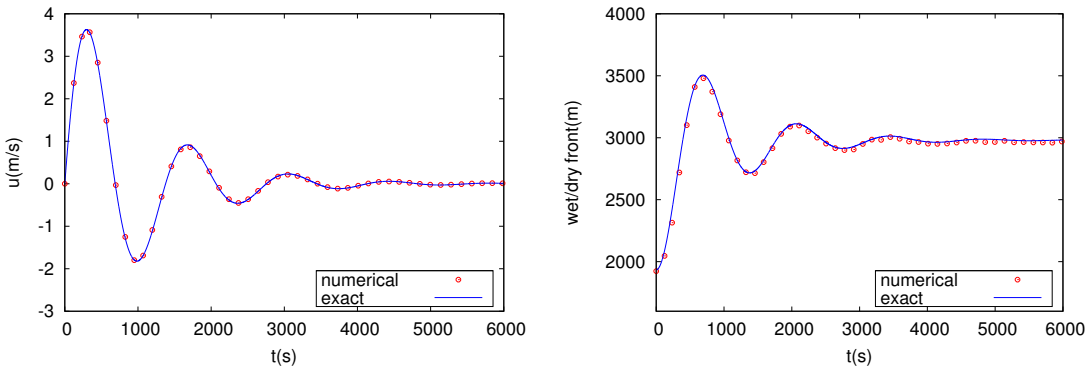

Figure III .37: Oscillatory flow with friction in a parabolic basin : Time evolution of the x-direction velocity (*left*) and shoreline location (*right*) - Analytic vs numeric.

observe an accurate description of the flow evolution, and a clear difference with the profiles depicted at the same moments in absence of resistance (Fig. II .20). After four periods, the flow is almost at rest, as evidenced by the time history of wet/dry front location (Fig. III .37) (right), also properly tracked. Again, in accordance with the theoretical solution, the free surface stays perfectly planar during the entire simulation time, notably in the neighbourhood of dry areas. Numerical and theoretical values for the $x-$velocity component at point (1 000,0) are taken over a four period simulation and depicted on Fig. III .37 (left), allowing to follow the decay of the flow motion over time. Once again we can observe a reasonable correspondence between predicted and exact values.

III.3.4.e Dam-break flow over two frictional humps

We continue the exploration of the friction scheme's abilities considering the 1d dam break experiment presented in [13]. The basin is $7m$ length and its width is fixed to $1m$ for purpose of a 2d application. Details on the topography are given in Fig. III .38. In the physical model the base of the reservoir is located in the middle of the first plane area, that is $x = 2.25m$, and the initial upstream free surface is set to $0.5m$. A Manning roughness coefficient $n = 0.01$ is imposed. Computations are run on a regular triangulation made of 5 901 vertices, corresponding to a space step $\Delta x = \Delta y = 0.025$. Reflective conditions are set at the lateral and upstream boundaries, and free outflow is assumed downstream.

Though stemming from a 1d problem, this test deals with quite subtle issues that are not obvious. It should be noted, indeed, the abrupt topography variations and entailed reflections, put together with the presence of dry bed, as well as the relative high roughness value that controls the flow. These different matters requisition all the capabilities of the numerical model, making this test particularly interesting to evaluate a friction approach.

On Fig. III .39 we can focus on the first steps of the propagation. It transpires that the first set of reflections is properly described. Computations on dry areas are very well handled in spite of being perturbed by resistance terms. Approx-

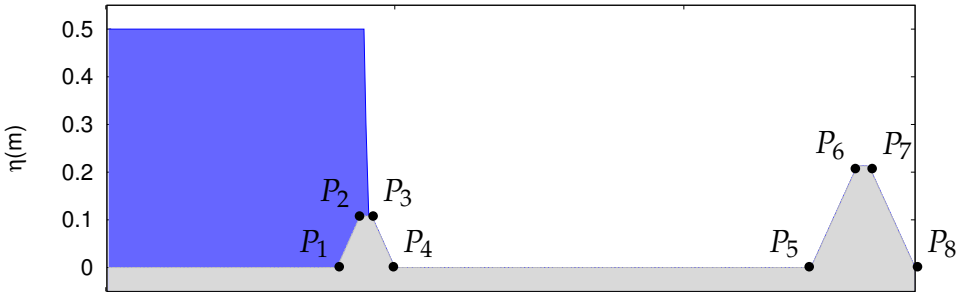

	$x(m)$	$z(m)$
P_1	2.00	0.000
P_2	2.20	0.108
P_3	2.30	0.108
P_4	2.50	0.000
P_5	6.10	0.000
P_6	6.50	0.213
P_7	6.60	0.213
P_8	7.00	0.000

Figure III .38: Dam-break flow over two frictional humps : Sketch of the basin and initial condition.

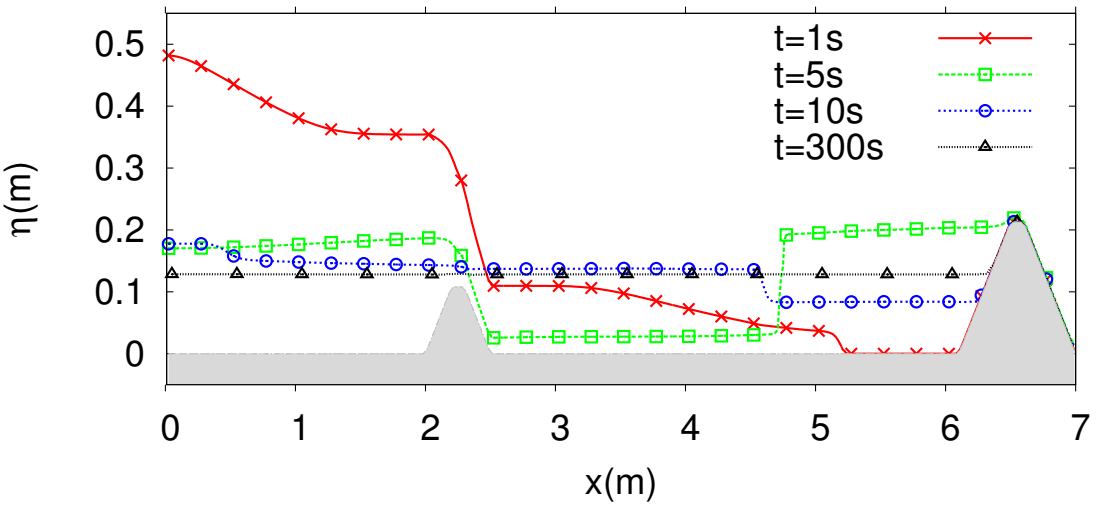

Figure III .39: Dam-break flow over two frictional humps : Free surface profiles at t=1, 5, 10 and 300s.

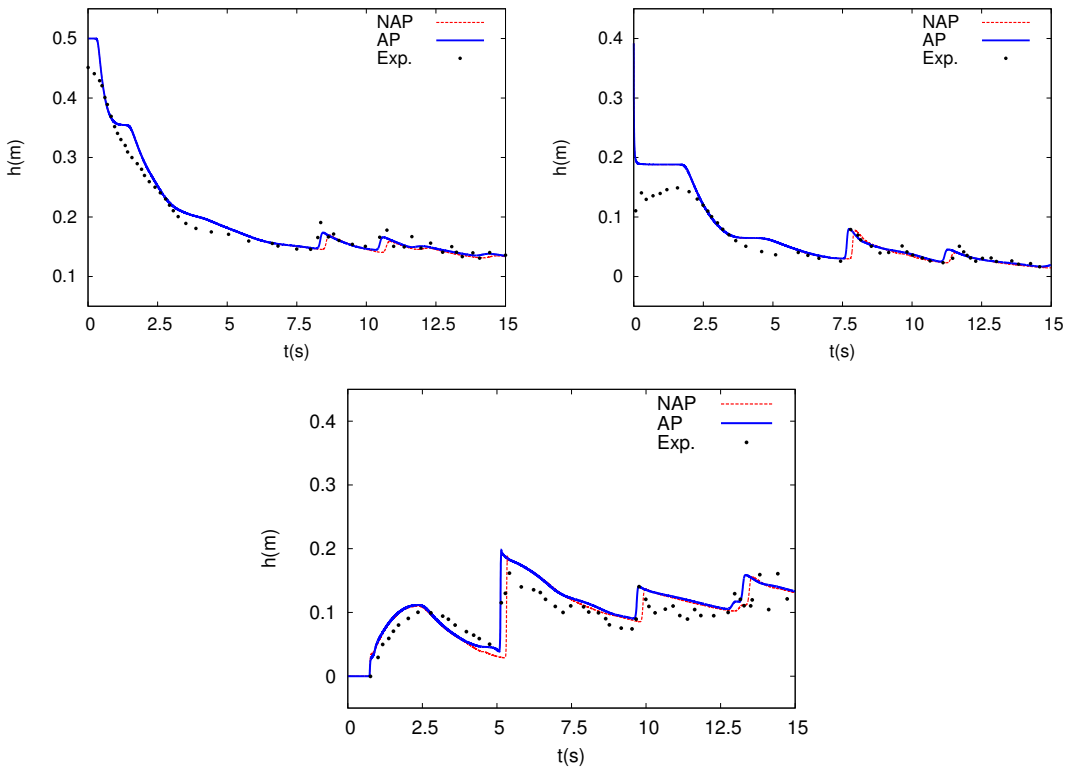

Figure III .40: Dam-break flow over two frictional humps : Time history of the free surface.

imatively around t=300, a *lake at rest* steady state is reached within the left portion of the domain. Very similar results are obtained with the high order RKDG schemes of Kesserwani and Liang presented in [171], based on the same set of *pre balanced* equations. We finally plot on Fig. III .40 the evolution of the water height up to $t = 15s$ at three reference points along the basin, for which experimental data are known. Our simulations are satisfying and follow the ones reported on the reference above. Note that, in the current context, where friction dominates the flow, the use of the AP scheme perceptibly helps to obtain a more adequate matching with the results from the physical model.

III.3.4.f Toce River dam break

As a final experiment we propose to study a dam break flow in a realistic river, employing the benchmark test of the Toce river valley (Northern Alps, Italy). Topographic data and reference results are provided by a 1:100 scale physical model, allowing comparisons with our numerical observations. In the same way, inflow boundary conditions are calibrated on the discharge hydrograph used to initiate the motion in the laboratory studies. Opened boundary conditions are set downstream. This benchmark test was used within the CADAM project [259], and is also performed in [45, 67, 92, 282, 294, 293]. Computations are run with the first order U-HY NAP scheme on an unstructured mesh composed of 30 529 elements,

and a Manning roughness coefficient equal to $n = 0.0162$. We stress out the difficulties represented by this test, since it is expected to describe the evolution of an advancing front dragged in a complicated bed river, and submitted to resistance laws. The geometry of the floodplain is indeed not trivial, and induces a flow with a complex structure, subject to multiple variations of regime throughout its propagation. Some 3d views of the free surface are available in Fig. III .41, describing the overall propagation of the flood wave. These indications on flooded areas can be put in comparison with some of the reference previously mentioned to corroborate our results. The main steps of the flow evolution and corresponding times seems to be respected, from the inundation of the central reservoir to the arrival at the downstream basin. The relevance of our predictions can be further assessed analysing the arrival time of the flood wave at several gauges disposed along the bed river, for which we have reference data (Fig. III .42). We report a good concordance with the data of the physical model, in the same order of quality with the studies above mentioned. We lastly remark that similar results have been raised with the PB and the U-HY AP schemes. We again conclude on the good accuracy and stability properties provided by our friction approaches in the context of real life applications.

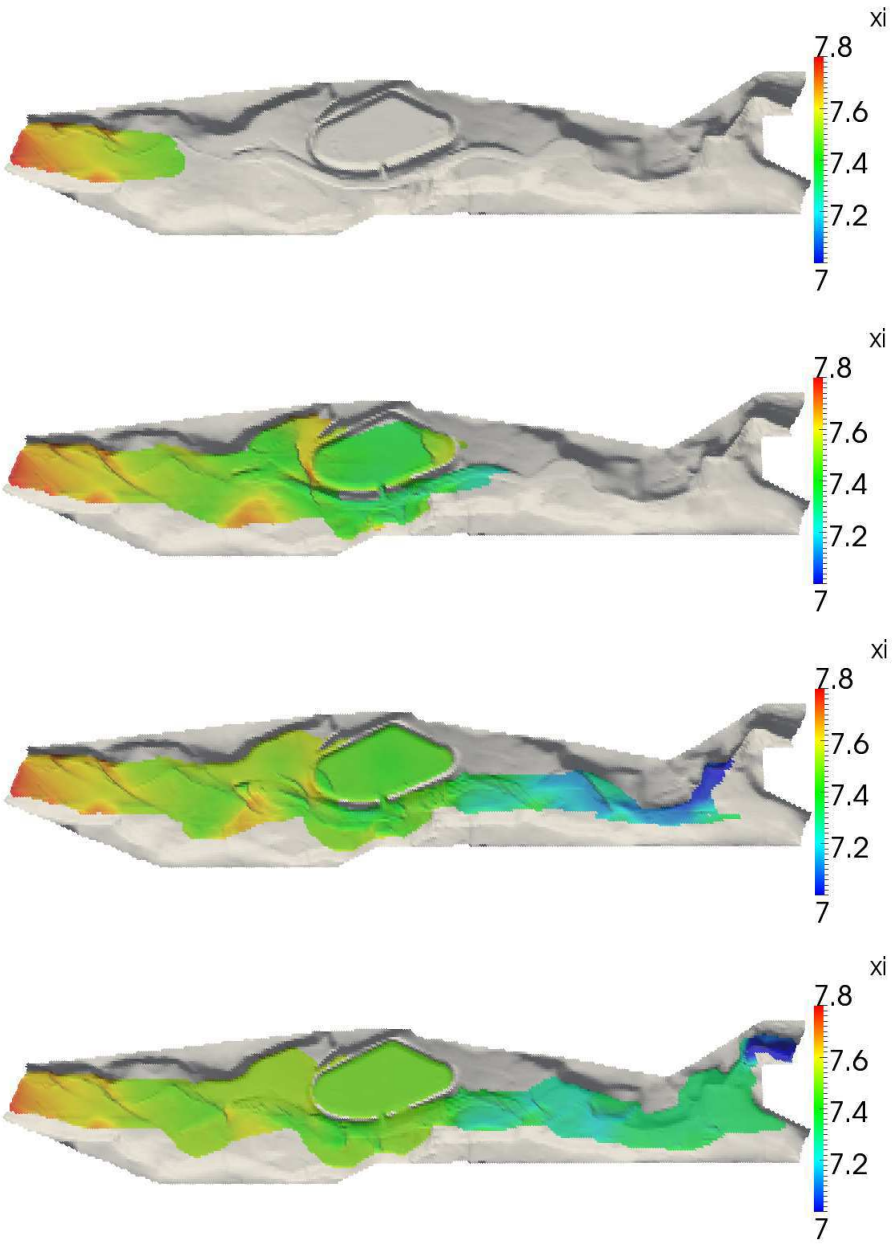

Figure III .41: Toce River dam break. 3d views of the free surface at t=20, 40, 50 and 60s.

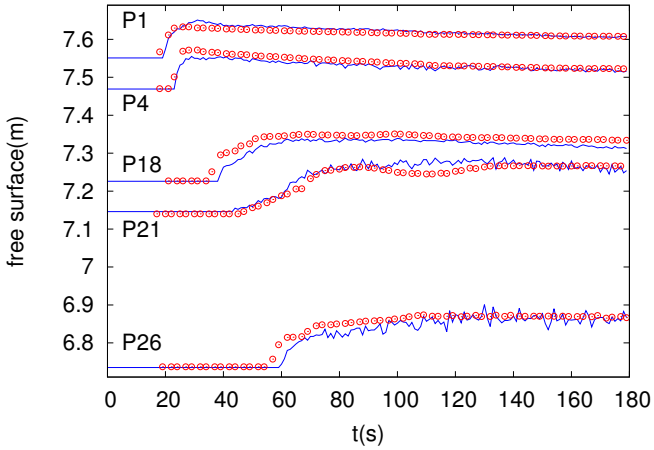

Figure III .42: Toce River dam break. Free surface history at several gauges. Numerical (*dots*) vs Experimental (*solid lines*).

III.4 Conclusion

The main object of this chapter concerns the introduction of a new way to account for friction effects in the context of the 2d Shallow Water equations, on unstructured meshes, with the general purpose to cure the typical problem of vanishing water heights encountered during most of real life applications notably. To accomplish this, the prevalent idea was to extend the properties of the 1d approaches proposed in [28, 27], based on the use of modified HLL solvers.

That way, in a first time, we proposed an improvement of the *pre balanced* scheme introduced in the previous chapter, allowing to account for such perturbed flows, and without deteriorating its features. Indeed, thanks to an appropriate re-interpretation of the HLL solver's wave structure, the friction terms are incorporated within the numerical model through a modification of the momentum equations only. Thus, one easily obtains the C-property, the preservation of the water height positivity is also straightforwardly maintained without additional time limitation, and this also stands for the MUSCL reconstructions. The stability of the method has been assessed considering some severe test cases, justifying the effectiveness of the method.

Secondly, a similar construction has been implemented on the very recent Upwind Hydrostatic scheme [24], leading again to strong stability properties. This time, the mass equation is also modified, but this does not preclude the establishment of well-balanced and robustness properties. Exploiting the entailed latitude as regards the evaluation of the water height, an asymptotic preserving correction is subsequently performed, which stands for a novelty in the context of unstructured triangulations. We proposed some tests to exhibit the potential benefits of the AP property for the NSW equations. If similar results are obtained in standard situations, very different behaviours can be observed

when friction terms tends to control the flow. A flagrant illustration of such a phenomena is given by the propagation of flood waves on dry areas, which velocity may actually appear as over-estimated by the classical approaches. Concerning real - life applications, it is difficult to determine the real impact of the AP correction in terms of accuracy, since these nuances are generally swallowed by approximations of various origins linked to the physical models from which reference data are extracted.

As a whole, with or without correction, numerical results clearly highlight the capabilities of the U-HY friction scheme in handling in parallel dry areas and friction, in a large variety of configurations. To summarize, at the outcome of the investigations carried out so far, we dispose of two efficient numerical approaches enabling to approximate efficiently the NSW equations. Both PB and U-HY schemes have been conceived to deal with all the classical constraints that apply to a Shallow Water model : in addition of satisfying the usual well-balanced and robustness properties, they are able to account for irregular bottoms, friction, dry cells, and offer interesting stability properties. Both admits simple formulations and an interesting ease of implementation. These points are a notable feature in the context of unstructured triangulations, and are particularly important in the perspective of practical applications to environmental flows.

Chapter IV

Discontinuous Galerkin Method

IV.1 Introduction

Nowadays, a large variety of numerical models are able to produce accurate approximations of weak solutions of NSW equations. As illustrated previously, Finite Volume methods are known to be very efficient, notably for their low computational cost, their capability in capturing shocks, and may enjoy a certain freedom in the discretization of source terms. However, basic FVM usually offer low accuracy and one generally needs to use some reconstruction methods to offset the low order of convergence and the diffusive losses, as was the case in the FVM that have been introduced. Alternatively, other general methods have been envisaged to augment the quality of the resolutions.

Discontinuous Galerkin (dG in the following) methods have raised great interest during the past twenty years. They combine the background of the Finite Element methods, Finite Volume methods and Riemann solvers, taking into account the physic of the problem. An arbitrary order of accuracy can be obtained with the use of high-order polynomials within elements and they are able to handle complex geometries with the use of unstructured meshes. They are highly parallelizable, and exhibit nice strong stability properties. The reader is referred to the following pioneering works [78, 79] for the general background.

It is only recently that the dG approach has been applied to the Shallow Water equations and we can find a growing number of studies, including flows with shocks, such as dam-break and oblique hydraulic jumps ([192, 251, 265]). Several approaches involving arbitrary orders methods on unstructured triangulations have been developed for the NSW system [110, 177], possibly with dynamic p-adaptivity [176], adaptive refinement [153], discretizations of the viscous equations relying on a Local Discontinuous Galerkin (LDG) treatment of the second order derivatives [2, 86], discretizations of the equations on the sphere [228, 125, 203, 219], or even space-time dG methods [4]. The list is of course non-exhaustive.

More recently, several authors have focused on the two fundamental issues that are the preservation of the motionless steady states, and the preservation of the water height positivity, to properly handle flooding and drying events. It is all the more difficult to cope with these concerns at the discrete level, given the introduction of arbitrary degrees of freedom within elements. This represents a major difference with the Finite Volume background where the states are supposed to be constant at both sides of the exchanging interfaces. Additional efforts are consequently required. Here again, an upstream use of the *pre balanced* system is going to be helpful.

Contribution and objectives

In this part, we illustrate the efficiency of a particular combination of selected ingredients, leading to a simple well-balanced and robust dG 2d discretization

on unstructured triangulations. Motivated by our previous works, we make a slightly different choice compared to [108, 291, 290], as we use the PBSW equations (II .1, II .2) instead of the classical model (I .1). Again, the use of this formulation is expected to facilitate the preservation of motionless steady states. As shown in §IV.3.6 , this is achieved for polynomial expansions of arbitrary orders, providing that the interface fluxes are slightly modified, adapting some of the ideas advanced earlier. A limiting strategy is introduced to handle discontinuities and prevent the generation of spurious oscillations. While the TVB-generalized limiter [78] is widely used, we choose to combine the discontinuity detector [174] and the moment limiting approach of [53]. Some comparison with the TVB-generalized limiter [78] are performed in the next section. The robustness of the resulting scheme is ensured, adapting the recent approach of [291, 290] to the *pre-balanced* formulation. This work is now available in [99].

The outlines of the present study are the following : in Section §IV.2 , we propose a review of some of the existing methods recently introduced to satisfy well-balanced and robustness properties, and recall some of the main limiting technics. In §IV.3 , we gather some of these ideas and propose an arbitrary order robust and well-balanced nodal discontinuous-Galerkin discretization of the Shallow Water system on unstructured meshes, relying on the PBSW model, and the recent method introduced in [291, 299] to ensure the preservation of the water depth positivity. The local limiting process, allowing the possible occurrence of shocks and contact discontinuities is described in §IV.3.3 . In §IV.3.6 , we establish the main well-balancing and robustness properties of this combination. §IV.4 is devoted to extensive numerical validations in the case of second and third order schemes, including convergence and accuracy analysis, comparisons with analytical solutions and experimental data for cases involving steady states preservation and occurrence of dry areas. Some comparisons with the M2 *pre balanced* FVM are also performed.

IV.2 A survey of existing methods

IV.2.1 Well-balancing

In the introductory part (I.5.3), and throughout the section devoted to MUSCL extensions II.3 , we mentioned a large number of Finite Volume approaches able to offer the C-property, for first and higher order schemes. By contrast, the development of well-balanced dG schemes for the NSW system is recent, and there is very few existing works, especially when considering the case of unstructured grids.

In [241], general space and space-time dG formulations are introduced for hyperbolic nonconservative partial differential equations, and applications are performed for the one-dimensional equations with topography, regarding the topography as an additional variable in the spirit of [138]. The resulting space method is shown to preserve the *C-property*.

A well-balanced method is developed for second order accuracy in [170, 169, 171], for the 1d and 2d case on rectangular meshes, using the PBSW equations and borrowing some ideas coming from the *hydrostatic reconstruction* [10] and [195].

In [108], the well-balancing is ensured for polynomial expansions of arbitrary orders and on unstructured meshes, using again the ideas of the *hydrostatic reconstruction*. Non-negative reconstructions of the water height are introduced element-wise, for each edge, together with an additional flux modification term directly accounted for in the weak formulation.

Recently, a more general approach has been introduced in [287] for a general class of conservation law with separable source terms, leading to a class of high-order dG methods with the well-balanced property. The key ingredient is a suitable decomposition of the integral of the source terms into a sum of several terms, each of which is discretized independently in a consistent way with the discretization of the corresponding flux derivative terms. This ensures the well-balancing and preserves the high-accuracy of the method. However, the overall algorithm is quite complex both to understand and implement.

An easier and less computationally expensive approach is subsequently introduced by the same authors in [288], based on a generalization of the methods introduced in [10, 222].

To conclude this section, let us mention the positivity-preserving high-order well-balanced dG approach for the NSW system developed in [285] in the 1d case, enabling the preservation of moving water steady states. This is, to the author's knowledge, the first dG method that addresses this issue.

IV.2.2 Robustness

Again, some of the ideas developed for the FVM have been adapted to the dG approach. A popular approach, adapted for $\mathbb{P}^1$ polynomial expansions basically consists of locally modifying the slope of the linear expansions if negative values of the water height appear. The local gradients are moderated element-wise until such negative values are avoided, and usually until the water height values

are above a tolerance. Provided that the whole Runge-Kutta dG scheme preserves the positivity of the average water height, this approach leads to a robust scheme. This strategy can of course be applied to higher order dG schemes, providing that the discrete solution is first locally projected onto linear polynomials, entailing some loss of accuracy. In [169, 171] such ideas are used in combination with some positive reconstructions of the water height, inspired from the *hydrostatic reconstruction* [10], for 1d and 2d case on rectangular meshes, and for the second order accuracy dG scheme (linear polynomial expansion of the solution).

In [108], this strategy is adapted to the unstructured meshes framework. Considering a $\mathbb{P}^1$ expansion of the water height, the idea is to locally post-process the gradients of h in elements such that a positive mean value is observed, but with occurrences of negative values at one or two vertices. The gradients are modified in such a way that the water height vanishes at such vertices. However, the resulting scheme can possibly lead to negative mean water height values, which are arbitrarily set to zero.

A similar strategy is introduced in [52], but with *a posteriori* modifications of the water height that preserve the overall accuracy and the mass and momentum conservation properties. Additionally, a sufficient condition ensuring the positivity of the mean water depth in each element is provided.

Alternatively, a strategy for a robust treatment of wetting and drying is introduced in [33], allowing to identify and accurately discriminate the wet and dry areas and moving the mesh accordingly. The reader is also referred to [251, 274] for some other recent studies.

More generally, the preservation of the water height positivity for an arbitrary order dG method is not a simple problem and a general method was recently introduced in [298]. This method ensures an accuracy preserving maximum-principle property for dG schemes of arbitrary order, in a general scalar conservation laws framework, under a suitable CFL-like condition. This method is extended to triangular meshes in [299], to the NSW equations in 1d and 2d on rectangular meshes in [291], and very recently on triangular meshes in [290]. The method, based on the positivity of the associated first order scheme and a simple positivity and accuracy preserving limiter, is detailed in §IV.3 . Note that the method introduced in [290] also preserves the *C-property*.

IV.2.3 Limiting strategies

In the context of hyperbolic conservation laws, special interest has to be given to the way discontinuities are handled. High-order numerical schemes produce spurious oscillations near discontinuities, which may, indeed, lead to non-physical solutions (like negative water heights), numerical instabilities and unbounded computational solutions.

A very popular approach is to use a limiting procedure which is capable to detect and control the high variations of the approximation, leading to local modifications of the solution at each time step. A very popular approach is the TVB-generalized slope-limiter technic introduced in [78], which is used in many studies, see [52, 108, 169, 192, 241] for instance. This approach, relying on a modified

minmod function, maintains the conservation of mass element by element, does not degrade the accuracy of the method for piecewise linear approximations and does not flatten smooth extrema. The higher order modes are set to zero when limiting is needed.

An interesting approach is proposed in [239] to the case of higher-order slope limiting, which consists of adaptively and successively differentiating the numerical solution. The derivations raise linear terms that can be limited as in the case of a linear approximation. An efficient parameter-free (and consequently problem independent) alternative, relying on the *maxmod* function is proposed in [53] and is detailed in §IV.3.3 . Of course, many slope limiters used within FVM can be adapted to the needs of the dG method, like the van Albada type limiting method [275] in which the gradient in an element is limited using the weighted average of face gradients. Let us also mention [69, 146] for some extensions of van Leer's slope limiter for two-dimensional dG method and relying on the solution of a least squares problem.

To deal with spurious oscillations around discontinuities, an alternative approach is to introduce a dissipation operator, see for instance [277]. This can be done by adding the operator into the weak formulation, see [4, 265].

However, the main drawback of these approaches is that they can decrease the high order of accuracy of the method, when used in smooth regions of the solution. To avoid this, an important issue is to determine the area of application of the limiting procedure (or the smoothing operator) to avoid a possible loss of accuracy. A popular method, widely used in CFD, is to use a discontinuity detector. Using such a detector, it is possible to limit spurious oscillations only near steep gradients and the high order of accuracy can be preserved away from troubled elements. This has been investigated in [238], where several discontinuity detectors are reviewed and compared. In the framework of dG method, a very popular approach is the one introduced in [174, 173]. They developed a discontinuity detector based on a strong super-convergence properties at the outflow boundaries of each element in smooth regions. This method has been proved to be efficient and is used in several studies, see for instance [4, 108, 171, 153, 265, 304].

In [238, 303], an alternative approach is proposed, which uses traditional ENO or WENO methodology as limiters for the dG methods, maintaining the high-order of accuracy. The key ideas are first to identify cells which might need some limiting procedure and then to replace the solution polynomials in those cells with reconstructed polynomials, maintaining the original cells mean values and preserving orders of accuracy as before while being less oscillatory. However, this approach relies on a wide stencil, especially for high order of accuracy, even with the use of Hermite-WENO based limiters [201, 237]. To overcome these drawbacks, a new WENO limiting procedure on structured and unstructured meshes is recently introduced in [300, 304]. The main idea is to reconstruct the entire polynomial, instead of reconstructing point values or moments in the classical WENO reconstructions. A smaller stencil is needed, without extensive usage of meshes geometric informations, leading to a simpler implementation and very efficient results.

IV.3 *Pre-Balanced* RKDG scheme

IV.3.1 Discrete formulation

We consider a triangulation $\mathcal{T}$ of the computational domain Ω, and employ the notations introduced in §I.2 . We aim at computing an approximate vector solution on this triangulation. We define :

$$\mathcal{V} := \{v \in L^2(\Omega) \,|\, \forall\, T \,\in\, \mathcal{T}\,,\, v_{|T} \,\in\, \mathbb{P}^N(T)\}, \tag{IV .1}$$

where $\mathbb{P}^N(T)$ denotes the space of 2-variables polynomials in T of degree at most N.

A weak formulation of the problem is obtained by multiplying (II .1) by a test function $\phi \in \mathcal{V}$. The result is integrated on a given element T_i and the flux term is integrated by part to obtain :

$$\int_{T_i} \frac{\partial}{\partial t} V(\mathbf{x},t)\phi(\mathbf{x})d\mathbf{x} - \int_{T_i} H(V,z).\nabla\phi(\mathbf{x})d\mathbf{x} + \int_{\partial T_i} H(V,z)\cdot\vec{n}_{\partial T_i}\,\phi(s)ds = \int_{T_i} S(V,z)\phi(\mathbf{x})d\mathbf{x}\,, \tag{IV .2}$$

where ∂T_i is the boundary of T_i and $\vec{n}_{\partial T_i}$ its unit outward normal. The local approximated vector solution $V_\mathfrak{h} \in \mathcal{V}^3$ is expressed as a polynomial of order N on each element T_i :

$$V_\mathfrak{h}(\mathbf{x},t) = \sum_{l=1}^{N_d} V_i^l(t)\theta_i^l(\mathbf{x}), \quad \forall \mathbf{x} \in T_i, \forall t \in [0, t_{max}]\,, \tag{IV .3}$$

where $\{\theta_i^l\}_{l=1}^{N_d}$ is a polynomial expansion basis for $\mathbb{P}^N(T_i)$, and $\{V_i^l(t)\}_{l=1}^{N_d}$ are the local expansion coefficient vectors with $V_i^l(t) = {}^t(\eta_i^l, (q_x)_i^l, (q_y)_i^l)$. Many choices are possible for the expansion basis, and we opt in the following for a *nodal* approach: $\{\theta_i^l\}_{l=1}^{N_d}$ will refer to the interpolant Lagrangian expansion basis, with $N_d = (N+1)(N+2)/2$. Let also consider a polynomial expansion of the topography parameterization z :

$$z_\mathfrak{h}(\mathbf{x}) = \sum_{l=1}^{N_d} z_i^l\theta_i^l(\mathbf{x})\,, \quad \forall \mathbf{x} \in T_i\,. \tag{IV .4}$$

Thus, a discrete formulation of (IV .2) is obtained by replacing the exact solution $V(\mathbf{x},t)$ by the approximation $V_\mathfrak{h}(\mathbf{x},t)$ and the test function ϕ by each element of the expansion basis, successively :

$$\int_{T_i}\Big(\sum_{l=1}^{N_d}\frac{d}{dt}V_i^l(t)\theta_i^l(\mathbf{x})\Big)\theta_i^p(\mathbf{x})d\mathbf{x} - \int_{T_i} H(V_\mathfrak{h},z_\mathfrak{h}).\nabla\theta_i^p(\mathbf{x})d\mathbf{x} + \int_{\partial T_i} H(V_\mathfrak{h},z_\mathfrak{h})\cdot\vec{n}_{\partial T_i}\,\theta_i^p(s)ds = \int_{T_i} S(V_\mathfrak{h},z_\mathfrak{h})\theta_i^p(\mathbf{x})d\mathbf{x} \quad , \quad 1 \le p \le N_d\,. \tag{IV .5}$$

Noting that we have :

$$\int_{\partial T_i} H(V_\mathfrak{h}, z_\mathfrak{h}) \cdot \vec{n}_{\partial T_i} \theta_i^p(s) ds = \sum_{k=1}^{3} \int_{\Gamma_{ij(k)}} \mathcal{H}_{ij(k)} \theta_i^p(s) ds \,,$$

where we have set :

$$\mathcal{H}_{ij(k)} = H(V_\mathfrak{h}, z_\mathfrak{h}) \cdot \vec{n}_{ij(k)} \,,$$

we obtain the following semi-discrete formulation, where the space dependency of the basis functions is omitted, for the sake of simplicity :

$$\sum_{l=1}^{N_d} \left(\frac{d}{dt} V_i^l(t) \int_{T_i} \theta_i^l \theta_i^p \, d\mathbf{x} \right) - \int_{T_i} H(V_\mathfrak{h}, z_\mathfrak{h}) \cdot \nabla \theta_i^p \, d\mathbf{x} + \sum_{k=1}^{3} \int_{\Gamma_{ij(k)}} \mathcal{H}_{ij(k)} \theta_i^p \, ds = \int_{T_i} S(V_\mathfrak{h}, z_\mathfrak{h}) \theta_i^p \, d\mathbf{x} \quad , \quad 1 \leq p \leq N_d \,. \tag{IV .6}$$

Remark IV.3 .1. *As we use the Lagrangian expansion basis, the expansion coefficients in (IV .3) and (IV .4) can be regarded as the nodal values at the corresponding N_p nodes. Consequently, the topography parameterization expansion coefficients in (IV .4) are obtained by "reading" the value of the topography at these nodes, for each element.*

IV.3.2 Numerical flux

Classically, since matching conditions are not enforced on the approximated vector solution $V_\mathfrak{h}(\mathbf{x}, t)$ at element interfaces, the boundary flux $H(V_\mathfrak{h}, z_\mathfrak{h}).\vec{n}_{\partial T_i}$ is not uniquely defined. We propose in the following a simple choice for the interfaces numerical fluxes $\mathcal{H}_{ij(k)}$, inspired from the Finite-Volume well-balanced discretization explained in preceding sections. This modified flux can also be seen as the adaptation of the ideas of [291] to the *pre-balanced* formulation (II .1).

In accordance with the notations in place, let us define, for a given interface $\Gamma_{ij(k)}$, V_k^- and V_k^+ respectively the restrictions of $V_{\mathfrak{h}|T_i}$ and $V_{\mathfrak{h}|T_{j(k)}}$ to $\Gamma_{ij(k)}$ (the *interior* and *exterior* traces, with respect to the element T_i). Similarly, z_k^- and z_k^+ stand for the *interior* and *exterior* values of $z_\mathfrak{h}$ on $\Gamma_{ij(k)}$. For each interface $\Gamma_{ij(k)}$, $k = 1, .., 3$, we follow exactly the same procedure as in the Finite Volume frame :

$$\tilde{z}_k = \max(z_k^-, z_k^+) \quad , \quad \check{z}_k = \tilde{z}_k - \max(0, \tilde{z}_k - \eta_k^-) \,, \tag{IV .7}$$

and

$$\check{h}_k^- = \max(0, \eta_k^- - \tilde{z}_k) \quad , \quad \check{h}_k^+ = \max(0, \eta_k^+ - \tilde{z}_k) \,, \tag{IV .8}$$

$$\check{\eta}_k^- = \check{h}_k^- + \check{z}_k \quad , \quad \check{\eta}_k^+ = \check{h}_k^+ + \check{z}_k \,, \tag{IV .9}$$

leading to the new *interior* and *exterior* values :

$$\check{V}_k^- = {}^t(\check{\eta}_k^-, \frac{\check{h}_k^-}{h_k^-} \mathbf{q}_\mathbf{k}^-) \,, \quad \check{V}_k^+ = {}^t(\check{\eta}_k^+, \frac{\check{h}_k^+}{h_k^+} \mathbf{q}_\mathbf{k}^+) \,. \tag{IV .10}$$

Now we set :

$$\mathcal{H}_{ij(k)} = \mathcal{H}(\check{V}_k^-, \check{V}_k^+, \check{z}_k, \check{z}_k, \vec{n}_{ij(k)}) + \check{\mathcal{H}}_{ij(k)}\,, \tag{IV .11}$$

as the numerical flux function through the interface between T_i and $T_{j(k)}$, where :

i) $\mathcal{H}(V^-, V^+, z^-, z^+, \vec{n})$ is a consistent numerical flux function, as usually computed from some 1d scheme.

ii) $\check{\mathcal{H}}_{ij(k)}$ is a correction term needed to ensure flux balancing at motionless steady states, defined as follows :

$$\check{\mathcal{H}}_{ij(k)} = \begin{pmatrix} 0 & 0 \\ g\check{\eta}_k^-(\check{z}_k - z_k^-) & 0 \\ 0 & g\check{\eta}_k^-(\check{z}_k - z_k^-) \end{pmatrix} \cdot \vec{n}_{ij(k)}. \tag{IV .12}$$

Note that the modified interface fluxes (IV .11) induce perturbations of order $N+1$ when compared to the traditional interface fluxes. In the following, we choose to use the global Lax-Friedrichs flux (I.3.1) :

$$\mathcal{H}(V^-, V^+, z^-, z^+, \vec{n}) = \frac{1}{2}\left(H(V^-, z^-)\cdot\vec{n} + H(V^+, z^+)\cdot\vec{n}\right) - \frac{a}{2}(V^+ - V^-)\,, \tag{IV .13}$$

with $a = \max_{i\in\mathbb{Z}} \lambda_i$ and $\lambda_i = \max_{\partial T_i}\left(|\mathbf{u}_i\cdot\vec{n}_{ij(k)}| + \sqrt{gh_i}\right)$.
Above, and in the forthcoming developments, we adopt the simplified notation V_i to refer to the restriction of $V_\mathfrak{h}$ on the element T_i. This also stands stand for z and each scalar component of $V_\mathfrak{h}$.

IV.3.3 Limiting procedure

Denoting $V_\mathfrak{h} \leftarrow \Pi V_\mathfrak{h}$ the limitation operator, acting on the approximated vector solution $V_\mathfrak{h}$, the main steps of the limiting process are the following :

i) detect the shocks using the criterion proposed in [174]. This criteria is based on a strong superconvergence property of the dG method at the outflow boundary of each element in smooth regions of the flow. More precisely, for a given element T_i, let us denote ∂T_i^{in} the inflow part of ∂T_i and identify K_i^{in} the set of superscripts k of the neighboring elements such that $\Gamma_{ij(k)}$ is a part of ∂T_i^{in}. Afterwards, once recovered the water heights by $h = \eta - z$, we use the following quantity :

$$\mathfrak{I}_i = \frac{\sum_{k\in K_i^{in}} \int_{\Gamma_{ij(k)}} (h_i - h_{j(k)})\, ds}{\mathfrak{d}_i^{(N+1)/2}\left(\sum_{\sigma\in K_i^{in}} \ell_{ij(k)}\right)\|h_i\|_\infty}. \tag{IV .14}$$

If $\mathfrak{I}_i \geq 1$ then we apply a slope limiter on each scalar component w_i of $V_i = V_{\mathfrak{h}|T_i}$. This limiting strategy is described in the next step.

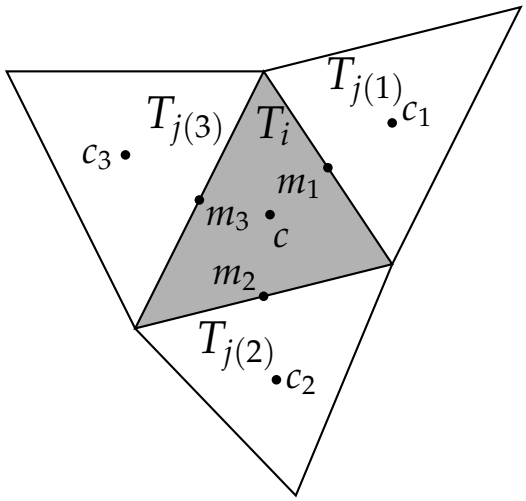

Figure IV .1: Limitation step : geometric configuration.

ii) restrict the polynomial order to $N = 1$ in the element T_i such that $\mathfrak{I}_i \geq 1$ (called *troubled elements*, following [238]) and limit the slope of the resulting $\mathbb{P}^1$ approximation following the simple and efficient procedure introduced in [53]. Furthermore, this limiting procedure is free of problem dependence and there is no parameters needed to be calibrated unlike in the widely used TVB limiter [78]. Let us quickly recall this procedure with some simplified notations. Considering the four elements patch neighborhood described in Fig. IV .1, let us denote c and $(c_k)_{k=1..3}$ the respective barycenters of elements T_i and its three neighbors $(T_{j(k)})_{k=1..3}$. We also denote by $(m_k)_{k=1..3}$, the midpoints of the shared edges between T_i and $T_{j(k)}$ respectively. Following [78], for each neighboring element $T_{j(k)}$, we can find $T_{j(l)}$ and two positive parameters α_k and β_k such that :

$$\vec{cm}_k = \alpha_k \vec{cc}_k + \beta_k \vec{cc}_l \,.$$

Then, for any linear function w we can write :

$$w(m_k) - w(c) = \alpha_k (w(c_k) - w(c)) + \beta_k (w(c_l) - w(c)).$$

Considering that the value of the function w_i at the element barycenter is nothing but the cell average $\overline{w}_i$, and coming back to the general case of piecewise linear functions w, the limiting procedure consists of replacing the values $(w_i(m_k) - \overline{w}_i)_{k=1,..,3}$ by limited values, denoted $(\Delta_k)_{k=1,..,3}$, and defined as follows :

$$\Delta_k = \text{maxmod}\big(\Delta_k^{in}, \Delta_k^{out}\big), \tag{IV .15}$$

$$\Delta_k^{in} = \text{minmod}\Big(w_i(m_k) - \overline{w}_i, \nu\big(\alpha_k(\overline{w}_k - \overline{w}_i) + \beta_k(\overline{w}_l - \overline{w}_i)\big)\Big)\,,$$

$$\Delta_k^{out} = \text{minmod}\big(w_i(m_k) - \overline{w}_i, w_{j(k)}(m_k) - \overline{w}_i\big)\,,$$

where

$$\text{maxmod}(a,b) = \begin{cases} s\max(|a|,|b|) & \text{if} \quad s = sgn(a) = sgn(b)\,, \\ 0 \quad \text{otherwise}\,, \end{cases} \tag{IV .16}$$

$\nu > 1$ and the *minmod* function is available in (II .36). Note that this modification may not be mass conserving. Consequently, if $\sum_{k=1}^{3} \Delta_k \neq 0$, we replace $(\Delta_k)_{k=1,..,3}$ with $(\hat{\Delta}_k)_{k=1,..,3}$, defined as follows (the principle is the same as II .37) :

$$\hat{\Delta}_k = \min(1, \frac{\mathfrak{s}_-}{\mathfrak{s}_+})\max(0, \Delta_k) - \min(1, \frac{\mathfrak{s}_+}{\mathfrak{s}_-})\max(0, -\Delta_k)\,,$$

$$\text{with : } \mathfrak{s}_+ = \sum_{k=1}^{3} \max(0, \Delta_k), \quad \mathfrak{s}_- = \sum_{k=1}^{3} \max(0, -\Delta_k)\,.$$

IV.3.4 Additional limiting for robustness

We briefly recall the main ideas of the strategy introduced in [291, 290, 299] to enforce a strict maximum principle that ensures the robustness property. The ideas are developed for an explicit first order Euler scheme in time for the sake of clarity. As shown in §IV.3.6 , these ideas can be extended to the PBSW equations.

We first need to compute the new quadrature points for every element T_i. Considering the scheme (IV .6) for the update of $\eta_\mathfrak{h}$, with polynomial expansions of order N, we assume that the line integrals are computed using a α-point Gauss quadrature. The Zhang and Shu quadrature rules are obtained by a transformation of the tensor product of a β-point Gauss-Lobatto quadrature, where β is the smallest integer such that $2\beta - 3 \geq N$, and the α-point Gauss quadrature. This special quadrature includes all α-point Gauss quadrature nodes for each edge $\Gamma_{ij(k)}, k = 1, 2, 3$, involves positive weights and its degree is chosen such that it is exact for the integration of η_i over T_i. In the following, let us denote S_i^N the set of points of this new quadrature rule and $\hat{\omega}_1$ the weight associated with the first node of the β-point Gauss-Lobatto quadrature. We do not give further details and the reader is referred to [299] for explicit nodes coordinates and weights. In §IV.4 , we focus on $\mathbb{P}^1$ and $\mathbb{P}^2$ approximations of the weak solutions of PBSW equations, and we show in Fig. IV .2 the quadrature nodes used for these two orders of approximation on a reference element. The robustness property is then enforced in 2 steps :

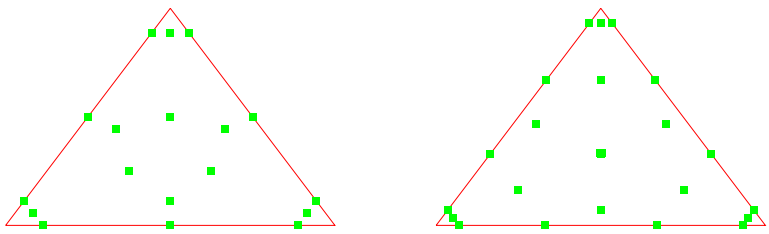

Figure IV .2: Nodes locations for the Zhang and Shu quadrature - $\mathbb{P}^1$ and $\mathbb{P}^2$ cases.

i) First, for each element T_i, we compute the polynomial expansions for the water height $h_i^n(\mathbf{x})$ from $\eta_i^n(\mathbf{x})$ and $z_i(\mathbf{x})$ (this is achieved straightforwardly, as we are working with the *nodal* basis). We then extract the quantities

$$m_{T_i} = \min_{\mathbf{x}\in S_i^N} h_i^n(\mathbf{x}) \,. \tag{IV .17}$$

ii) Next, we need to ensure that $h_i^n(\mathbf{x}) \geq 0$, $\forall \mathbf{x} \in S_i^N$, which is a sufficient condition to ensure a robustness property for the dG scheme (IV .6), under a suitable CFL-like condition, as shown in §IV.3.6 . In practice, we ensure that $h_i^n(\mathbf{x}) \geq \epsilon$, $\forall \mathbf{x} \in S_i^N$, where ϵ is a small positive threshold value.
This can be enforced using the accuracy preserving limiter introduced in [299]. Denoting $\overline{h}_i^n = \dfrac{1}{|T_i|}\int_{T_i} h_i \, dx$ the mean value of the water height at time t^n on the element T_i, and assuming that $\overline{h}_i^n \geq 0$, we replace h_i^n by a conservative linear scaling around the cell average :

$$\hat{h}_i^n = \theta_{T_i}(h_i^n - \overline{h}_i^n) + \overline{h}_i^n \,, \tag{IV .18}$$

where

$$\theta_{T_i} = \min\left(\frac{\epsilon - \overline{h}_i^n}{m_{T_i} - \overline{h}_i^n}, 1\right).$$

Remark IV.3 .2. *Following steps i), ii) at each time step (or eventually substep if a higher order time-discretization is used), and assuming that $\overline{h}_i^0 \geq \epsilon$, we ensure that $\overline{h}_i^n$ remains positive at every time step n. Additionally, the scaling (IV .18) ensures that the values of $\hat{h}_i$ remain positive at the (N+1)-point Gauss quadrature nodes used to compute the line integrals of (IV .6), the eigenvalues used in the Lax-Friedrichs flux (IV .13) and the CFL condition (IV .28). In practice, the parameter ϵ is the threshold introduced to identify what is numerically called a dry cell and arbitrarily set the velocity to zero.*

Remark IV.3 .3. *The Zhang and Shu quadrature rules are not used to compute the surface integrals, as we prefer to use more efficient cubature rules on triangles. Practically, its only purpose is to allow the computation of the quantities m_{T_i} and therefore enables to enforce the robustness sufficient condition introduced in [299].*

IV.3.5 Time discretization

The time stepping is carried out making use of the method of lines, based on SSP-RK schemes (see §I.5.1). Writing the semi-discrete equations as $\dfrac{d}{dt}V_\mathfrak{h} + \mathcal{A}_\mathfrak{h}(V_\mathfrak{h}) = 0$, advancing from time level n to $n+1$ is computed as follow for the second-order scheme :

$$\begin{cases} V_\mathfrak{h}^{n,1} = V_\mathfrak{h}^n - \Delta t \tilde{\mathcal{A}}_\mathfrak{h}(V_\mathfrak{h}^n) \,, \\ V_\mathfrak{h}^{n+1} = \frac{1}{2}(V_\mathfrak{h}^n + V_\mathfrak{h}^{n,1}) - \frac{1}{2}\Delta t \tilde{\mathcal{A}}_\mathfrak{h}(V_\mathfrak{h}^{n,1}) \,, \end{cases} \tag{IV .19}$$

and for the third-order scheme :

$$\begin{cases} V_{\mathfrak{h}}^{n,1} = V_{\mathfrak{h}}^{n} - \Delta t \tilde{\mathcal{A}}_{\mathfrak{h}}(V_{\mathfrak{h}}^{n}) , \\ V_{\mathfrak{h}}^{n,2} = \frac{1}{4}(3V_{\mathfrak{h}}^{n} + V_{\mathfrak{h}}^{n,1}) - \frac{1}{4}\Delta t \tilde{\mathcal{A}}_{\mathfrak{h}}(V_{\mathfrak{h}}^{n,1}) , \\ V_{\mathfrak{h}}^{n+1} = \frac{1}{3}(V_{\mathfrak{h}}^{n} + 2V_{\mathfrak{h}}^{n,2}) - \frac{2}{3}\Delta t \tilde{\mathcal{A}}_{\mathfrak{h}}(V_{\mathfrak{h}}^{n,2}) . \end{cases} \tag{IV .20}$$

with the formal notation $\tilde{\mathcal{A}}_{\mathfrak{h}} = \mathcal{A}_{\mathfrak{h}} \circ \Pi$, and Δt being the time discretization step, obtained from the following CFL condition [79] :

$$\max_{i \in \mathbb{Z}} \left(\lambda_i \frac{\mathfrak{p}_i}{|T_i|} \right) \Delta t \leq \frac{1}{2N+1}. \tag{IV .21}$$

IV.3.6 Main properties

We focus here on two suitable properties verified by the scheme (IV .6). We first show that the well-balancing property is inherited from the particular interface fluxes discretization (IV .11) for polynomial expansions of arbitrary orders. Next, we show that the method of [291, 290] can be adapted to the PBSW equations (II .1) to ensure the robustness.

Proposition 10. *The scheme (IV .6), with the interface fluxes discretization (IV .11), preserves the motionless steady states.*

Proof. We adapt the ideas of [291] to the reconstruction introduced in §IV.3.2 . We consider T_i an element of $\mathcal{T}$, together with his neighbors $(T_{j(k)})_{k=1,..,3}$. Denoting that (I .58) is equivalent to the following local formulation of the well-balancing property, for all $n \in \mathbb{N}$:

$$\left(\begin{cases} \eta_i^n \equiv \eta_{j(k)}^n \equiv \eta_c \\ \mathbf{q}_i^n \equiv \mathbf{q}_{j(k)}^n \equiv 0 \end{cases} , k = 1,2,3 \right) \Rightarrow \left(\begin{cases} \eta_i^{n+1} \equiv \eta_c \\ \mathbf{q}_i^{n+1} \equiv 0 \end{cases} \right), \tag{IV .22}$$

let's assume that the left brace of (IV .22) holds. Let's also assume that a first order Euler time discretization is used to compute $V_{\mathfrak{h}}^{n+1}$ from $V_{\mathfrak{h}}^{n}$. Considering (IV .6), we have to show that the residues

$$R_p = -\int_{T_i} H(V_{\mathfrak{h}}^{n}, z_{\mathfrak{h}}) \cdot \nabla \theta_i^p \, d\mathbf{x} + \sum_{k=1}^{3} \int_{\Gamma_{ij(k)}} \mathcal{H}_{ij(k)} \, \theta_i^p \, ds - \int_{T_i} S(V_{\mathfrak{h}}^{n}, z_{\mathfrak{h}}) \theta_i^p \, d\mathbf{x} , \tag{IV .23}$$

vanishes for $1 \leq p \leq N_d$, when a motionless steady state is reached. We assume that the integrals in (IV .23) are computed exactly, and we notice that we have for $V_{\mathfrak{h}}^{n}$ at steady state :

$$\nabla \cdot H(V_{\mathfrak{h}}^{n}, z_{\mathfrak{h}}) = S(V_{\mathfrak{h}}^{n}, z_{\mathfrak{h}}).$$

Looking at (IV .11), and highlighting that, for each interface $\Gamma_{ij(k)}$, we have $\check{\eta}_k^- = \check{\eta}_k^+ = \eta_c$, it is easy to check that $\mathcal{H}_{ij(k)} = H(V_k^-, z_k^-) \cdot \vec{n}_{ij(k)}$, with the notations

introduced in §IV.3.2 . Consequently, we have :

$$-\int_{T_i} H(V_\mathfrak{h}^n, z_\mathfrak{h}) \cdot \nabla \theta_i^p \, d\mathbf{x} + \sum_{k=1}^{3} \int_{\Gamma_{ij(k)}} \mathcal{H}_{ij(k)} \, \theta_i^p \, ds = \int_{T_i} \nabla \cdot H(V_\mathfrak{h}^n, z_\mathfrak{h}) \theta_i^p \, d\mathbf{x} \,, \tag{IV .24}$$

and $R_p = 0$. □

Now, let us consider the robustness property. At first order in time, the scheme satisfied by the cell averaged values of the free surface in the dG approximation (IV .6) is :

$$\overline{\eta}_i^{n+1} = \overline{\eta}_i^n - \frac{\Delta t}{|T_i|} \sum_{k=1}^{3} \int_{\Gamma_{ij(k)}} \mathcal{H}_{ij(k)}^{\eta} \, ds \,, \tag{IV .25}$$

with $\mathcal{H}_{ij(k)}^{\eta}$ the first component of the numerical flux, written as :

$$\mathcal{H}_{ij(k)}^{\eta} = \mathcal{H}^{\eta}(\check{V}_k^-, \check{V}_k^+, \check{z}_k, \check{z}_k, \vec{n}_{ij(k)}). \tag{IV .26}$$

To apply the strategy of [291, 290], we first have to specify that the first order scheme associated with (IV .25) preserves the positivity of the water height. This property has actually been established in the Finite Volume context for the current Lax Friedrichs fluxes (Proposition 2), leading to the following CFL :

$$\max_{i \in \mathbb{Z}} \lambda_i \frac{\mathfrak{p}_i}{|T_i|} \Delta t \leq 1 \,. \tag{IV .27}$$

We can now state the robustness result :

Proposition 11. *We consider the (N+1)-th order scheme (IV .6), together with the interface fluxes (IV .11) and a first order Euler time discretization. We assume that* $\overline{h}_i^n \geq 0$ *and that the quantities* $\left(h_i^n(\mathbf{x})\right)_{\mathbf{x} \in \mathcal{S}_i^N}$ *are modified according to (IV .18), for all* T_i*. Then we have* $\overline{h}_i^{n+1} \geq 0$ *under the condition :*

$$\max_{i \in \mathbb{Z}} \lambda_i \frac{\mathfrak{p}_i}{|T_i|} \Delta t \leq \frac{2}{3} \hat{\omega}_1 \,. \tag{IV .28}$$

Proof. Noting that the scheme (IV .25) can be written as follows, subtracting $\overline{z}_i$ on both sides :

$$\overline{h}_i^{n+1} = \overline{h}_i^n - \frac{\Delta t}{|T_i|} \sum_{k=1}^{3} \int_{\Gamma_{ij(k)}} \mathcal{H}_{ij(k)}^{\eta} \, ds, \tag{IV .29}$$

we adapt the proof of [290], using the positivity preserving features of the scheme (IV .25). In what follows, keeping in mind that the interface value for the topography is given by (IV .7), the flux function (IV .26) will be denoted $\mathcal{H}^{\eta}(\check{V}_k^-, \check{V}_k^+, \vec{n}_{ij(k)})$ for reasons of simplicity. Using the α-point Gauss quadrature rule, supposed to be exact for polynomials of order N, (IV .29) is re-written as :

$$\overline{h}_i^{n+1} = \overline{h}_i^n - \frac{\Delta t}{|T_i|} \sum_{k=1}^{3} \left(\ell_{ij(k)} \sum_{a=1}^{\alpha} \omega_a \mathcal{H}^{\eta}(\check{V}_{k,a}^-, \check{V}_{k,a}^+, \vec{n}_{ij(k)}) \right) , \tag{IV .30}$$

where $\check{V}^-_{k,a}, \check{V}^+_{k,a}$ stand for the *interior* and *exterior* values at the a^{th} quadrature point of the edge $\Gamma_{ij(k)}$, and ω_a are the associated weights. After a straightforward rearrangement, we write :

$$\overline{h}_i^{n+1} = \overline{h}_i^n - \frac{\Delta t}{|T_i|} \sum_{a=1}^{\alpha} \omega_a I_a \,, \tag{IV .31}$$

with

$$I_a = \sum_{k=1}^{3} \ell_{ij(k)} \mathcal{H}^\eta(\check{V}^-_{k,a}, \check{V}^+_{k,a}, \vec{n}_{ij(k)}) \,.$$

These terms are subsequently fragmented as follows, thanks to the conservativity property (I .23) :

$$\begin{aligned} I_a =& \mathcal{H}^\eta(\check{V}^-_{1,a}, \check{V}^+_{1,a}, \vec{n}_{ij(1)})\ell_{ij(1)} + \mathcal{H}^\eta(\check{V}^-_{1,a}, \check{V}^-_{2,a}, -\vec{n}_{ij(1)})\ell_{ij(1)} + \\ & \mathcal{H}^\eta(\check{V}^-_{2,a}, \check{V}^-_{1,a}, \vec{n}_{ij(1)})\ell_{ij(1)} + \mathcal{H}^\eta(\check{V}^-_{2,a}, \check{V}^+_{2,a}, \vec{n}_{ij(2)})\ell_{ij(2)} + \mathcal{H}^\eta(\check{V}^-_{2,a}, \check{V}^-_{3,a}, \vec{n}_{ij(3)})\ell_{ij(3)} + \\ & \mathcal{H}^\eta(\check{V}^-_{3,a}, \check{V}^-_{2,a}, -\vec{n}_{ij(3)})\ell_{ij(3)} + \mathcal{H}^\eta(\check{V}^-_{3,a}, \check{V}^+_{3,a}, \vec{n}_{ij(3)})\ell_{ij(3)} \,. \end{aligned}$$

By setting $\overline{S}_i^N$ the subset of quadrature points lying in the interior of T_i, formula (IV .30) becomes :

$$\begin{aligned} \overline{h}_i^{n+1} &= \sum_{k=1}^{3} \sum_{a=1}^{\alpha} \frac{2}{3} \omega_a \hat{\omega}_1 h^-_{k,a} + \sum_{\mathbf{x} \in \overline{S}_i^N} h_i^n(\mathbf{x}) - \frac{\Delta t}{|T_i|} \sum_{a=1}^{\alpha} \omega_a I_a \\ &= \sum_{\mathbf{x} \in \overline{S}_i^N} h_i^n(\mathbf{x}) + \sum_{a=1}^{\alpha} \frac{2}{3} \omega_a \hat{\omega}_1 \Big[H_{1,a} + H_{2,a} + H_{3,a} \Big] \,, \end{aligned}$$

where :

$$\begin{aligned} H_{1,a} &= h^-_{1,a} - \frac{3\Delta t}{2\hat{\omega}_1 |T_i|} \Big[\mathcal{H}^\eta(\check{V}^-_{1,a}, \check{V}^+_{1,a}, \vec{n}_{ij(1)}) + \mathcal{H}^\eta(\check{V}^-_{1,a}, \check{V}^-_{2,a}, -\vec{n}_{ij(1)}) \Big] \ell_{ij(1)} \,, \\ H_{2,a} &= h^-_{2,a} - \frac{3\Delta t}{2\hat{\omega}_1 |T_i|} \Big[\mathcal{H}^\eta(\check{V}^-_{2,a}, \check{V}^+_{1,a}, \vec{n}_{ij(1)})\ell_{ij(1)} + \\ &\qquad \mathcal{H}^\eta(\check{V}^-_{2,a}, \check{V}^+_{2,a}, \vec{n}_{ij(2)})\ell_{ij(2)} + \mathcal{H}^\eta(\check{V}^-_{2,a}, \check{V}^-_{3,a}, \vec{n}_{ij(3)})\ell_{ij(3)} \Big] \,, \\ H_{3,a} &= h^-_{3,a} - \frac{3\Delta t}{2\hat{\omega}_1 |T_i|} \Big[\mathcal{H}^\eta(\check{V}^-_{3,a}, \check{V}^+_{3,a}, \vec{n}_{ij(3)}) + \mathcal{H}^\eta(\check{V}^-_{3,a}, \check{V}^-_{2,a}, -\vec{n}_{ij(3)}) \Big] \ell_{ij(3)} \,. \end{aligned}$$

We conclude remarking that quantities $H_{1,a}, H_{2,a}, H_{3,a}$ are positive under the CFL condition (IV .28), ant that the positivity of $h_i^n(\mathbf{x})$ at the quadrature points is ensured according to the reconstruction (IV .18). □

Remark IV.3 .4. *Even if the limiter (IV .18) does not modify the (N+1)-th order accuracy of the polynomial expansion $V_\mathfrak{h}$, it is necessary to use a (N+1)-th order time SSP-RK discretization to achieve an overall (N+1)-th order accuracy in space and time. Therefore, steps i), ii) should be applied at every intermediate step of the RK algorithms (IV .19) and (IV .20). To fulfill the CFL restriction (IV .28) rigorously, we have to provide an accurate estimation of $\max_{i \in \mathbb{Z}} \lambda_i$ for all the stages of the SSP-RK method. As suggested in [290], this can be achieved with applying a more stringent CFL condition only when a preliminary computation to the next intermediate time step produces negative water height.*

IV.4 Numerical validations

In this section, we highlight the good behavior of the combination suggested above. The Lagrangian interpolant $\mathbb{P}^1$ and $\mathbb{P}^2$ basis functions are used, together with the global Lax-Friedrichs flux (IV .13). We will refer to the limiter of Cockburn and Shu [78] as CS-limiter and to the limiter of Burbeau *et al* [53] described in §IV.3.3 as BSB-limiter. In the following computations, the parameter ν is set to 2 and the threshold value ϵ for the robustness limiter is set to 10^{-7}. In the two dimensional case on unstructured meshes, the CFL condition (IV .28) is always more stringent than the usual CFL (IV .21), and therefore only condition (IV .28) is applied. For the $\mathbb{P}^1$ expansion, we use a 3-point Gauss quadrature rule (*i.e.* $\alpha = 3$ with the notations of §IV.3.4) to compute the line integrals of the first equation of (IV .6). For the $\mathbb{P}^2$ expansion, we use a 4-point Gauss quadrature rule. In both case a 3-point Gauss-Lobatto rule is enough to build the required Zhang and Shu quadratures (see Fig. IV .2), leading to the value $\hat{\omega}_1 = \frac{1}{6}$.

IV.4.1 Collapsing of a Gaussian profile

The following test is commonly used in order to evaluate the diffusive properties of first and higher order schemes, see [12, 290] for instance. We study the evolution of the flow resulting from a water drop in a center of a square basin with dimensions $[0, 20] \times [0, 20]$. The computational domain is meshed with a regular triangulation, with a discretization step fixed to $\Delta x = \Delta y = 0.4$. Solid wall conditions are enforced at the boundaries. The bottom is assumed to be flat, and the initial conditions are given by :

$$h(x, y) = 2.4 \left(1 + e^{\frac{1}{4}((x-10)^2+(y-10)^2)}\right) \quad , \quad \mathbf{q} = 0\,. \tag{IV .32}$$

Free surface profiles along the section y=0 provided by the $\mathbb{P}^1$ approximation are shown on Fig. IV .3 (left) at several times during the simulation between $t = 0\,s$ and $t = 2\,s$. They appear together with a $\mathbb{P}^2$ highly resolved solution standing for a reference, and their corresponding overall 3d views (right). Numerical results obtained with the *pre balanced* MUSCL M2 Finite Volume scheme are also displayed. Note that dG and FV computations involve the same number of freedom degrees. There is a slight improvement provided by the current dG approach. These results, put in comparison against other high order models as those above mentioned, attest of the low diffusive properties of the MUSCL and dG methods.

IV.4.2 Dam break problems

This second test case aims at validating the shock capturing abilities of the scheme (IV .6), together with the efficiency of the limiting strategies in the vicinity of a dry area.

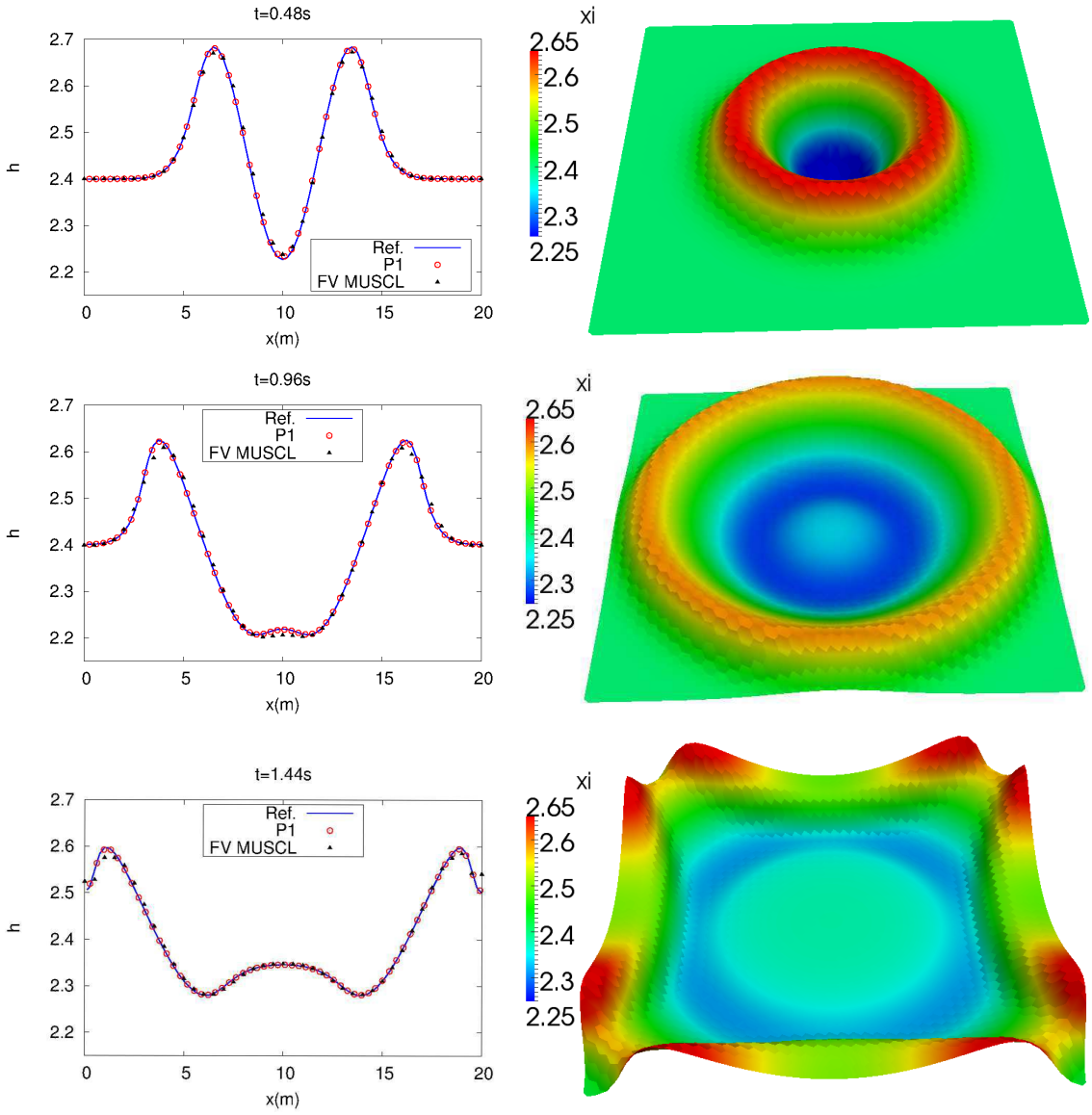

Figure IV .3: Collapsing of a Gaussian profile : Free surface profiles for the MUSCL M2 FVM and $\mathbb{P}^1$ approaches at t = 0.48, 0.96, 1.44 s along the middle section - Comparison with the reference solution (*left*). Corresponding 3d captures coming from the $\mathbb{P}^1$ scheme (*right*).

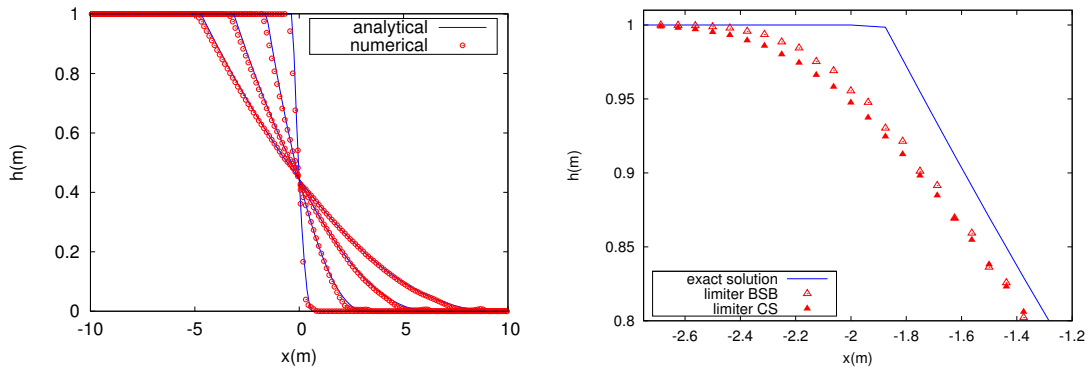

Figure IV .4: Dam break on a dry bed : Water depth profiles at t=0.1, 0.6, 1.2 and 1.8s. (*left*) - Zoom on the top at t=0.6s (*right*).

IV.4.2.a Dam break on a dry bed

Here, the computational domain is a $[-10, 10] \times [0, 4]$ rectangular basin, regularly meshed with 5 200 nodes. The initial condition is given by $h = 1$ and $\mathbf{q} = 0$ on the left part of the domain and $h = 0$ on the right part. We can observe on Fig. IV .4 (left) some water depth profiles during the evolution: they exhibit an excellent agreement with the analytical solution. The evolution of the wet/dry interface is accurately computed. For the records, the results are compared with those provided by the CS limiter. The discrepancies are almost indistinguishable at this level of zoom. We show zoom on Fig. IV .4 (right), focusing on the top part of the free surface profile at $t = 0.6\,s$. Although the discontinuity sensor is no longer active at this time, the limiting process engaged during the first steps to handle the initial discontinuity impacts the evolution of the flow. We observe a slight advantage of the BSB limiter.

IV.4.2.b Two-dimensional dam-break

We study now the ability of the scheme in dealing with discontinuities in a real 2d context. In this simulation, the computational domain is a square basin with dimensions 200×200, and the bottom is flat. The dam is located along the y-direction centreline, and the initial flow is supplied by a $75\,m$ breach on the dam wall, centred at $y = 125$. We consider an upstream water height of $10\,m$, while the initial downstream water level is fixed to $h_d = 5$. We run the simulation on an unstructured triangulation involving 13 000 nodes, until $t = 8\,s$. As shown in Fig. IV .5 (left), the propagation of the flood wave is properly described, and the stiffness of the water front profile is correctly handled by the limitation procedure. The numerical predictions are in good agreement with other results reported in the literature ([101, 141]), notably those provided in [281]. Lastly, we run again the simulation setting $h_d = 0$. We can observe on Fig IV .5 (right) a 3d view of the free surface at $t = 6.5\,s$ and highlight that the wet/dry interface is handled in a very robust way.

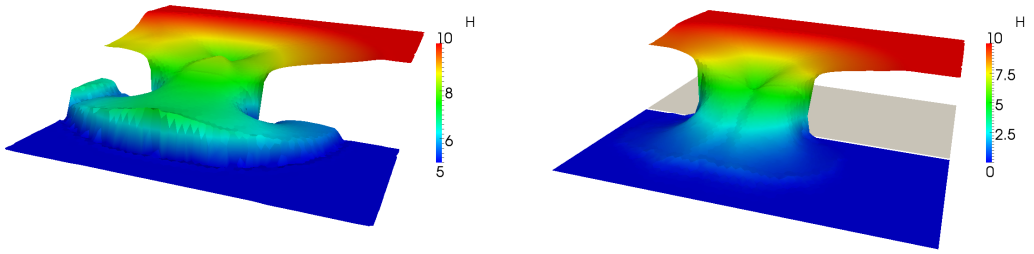

Figure IV .5: Two-dimensional dam break : Free surface profile at t=7.5s for $h_d = 5m$ (*left*), and at t=6.5s for $h_d = 0m$ (*right*).

	L^1	L^∞
e_η	0.264E-14	0.133E-14
e_{q_x}	0.101E-13	0.710E-14
e_{q_y}	0.813E-14	0.712E-14

Table IV .1: Preservation of a motionless steady state - Numerical errors at $t = 10\,s$.

IV.4.3 On steady states

We assess here the well-balanced property, together with the ability of the scheme to accurately describe the evolution of a small disturbance of a motionless steady state, with a varying topography. We conclude by the classical subcritical flow over a bump to study steady states in motion and perform some accuracy analysis.

IV.4.3.a Preservation of a motionless steady state

We first revisit the classical test case II.4.5 , considering a *lake at rest* configuration with a $1\,m$ total free surface on the whole computational domain. After a simulation time of $10\,s$, the motionless steady state is preserved up to the machine accuracy. We show the resulting numerical errors in Tab. IV .1 computed with the $\mathbb{P}^1$ scheme at $t = 10\,s$ for η and $\mathbf{q}$ in L^1 and L^∞ norms. Similar results are obtained with the third order scheme.

IV.4.3.b Perturbation of a motionless steady state

Second, as done in II.4.5 , we enforce an initial water height of 1.01 in the rectangular band $0.05 < x < 0.15$, and follow the motion of the flow until $t = 0.5\,s$. In this test we use a 3 321 elements mesh. We can observe on Fig. IV .6 a 3d view of the free surface as the flow reaches the top of the bump in the center of the basin. The whole propagation is not entirely depicted here since the profiles are very similar to those available in II.4.5 . Here again, we indeed obtain comparable results to those obtained in the literature with high order schemes ([46, 243, 288]),

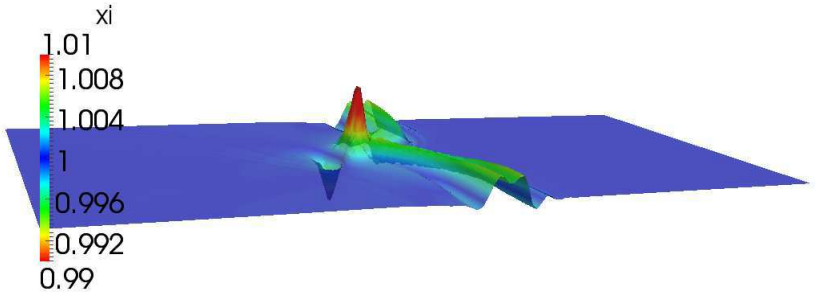

Figure IV .6: Perturbation of a motionless steady state : Snapshot of the free surface at $t = 0.3\,s$.

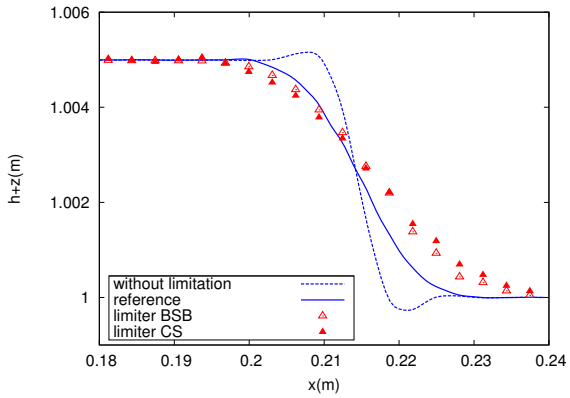

Figure IV .7: Perturbation of a motionless steady state : Zoom on the discontinuity at t = 0.015 s.

assessing an accurate computation of the propagation. Focusing on the way the initial discontinuity is handled, Fig. IV .7 shows the influences of both CS and BSB limiters. Like in IV.4.2.a , there is a small discrepancy arising from the choice of the limiting process used to handle the initial discontinuity. A slight improvement is observable with the use of BSB approach.

In a second time, we can observe on Fig. IV .8 some middle sections of the free surface profiles obtained with the $\mathbb{P}^1$ scheme as the flow is evolving over the bump. These results are compared with a reference solution, computed with the $\mathbb{P}^2$ scheme on a 20 000 nodes mesh, and those issued from the high order M2 FV scheme. The number of freedom degrees for the Finite Volume test is set to 10 000, so that a relevant comparison can be performed between the FV and dG approaches; the efficiency of the $\mathbb{P}^1$ dG approximation is similar to the MUSCL reconstruction method of the FV scheme for this test. The reader is referred to test cases IV.4.3.c and IV.4.4 for a more detailed comparison of the two methods.

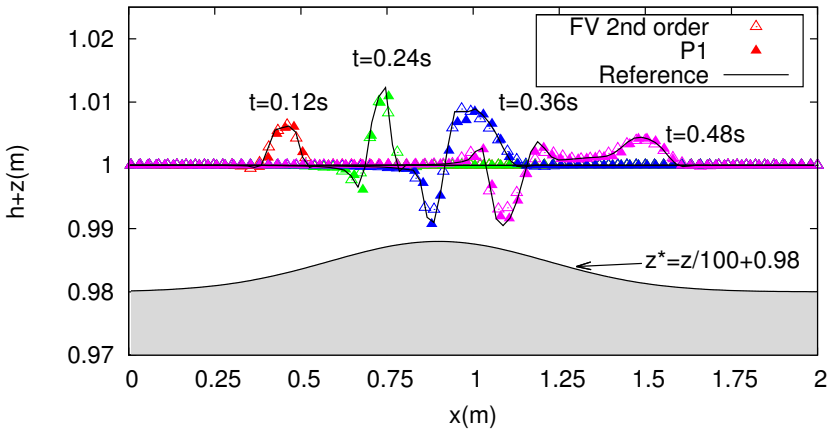

Figure IV .8: Perturbation of a motionless steady state : Vertical middle section at t = 0.12, 0.24, 0.36, 0.48 s. Comparison with the M2 Finite Volume scheme and the reference.

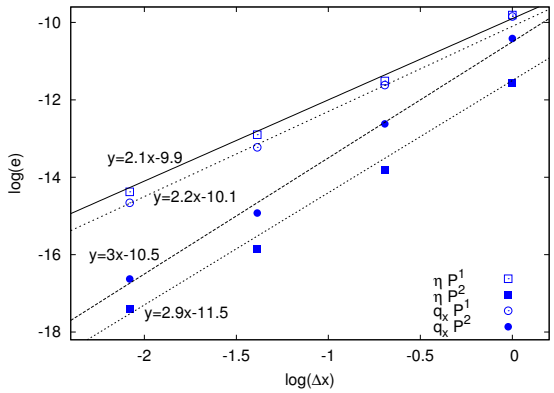

	h		hu	
Δx	$\mathbb{P}^1$	$\mathbb{P}^2$	$\mathbb{P}^1$	$\mathbb{P}^2$
1	0.55e-4	0.96e-5	0.53e-4	0.30e-4
0.5	0.10e-4	0.10e-5	0.90e-5	0.33e-5
0.25	0.25e-5	0.13e-6	0.18e-5	0.33e-6
0.125	0.57e-6	0.28e-7	0.43e-6	0.60e-7

Figure IV .9: Subcritical flow over a bump : Convergence analysis : L^1 numerical error for the free surface and the discharge.

IV.4.3.c Subcritical flow over a bump

We re-employ the test case already presented in II.4.2 . We thus intend to study the ability in converging toward a non trivial stationary state and propose additional convergence studies. Comparing numerical results with the analytical solution, we observe an excellent agreement for both free surface and normal discharge. The resulting figure is identical to the one obtained in the Finite Volume context (Fig. II .13). These results are provided by the $\mathbb{P}^1$ scheme on a mesh involving 800 elements. Concerning well balancing issues, this test also highlights the satisfying performance of the numerical scheme for the preservation of steady states involving flows in motion.

Afterwards we perform an accuracy analysis for the $\mathbb{P}^1$ and $\mathbb{P}^2$ schemes, considering regular meshes, with a discretization step $\Delta x = 20/n$ and an increasing level of refinement: $n = 20, 40, 80, 160$. At the end of the simulation, numerical results are compared to the analytical steady state allowing to com-

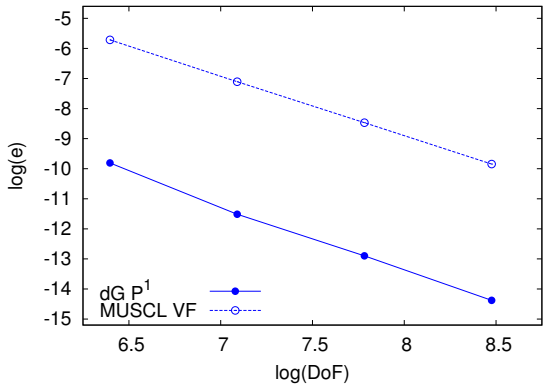

$\mathbb{P}^1$ dG		MUSCL-FV	
DoF	*h*	*DoF*	*h*
600	5.5e-5	750	3.3e-3
1200	1.0e-5	1470	8.2e-4
2400	2.5e-6	2910	2.1e-4
4800	5.7e-7	5790	5.3e-5

Figure IV .10: Subcritical flow over a bump : Comparison between $\mathbb{P}^1$ dG and MUSCL FV schemes : numerical error for an increasing number of DoF.

pute numerical errors for the free surface and the normal discharge. Fig. IV .9 shows the L^1-error with respect to the value of Δx in logarithmic scale. Optimal convergence is reached for both schemes.

To further investigate the comparison between the $\mathbb{P}^1$ dG scheme and the MUSCL M2 FV scheme, additional investigations are performed involving the total number of freedom degrees (DoF) and numerical errors. At $t = 150\,s$, we compute the L^1-error for an increasing number of DoF. Results are reported in Fig. IV .10 (right) and plotted on Fig. IV .10 (left) in a log-log scale. We focus on the water height, as similar observations stands for the discharge. We point out the performances of the $\mathbb{P}^1$ scheme, clearly more accurate for comparable DoF.

IV.4.4 Carrier and Greenspan transient solution

We use again the Carrier and Greenspan test case presented in II.4.7 to exhibit the ability of the scheme in describing complex flooding and drying phenomena. Computations involve the $\mathbb{P}^1$ scheme and numerical results are compared with the analytical solution. We use a regular triangulation with a space step fixed initially to $\Delta x = 0.5$. The flooding mechanism is still controlled by the offshore boundary condition given by $Vex(-20, y, t)$, and we observe again an asymptotic convergence towards the steady state with a planar free surface, observed at approximately $t = 40\,s$, see Fig. II .27 (bottom).

We show on Fig. IV .11 the evolution of the analytical and predicted free surface profiles along the middle section during the simulation; we can see an excellent description of the moving interface location. These results are in the same order of quality than those provided by the M2 Finite Volume approach (Fig. II .26). The 3d profiles are not reproduced here, being indistinct from Fig. II .27.

To evaluate accuracy performances, several computations are subsequently

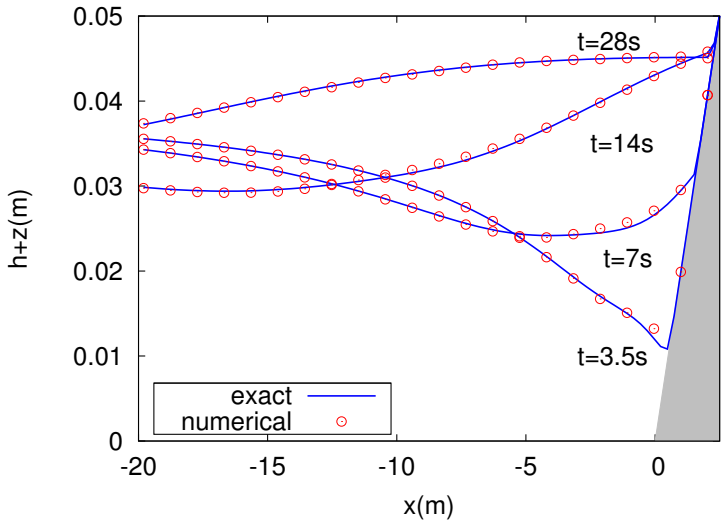

Figure IV .11: Carrier and Greenspan transient solution : Evolution of η along the x direction centreline.

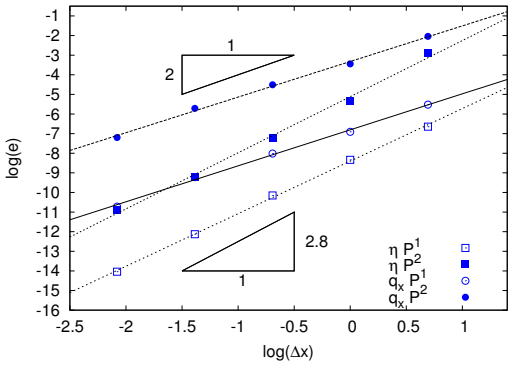

	h		hu	
Δx	$\mathbb{P}^1$	$\mathbb{P}^2$	$\mathbb{P}^1$	$\mathbb{P}^2$
2	4.0e-3	1.3e-3	1.3e-1	5.5e-2
1	1.0e-3	2.4e-4	3.2e-2	4.9e-3
0.5	3.3e-4	3.9e-5	1.1e-2	7.5e-4
0.25	9.9e-5	5.4e-6	3.3e-3	1.0e-4
0.125	2.2e-5	8.0e-7	7.5e-4	1.9e-5

Figure IV .12: Carrier and Greenspan transient solution : Convergence analysis : L^1 error for the free surface and the normal discharge.

run on a set of regular meshes with space step $\Delta x = 2/2^n, n = 0, \cdots, 4$, and the L^1 error is computed at $t = 0.1\,s$. As shown in Fig. IV .12, we reach rates of 2 and 2.8 respectively in the $\mathbb{P}^1$ and $\mathbb{P}^2$ case, for free surface and normal discharge.

As before, we further investigate the comparison between $\mathbb{P}^1$ dG and MUSCL FV schemes. The same analysis are performed, at $t = 0.5\,s$, and results are reported in Fig. IV .13. It is interesting to notice that even with the occurrence of the wet/dry fronts, the dG scheme provides the expected rates of convergence, whereas the MUSCL FV scheme only provides a convergence rate of 1.6 (see II.4.7). This clearly highlights the accuracy preserving feature of the strategy of [299]. However, unlike the previous test case, numerical errors are smaller for the MUSCL FV scheme, for comparable number of DoF.

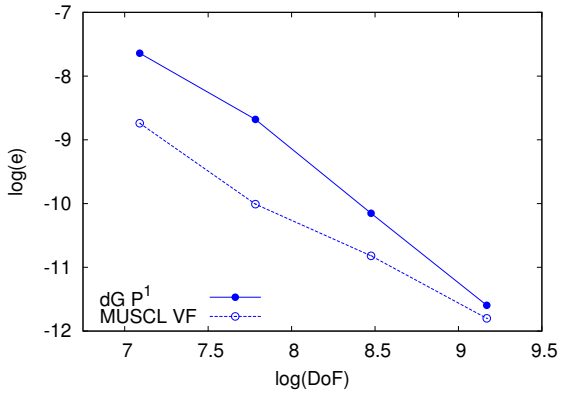

$\mathbb{P}^1$ dG		MUSCL-FV	
DoF	*h*	*DoF*	*h*
1200	4.8e-4	1470	1.6e-4
2400	1.7e-4	2910	4.5e-5
4800	3.9e-5	5790	2.0e-5
9600	9.2e-6	11550	7.5e-6

Figure IV .13: Carrier and Greenspan transient solution : Comparison between $\mathbb{P}^1$ dG and MUSCL FV schemes : numerical error for an increasing number of DoF.

IV.4.5 Tsunami wave on a conical island

We now consider a true two-dimensional case and study the propagation of a solitary wave over a conical island, based on laboratory experiments [198]. Several authors have used this test as a benchmark to study the run up phenomena [34, 151, 221, 243]. The basin dimensions are $[0,25] \times [0,30]$, and we use an unstructured triangulation involving 23 000 nodes. Denoting r the distance from the center of the domain, we consider an ideal island defined as follows :

$$z(r) = \begin{cases} \max\left(0.625, 0.9 - 1/(4\,r)\right) & \text{if } r < 3.6\,, \\ 0 \quad \text{elsewhere}\,. \end{cases}$$

We enforce an initial motionless configuration with a mean water depth $h_0 = 0.32$. The tsunami wave generation is supplied by a time dependent offshore boundary condition, as described in (III .28) :

$$\begin{cases} h(t) = h_0 + \alpha h_0 \operatorname{sech}^2\left(\dfrac{\sqrt{g h_0}}{L}\,\chi\, t\right), \\ \chi = \sqrt{\dfrac{3\alpha}{4\beta}\,(1+\alpha)}\,,\ \beta = (h_0/L)^2\,,\ L = 15\,,\ \alpha = 0.3\,. \end{cases} \tag{IV .33}$$

We follow the evolution of the solitary wave after the impact at the front side of the island, and observe that all the features of the propagation are properly reproduced, according to the data from the experiment. We can clearly observe on Fig. IV .14 the run up issuing from the reflection at the front of the island ; then, Fig. IV .15 shows that the separation in two secondary waves surrounding the island, and finally colliding at the rear side, is also accurately reproduced.

Lastly, we display in Fig. IV .16 time series of the free surface at several locations along the basin and the comparison between our numerical results and the data obtained from wave gauges shows reasonable agreement, qualitatively similar to the numerical results found in the references mentioned hereinabove.

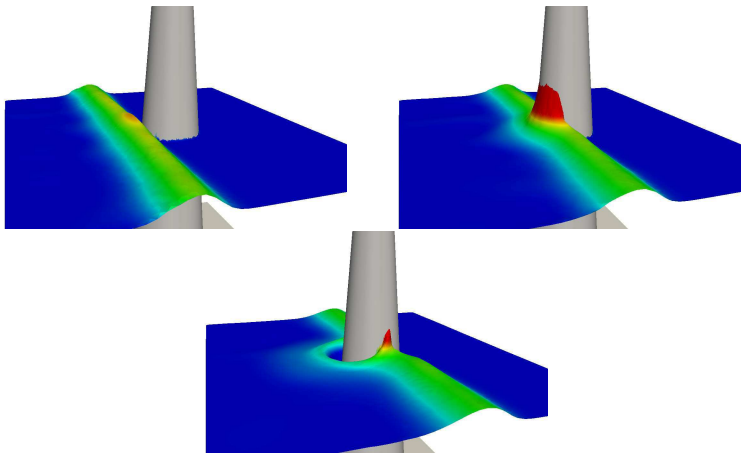

Figure IV .14: Tsunami wave over a conical island : Lateral view of the free surface at times t=5, 6 and 7s.

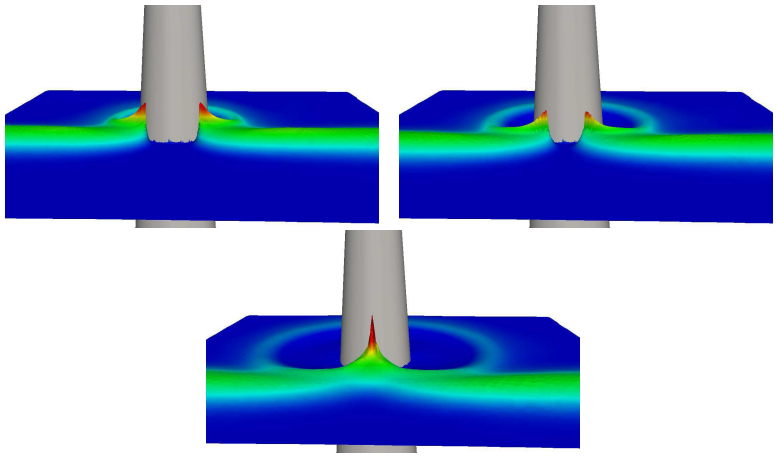

Figure IV .15: Tsunami wave over a conical island : Rear view of the free surface at times t=8, 9 and 10s.

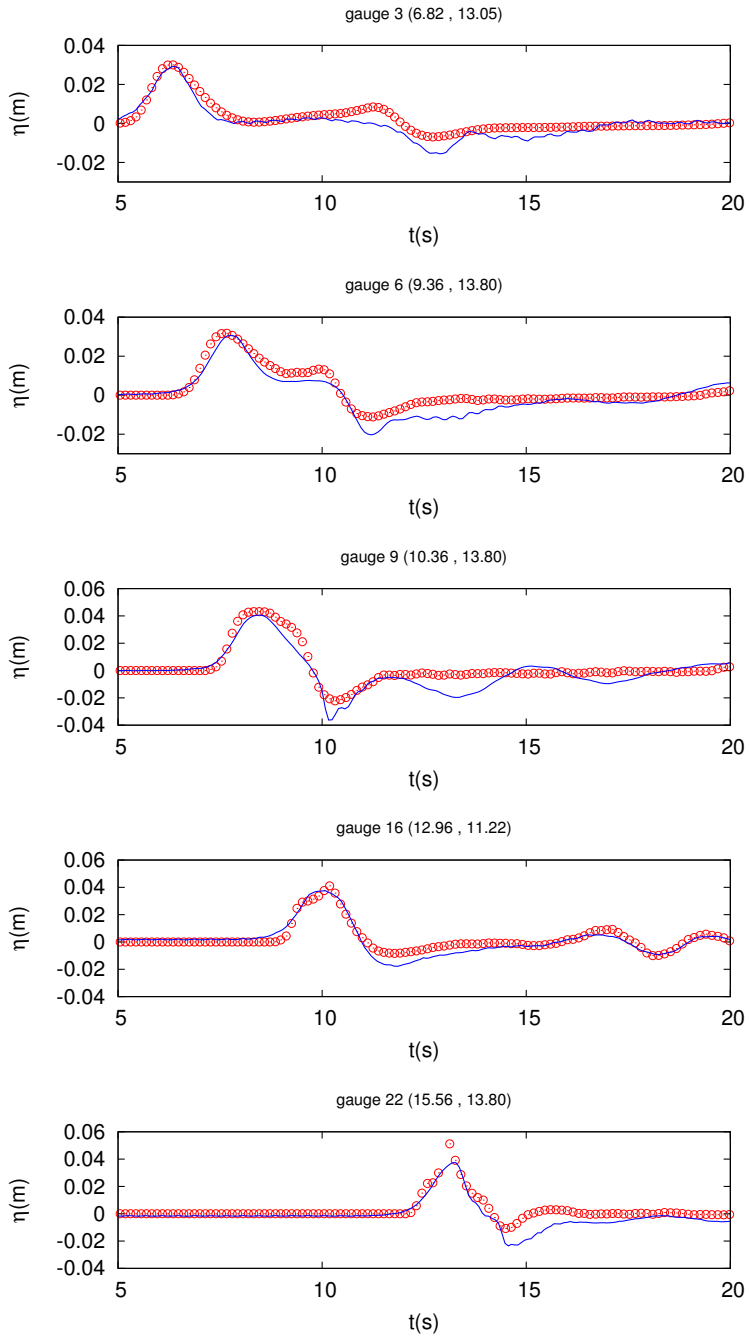

Figure IV .16: Tsunami wave on a conical island : Time history of the free surface at gauges 3, 6, 9, 16 and 22. Numerical (*dots*) vs experimental data (*solid lines*).

IV.4.6 Cox experience

In this test we compare our numerical results with experimental data issuing from the study carried out by Cox [82]. Our goal is to highlight the efficiency of the discontinuity sensor (IV .14) and the subsequent limitation process described in §IV.3.3 . This experiment was carried out in a wave flume of 33 m long. Waves were generated on a horizontal bottom at a depth $h_0 = 0.40$, shoaled and broke on a $1/35$ sloping beach. The wave height at the wave-maker is $a = 0.115$ and the period is $T = 2.2\,s$. Measurements of the surface elevation and velocity were taken at four locations along the basin. The simulation involves a domain with dimensions $[0, 8] \times [0, 1]$, regularly meshed with a space step $\Delta x = 0.01$. The first set of data is used as a time evolving inflow boundary condition at the left side of the domain, to simulate the wave-maker. In order to reproduce at best physical conditions, friction terms are considered through a Darcy law (III .2b), with a coefficient d calibrated at 0.01. According to the law under consideration and the value of d, this can be done straightforwardly by a direct approach, without particular fear of troubling wet/dry transitions with numerical noise. After 200 s of simulation approximatively, we obtain a regular sequence of breaking waves. We can observe a very good description of the wave distortion in the vicinity of the shoreline, with the expected sharped wave profiles. In order to demonstrate the good numerical description of the periodic process, time history of the free surface profiles at gauges $x = 1.2$, $x = 2.4$ and $x = 3.6$ are available on Fig. IV .17. We observe a good agreement with the data provided by Cox. In particular, it is worth emphasizing that the shock detector (IV .14) perfectly allows to capture the discontinuities generated during the breaking of the waves, activating the local limitation only in the steep wave front areas (see Fig. IV .18).

IV.4.7 Solitary wave on a sloping beach

We finally consider the two-dimensional problem of moving shoreline of Zelt [295] used in III.2.4.a . The basin is meshed with an unstructured triangulation of 15 000 elements. We mainly focus on the description of the run up and run down phenomena occurring when the wave reaches the shore. In Fig. IV .19, free surface snapshots are exhibited at several times during the flooding process. They follow closely the ones provided by the MUSCL Finite Volume approach (Fig. III .15). Again, due the lateral slopes, more pronounced, the flooding and drying process tends to concentrate the flow's energy in the center of the domain. Its evolution can be assessed on Fig. IV .20 through a focus at several cross sections regularly spaced, for both FV and dG *pre balanced* methods. Although each approach let express its own characteristics, we remark an good overall coherence with other published results. Maximum run-up and minimum run-down computed during the propagation are available on Fig. IV .21; these results highlight the robustness of the model and are in agreement with those observed in other works, see [151, 209, 227] for instance.

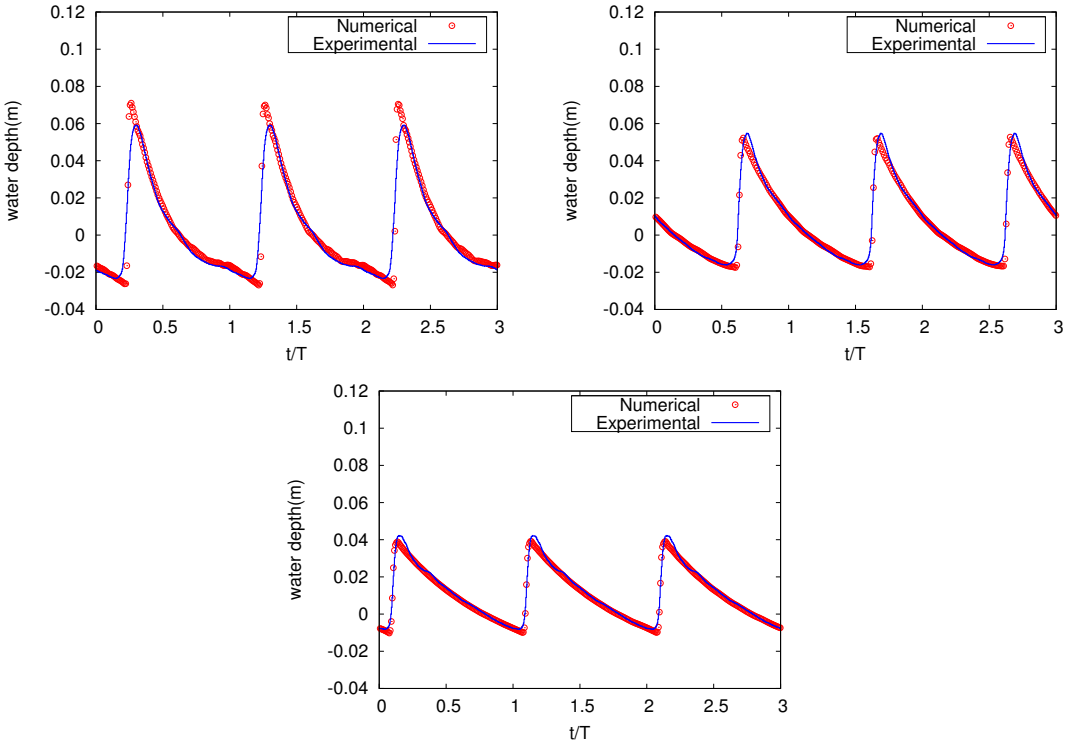

Figure IV .17: Cox experience : Time history of the water level at x=1.2, 2.4 and 3.6m.

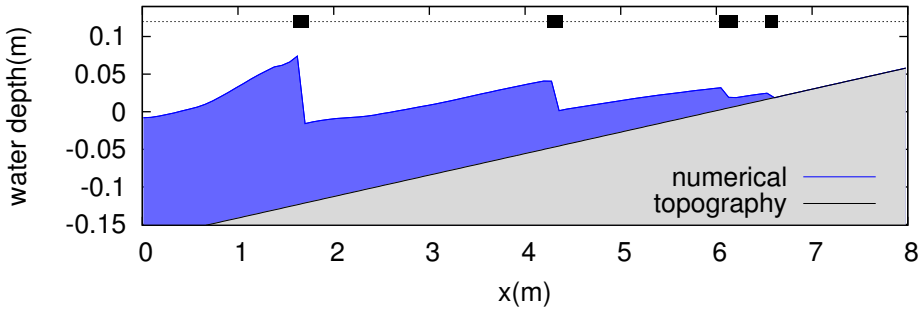

Figure IV .18: Cox experience : Snapshot of the water depth profile during the breaking process. Areas in need of limiting are specified along the dotted line.

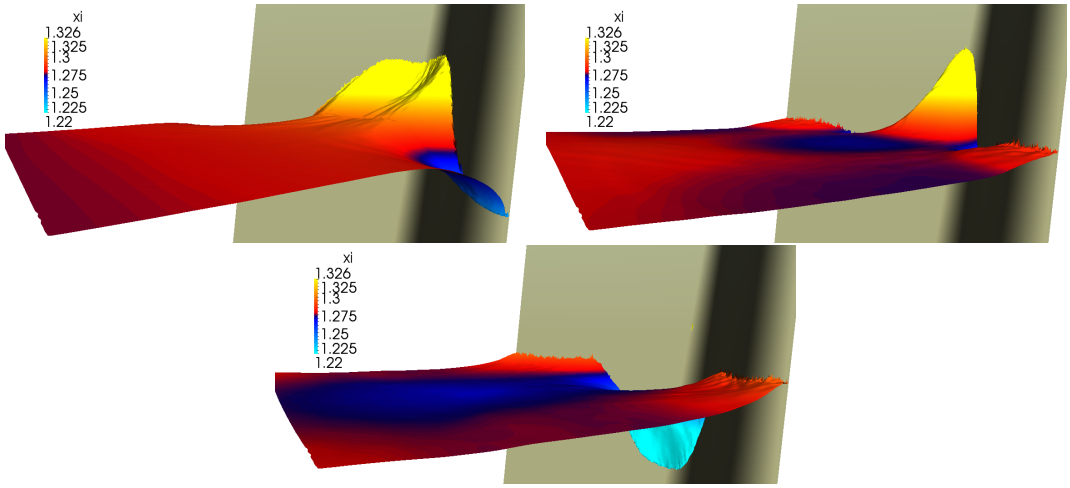

Figure IV .19: Solitary wave on a sloping beach : Free surface profiles at t=0, 11, 14 and 17s.

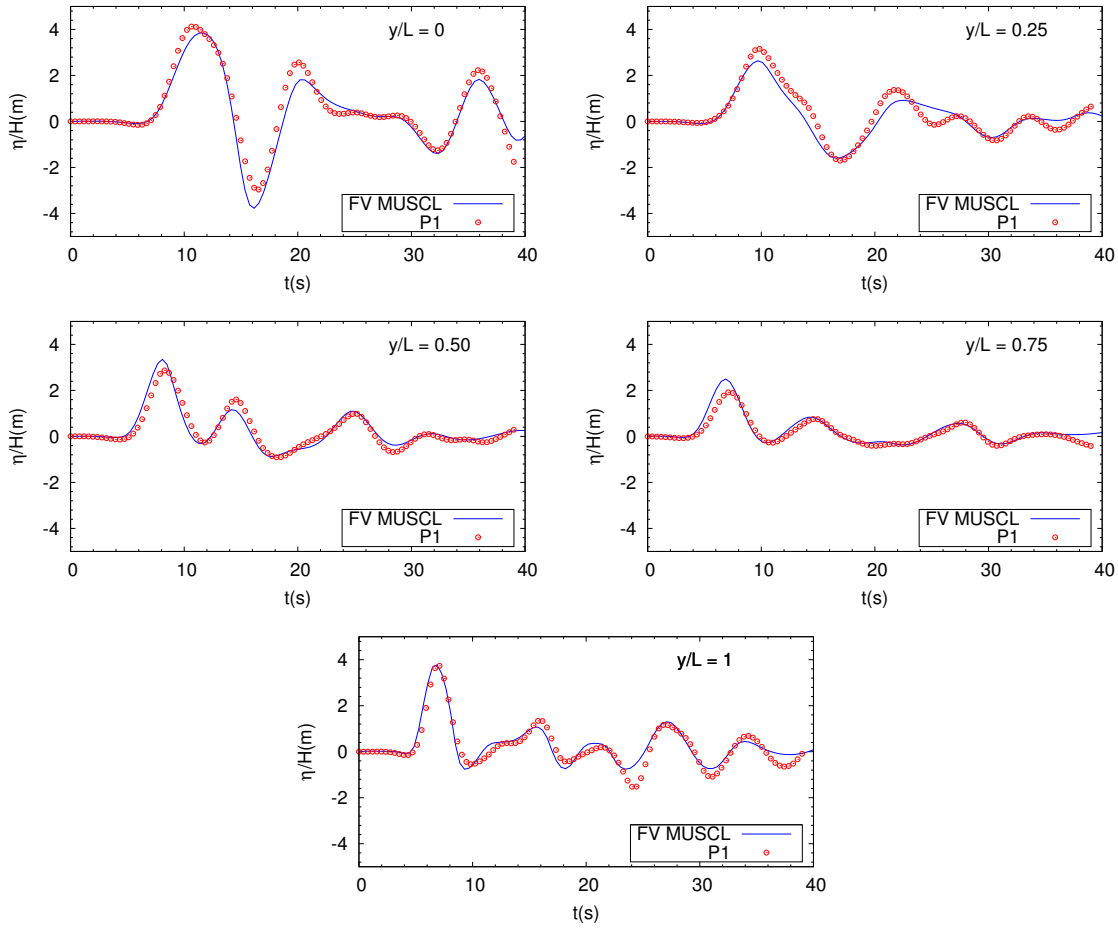

Figure IV .20: Solitary wave on a sloping beach : Time series of the run up along five cross sections.

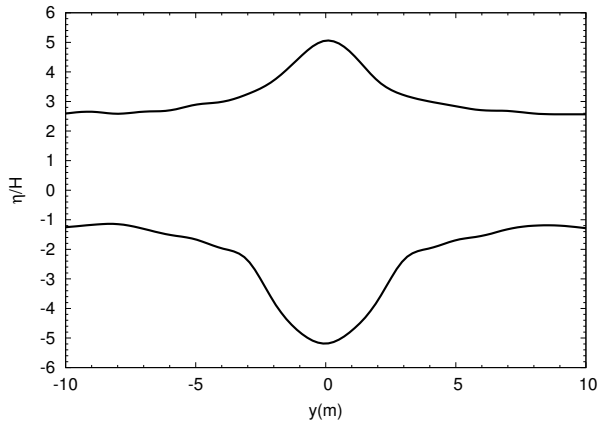

Figure IV .21: Solitary wave on a sloping beach : Maximum run up and minimum run down during the evolution.

IV.5 Conclusion

In this part, we perform a review of the existing dG methods for the Shallow Water equations and we focus on the issues of limiting, well-balancing and robustness. We then introduce a combination of ingredients leading to a robust and well-balanced discretization of the two dimensional NSW system with topography source term, on unstructured triangular grids. This well-balancing property is reached adapting the *pre balanced* Finite Volume method to the dG framework and the robustness is achieved adapting the ideas of [290] to the PBSW equations. An efficient shock detecting and local limitation process are implemented. The resulting scheme is shown to be accurate, stable and very efficient for the simulation of a large variety of flows involving flooding and drying phenomena.

The overall performances of the second order *pre balanced* dG scheme are shown to be slightly better than those offered by the MUSCL reconstructions. A more comprehensive study incorporating CPU time to the evaluation of relative error and DoF would be helpful to get a better idea of their relative effectiveness. This problem has to be broached carefully, since it mostly depends on implementing choices. Some additional works have been carried out to this end yet. Even if we did not clearly identify tendencies allowing to prefer one or other of the two methods in the general case, the $\mathbb{P}^1$ dG scheme seems to systematically provide better results for purely wet-type applications.

The objective now is to integrate these convenient features within a numerical approach for a more complex flow model, where higher order space derivatives are involved. Notably with the consideration of dispersive terms, we thus intend to extend the range of validity of our applications. These investigations are carried out in the 1d framework, and exposed in a last chapter.

Chapter V

The dGM applied to Green Naghdi equations

V.1 Introduction

Depth-averaged equations are widely used in coastal engineering for the simulation of nonlinear waves propagation and transformations in nearshore areas. The full description of surface water waves in an incompressible, homogeneous, inviscid fluid, is provided by the free surface Euler (or water waves) equations but this problem remains mathematically and numerically challenging. As a consequence, the use of depth averaged equations helps to reduce the three-dimensional problem to a two-dimensional problem, while keeping a good level of accuracy in many configurations.

As we already seen, the NSW equations belong this category, and are indeed of particular interest in many contexts, in that they avoid the complexity of the water waves equations and in the mean time offer a very respectable level of accuracy. In the light of their increasing interest within the scientific community, lots of numerical methods have been developed since the last decades to provide suitable approximations of NSW equations. Finite Volume Methods are generally preferred for their natural ability to handle the discontinuities that may arise from the hyperbolic structure of the model, but nowadays a large variety of different approaches can be found, based on Finite Differences Methods (FDM) or Finite Elements Methods (FEM) and we just illustrated the interest of discontinuous Galerkin Methods. Numerical challenges of paramount importance such as the problem of vanishing water heights, steady states preservation, or preservation of the water height positivity have been widely investigated. For all these reasons, the NSW model appears to be particularly well suited to reproduce a large class of unsteady processes connected to these numerical issues, notably wave breaking or free surface displacements with moving boundaries. In counterpart of their simple formulation, these equations do not include the dispersive terms of the full water waves equations. Such derivatives can be really important, in particular if we aim at giving a complete description of a shoaling process. Indeed, until initiation of wave breaking,

non-linear terms are playing an important role, and such a situation oversteps the range of validity of the NSW equations.

As an alternative, one can consider a more precise class of equations, often referred to as Boussinesq models in the literature. These models result from a more accurate derivation of the full water waves equations, in which high order non-linear and dispersion terms have not been neglected. Many Boussinesq like models are used nowadays and a detailed review can be found in [183] and the recent monograph [182]. Denoting by λ the typical horizontal scale of the flow and h_0 the typical depth, the shallow water regime usually corresponds to the configuration where $\mu := \dfrac{h_0^2}{\lambda^2} \ll 1$. If approximations of order $\mathcal{O}(\mu^2)$ of the free surface Euler equations are furnished by the Boussinesq-Type (BT equations in the following) equations, see [207, 224, 230] for instance, an additional smallness amplitude assumption on the typical wave amplitude a is classically performed: $\epsilon := \dfrac{a}{h_0} = \mathcal{O}(\mu)$. This assumption often appears as too restrictive for many applications in coastal oceanography. Removing the small amplitude assumption while still keeping all the $\mathcal{O}(\mu)$ terms, we obtain the so-called *Green Naghdi* equations (GN equations in the following) [137], also referred to as *Serre* equations [253] or *fully non-linear Boussinesq* equations [283]. Since these pioneering works, a large variety of models has been developed. One can now find lots of approaches with improved dispersive properties, such as [207, 224], or the recent enhancements [31, 70, 127, 204], allowing to significantly extend the domain of validity of the mathematical model.

It results from these works models asymptotically more accurate than the NSW equations, but their resolution is undeniably much more demanding. Regarding the methods classically employed to integrate GN equations, it is worthwhile to recall that in spite of their low computational cost and shock-capturing abilities, the FVM are not well-suited in the evaluation of high order derivatives, unlike more versatile methods such as FDM or FEM for instance. Some gradient reconstructions can be found in the literature to evaluate properly the dispersive components yet (see the FVM for 1d equations [100]), even on unstructured meshes, with the purely 2d FVM proposed in [94], or [165], allowing for mesh refinement and flexibility for large scale simulations. An alternative point of view is to combine the benefits of FDM and FVM in an hybrid method, such as those suggested in [168, 105, 258, 269, 226]: it allows a practical computation of the high order derivatives, enjoying in parallel the advantages of FVM in the integration of the conservative part. This being so, although appearing as a natural choice, incorporating a Finite Volume scheme at this stage is not an absolute necessity. Let us mention for instance some purely FDM [204, 224, 260, 283] and FEM [193, 244, 261].

As far as flexibility is concerned, the use of discontinuous-Galerkin methods would appear as a natural choice. Indeed, it is useful to recall that this class of method provides several appealing features, like compact discretization

stencils and hp-adaptivity, flexibility with a natural handling of unstructured meshes, easy parallel computation and local conservation properties in the approximation of conservation laws. This is a considerable asset when dealing with the challenging numerical problem we are interested in. Concerning the approximation of general problems, involving higher-order derivatives, several methods and important developments have been proposed in recent years, following [17] on Navier-Stokes equations and [77] on convection-diffusion systems. A recent review is performed in [292] and a unified analysis can be found in [9], and [106, 107], respectively for elliptic problems and both 1^{st} and 2^{nd} order problems in the framework of Friedrichs' systems.

The application of dG methods to the NSW equations has recently lead to several improvements. However, dG methods for BT equations have been under-investigated. In [109], a *hp*/spectral element model is introduced for the 1d enhanced equations of Nwogu [224], while the 2d equations of Peregrine [230] are studied in [111], in the flat bottom case, relying on a scalar reformulation that allowed some computational savings. This formulation is further investigated in [112], accounting for variable depth, and in [113] with the study of the enhanced equations of Madsen and Sorensen [206]. In [103, 104], an arbitrary order nodal dG-FEM method is developed for the set of highly-dispersive BT equations introduced in [205], respectively in 1d and 2d on unstructured meshes. These equations have a larger range of validity and can theoretically model fully nonlinear waves transformation, but they are also more complex, introducing a dependence in the vertical velocity, and consequently additional degrees of freedoms in the discrete approximations. As stated by the authors themselves, the bottleneck of their approach lies in the need of reconstruction and resolution of the large associated linear systems: this process can rapidly become a drawback for large-scale simulations.

Surprisingly, the GN equations have received far less attention. In the 1d framework and formulated in terms of free-surface elevation above the still water depth ζ and horizontal velocity u, these equations read as follows (see [3, 37] for the derivation of this particular formulation) :

$$\left\{\begin{array}{l} \partial_t\zeta + \partial_x(hu) = 0\,, \\ \Big[1+\alpha\mathbb{T}[z,h]\Big]\Big(\partial_t(hu)+\partial_x(hu^2)+\dfrac{\alpha-1}{\alpha}gh\partial_x\zeta\Big)+\dfrac{1}{\alpha}gh\partial_x\zeta+h\mathcal{Q}_1(u)=0\,, \end{array}\right. \tag{V.1}$$

with the differential operators

$$\mathcal{Q}_1(u) = 2h\partial_x h(\partial_x u)^2+\frac{4}{3}h^2\partial_x u\partial_x^2 u\,+h\partial_x z(\partial_x u)^2+h\partial_x^2 z\,u\partial_x u+\big(\partial_x\zeta\partial_x^2 z+\frac{h}{2}\partial_x^3 z\big)u^2, \tag{V.2}$$

and $\mathbb{T}[z,h] = h\mathcal{T}[z,h]\dfrac{1}{h}$, with for any scalar valued function w :

$$\mathcal{T}[z,h]w = -\frac{h^2}{3}\partial_x^2 w - h\partial_x h\partial_x w + \big(\partial_x\zeta\partial_x z+\frac{h}{2}\partial_x^2 z\big)w\,, \tag{V.3}$$

Here, z still stands for the parametrization of the bottom variations, and $h = \zeta + h_0 - z$ refers to the water height (see Fig. V .1). In fact, the family of equations (V .1) indexed by the optimization parameter $\alpha \geq 1$ is derived from the original formulation, available in [183, 182] for instance, issuing from a $\mathcal{O}(\mu^2)$ approximation of the full water waves equations. The parameter α is introduced to reach more adequate dispersion relations, entailing the introduction of additional terms of order $O(\mu^2)$ to the momentum equations, which consequently does not affect the precision of the model. In the continuity of this work, the three parameters model developed by Chazel *et al* [70] provides another advancement of the dispersive properties.

As regards numerical studies on GN equations, a compact FVM approach is proposed for the 1d case in [74] and a FVM for a particular 2d flat bottom system in [213]. A pseudo-spectral approach is introduced in [229] and FEM discretization in [214] for the 1d case on flat bottom. To the authors knowledge, the only dG method for GN equations has been recently proposed in [191], for the 1d equations with uneven bottom, relying on a centered dG approach and applications with second-order polynomial approximations. The issue of robustness is however not addressed. In [37, 70, 268], a high-order accurate hybrid FVM-FDM model is introduced, embedded in a splitting approach. A robust treatment of moving shoreline and well-balancing for motionless steady states are ensured. The 2d extension on cartesian meshes has recently been performed in [184]. Let us also mention [72] and more recently [254] for a 2d cartesian numerical model based on fully non-linear BT equations of [283]. However, it would appear that no arbitrary order dG discretization of the GN equations has been proposed yet, and this is one of the goals of this work.

Although GN equations provide a good description before the breaking point, they are unable to correctly describe some phenomena of central interest in wave modelling such as breaking waves notably. As a consequence, they cannot be considered either as an entirely satisfactory model for nearshore flows simulation. To amend this limitation, several approaches have been proposed. An interesting idea is to introduce artificial viscosity in the momentum equations [72, 167, 296] to modelize the energy dissipation caused by wave breaking. This is also the method chosen in [104], embedded in the nodal-dG method. Although being generally satisfactory, the weakness of the aforementioned *ad hoc* methods stands in the necessity of an appropriate scaling of several physical constants. Now, most of these parameters revolve around well established reference values, but the persisting complexity of wave breaking processes makes the elaboration of a universal calibration far from being obvious yet. As mentioned by Cienfuegos *et al* [76], the resolution remains sensitive to the way dissipation parameters are fixed, and can lead to incongruous results in some cases.

Considering the general features assigned to NSW and GN equations, an alternative approach to handle broken waves, which is gaining popularity, consists of proposing a way to unify the benefits of the two mathematical models

in their respective domain of physical validity. From a schematic point of view, the objective is to use the GN equations in the shoaling zone up to the initiation of wave breaking, and handle propagation of shocks with the NSW equations. Indeed, NSW equations actually provide a good description of broken waves [35], which are regarded as shock waves, and can therefore be accurately computed using shock-capturing methods. To achieve this, one can naturally plan to skip the dispersive terms in the vicinity of shocks, keeping in mind that the GN system naturally degenerates into Shallow Water equations when these terms are neglected. This switching strategy can be performed in a very simple fashion, provided the dispersive BT or GN equations are written in conservative forms. This strategy is employed in [37, 226, 271] for instance. Naturally, the method requires the introduction of a system of numerical criteria devoted to identify the general characteristics of wave breaking, and eventually follow broken waves to detect if a "switch-back" to dispersive equations is needed. In [269] a criterium relying on the wave height to water depth ratio is introduced and subsequently used in [270] and [254] for instance. Another criterium based on the momentum gradient is successfully used in [246]. In [268], the problem of breaking waves is handled through a relevant combination of three criteria involving the local energy dissipation, front slope and Froude number. Here again, the method requires some critical values to be calibrated, but their choice is governed by specific physical considerations, and is not particularly problematic. Actually, the main drawback is the potential appearance of oscillations in the transition areas, especially when high order methods or refined meshes are used. Let us also mention the recent 2d approach of [166] for some applications and additional studies regarding wave breaking.

Among the tools available in shock detection, one can mention the strong super-convergence criteria (IV .14) introduced by Krivodonova [174], and successfully involved in the preliminary step of the limiting procedure to detect occurrence of discontinuities in our 2d *pre balanced* dG scheme (see also [108]). According to its efficiency in discriminating areas in need of limiting, it may appear relevant to handle wave breaking by the mean of this criteria. Such an objective is reached here. As in [258, 271], the dispersive part of the system is written as an additional source term of the NSW equations; it results from this decomposition a very convenient way to shift from GN to NSW equations, and motivates the use of a switching strategy rather than an *ad hoc* technique. The shock indicator is used to detect steep wave fronts and locally suppress the dispersive effects, and the corresponding shock waves are subsequently computed using the natural shock-capturing abilities of the dG approach, combined with an efficient local limiting process. Note that the hybrid FDM/FVM approaches proposed in [37, 70, 268] have been developed in this spirit : the solution operator associated with the dispersive part is straightforwardly exhibited, and locally switched off depending if the breaking criteria is activated or not. The proposed work follows a similar methodology, avoiding the possible limitations of a splitting algorithm.

Contribution and objectives

In the present work, we describe a strategy to compute discontinuous-Galerkin approximations of the solutions of some one-dimensional GN equations, including an efficient wave-breaking method. Indeed, the use of such *fully nonlinear* equations appear as a reasonable compromise between the *weakly non-linear* equations studied in [111, 112] and the *highly-dispersive* (and computationally costly) three-variables equations investigated in [103, 104]. Additionally, it is easily possible to extend the range of validity of the GN equations to moderately deep water by the introduction of some optimization parameters, as shown in [70, 184]. A closer look to equations (V .1) highlights that, if this formulation has real advantages (*i.e.* it does not involve any third order derivatives, and the presence of the second-order operator $1 + \alpha\mathbb{T}[z,h]$ makes the model very stable with respect to high frequency perturbations, see [37]), its main drawback is the *time-dependency* of this operator, through the water height h. Indeed, on computational aspects, the dG discretization of $1 + \alpha\mathbb{T}[z,h]$ with a *Local Discontinuous Galerkin* approach [77] for higher order derivatives, and the associated linear system resolution, implies a global assembly process, for gathering the local discrete operators into the global one. And this should be done at each time step, or even sub step if high order time marching algorithms are used, together with the corresponding algebraic system resolution.

To overcome this, the strategy recently proposed in [184], and also applied here, consists of using a new class of GN equations, asymptotically equivalent to the formulation (V .1) but for which the time dependency of the operator $I + \alpha\mathbb{T}[z,h]$ is removed. The resulting model shares the same level of accuracy with the original GN equations, with respect to the approximation of the full water waves equations, but allows to build the global discrete operator in a pre-processing step. This operator is then used throughout all the computation, leading to dramatic computational savings. As a consequence, the computational effort can be oriented towards a high order of accuracy in space and time, and the enforcement of some essential robustness properties. An arbitrary order of accuracy in space is obtained through the use of the Legendre polynomials hierarchical basis, and low storage SSP-RK schemes (IV.3.5) are used for the time discretization. The whole model is shown to exactly preserve the motionless steady states, thanks to the *pre-balanced* reformulation of the surface gradient term and suitable interface fluxes, and a robust treatment is implemented for the moving shoreline, based on the enforcement of an element-wise water height positivity preservation property, borrowing again the recent accuracy-preserving method introduced for the dGM in [291, 298].

To summarize, the main features of the 1d dG-based GN numerical model described in this work are :

♯ 1 an improved computational efficiency when compared to the original equations (V .1), due to the *time-independency* of the involved regularizing second order dispersive operator,

♯ 2 an *arbitrary order* of spatial accuracy,

♯ 3 a *well-balanced* property for the motionless steady states,

♯ 4 a *robust treatment of the shoreline* motions,

♯ 5 an efficient and simple way of *handling broken waves*, based on a GN/NSW equations switching strategy.

This work lead to the recent article [-5-].

The study is organized as follows: in a first part we introduce the new family of 1d GN models with time-independent dispersive operator. The second part is devoted to the description of a robust arbitrary order of accuracy nodal dG approach for this family of model. The emphasize is put on the discretization of the higher order derivatives. Based on the 2d dG scheme, we then rapidly treat the well-balanced and robustness properties, and detail the switching strategy. Finally, the performances of the resulting numerical model are assessed through extensive 1d numerical validations. Two-dimensional validations are left for future works.

V.2 Governing equations

In this section, we detail the simplified new class of GN equations for which the *time dependency* of the second-order differential operator $1+\alpha\mathbb{T}[z,h]$ is amended. Choosing h_0 a reference water depth, we recall that $\zeta(x,t)$ stands for the free surface elevation, $z(x)$ the variation of the bottom with respect to the rest state, $u(x,t)$ the horizontal velocity, and $h(x,t)=\zeta(x,t)+h_0-z(x)$ the water height (see Fig. V .1).

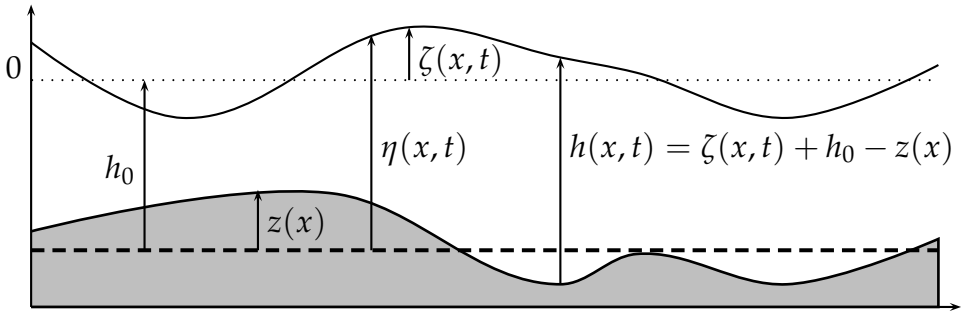

Figure V .1: 1d configuration

These equations have recently been derived in [184] in the 2d frame and their 1d formulation reads as follows (see also [-5-]) :

$$\begin{cases} \partial_t\zeta+\partial_x(hu)=0\,, \\ \big[1+\alpha\mathfrak{T}[h_b]\big]\Big(\partial_t hu+\partial_x(hu^2)+\dfrac{\alpha-1}{\alpha}gh\partial_x\zeta\Big)+\dfrac{1}{\alpha}gh\partial_x\zeta \\ \qquad\qquad +h\big(\mathcal{Q}_1(u)+g\mathcal{Q}_2(\zeta)\big)+g\mathcal{Q}_3\Big(\big[1+\alpha\mathfrak{T}[h_b]\big]^{-1}(gh\partial_x\zeta)\Big)=0\,. \end{cases} \tag{V .4}$$

The operator $\mathcal{Q}_1$ is obtained from (V .2), and :

$$\mathcal{Q}_2(\zeta)=-\big(\partial_x\zeta\partial_x z+\frac{h}{2}\partial_x^2 z\big)\partial_x\zeta\,. \tag{V .5}$$

For a given scalar function w, the operator $\mathfrak{T}$ is defined as follows :

$$\mathfrak{T}[h]w=-\frac{h^3}{3}\partial_x^2\left(\frac{w}{h}\right)-h^2\partial_x h\partial_x\left(\frac{w}{h}\right)\,, \tag{V .6}$$

and $\mathcal{Q}_3$ admits the simplified notation :

$$\mathcal{Q}_3(w)=\mathcal{Q}_3[h^2-h_b^2]w=\frac{1}{6}\partial_x(h^2-h_b^2)\partial_x w+\frac{h^2-h_b^2}{3}\partial_x^2 w-\frac{1}{6}\partial_x^2(h^2-h_b^2)w\,, \tag{V .7}$$

where h_b corresponds to the initial state :

$$h_b=\max(h-\zeta,\epsilon_b)\,. \tag{V .8}$$

Remark V.2 .1. *The use of ϵ_b in (V .8) is only to ensure that the new quantity h_b remains positive in dry areas and preserves the regularization properties of $1+\alpha\mathfrak{T}[h_b]$. It obviously does not modify the consistency of the model, and our numerical investigations did not show any dependency of the results with respect to the (reasonable) value of ϵ_b. In the validations of §V.4 we use $\epsilon_b = 0.1$.*

Before describing in details the dG discretization of (V .4), let us reformulate the model under the *pre-balanced* formulation, to adapt the dG well-balanced scheme previously introduced. In 1d, the splitting relying on the use of the total free surface elevation $\eta = h + z$ can be written as (see Fig. V .1) :

$$gh\partial_x\eta = \frac{1}{2}g\partial_x(\eta^2 - 2\eta z) + g\eta\partial_x z\,, \tag{V .9}$$

leading to the following formulation of the NSW system :

$$\partial_t V + \partial_x H(V,z) = S(V,z)\,, \tag{V .10}$$

with $V = {}^t(\eta, q)$, $q = hu$ and

$$H(V,z) = \begin{pmatrix} H^\eta(V) \\ H^q(V,z) \end{pmatrix} = \begin{pmatrix} q \\ uq + p(\eta,z) \end{pmatrix},\ S(V,z) = \begin{pmatrix} S^\eta(V) \\ S^q(V,z) \end{pmatrix} = \begin{pmatrix} 0 \\ -g\eta\partial_x z \end{pmatrix}, \tag{V .11}$$

and the hydrostatic pressure term now expressed as :

$$p(\eta,z) = \frac{1}{2}g\eta(\eta - 2z)\,.$$

We recall that the velocity is computed from $u = \frac{q}{\eta - z}$ in the above relations. Using dG approximations for NSW equations, we can reproduce the strategy presented in the 2d frame, to obtain the balance between fluxes and topography source term, provided that the corresponding integral terms are computed exactly. To benefit from this property for the GN equations, we notice that using (V .9), the second equation of (V .4) can be equivalently written as follows :

$$\partial_t q + \partial_x\big(uq + p\big) + \mathfrak{D}_c(\eta,u) = -g\eta\partial_x z\,, \tag{V .12}$$

with

$$\begin{aligned}\mathfrak{D}_c(\eta,u) = \big[1+\alpha\mathfrak{T}[h_b]\big]^{-1}\Big(&\frac{1}{\alpha}gh\partial_x\eta + h\big(\mathcal{Q}_1(u) + g\mathcal{Q}_2(\eta)\big) \\ &+ g\mathcal{Q}_3\big(\big[1+\alpha\mathfrak{T}[h_b]\big]^{-1}(gh\partial_x\eta)\big)\Big) - \frac{1}{\alpha}gh\partial_x\eta\,,\end{aligned} \tag{V .13}$$

Remark V.2 .2. *The original system (V .1) can of course also be written as follows :*

$$\partial_t q + \partial_x(uq + p) + \mathfrak{D}_o(\eta,u) = -g\eta\partial_x z\,, \tag{V .14}$$

with

$$\mathfrak{D}_o(\eta,u) = \Big[1+\alpha\mathbb{T}[z,h]\Big]^{-1}\Big(\frac{1}{\alpha}gh\partial_x\eta + h\mathcal{Q}_1(u)\Big) - \frac{1}{\alpha}gh\partial_x\eta\,. \tag{V .15}$$

From this, equations (V .1) and (V .4) are nothing but the *pre-balanced* NSW equations (V .10) supplemented by a dispersive source term :

$$\partial_t V + \partial_x H(V,z) = S(V,z) + \mathfrak{D}(V)\,, \tag{V .16}$$

with

$$\text{model (V .1)} \quad : \quad \mathfrak{D}(V) = \begin{pmatrix} 0 \\ -\mathfrak{D}_o(\eta,u) \end{pmatrix}, \tag{V .17a}$$

$$\text{model (V .4)} \quad : \quad \mathfrak{D}(V) = \begin{pmatrix} 0 \\ -\mathfrak{D}_c(\eta,u) \end{pmatrix}. \tag{V .17b}$$

V.3 Discontinuous Galerkin discretization

To implement a discontinuous Galerkin scheme, let $\mathcal{P}$ be a partition of the computational domain $\Omega = [L,R]$ into N_e non-overlapping elements, denoted $C_i, 1 \leq i \leq N_e$. The element $C_i = [x_i^l, x_i^r]$ has a length $|C_i|$ and a boundary ∂C_i (reduced to the 2 boundary nodes x_i^l and x_i^r). Let x be the coordinate in Ω and we denote $\mathfrak{h} = \max\limits_{1\leq i\leq N_e} |C_i|$. We aim at computing an approximated solution, denoted $V_\mathfrak{h} = (\eta_\mathfrak{h}, q_\mathfrak{h})$, on this partition. Let us define :

$$\mathcal{V} := \{v \in L^2(\Omega)\,|\,\forall C \in \mathcal{P}\,,\, v_{|C} \in \mathbb{P}^N(C)\}\,, \tag{V .18}$$

where $\mathbb{P}^N(C)$ denotes the space of polynomials in C of degree at most N. We consider only the new model (V .4) but the subsequent weak formulation and discretization can of course be straightforwardly applied to the original model (V .1).

V.3.1 Weak formulation

Due to the number of terms and derivatives (up to 3^{rd} order) involved in the dispersive source term $\mathfrak{D}_c(\eta,u)$, trying to write equation (V .12) as a first-order system, with the use of several auxiliary variables, would only bring up some unnecessary complexity in the formulation. Instead, we reformulate (V .16, V .17b) as follows :

$$\partial_t \eta + \partial_x q = 0\,, \tag{V .19a}$$

$$\partial_t q + \partial_x\big(uq + p\big) + \mathcal{A} = -g\eta\partial_x z\,, \tag{V .19b}$$

with $\mathcal{A}$ is an auxiliary scalar valued variable, obtained as the solution of the following auxiliary problem :

$$\big[1 + \alpha\mathfrak{T}[h_b]\big]\big(\mathcal{A} + \frac{1}{\alpha}gh\partial_x\eta\big) = \mathcal{K}\,, \tag{V .20a}$$

$$\mathcal{K} = \frac{1}{\alpha}gh\partial_x\eta + h\big(\mathcal{Q}_1(u) + g\mathcal{Q}_2(\eta)\big) + g\mathcal{Q}_3(\mathcal{X})\,, \tag{V .20b}$$

$$\big[1 + \alpha\mathfrak{T}[h_b]\big]\mathcal{X} = gh\partial_x\eta\,. \tag{V .20c}$$

From this, a weak formulation of the problem (V .19) is obtained by multiplying by test functions $(\phi, \pi) \in (\mathcal{V})^2$ and integrating over a given element C_i. The flux term is integrated by parts and the problem becomes :

Find $V_\mathfrak{h} = (\eta_\mathfrak{h}, q_\mathfrak{h}) \in (\mathcal{V})^2$ *such that,* $\forall (\phi, \pi) \in (\mathcal{V})^2$, *and* $\forall\, C_i \in \mathcal{P}$ *we have :*

$$\int_{C_i} \partial_t \eta_\mathfrak{h} \phi dx - \int_{C_i} H^\eta(V_\mathfrak{h}, z_\mathfrak{h}) \frac{d}{dx}\phi \, dx + \left[H^\eta(V_\mathfrak{h}, z_\mathfrak{h})\phi\right]_{x_i^l}^{x_i^r} = 0, \tag{V .21}$$

$$\int_{C_i} \partial_t q_\mathfrak{h} \pi dx - \int_{C_i} H^q(V_\mathfrak{h}, z_\mathfrak{h}) \frac{d}{dx}\pi \, dx + \left[H^q(V_\mathfrak{h}, z_\mathfrak{h})\pi\right]_{x_i^l}^{x_i^r} = \int_{C_i} S^q(V_\mathfrak{h}, z_\mathfrak{h})\pi dx - \int_{C_i} \mathcal{A}\pi dx \,. \tag{V .22}$$

V.3.2 Semi-discrete formulation

On each element C_i, we write $\forall x \in C_i, \forall t \in [0, t_{max}]$:

$$\eta_i := \eta_{\mathfrak{h}|C_i}(x,t) = \sum_{l=1}^{N_d} \eta_i^l(t)\theta_i^l(x) \;, \quad \text{and} \quad q_i := q_{\mathfrak{h}|C_i}(x,t) = \sum_{l=1}^{N_d} q_i^l(t)\theta_i^l(x) \;, \tag{V .23}$$

where $N_d = N + 1$ is the number of freedom degrees per element, $\{\theta_i^l\}_{l=1\ldots N_d}$ is a polynomial expansion basis for $\mathbb{P}^N(C_i)$, and

$$\tilde{\eta}_i = {}^t(\eta_i^1(t), \ldots, \eta_i^{N_d}(t)), \qquad \tilde{q}_i = {}^t(q_i^1(t), \ldots, q_i^{N_d}(t)),$$

are the local expansion coefficients vectors. In the following, $\{\theta_i^l\}_{l=1,\ldots,N_d}$ refers to the local Lagrange interpolating polynomial basis on the element C_i, defined on the *Legendre-Gauss-Lobatto (LGL)* set of N_d nodes (a *nodal-element* basis).

Remark V.3 .1. *It should be stressed that one can also consider a modal decomposition basis :*

$$\eta_i = \sum_{n=1}^{N_d} \mathring{\eta}_i^n(t) P_{n-1}(x) \quad , \quad q_i = \sum_{n=1}^{N_d} \mathring{q}_i^n(t) P_{n-1}(x)$$

where, $\{P_0, \cdots, P_{N_d-1}\}$ *is the basis associated with the Legendre polynomials. For a generic scalar component* w *the connexion between the freedom degrees coefficients stocked in the vectors* $\tilde{w}_i = {}^t(w_i^1(t), \ldots, w_i^{N_d}(t))$ *and* $\mathring{w}_i := {}^t(\mathring{w}_i^1(t), \ldots, \mathring{w}_i^{N_d}(t))$ *is governed by the following relation :*

$$\tilde{w}_i = \mathbf{V}_i \mathring{w}_i \,,$$

where the coefficients of the Vandermonde matrix $\mathbf{V}_i$ *are defined via :*

$$\mathbf{V}_i^{lp} = P_{p-1}(g_i^l) \;,\; 1 \le l \le N_d \;,\; 1 \le p \le N_d \,, \tag{V .24}$$

$\{g_i^l\}_{l=1,\ldots,N_d}$ *being the LGL nodes on* C_i.

This correspondence is useful in practice since high order modes are generally source

of instabilities, and need to be appropriately controlled; thus, modal formulations are naturally adapted to limiting procedures and de-aliasing techniques, as those exposed later.

We consider now the local polynomial expansion for the topography parametrization :

$$z_i := z_{\mathfrak{h}|C_i}(x) = \sum_{l=1}^{N_d} z_i^l \theta_i^l(x),$$

and we assume that a local expansion is available for $\mathcal{A}$, given by :

$$\tilde{\mathcal{A}}_i = {}^t(\mathcal{A}_i^1(t), \ldots, \mathcal{A}_i^{N_d}(t)). \tag{V .25}$$

Injecting these expansions into the weak formulation (V .21)-(V .22), replacing the test functions (ϕ, π) by the local basis functions and classically substituting numerical flux functions $\widehat{q}$ and $\widehat{H}$ to the discontinuous intercell flux functions arising in the interface terms, we obtain the semi-discrete formulation of our dG approximation :

$$\sum_{l=1}^{N_d} \frac{d}{dt} \eta_i^l(t) \mathbf{M}_i^{lp} - \sum_{l=1}^{N_d} q_i^l(t) \mathbf{S}_i^{lp} + \left[\widehat{q}\theta_i^p\right]_{x_i^l}^{x_i^r} = 0, \tag{V .26}$$

$$\sum_{l=1}^{N_d} \frac{d}{dt} q_i^l(t) \mathbf{M}_i^{lp} - \int_{C_i} H^q(V_{\mathfrak{h}}, z_{\mathfrak{h}}) \frac{d}{dx}\theta_i^p dx + \left[\widehat{H}\theta_i^p\right]_{x_i^l}^{x_i^r} = \int_{C_i} S^q(V_{\mathfrak{h}}, z_{\mathfrak{h}}) \theta_i^p dx - \sum_{l=1}^{N_d} \mathcal{A}_i^l(t) \mathbf{M}_i^{lp}, \tag{V .27}$$

for $1 \leq p \leq N_d$, and $1 \leq i \leq N_e$, where

$$\mathbf{M}_i^{lp} = \int_{x_i^l}^{x_i^r} \theta_i^l(x) \theta_i^p(x) dx \quad \text{and} \quad \mathbf{S}_i^{lp} = \int_{x_i^l}^{x_i^r} \theta_i^l(x) \frac{d}{dx}\theta_i^p(x) dx$$

are respectively the local *mass* and *stiffness* matrix coefficients on C_i.

Remark V.3 .2. *In (V .27), the integrals $\int_{C_i} H^\eta(V_{\mathfrak{h}}, z_{\mathfrak{h}}) \frac{d}{dx}\theta_i^p dx$ and $\int_{C_i} S^q(V_{\mathfrak{h}}, z_{\mathfrak{h}}) \theta_i^p dx$ have to be computed exactly when motionless steady states are reached, with a suitable quadrature formula, in order to obtain a well-balanced scheme, as shown in §V.3.5 . On the other hand, the computation of $\tilde{\mathcal{A}}_i$, which involves higher order derivatives, is done directly, in a collocation way. This is temporarily postponed to §V.3.3 .*

Remark V.3 .3. *At a given interface, the computation of the exchanging flux term $\widehat{q}$ and $\widehat{H}$ is classically performed with appropriate numerical flux functions, as done in the previous 2d works. To ensure the positivity of the water height, we also need to use a water height positivity preserving flux (see §V.3.6). As in the 2d case, we use the global Lax-Friedrichs flux in the numerical validations of §V.4 . These interface fluxes computations, carefully chosen to ensure the preservation of motionless steady-states, are detailed in §V.3.5 .*

V.3.3 High-order derivatives and dispersive terms computation

We are now left with the resolution of systems (V .20a - V .20c), to compute the expansion $\mathcal{A}$. Although the semi-discrete formulation (V .26), (V .27) could appear purely local, the computation of the dispersive term expansions $\mathcal{A}$ requires a global assembly process, for gathering the local discrete operators into a global one, in the computation of the inverse of the operator $1 + \alpha\mathfrak{T}[h_b]$. Additionally, this computation involves the discrete approximation of space derivatives up to 3^{rd} order. We use the *Local Discontinuous Galerkin (LDG)* approach [77] to compute these derivatives.
To illustrate this procedure, let consider the following 2^{nd} order equation, for an arbitrary scalar valued function w :

$$\ell - \partial_x^2 w = 0\,, \tag{V .28}$$

reformulated as a set of two coupled 1^{st} order equations using an auxiliary variable b :

$$b + \partial_x w = 0 \quad , \quad \ell + \partial_x b = 0\,. \tag{V .29}$$

Then, multiplying by a test function $\phi \in \mathcal{V}$ and integrating over an element C_i, we have the associated weak formulation :

$$\begin{aligned} \int_{x_i^l}^{x_i^r} b\phi - \int_{x_i^l}^{x_i^r} w\frac{d}{dx}\phi + \widehat{w}_r\phi(x_i^r) - \widehat{w}_l\phi(x_i^l) = 0\,, \\ \int_{x_i^l}^{x_i^r} \ell\phi - \int_{x_i^l}^{x_i^r} b\frac{d}{dx}\phi + \widehat{b}_r\phi(x_i^r) - \widehat{b}_l\phi(x_i^l) = 0\,. \end{aligned} \tag{V .30}$$

To define the exchanging terms $\widehat{w}$ and $\widehat{b}$ at a given interface, we use the following fluxes [79] :

$$\begin{aligned} \widehat{w} &= \overline{w} - \xi\{w\}\,, \\ \widehat{b} &= \overline{b} + \nu\{b\} + \frac{\lambda}{\mathfrak{h}}\{w\}\,, \end{aligned} \tag{V .31}$$

with the interface average $\overline{w} = (w^+ + w^-)/2$ and jump $\{w\} = (w^+ - w^-)/2$, w^+ and w^- respectively the right and left interface values of w (and similar notations for b). Taking $\xi = \nu = \lambda = 0$ gives the centered Bassi and Rebay (BR) fluxes [17], initially introduced for compressible Navier Stokes equations. The method is simple, but unstable and usually provides sub-optimal convergence rates for odd values of N, while the choice $\xi = \nu = 1$, corresponding to the Cockburn and Shu alternate upwind discretization (refers to as LDG flux in the following), may have stabilizing effects and increase the order of convergence.

Remark V.3 .4. *Note that $\frac{\lambda}{\mathfrak{h}}\{w\}$ is a penalization term, with a $\mathcal{O}(\mathfrak{h}^{-1})$ scaling. Taking for instance $\xi = \nu = 0$ and $\lambda \neq 0$ gives the stabilized centered fluxes (sBR), sometimes helping to recover optimal convergence rates. In the numerical validation of §V.4 , we only investigate and compare the BR and LDG choices. Note that extensive comparisons of fluxes including their stabilized versions and the impact of the coefficient λ are performed in [112] for weakly non-linear BT equations.*

Let us now come back to (V .30). At the discrete level, starting from the N_e expansion coefficients vectors $\{\tilde{w}_i\}_{i=1..N_e}$, which are gathered in a $N_d \times N_e$ vector $\mathcal{W} = {}^t(\tilde{w}_1, \dots, \tilde{w}_{N_e})$, we aim at computing the $N_d \times N_e$ vector $\mathcal{L} = {}^t(\tilde{\ell}, \dots, \tilde{\ell}_{N_e})$ of expansion coefficients for the 2^{nd} order derivative $\partial_x^2 w$.
This is done globally, using (V .31) to build the differentiation matrices, that also account for exchanging interface fluxes. Injecting $w_\mathfrak{h}$ into (V .30) and replacing ϕ by the local basis functions $\{\theta_i^l\}_{l=1}^{N_d}$, for all elements $\{C_i\}_{i=1..N_e}$, we obtain the global discrete formulation :

$$\begin{aligned} \mathbb{M}\mathcal{B} &= \mathbb{S}\mathcal{W} - (\mathbb{E} - \xi\mathbb{F})\,\mathcal{W}\,, \\ \mathbb{M}\mathcal{L} &= \mathbb{S}\mathcal{B} - (\mathbb{E} + \nu\mathbb{F})\,\mathcal{B} - \frac{\lambda}{\mathfrak{h}}\mathbb{F}\mathcal{W}\,, \end{aligned} \tag{V .32}$$

where the square $N_d \times N_e$ global mass and stiffness matrices $\mathbb{M}$ and $\mathbb{S}$ have a block-diagonal structure :

$$\mathbb{M} = \begin{pmatrix} \boxed{\mathbf{M}_1} & & \\ & \ddots & \\ & & \boxed{\mathbf{M}_{N_e}} \end{pmatrix} \quad , \quad \mathbb{S} = \begin{pmatrix} \boxed{\mathbf{S}_1} & & \\ & \ddots & \\ & & \boxed{\mathbf{S}_{N_e}} \end{pmatrix} , \tag{V .33}$$

and the matrices $\mathbb{E}$ and $\mathbb{F}$ accounting for the inter-element exchanging fluxes have the following structure :

$$\mathbb{E} = \begin{pmatrix} 1 & & & \\ & \begin{array}{c|c} 1/2 & 1/2 \\ \hline -1/2 & -1/2 \end{array} & (0) & \\ & \longleftrightarrow N_d & \ddots & \\ & (0) & & \begin{array}{c|c} 1/2 & 1/2 \\ \hline -1/2 & -1/2 \end{array} \\ & & & 1 \end{pmatrix} , \; \mathbb{F} = \begin{pmatrix} 1 & & & \\ & \begin{array}{c|c} -1/2 & 1/2 \\ \hline 1/2 & -1/2 \end{array} & (0) & \\ & \longleftrightarrow N_d & \ddots & \\ & (0) & & \begin{array}{c|c} -1/2 & 1/2 \\ \hline 1/2 & -1/2 \end{array} \\ & & & 1 \end{pmatrix} \tag{V .34}$$

Note that the issue of boundary conditions is postponed to §V.3.8 . We obtain a global discrete formulation of the first and second order derivative operators, based on the LDG approach (V .31) :

$$\mathcal{B} = -\mathbb{D}_x\mathcal{W} \quad , \quad \mathcal{L} = \mathbb{D}_x^2\mathcal{W}\,, \tag{V .35}$$

with

$$\mathbb{D}_x = -\mathbb{M}^{-1}\left(\mathbb{S} - \mathbb{E} + \xi\mathbb{F}\right)\,, \tag{V .36}$$

$$\mathbb{D}_x^2 = \mathbb{M}^{-1}\Big(- (\mathbb{S} - \mathbb{E} - \nu\mathbb{F})\,\mathbb{D}_x - \frac{\lambda}{\mathfrak{h}}\mathbb{F}\Big)\,. \tag{V .37}$$

		K						
Fluxes	N	20	40	80	160	320	640	order
BR	1	1.99e-3	1.08e-3	5.56e-4	2.82e-4	1.42e-4	7.09e-5	1.4
	2	3.46e-4	4.87e-5	6.18e-6	7.80e-7	9.79e-8	1.22e-8	2.8
	3	1.70e-5	2.15e-6	2.69e-7	3.24e-8	3.90e-9	5.33e-10	2.8
	4	2.91e-7	1.03e-8	2.39e-9	1.34e-9	4.06e-10	8.22e-11	2.5
LDG	1	6.11e-3	2.02e-3	5.07e-4	1.27e-4	3.18e-5	7.95e-6	2
	2	3.62e-4	6.95e-5	8.99e-6	1.13e-6	1.42e-7	1.78e-8	2.9
	3	1.27e-5	9.54e-7	5.99e-8	3.75e-9	2.34e-10	1.46e-11	3.9
	4	4.22e-7	1.42e-8	4.53e-10	1.43e-10	4.53e-13	9.58e-14	4.8

Table V .1: Heat equation : Comparative study between BR and LDG fluxes.

A similar construction can be performed for the 3^{rd} order derivatives. Using these global differentiation matrices, we are now able to approximate all the derivatives occurring in (V .20a - V .20c). The nonlinear products are treated directly, in a collocation manner, inspired from [103].

The influence of the upwind/downwind strategy of Cockburn and Shu can already be simply highlighted by a brief study around the heat equation :

$$\partial_t u - \partial_x^2 u = 0\,. \tag{V .38}$$

Numerical solutions provided by the BR and LDG fluxes are compared with the exact solution for a given set of initial conditions. Results are reported in Tab. V .1 (numerical errors are in L^1 norm). They confirm that making use of the BR fluxes provide sub optimal convergence for $N = 1$ and $N = 3$, with sometimes even a more anarchic behaviour (see N=4 on Fig. V .2 and corresponding reported errors), while the LDG choice effectively helps recovering optimal convergence rates.

We now return to the problem under study. Using these differentiation matrices, we can also build the global square $N_d \times N_e$ matrix of the discrete version of $1 + \alpha\mathfrak{T}[h_b]$. For instance, considering the simplified flat bottom case ($h_b = h_0$), we approximate the corresponding operator as follows :

$$1 + \alpha\mathfrak{T}[h_0] = 1 - \alpha\frac{h_0^2}{3}\partial_x^2 \quad \longrightarrow \quad I - \alpha\frac{h_0^2}{3}\mathbb{D}_x^2\,,$$

where I is the $N_d \times N_e$ identity matrix. The locality of the LDG approach results in a sparse block-structure matrix which is stored in a sparse format and LU-factorized at the beginning of the computation, in a pre-processing step. For the validations of §V.4 , the factorization and the resolution of the resulting triangular linear systems are performed using the unsymmetric multi-frontal method [85].

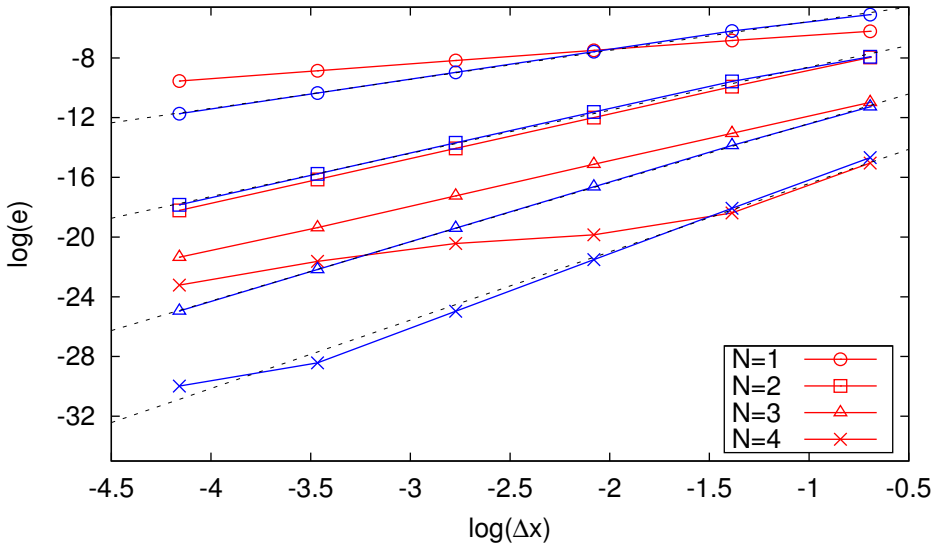

Figure V .2: Heat equation : Convergence rate study for BR (*red*) and LDG (*blue*) methods. Reference slopes corresponding to LDG appear in dotted lines.

Remark V.3 .5. *The same approach can of course also be used for the original model (V .1), the only difference being that the* $1 + \alpha\mathfrak{T}[z, h]$ *matrix has to be build and factorized at each time step (or substep).*

V.3.4 Stabilisation procedure

The use of direct interpolation/collocation methods for the computation of the nonlinear products in the dispersive source terms reduces the computational cost but can generate some aliasing which deteriorates the solution quality and can lead to instabilities. Indeed, these quantities may be N^{th} order approximations of higher order polynomials. The situation is even more complicated in the case of general functions such as those involved by the dispersive term $\mathcal{A}$, which evaluation will consistently introduce aliasing error. To amend this, we use the stabilization filtering method (mild nodal filter), as suggested in [103]. We introduce artificial dissipation to reduce (or even switch off) the influence of higher order coefficients in the modal expansion. The method relies in the introduction of a filter defined by :

$$\sigma(\tau) = \begin{cases} 1 \quad \text{if} \quad 0 \leq \tau \leq \tau_c = \dfrac{N_c}{N}, \\ \exp\left(-A\left(\dfrac{\tau - \tau_c}{1 - \tau_c}\right)^s\right) \quad \text{otherwise}, \end{cases} \tag{V .39}$$

where s, A are real parameters and N_c is a threshold defining the impacted modes. At each time step the filter is applied locally to the approximated vector solution V_h by multiplication with the following matrix :

$$\mathbf{F} = \mathbf{V}\mathbf{D}\mathbf{V}^{-1}, \tag{V .40}$$

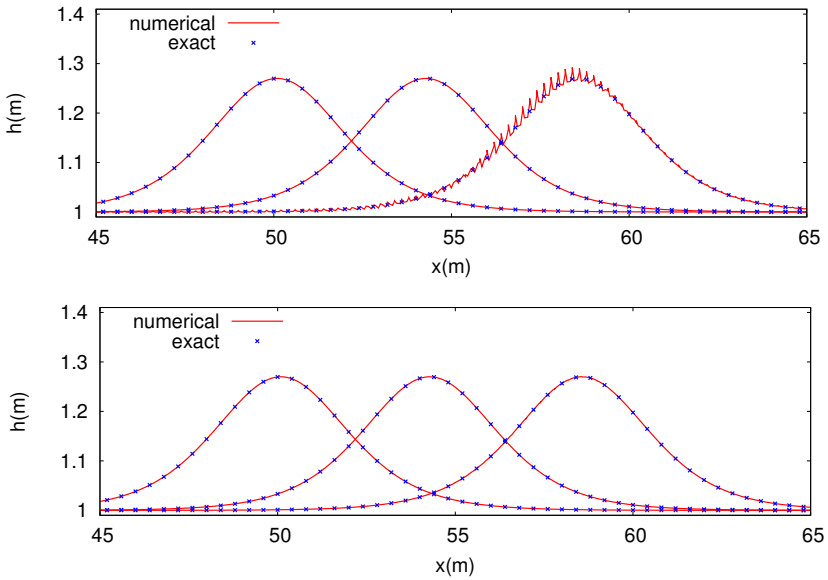

Figure V .3: De-aliasing procedure : Free surface profiles without filter (*top*) and with filter (*bottom*) at t=0, 1.2 and 2.4s .

where $\mathbf{V}$ is given by (V .24) and $\mathbf{D}$ is a diagonal matrix with coefficients :

$$\mathbf{D}_{ll} = \sigma(\frac{l-1}{N}) , \quad l = 1, \cdots , N_d . \tag{V .41}$$

To illustrate the efficiency of the procedure, we propose to lightly pre-empt the experimental part, studying the propagation of a solitary wave (see test V.4.3). In this test, we set $h_0 = 1$ and the non linearity parameter is $a = 0.27$. The order of approximation is $N = 3$, and the space step is equal to 0.25. The parameters involved in the filter are $s = 8$, $\alpha = 0.1$ and $N_c = 0$. A glance towards the water profiles available in Fig. V .3 helps convincing about the necessity of the stabilisation procedure.

V.3.5 Preservation of motionless steady states

In this section, we detail the computation of the interface fluxes $\left[\widehat{q}\theta_i^p\right]_{x_i^l}^{x_i^r}$ and $\left[\widehat{H}\theta_i^p\right]_{x_i^l}^{x_i^r}$ appearing in the semi-discrete local discretization (V .27). To ensure the preservation of motionless steady states, we adapt to the 1d framework the method previously employed, relying on the PBSW equations. At a given boundary interface (say between cells i and $i+1$), the *interior* and *exterior* values are recovered as follows :

$$V^- = V_\mathfrak{h}(x_i^r) \ , \quad z^- = z_\mathfrak{h}(x_i^r) \quad , \qquad V^+ = V_\mathfrak{h}(x_{i+1}^l) \ , \quad z^+ = z_\mathfrak{h}(x_{i+1}^l) \ . \tag{V .42}$$

At this point, we follow exactly the same protocol as in the 1d FV context. We

hence define at each boundary :

$$z^* = \max(z^-, z^+)\,, \qquad \check{z} = z^* - \max(0, z^* - \eta^-)\,, \tag{V .43}$$

$$\check{h}^\pm = \max(0, \eta^\pm - z^*)\,, \qquad \check{\eta}^\pm = \check{h}^\pm + \check{z}\,, \tag{V .44}$$

leading to new *interior* and *exterior* values :

$$\check{V}^- = (\check{\eta}^-, \frac{\check{h}^-}{h^-} q^-) \quad \text{and} \quad \check{V}^+ = (\check{\eta}^+, \frac{\check{h}^+}{h^+} q^+)\,, \tag{V .45}$$

with $h^\pm = \eta^\pm - z^\pm$. Then, the interface fluxes in (V .26)-(V .27) are computed as follows :

$$\widehat{q} = \mathcal{H}^\eta(\check{V}^-, \check{V}^+)\,, \tag{V .46}$$

$$\widehat{H} = \mathcal{H}^q(\check{V}^-, \check{V}^+, \check{z}, \check{z}) - g\check{\eta}^-(z^- - \check{z}) \tag{V .47}$$

where $\mathcal{H} = {}^t(\mathcal{H}^\eta, \mathcal{H}^q)$ is the Lax-Friedrich flux function (I .21).

Proposition 12. *The dG scheme (V .26)-(V .27), with the interface fluxes defined in (V .46)-(V .47), preserves the motionless steady states.*

Proof. We adapt the ideas of [288] to the *pre-balanced* formulation (V .16). We want to show that :

$$\frac{d}{dt}\tilde{\eta}_i(t) = 0 \quad \text{and} \quad \frac{d}{dt}\tilde{q}_i(t) = 0\,, \quad \text{for } 1 \le i \le N_e\,.$$

If a motionless steady state is reached, that is :

$$V_\mathfrak{h} = {}^t(\eta_c, 0)\,, \tag{V .48}$$

we have $\tilde{q}_i(t) = 0$ on each element and using (V .26), $\frac{d}{dt}\tilde{\eta}_i(t) = 0$ obviously holds. For the second equation (V .27), we this time need the residue

$$R_p = -\int_{C_i} H^q(V_\mathfrak{h}, z_\mathfrak{h}) \frac{d}{dx}\theta_i^p dx + \left[\widehat{H}\theta_i^p\right]_{x_i^l}^{x_i^r} + g\int_{C_i} \eta_\mathfrak{h} \frac{d}{dx} z_\mathfrak{h} \theta_i^p dx + \sum_{l=1}^{N_d} \mathcal{A}_i^l(t) \mathbf{M}_i^{lp}$$

to vanish when a motionless steady state is reached, for $1 \le p \le N_d$ and $1 \le i \le N_e$. We first notice that the definition of the differential operators $\{\mathcal{Q}_k\}_{1\le k\le 3}$, combined with (V .48), directly leads to $\mathcal{A}(V_\mathfrak{h}) = 0$ at the discrete level, as a solution of (V .20a)-(V .20b)-(V .20c).
When (V .48) holds, (V .43)-(V .44)-(V .45) leads to $\check{\eta}^- = \check{\eta}^+ = \eta_c$ for both interfaces, and using (V .47), the interface flux $\widehat{H}(x_i^r)$ reduces to :

$$\widehat{H}(x_i^r) = \frac{g}{2}(\eta_c^2 - 2\eta_c \check{z}_r) - g\eta_c(z_r^- - \check{z}_r) = \frac{g}{2}(\eta_c^2 - 2\eta_c z_r^-) = H^q(V^-, z^-).$$

We show in a similar way that such a relation also stands at the left boundary. As $V_\mathfrak{h}$ is a steady state solution, we have $\partial_x(H^q(V_\mathfrak{h}, z_\mathfrak{h})) = -g\eta_c \frac{d}{dx} z_\mathfrak{h}$, and provided the integral terms are computed exactly, we obtain :

$$R_p = \int_{C_i} \partial_x(H^q(V_\mathfrak{h}, z_\mathfrak{h}))\theta_i^p dx + g\int_{C_i} \eta_c \frac{d}{dx} z_\mathfrak{h}\, \theta_i^p dx = 0$$

□

V.3.6 Robustness

The problem of robustness property is addressed in an equivalent manner to the 2d approach, that is adapting the ideas developed in [291, 298] to the *pre-balanced* formulation. We first note that the scheme satisfied by the cell average of the free surface $\overline{\eta}_i^n = \dfrac{1}{|C_i|}\int_{C_i}\eta_i\,dx$ in the dG approximation (V .26) is :

$$\overline{\eta}_i^{n+1} = \overline{\eta}_i^n - \frac{\Delta t}{|C_i|}\left[\widehat{q}\right]_{x_i^l}^{x_i^r}, \tag{V .49}$$

with the interface fluxes $\widehat{q}$ given by (V .46). Again, as we work with η instead of h, we have to ensure that the first order scheme associated with (V .49) preserves the positivity of the water height, and such a result has been stated at the outcome of Proposition 2 for the Global Lax Friedrichs fluxes (see Remark II.2 .4).

Based on this, the ideas of [291] can be directly applied. Following the steps detailed in §IV.3.4 , assuming that $\bar{h}_i^n \geq 0$, we define $S_i^N = \{r_i^k\}_{k=1,..,\beta}$ the set of β LGL points on the element C_i, where β is chosen such that the associated quadrature rule is exact for polynomials of degree N (*i.e.* $2\beta - 3 \geq N$). We then compute the minimum water height m_{C_i} over S_i^N (IV .17) and apply the limiter (IV .18). We deduce a modified N^{th} order polynomial $\check{\eta}_i$, which is injected into (V .26)-(V .27) instead of (V .23). Thus, following [291, 298], the positivity of the mean water height $\bar{h}_i^{n+1}$ is ensured under the condition :

$$\max_{1\leq i\leq N_e}\lambda_i\frac{\Delta t}{|C_i|} \leq \hat{w}_1\,,$$

where $\lambda_i = \left(\max_{\partial C_i}(|u| + \sqrt{gh})\right)$. In practice, we have $\hat{w}_1 = \dfrac{1}{6}$ for $N = 2, 3$ and $\dfrac{1}{12}$ for $N = 4, 5$.

V.3.7 Handling broken waves and limiting strategy

We now broach the issue of broken waves detection and give further details on the *switching* strategy adopted in this work. As stated in the introductory lines, we can find several methods in the literature, since the last few years, that allow to handle broken waves in BT equations. They all rely on an accurate detection of potential instability regions, near the breaking point, in which the limit of validity of the BT equations is reached. We propose in this work to use a purely numerical criteria to detect such area, based on the strong superconvergence phenomena exhibited at element's outflow boundaries [174], and previously used in 2d. In 1d, for a given element C_i, (IV .14) becomes :

$$\mathfrak{I}_i = \frac{\Delta^-|h_i^1 - h_{i-1}^{N_d}| + \Delta^+|h_i^{N_d} - h_{i+1}^1|}{|C_i|^{(N+1)/2}\|h_i\|_\infty}, \tag{V .50}$$

where

$$\Delta^- = \begin{cases} 1 & \text{if} \quad q_i^1 \geq 0\,, \\ 0 & \text{otherwise}\,. \end{cases} \quad , \quad \Delta^+ = \begin{cases} 1 & \text{if} \quad q_i^{N_d} \leq 0\,, \\ 0 & \text{otherwise}\,. \end{cases} \tag{V .51}$$

Waves about to break are identified in elements such that $\mathfrak{I}_i \geq 1$ and we locally suppress the dispersive term in such elements (*i.e.* we *locally switch* to the NSW equations). After breaking, the wave fronts are handled as shocks by the NSW equations and only the hyperbolic part of the equations is solved for the wave fronts. The breaking wave dissipation is represented by shock local energy dissipation [35].
Practically, our numerical investigations have shown that, for a given breaking wave, the *switching areas* need to be slightly enlarged to prevent the possible occurrence of spurious oscillations. Consequently some neighboring cells are added to the switching area to include the steepening shore facing side of the wave, and a part of the offshore facing side. This can be simply done with the help of a mask, defining the switching area as a band of length $2r$ centred to the elements verifying $\mathfrak{I}_i \geq 1$ (see Fig. V .4).

Additionally, the use of a local limitation procedure $V_\mathfrak{h} \leftarrow \Pi V_\mathfrak{h}$ is classically required in troubled elements. In this work, we use again the improved moment limiting strategy of [53], which implementation has been detailed in the 2d case (see §IV.3.3).

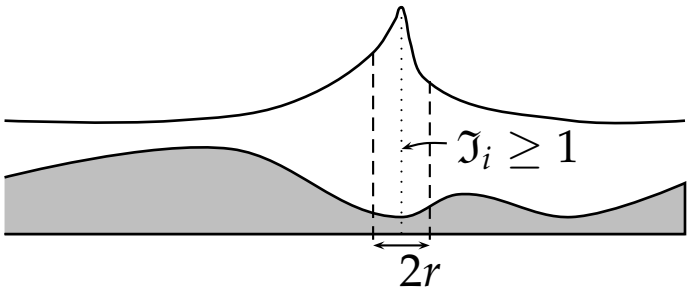

Figure V .4: Example of breaking area.

V.3.8 Boundary conditions

The boundary conditions are classically imposed weakly, by enforcing suitable reflecting relations at virtual *exterior* nodes, at each boundaries, through the boundary interface fluxes. *Periodic*, *Neumann* and *Dirichlet* conditions can be enforced following this simple process. For the approximation of second order derivatives with the LDG strategy, we classically enforce Neumann boundary conditions for the auxiliary variable. We also use Neumann boundary conditions for the derivatives involved in the discrete version of the operator $1 + \alpha\mathfrak{T}[h_b]$. The first and last rows of (V .34) should be adapted for *Dirichlet* conditions. As far as generation and absorption of waves are concerned, we use relaxation techniques, as described in §I.4.2 . The computational domain is slightly extended to include the sponge layers, which length has to be calibrated from the incoming waves. We enforce periodic waves generation with the use of a generation/relaxation zone, following [205]. We have implemented the relaxation functions proposed

in [283] and at the inlet boundary, we progressively impose on a two-wavelength long generation layer the targeted wave train.

V.4 Numerical examples

In this section, we assess the ability of our dG approach to compute waves propagation and transformations. The two models/schemes given by (V .26)-(V .27) involving (V .17a) or (V .17b) will be referred to as GNO (for *original*) and GNC (for *constant*) respectively. Unless stated otherwise, we use Neumann boundary conditions at both boundaries, the optimized value $\alpha = 1.159$ is used and we set $\epsilon_b = 0.1$. As regards the time scheme, we use again explicit SSP-RK schemes [135]. Up to $N = 3$, SSP-RK schemes of order $N+1$ are considered, to ensure equal orders of convergence in space and time. A 4^{th} order SSP-RK scheme is used for $N \geq 3$. We highlight that our numerical investigations have shown that the value of ϵ_b does not influence the numerical results. Accordingly with the robustness result, we do not suppress the dispersive effects in the vicinity of dry areas.

V.4.1 Motionless steady states preservation

We consider a 100 m channel and start from an initial steady state at rest $\eta = 0$ and $q = 0$, over the following topography (see Fig. V .5) :

$$z(x) = -h_0\, exp\big(-\big((x-d)/l\big)^2\big) + 0.8\,. \tag{V .52}$$

d is the center of the channel and we take $l = 10$, $h_0 = 1$. After 10 s of simulation, the steady state is still preserved up to the machine accuracy, regardless of the polynomials' order in the expansion basis or the refinement of the mesh. As an example, for $N = 3$ and $N_e = 300$, the computations give an L^1-error of $1.56\, e^{-16}$ for the free surface and $7.13\, e^{-15}$ for the discharge.

V.4.2 Accuracy analysis in the presence of non-flat bottom

We now focus on the evolution of a smooth gaussian profile over the previous non flat and smooth topography, to highlight the convergence properties of our approach. The initial water height is defined as $h(x) = az(x)$, where $a/h_0 = 0.2$ and z defined in the previous test case (V .52). No exact solution is available, so a reference solution is computed at $t = 0.15s$ with $N = 7$, $N_e = 1280$. Computations for both models (V .16)-(V .17a) and (V .16)-(V .17b) are run on a sequence of regular meshes with increasing refinement and polynomial expansions of increasing orders, from 1 to 5. For the approximation of high order derivatives, we use successively LDG and BR fluxes. The numerical L^1-errors computed using the reference solution at $t = 0.15\,s$ are reported in Tab. V .2 for the water height and plotted on Fig. V .6 for both water height and discharge, in log-log scale. As expected, we obtain similar orders of accuracy for both GNO and GNC

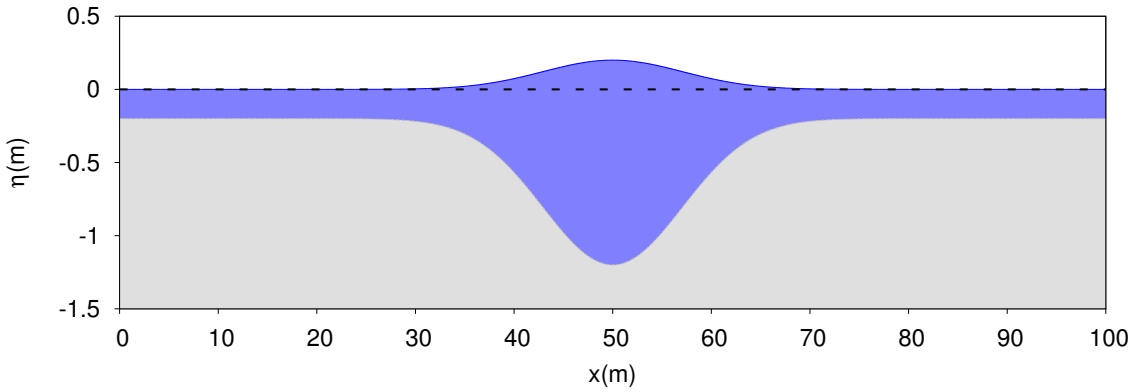

Figure V .5: Topography and initial conditions for test cases V.4.1 and V.4.2 .

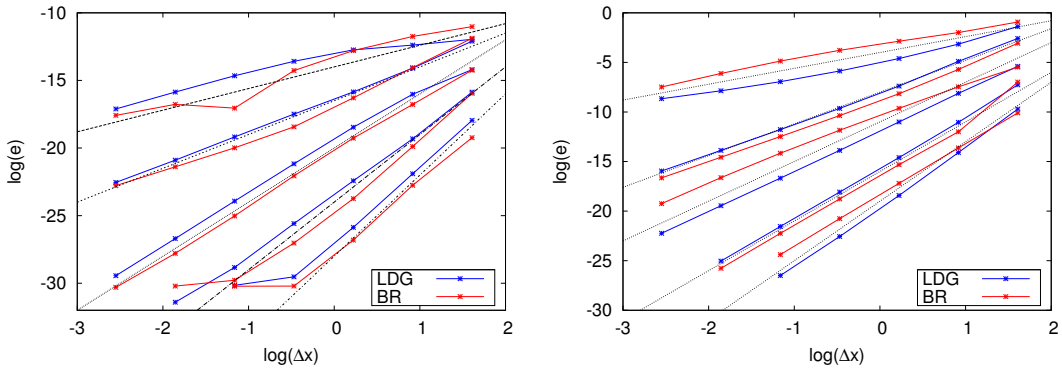

Figure V .6: Accuracy analysis in the presence of non-flat bottom : Convergence rates for the water height (*left*) and the discharge (*right*) - Reference slopes 1.6, 3.2, 4, 5 and 6 are plotted in dotted lines.

Model	Fluxes	N	N_e 20	40	80	160	320	640	order
GNO	BR	1	0.4	0.13	5.6e-2	2.2e-2	7.6e-3	2.2e-3	1.5
		2	4.4e-2	3.2e-3	2.9e-4	3.2e-5	3.9e-6	4.9e-7	3.3
		3	4.1e-3	5.4e-4	6.1e-5	6.7e-6	6.6e-7	5.6e-8	3.2
		4	7.7e-4	6.1e-6	2.2e-7	6.9e-9	2.1e-10	6.7e-12	5.3
		5	3.6e-5	1.1e-6	3.1e-8	8.7e-10	2.3e-11	/	5.1
	LDG	1	0.25	4.3e-2	1.0e-3	2.9e-3	9.7e-4	3.8e-4	1.9
		2	7.3e-2	7.3e-3	6.2e-4	6.6e-5	7.9e-6	9.8e-7	3.2
		3	4.3e-3	2.9e-4	1.6e-5	9.0e-7	5.5e-8	3.4e-9	4.0
		4	6.6e-4	1.5e-5	4.4e-7	1.4e-8	4.2e-10	1.3e-11	5.1
		5	5.2e-5	7.0e-7	9.6e-9	1.5e-10	2.8e-12	/	6.0
GNC	BR	1	0.4	0.14	5.7e-2	2.3e-2	7.7e-3	2.2e-3	1.5
		2	4.7e-2	3.3e-3	2.9e-4	3.2e-5	3.8e-6	4.7e-7	3.3
		3	4.2e-3	5.8e-4	6.5e-5	7.2e-6	7.1e-7	6.0e-8	3.2
		4	9.3e-4	6.2e-6	2.2e-7	7.0e-9	2.2e-10	6.4e-12	5.4
		5	4.1e-5	1.2e-6	3.4e-8	9.6e-10	2.6e-11	/	5.1
	LDG	1	0.25	4.2e-2	1.0e-3	2.8e-3	9.6e-4	3.9e-4	1.9
		2	7.5e-2	7.5e-3	6.2e-4	6.5e-5	7.7e-6	9.5e-7	3.2
		3	4.5e-3	3.0e-4	1.7e-5	9.4e-7	5.7e-8	3.6e-9	4.0
		4	7.0e-4	1.6e-5	4.6e-7	1.4e-8	4.4e-10	1.3e-11	5.1
		5	6.1e-5	7.6e-7	1.0e-8	1.6e-10	3.1e-12	/	6.1

Table V .2: Accuracy analysis in the presence of non-flat bottom : L^1 error for the water height.

models. Concerning the impact of the numerical flux choice on the convergence rates, we can observe on Tab. V .2 that, for both models and as mentioned in previous studies [77, 103, 111, 112], the use of BR fluxes may lead to sub-optimal convergence rates for odd values of N, while the LDG fluxes lead to optimal convergence rates. The corresponding convergence orders are reported on the last column of Tab. V .2.

Let us now investigate the computational improvements obtained with the new GNC model. To this purpose, an averaged cpu-time per time-step is measured for both models, for increasing values of polynomials' order and number of elements. These cpu times are denoted respectively ρ_o and ρ_c for the *original* and *constant* models. We focus on the ratio $\tau := \rho_o/\rho_c$ and the corresponding values are reported in Tab. V .3. They confirm the computational savings provided by the GNC model, clearly more efficient for all given couple (N, N_e). We observe that the ratio increases with respect to the polynomial's order, confirming the benefit of this new approach for high order simulations. For polynomial expansions of order 6 the speed-up can reach 7.15. Based on these investigations, all the following computations are performed with the GNC model.

	N_e					
N	1000	2000	3000	4000	5000	6000
1	3.23	3.21	3.04	2.96	2.94	2.90
2	4.09	4.27	4.14	4.01	3.90	3.84
3	5.32	5.11	5.03	4.97	4.91	4.87
4	6.01	5.77	5.67	5.63	5.51	5.55
5	6.66	6.38	6.32	6.30	6.26	6.16
6	7.15	6.99	7.05	6.97	6.86	6.54

Table V .3: Accuracy analysis in the presence of non-flat bottom : Time ratio $\tau = \rho_o/\rho_c$ for increasing values of N and N_e.

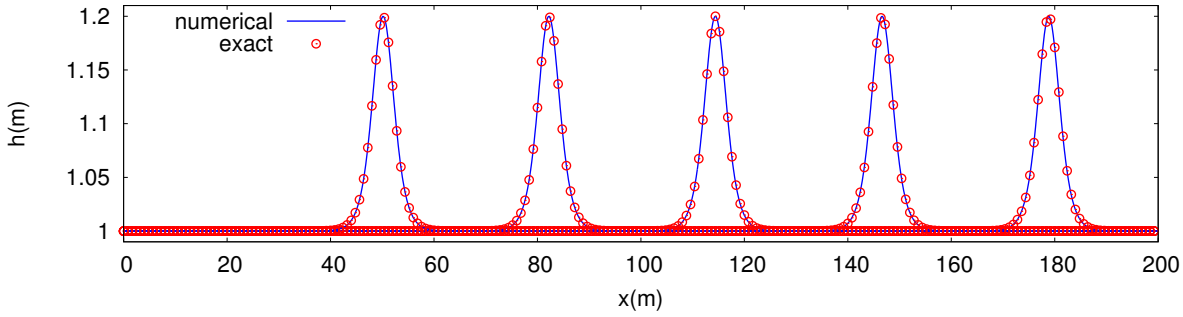

Figure V .7: Propagation of a solitary wave : Water surface profiles at t=0.4, 0.8, 1.2, 1.6 and 2s.

V.4.3 Propagation of a solitary wave

In this test, we investigate the propagation of a solitary wave over a flat bottom. We recall that the original model (V .1) admits the following class of solitary waves solution :

$$\begin{cases} h(x,t) = h_0 + a\, sech^2\left(\kappa(x-ct)\right), \\ u(x,t) = c(1 - \dfrac{h_0}{h(x,t)}), \end{cases} \tag{V .53}$$

where $\kappa = \sqrt{\dfrac{3a}{4h_0^2(h_0+a)}}$, and $c = \sqrt{g(h_0+a)}$. We also recall that these solitary waves are only solutions up to $O(\mu^2)$ of the new GNC family of models. For this test, the reference water height is fixed at $h_0 = 1\,m$ and we use the new model (V .4), with $\alpha = 1$ to compute the propagation of a solitary wave initially centred at $x_0 = 50\,m$, with a relative amplitude set to $a = 0.2h_0$. The computational domain is a $200m$ long channel, regularly meshed with 400 elements. We investigate several orders of polynomial expansions and follow the flow motion along the channel until $t = 2.2s$. We show on Fig. V .7 some free surface profiles at several times obtained with 3^{rd} order expansions and a fourth order SSP-RK time-marching scheme. We can observe an excellent agreement between numerical solutions provided by the new model (V .4) and formula (V .53),

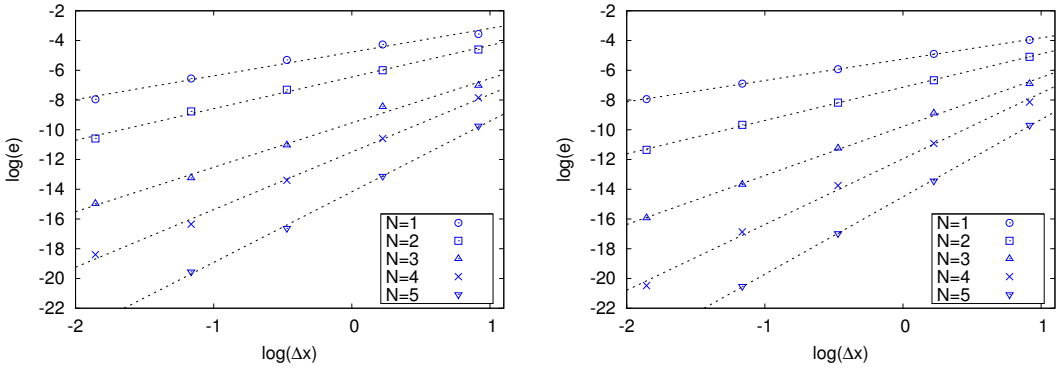

Figure V .8: Propagation of a solitary wave : Convergence rate analysis for the free surface (*left*) and discharge (*right*). L^1-error is plotted against Δx in a logarithmic scale. Reference slopes for the LDG fluxes are in dotted lines. They are equal to 1.4, 2.2, 3.3, 4.4 and 5.3 for the discharge. Similar data are observed for the free surface.

showing the negligible discrepancies introduced by the $O(\mu^2)$ approximation in the new family of models. The free surface profile is accurately preserved during the propagation. However, let us mention that some convergence studies have been performed for this particular test case (using the scheme based on the original model), and we obtain sub-optimal $N + \frac{1}{2}$ convergence rates for the LDG fluxes (see Fig V .8).

To complete this test, and have a deeper assessment regarding the influence of non linearities and dispersive terms, we study the interaction of two counter-propagating waves of equal amplitudes, initially located at x=1500m and x=2500m. Same mesh and order of polynomials are used. The overall behaviour of the propagation can be assessed through the series of snapshots proposed in Fig. V .9. As we can observe in the last pictures, the head-on collision generates dispersive tails of small amplitude. A zoom on these non-linear interactions is lastly proposed at t=200s, exhibiting a very proper description of the phenomenon. Indeed, this typical behaviour is also studied in [214], leading to very similar observations. The propagation and transformations of solitary waves of increased non-linearity are studied in the next test.

V.4.4 Shoaling of solitary waves

We now investigate the dispersive properties of the model and study the non-linear shoaling, using the data issued from a laboratory study performed at the LEGI (Grenoble, France). In this test, we consider a $36m$ channel with constant bed slope and a train of solitary waves generated at the inflow boundary. Measurements of the free surface are available at several wave gages in the vicinity of the breaking point during the simulation. We consider 4 series of experiments, involving an increasing relative amplitude, starting from $a/h_0 = 0.096$ and ending with $a/h_0 = 0.534$.

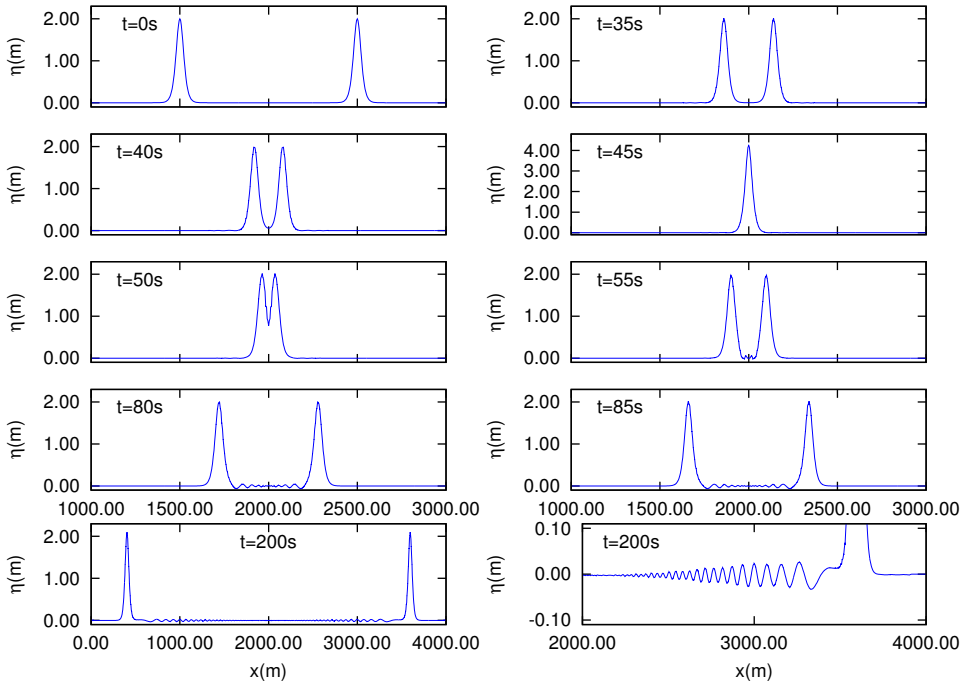

Figure V .9: Propagation of a solitary wave : Head on collision : water surface profiles at several times during the propagation.

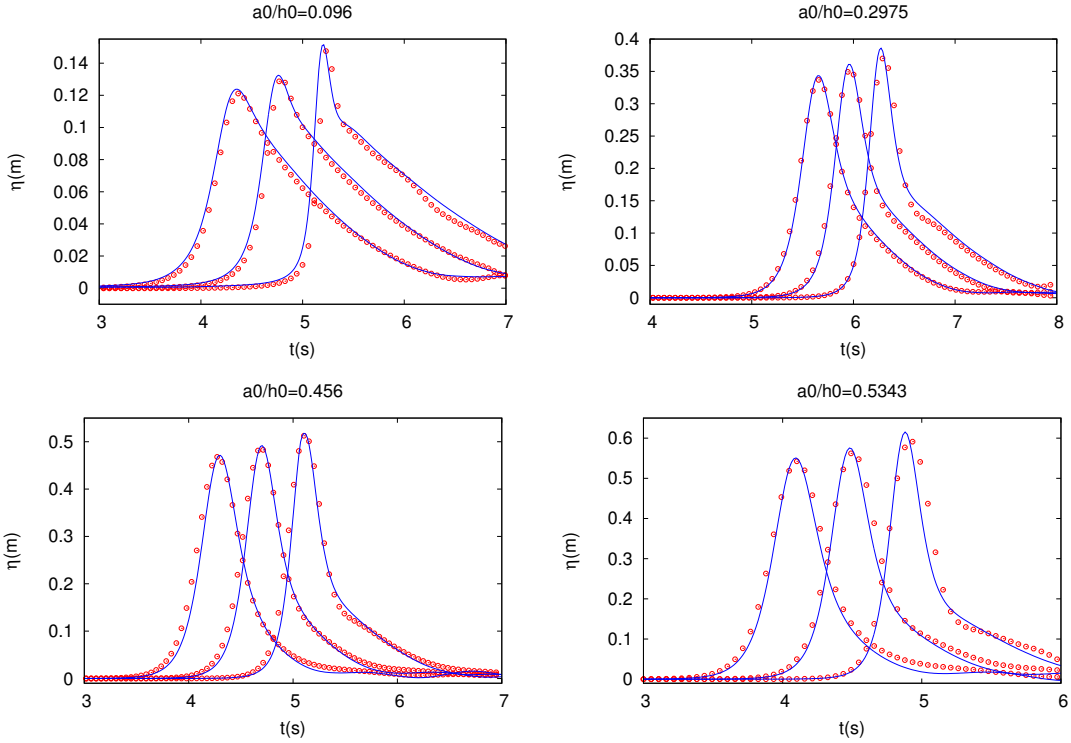

Figure V .10: Shoaling of solitary waves : Comparison between experimental (*solid lines*) and numerical (*dots*) time series of total free surface at several gauges before the breaking point.

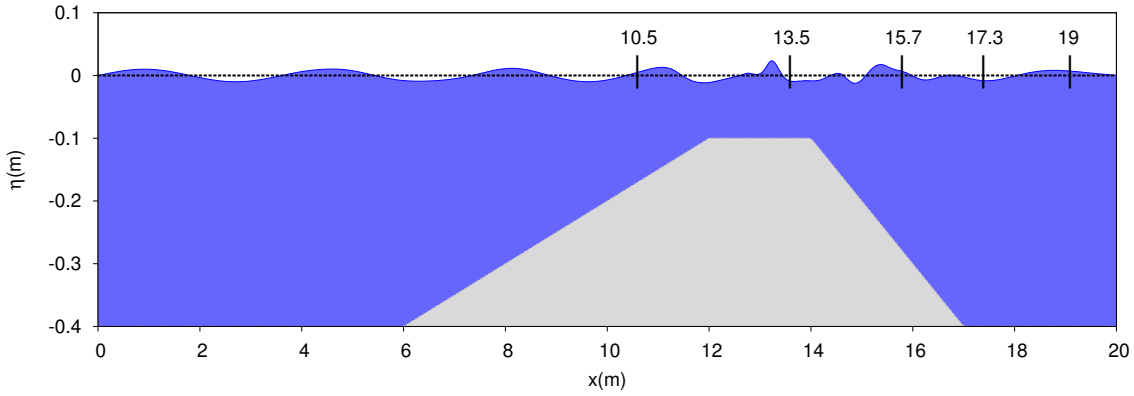

Figure V .11: Periodic waves over a submerged bar : Sketch of the basin and gauges location.

Numerical results are obtained with $(N, N_e) = (3, 400)$ and displayed on Fig. V .10, together with the experimental data available from [140]. We can observe a very good behavior of the numerical model, and even for large wave's amplitude. These results assess the good accuracy of our model in the reproduction of the shoaling process.

V.4.5 Periodic waves over a submerged bar

Going ahead in the assessment of the dispersive properties of the GNC model, we investigate now the propagation of periodic waves over a submerged bar, following the test proposed in [95]. The topography set-up and wave gauges locations are shown in Fig. V .11. We choose here to perform test A, in which the amplitude of the input waves is set to $a = 0.01m$. The time period T is 2.02 s and the initial depth h_0 is $0.4m$. When the incident waves encounters the upward part of the bar, it shoals and steepens, which generates higher-harmonics as the nonlinearity increases. These higher-harmonics are then freely released on the downward slope, and become deep-water waves behind the bar. The domain is regularly meshed with $N_e = 800$ elements, and computations are run with increasing orders of polynomial expansions. Incident waves do not encounter breaking during the propagation, so that the switching/limiting process is not activated in this test.

We show on Fig. V .12 some time series of the free surface elevation at several wave gauges located along the channel, compared with the experimental data. These results are obtained with 3^{rd} order polynomials. We obtain a very good agreement at the first gauges. Some discrepancies are noticed at the last gauge, mostly explained by the high non-linear interactions generated as the waves reaches the top of the bump. As exhibited in Fig. V .13, these effects are not correctly reproduced up to $N = 3$ at the reference point $x = 19m$ for this choice of space step and we tried to locally increase the model accuracy, leading

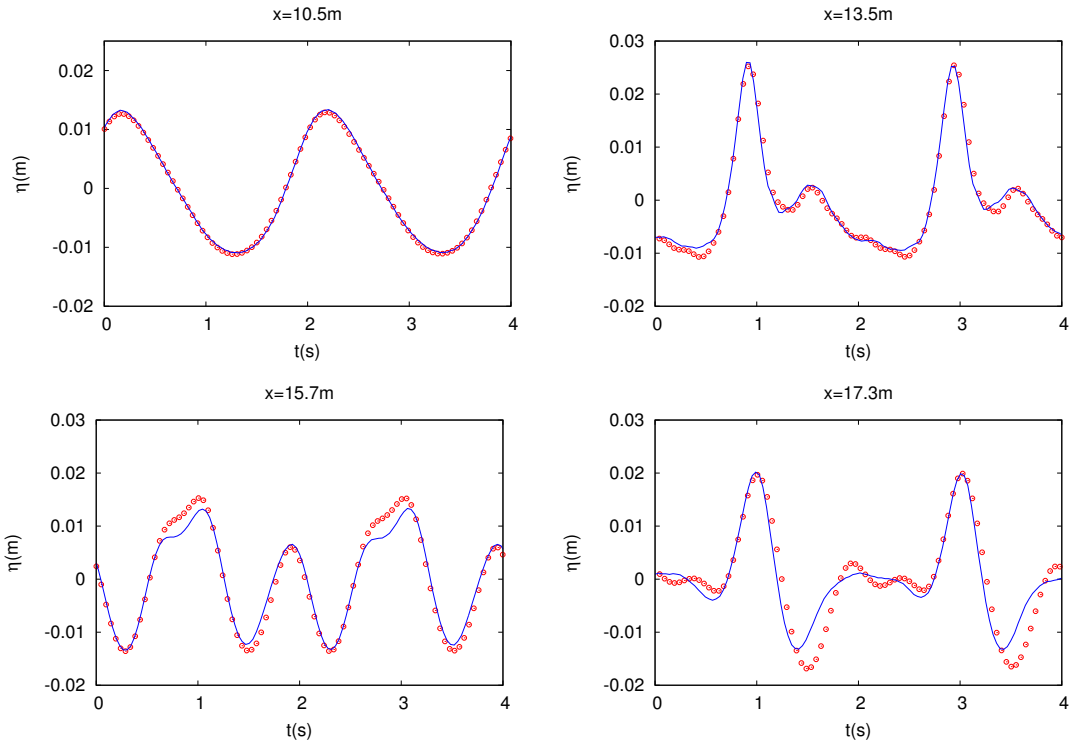

Figure V .12: Propagation of highly dispersive waves : Free surface evolution at the four first gauges. Experimental data are denoted by plain lines.

to sensible improvements. However, in the area of the last three gauges, the dispersion properties of the current model are no more satisfactory enough to accurately reproduce the complete release of the higher-harmonics, which can be regarded as highly dispersive waves. These results can be improved with the use of some optimized GN models, as for instance the *3 parameters* optimized Green-Naghdi models proposed in [70] and in the 2d case in [184]. The dG approximations of such enhanced GN equations are left for future works.

Using the same mesh and topography, the initial non linearity is increased and the time period T is set to 2.5s. This corresponds to the long wave plunging case described by Beji and Batjes in [18]. This time, the steepening of which is subject the train of waves is more pronounced and wave breaking is observed on the top part of the bar. Experimental data are also available in this case, allowing to assess the capacity in handling wave breaking in parallel with complex transformations due to dispersion. Time series of the free surface are plotted on Fig. V .14 at several reference points located along the channel. They exhibit a good correspondence with the data coming from the experimental model, in the same order of quality than the results obtained with the hybrid scheme [268] for example. In Fig. V .15 we also propose to follow the breaking process during a period, indicating areas where dispersive terms are suppressed and only the NSW equations are solved. These results attest of the relevancy of the numerical criteria used to initiate the switching strategy. The scheme is truly able to detect and follow breaking waves in this case, and switch-back to the GN equations

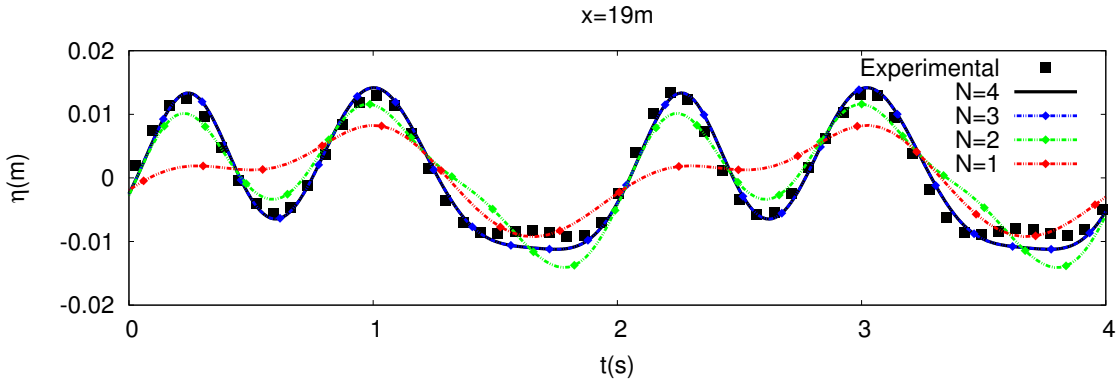

Figure V .13: Propagation of highly dispersive waves : Several profiles for increasing N at the last gauge.

once breaking is ended. The strategy allows a proper and accurate description of the flow dynamics.

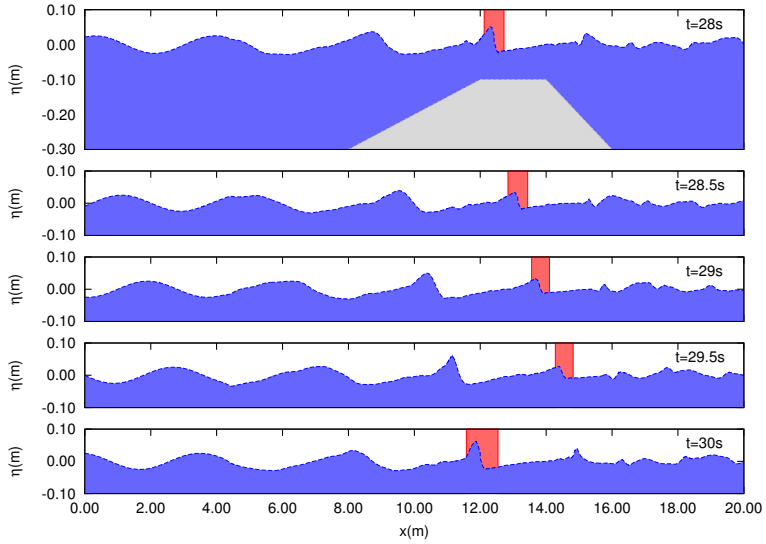

Figure V .15: Propagation of highly dispersive waves : Plunging breaking case : focus on the breaking process during a period. The NSW equations are used in areas delimited by the red bands to describe wave breaking.

V.4.6 Solitary wave breaking over a sloping beach

Let us now assess the ability of our numerical model to deal with breaking waves and dry areas. In this test, we study the propagation, shoaling, breaking and run-up processes of a solitary wave over a beach with constant slope s=1/19.85, following the experiments of [264]. The incident wave is supplied by formula (V .53), with a water level at rest $h_0 = 1m$ and an amplitude set to

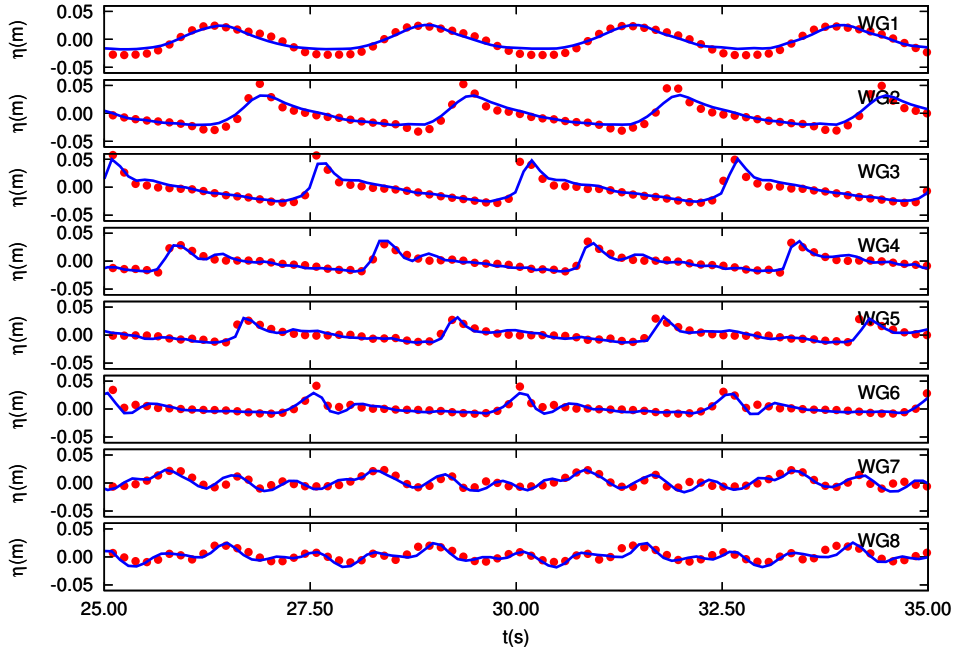

Figure V .14: Propagation of highly dispersive waves : Plunging breaking case : free surface evolution at gauge x=6m and seven gauges regularly spaced from x=11m to x=17m . Experimental data appear in plain lines.

$a = 0.28m$. The couple (N, N_e) is fixed to $(3, 600)$ for the computation and our numerical results are compared with the experimental data. We observe that the breaking wave method described in (§V.3.7) is able to identify the wave steepening, occurring approximatively around $t^* = 17s$. We emphasize the very satisfying agreement between the numerical results and the data, as shown on Fig. V .16, in the same order than other dispersive models ([37, 36, 268]).

V.4.7 Cox's experiment

To further investigate the breaking waves / switching strategy, we study in this test the evolution of an incoming train of regular waves over a beach with constant bed slope 1/35. The area of applicability of the physical model allows to extend test case IV.4.6 with a generation process in deeper waters. Waves of relative amplitude $a/h_0 = 0.29$ and period $T = 2.2s$ are generated at the inflow boundary. We set $N = 1$ and use two mesh sizes for this test: $|C_i| = 0.0575$ for $x < 11.5\,m$ and $|C_i| = 0.028$ for $x \geq 11.5\,m$. A sketch of the computational domain is available in Fig. V .17, with the location of the wave gauges. In this picture, we also point out the areas where the dispersive effects are turned off (in red) and the NSW equations are used, following the switching strategy detailed in §V.3.7 . In agreement with experimental observations, the first wave to break is detected between gauges ♯2 and ♯3. Note that, for this particular test case, the dispersive terms are switched off in the vicinity of the shoreline because the switching criteria $\mathfrak{I}$ is larger than 1 in this area. We can observe on Fig. V .18 the time series of the

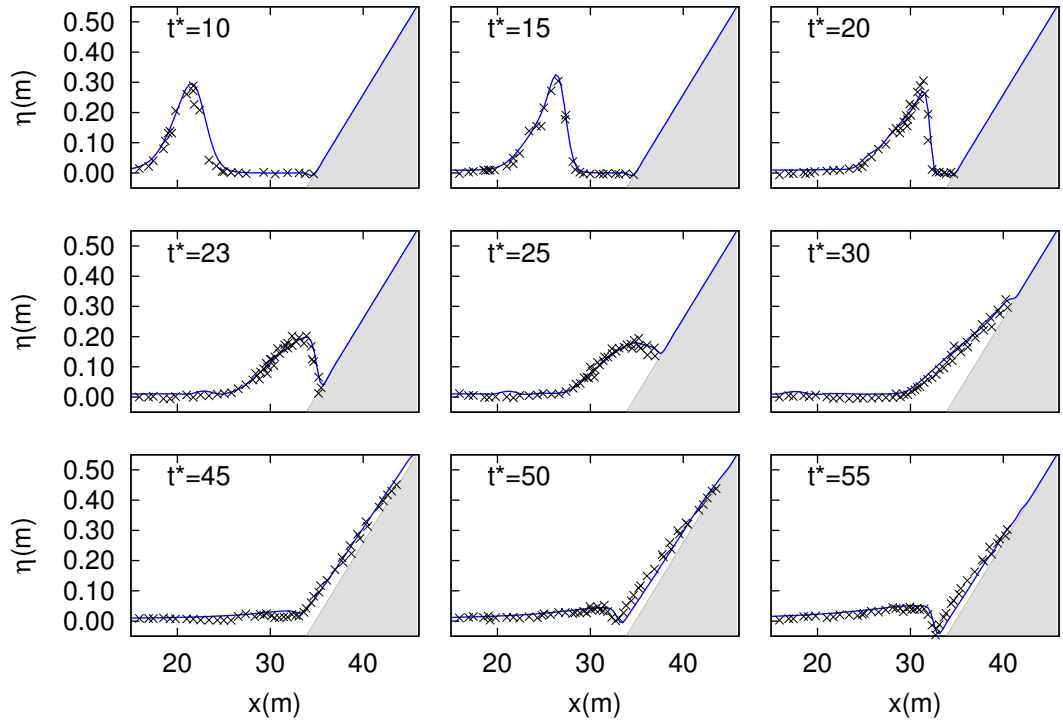

Figure V .16: Solitary wave breaking over a sloping beach : Free surface profiles comparison between numerical results (*solid lines*) and experimental data (*dots*) at several times during the breaking ; $t^* = t(g/h_0)^{1/2}$.

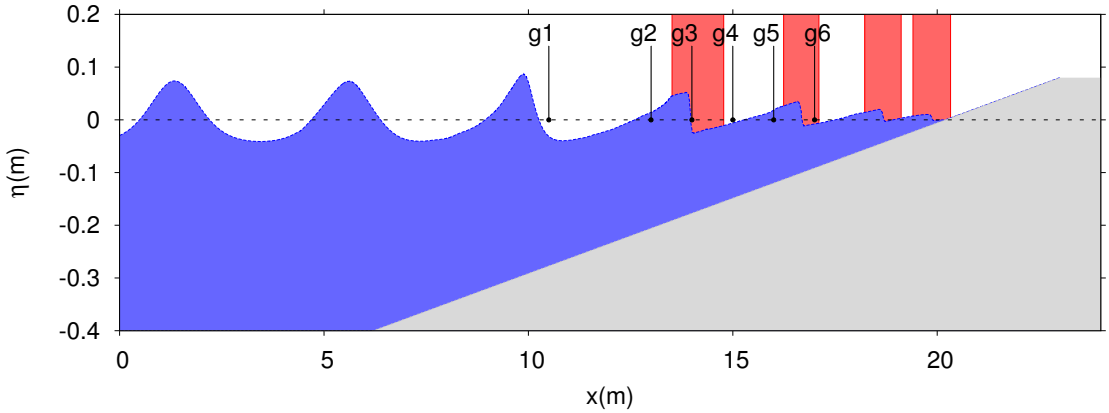

Figure V .17: Cox's experiment : Sketch of the basin and identification of breaking areas. The NSW equations are used in red areas to describe the breaking waves.

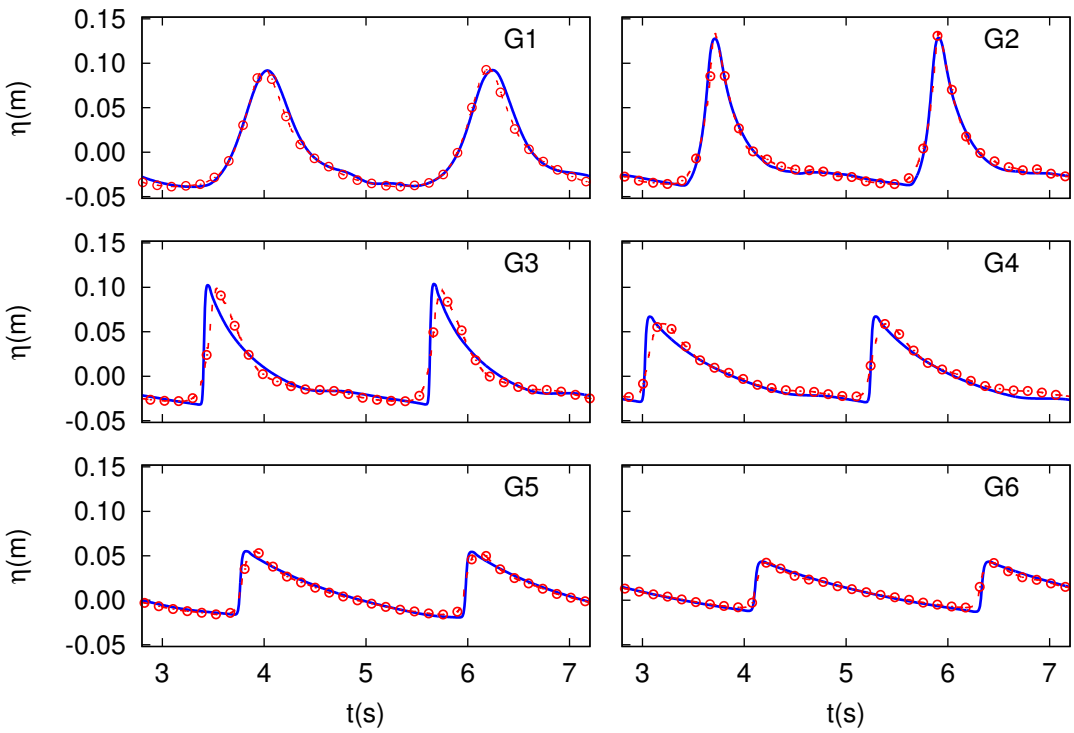

Figure V .18: Cox's experiment : Comparison between computed and experimental time series of total free surface at the gauges. Experimental data appear in solid lines.

free surface elevation at the six wave gauges along the domain and the comparison with the data taken from the experiment. We observe a very good matching. A similar level of agreement can be obtained by reducing the number of elements and increasing the polynomials order, for instance $N = 2$ and $|C_i| = 0.1$. Note also that the limiter [53] is not applied in the whole switching (red) areas but only on the few *troubled elements* in the vicinity of the discontinuities.

V.4.8 Wave overtopping a seawall

We aim at demonstrating that our numerical model appear as a promising tool for more complex simulations. The following test is based on the experiments carried on at the Tainan Hydraulics Laboratory (THL), National Cheng Kung University. It implies a tsunami-like solitary wave collapsing on a seawall located on a 1:20 sloping beach. A cross-section of the 22 m flume is described in Fig. V .19, together with the location of several gauges where measurements of the free surface are available (see [149] for more details). We consider an initial water depth of 0.2 m, and an incoming wave with a relative amplitude $a/h_0 = 0.35$. For this simulation we set $N = 2$ and we use two mesh sizes: $|C_i| = 0.03$ for $9 < x < 12$

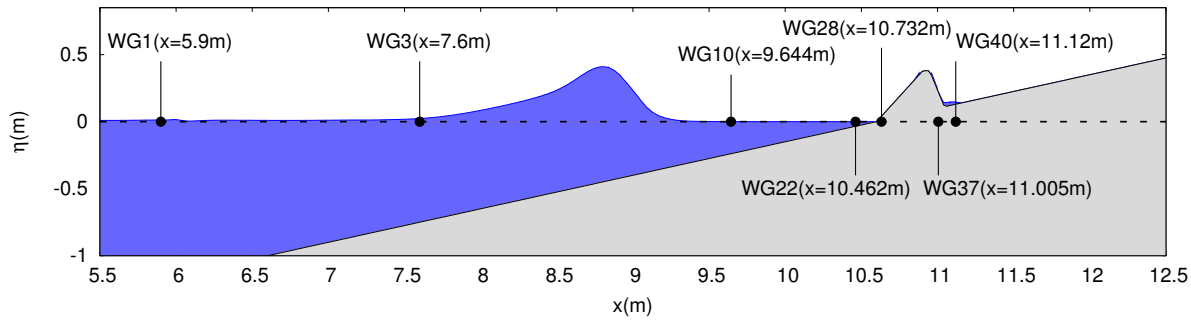

Figure V .19: Overtopping over a seawall : Sketch of the basin and gauge locations.

and $|C_i| = 0.09$ elsewhere, giving a total number of $N_e = 300$ elements. In this case, the solitary wave encounters breaking before reaching the seawall. It follows an overtopping flow supplemented by a train of reflected waves generated by the impact on the wall. The main steps of the propagation are available on Fig. V .20. Time series of the free surface were recorded at several gauges along the computational domain, and are compared with experimental data (see Fig. V .21). We can note a very good agreement, similar to those exhibited in [149] obtained with a Volume Of Fluid (VOF) method for the Reynolds averaged Navier-Stokes equations and [268] with a hybrid FVM discretization of the original GN equations. Note that a similar level of agreement can be obtained with a regular mesh of 500 elements.

V.4.9 Overtopping over fringing reefs

For our last validation we follow the test case issued from the database of hydraulic overtopping processes performed in [246]. We consider a 83.7m long wave flume, the mean water depth is $h_0 = 2.5\,m$. The reef slope is $1/12$ with a crest $0.065\,m$ above the mean water level. We study the propagation and transformations of a solitary wave of relative amplitude $a/h_0 = 0.3$. This is a discriminating test case, as the model has to simultaneously handle shoaling, wave-breaking, hydraulic jumps and wetting and drying processes, over a complex topography. Indeed, the wave shoals, encounters breaking on the crest of the reef, and propagates as a hydraulic jump towards the right side wall before being reflected.
A sketch of the computational domain is available on Fig. V .22, where the bottom variations can also be assessed. The location of the 14 wave gauges providing measurements of the free surface is also reported.

The computation is performed with $N = 2$ and $N_e = 500$. We enforce a solid-wall boundary condition at two boundaries. We show on Fig. V .23 some snapshots of the non-dimensionalized free surface η/h_0 at several times during the wave propagation (with the non-dimensionalized time $t^* = t\sqrt{g/h}$), and compare with the experimental data. We can observe very satisfying results during

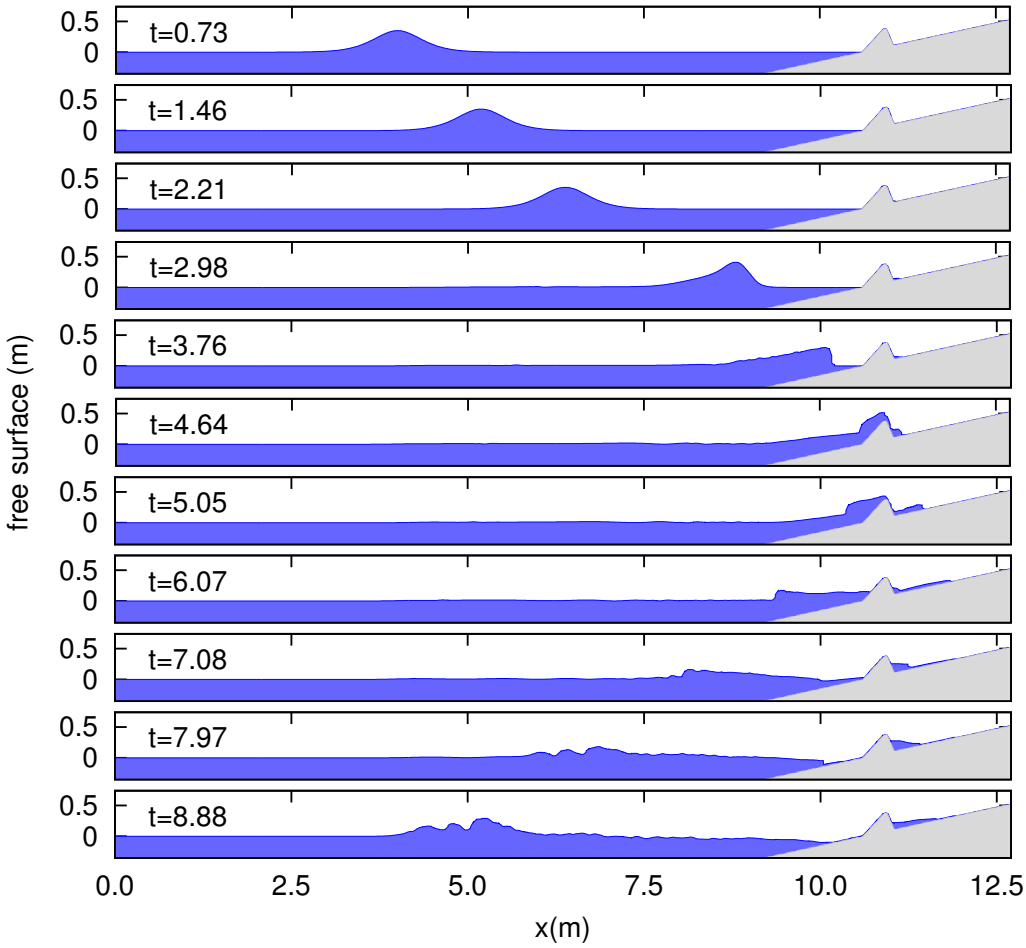

Figure V .20: Overtopping over a seawall : Free surface profiles at several times during the propagation.

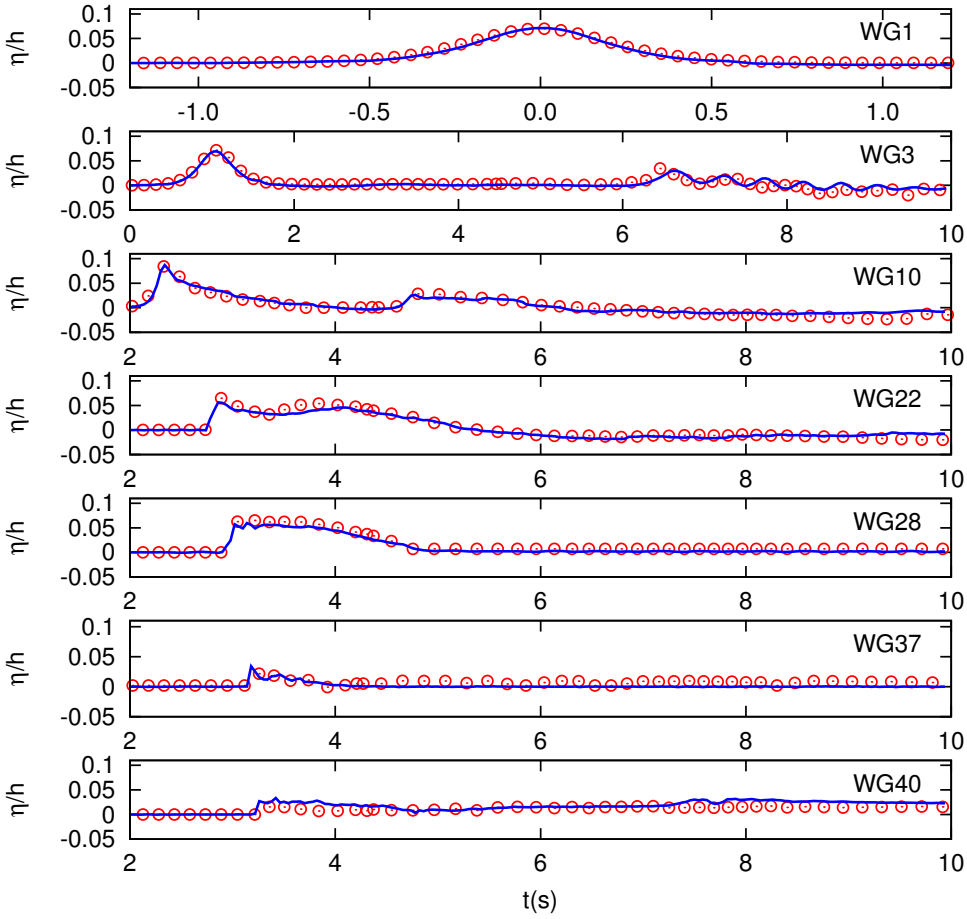

Figure V .21: Overtopping over a seawall : Comparison between computed and experimental data of total free surface at several times during the propagation. Circles denote numerical data.

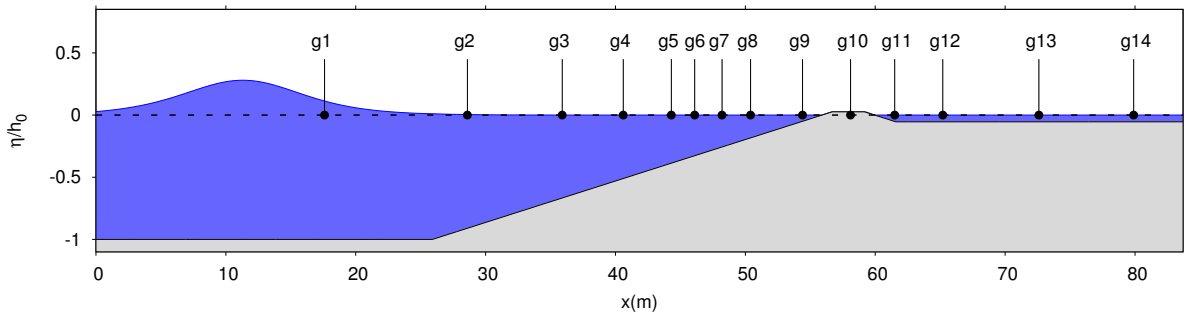

Figure V .22: Overtopping over fringing reefs : Sketch of the basin.

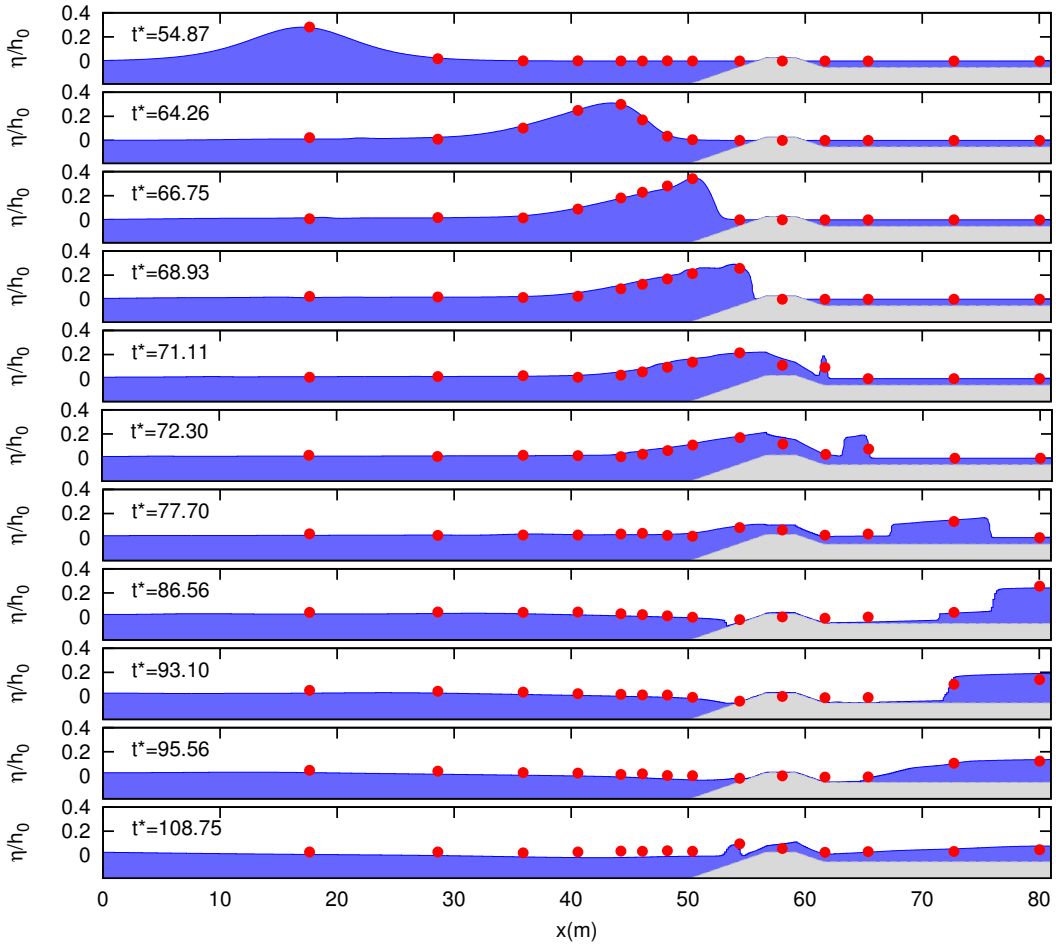

Figure V .23: Overtopping over fringing reefs : Comparison between computed and experimental data for the free surface elevation, at several times during the propagation. Circles denote experimental data.

all the propagation but there appear to be an under-prediction of the water level at the left of the crest, starting at approximatively $t^* = 95$, which may be due to the switching strategy. Indeed, we were not able to correctly stabilize the computation without suppressing the dispersive effects in a large area at the right of the crest.

Conclusion

In this work, an arbitrary order dG discretization is proposed for a new family of 1d Green-Naghdi equations for the simulation of fully non-linear and weakly dispersive waves propagation and transformation over uneven bottom. Based on the previous 2d works, this approach provides robustness and preservation of motionless steady states. These new models are shown to be more computationally efficient than the original ones, especially for high order polynomial expansions. We also propose a simple way to handle broken waves, which gives satisfying results. The proposed methodology can be straightforwardly extended

to the 2d framework, with the use of unstructured meshes. The 2d models with time-independent operator are already derived in [184] and the extension of the present dG method is studied in an on-going work. This appears as a promising tool in terms of possible decreasing of the degrees of freedom and local adaptivity in complex geometries.

Conclusion et perspectives

Au cours de ces travaux nous avons développé des outils numériques capables de fournir des approximations précises de plusieurs modèles d'écoulements. Les schémas proposés ont tous été conçus sur la base des contraintes identifiées au cours de la partie préliminaire, et sont donc capables de préserver les états d'équilibre au repos, produire systématiquement des hauteurs d'eau positives et tolérer la présence de fond sec. Le contexte dominant des maillages non structurés permet en outre une gestion très robuste et efficace de géométries complexes et topographies irrégulières, voire même discontinues.

Les premiers résultats présentés concernent des méthodes Volumes Finis, développées au cours des Chapitres II et III. Nous avons dans un premier temps étendu l'approche 1d *pre balanced* [194, 195] à des maillages non structurés, en déduisant de manière directe des resultats de well-balancing et robustesse. La méthode présente l'avantage d'une formulation simple et admet des extensions d'ordre élevé qui préservent naturellement ses caractéristiques. En particulier, le simple choix d'un flux consistant permet d'obtenir la C-propriété, même dans des configurations type "sec/mouillé". En outre, au cours de nos investigations sur les schémas MUSCL, nous avons été en mesure d'exhiber une CFL garantissant la préservation des états admissibles sous la condition que le schéma 1d d'ordre 1 préserve la positivité de la hauteur d'eau. Il en résulte un modèle stable, facile d'implémentation et potentiellement compatible avec plusieurs autres solveurs numériques que ceux proposés.

Nous nous sommes ensuite intéressés aux problèmes posés par l'inclusion des termes de friction, en particulier lorsqu'il s'expriment à travers des lois de type Manning ou Darcy, qui menacent la stabilité des calculs impliquant des profondeurs d'eau evanescentes. Nous avons apporté des éléments de réponse en procédant une fois encore à l'extension de schémas 1d, basés sur une modification des états intermédiaires dans le cône de dépendance du solveur HLL. La stratégie génère un terme source permettant d'approcher de manière consistante la loi de friction tout en s'affranchissant du problème des divisions par h. Nous avons pu incorporer cette méthode dans notre approche Volumes Finis et il en résulte un schéma bénéficiant d'un domaine d'application étendu à des situations réalistes et conservant de bonnes propriétés de stablilité. Deuxièmement, nous nous sommes aventurés dans les problématiques des schémas Asymptotic Preserving, en tentant d'assurer au niveau discret la préservation du régime diffusif obtenu à partir des équations relaxées. Nous avons pu identifier

quelques contextes dans lesquels ce nouveau schéma semble se distinguer des approches classiques. Sans surprise, ces disparités apparaissent assez clairement lorsque l'on s'approche du régime asymptotique. C'est typiquement le cas pour des simulations faisant intervenir de faibles hauteur d'eau et où les termes de résistance vont avoir tendance à contrôler l'évolution de l'écoulement. En l'absence de solution exacte dans ce contexte, de cas tests expérimentaux suffisamment discriminants et autres résultats de référence, il est toutefois difficile d'évaluer les bénéfices réels apportés par un telle propriété. Ce travail constitue une première proposition d'amélioration à laquelle d'autres modèles de même nature pourraient être comparés.

Se détachant du cadre des Volumes Finis, nous avons ensuite envisagé la discrétisation des équations Shallow Water *pre balanced* via les méthodes dG. Moyennant l'introduction d'un terme de correction induit par la présence d'intégrales de surface, la méthode de reconstruction proposée dans le contexte des Volumes Finis s'est naturellement étendue à ce cadre, assurant ainsi la préservation de configurations type "*lac au repos*" à tout ordre. Des méthodes de limitation ont dû être introduites pour prévenir l'apparition d'oscillations provoquées par les modes élevés au voisinage des forts gradients. La mise en place d'un détecteur de choc permet d'activer ces procédés uniquement dans les zones nécessitant leur application, maintenant ainsi un bon niveau de précision dans le reste du domaine. Une partie importante des travaux est consacrée à la robustesse du modèle, considérée à travers la hauteur d'eau moyenne. Le résultat s'établit grâce à un choix pertinent de règles de quadrature, qui nous amène à invoquer les propriétés de positivité du schéma Volumes Finis. Les résultats numériques obtenus témoignent de l'efficacité de la méthode, qui se montre stable dans un grand nombre de contextes relativement délicats. L'utilisation de polynômes d'ordre arbitraire au sein des éléments permet véritablement d'apporter un meilleur degré de précision. A première vue, il semblerait que le schéma dG d'ordre 2 se montre légèrement plus efficace que les méthodes MUSCL du schéma Volumes Finis.

Dans un dernier chapitre nous avons exploité la versatilité des méthodes dG pour étendre la méthode précédente aux équations dispersives. Nous y proposons un schéma numérique 1d pour une nouvelle classe de modèles Green Naghdi, présentant des caractérisitques très intéressantes dans la perspective de la résolution numérique. L'approche se base sur les principes de résolution déjà introduits, et aboutit à un schéma well balanced et robuste. Ce travail s'est vu considérablement facilité des lors que les termes dispersifs ont pu être interprétés comme un terme source additionnel dans les équations de Saint-Venant. Deux problématiques nouvelles sont apparues: la prise en compte du déferlement ainsi que l'évaluation des dérivées d'ordre élevé. Concernant le premier point, l'outil de détection des chocs précédemment utilisé pour marquer les forts gradients s'est révélé efficace, permettant la suppression du terme source dispersif dans les zones appropriées, et la mise en place d'une stratégie hybride. Les dérivées d'ordre élevé ont été traitées avec les méthodes *LDG*, dont on a pu apprécier la

supériorité par rapport aux flux centrés *BR*. Dans le cas de résolutions d'ordre élevé, l'introduction d'un filtre a été nécessaire pour tempérer l'impact des modes les plus élevés et stabiliser les calculs. Les simulations numériques ont confirmé les gains de temps apportés par ce nouveau modèle ainsi que l'efficacité de l'approche numérique, capable de gérer convenablement le déferlement dans des situations difficiles.

Perspectives

Les problématiques soulevées au cours de ces travaux sont nombreuses et de nature très variée.

Tout d'abord, l'introduction du concept de schéma AP dans le cadre des équations *Shallow Water* laisse un grand nombre de questions ouvertes. Il apparait que cette propriété pourrait avoir, même dans certains contextes réalistes, une influence majeure sur le comportement des approximations numériques. Ces résultats préliminaires semblent s'aligner avec ceux obtenus en 1d et appellent à être confirmés par une batterie d'expériences et validations supplémentaires. Des investigations plus poussées sont toutefois nécessaires pour s'assurer d'une discrétisation plus conforme du régime diffusif et une évaluation rigoureuse des termes de correction. Il s'agit là d'un objectif ambitieux car l'évaluation de la hauteur d'eau s'en voit affectée, avec des répercussions possibles sur les propriétés de well balancing et robustesse. Ces aspects ouvrent donc la voie à plusieurs pistes de travail et pourraient motiver des études supplémentaires.

Comme nous l'avons évoqué, la préservation des états d'équilibre constitue un enjeu de taille dans l'élaboration d'un modèle numérique. Dans la construction de nos schémas nous nous sommes uniquement focalisés sur la préservation des états d'équilibre au repos, mais il semblerait, d'après nos investigations numériques, que le schéma présente un bon comportement vis à vis d'autres types d'états stationnaires, et ce pour les approches Volumes Finis et Galerkin discontinu. Une analyse plus profonde des schémas dans cette optique pourrait s'avérer fructueuse. L'instauration de nouveaux résultats concernant la préservation d'états d'équilibre en mouvement paraît envisageable et permettrait d'améliorer la qualité de nos modèles.

Même si en pratique le solveur VFRoe a produit des hauteurs d'eau positives sous des CFL appropriées, les propriétés de robustesse restent à établir pour ce solveur, et plus généralement pour d'autres méthodes d'approximation des flux. Dans la continuité, des travaux additionnels sont nécessaires pour adapter les approches proposées pour intégrer la friction, présentement basées sur le schéma de Rusanov, à d'autres types de flux numériques. Des résultats de robustesse concernant les reconstructions MUSCL appliquées au schéma AP sont aussi à étudier.

Malgré le léger avantage que laisse apparaître la méthode dG d'ordre 2 sur les méthodes MUSCL pour les exemples traités, il est à ce stade toujours difficile de donner des éléments d'appréciation précis permettant de choisir une méthode plutôt qu'une autre. La composante temps de calcul doit être intégrée à cette évaluation et rend l'analyse très dépendante des choix d'implémentation, qui sont particulièrement larges pour les méthodes dG (base d'expansion, méthodes de quadrature, évaluation des flux numériques...). Un important travail d'optimisation doit être mené sur un plan informatique pour les deux méthodes afin d'apporter des réponses. Comme sujet connexe, des études en termes d' "*h/p*" adaptativité restent à être effectuées sur le schéma dG, dont l'extension à des polynômes d'ordre arbitraire est plus récente.

L'approche numérique du modèle Green-Naghdi par les méthodes dG offre à elle seule des perspectives de travail très nombreuses.

L'étude 1d a permis de soulever toute l'importance et la difficulté du problème des conditions limites. La mise en place de zones de relaxation nécessite la calibration d'un jeu de constantes pouvant présenter des profils totalement différents selon le type de simulation considéré, et ne suffit pas toujours à assurer la stabilité des calculs. A ceci s'ajoutent les difficultés propres à la méthode comme la prise en compte des conditions de bord dans les matrices de différentiation. Des travaux supplémentaires sembleraient donc nécessaires dans cette direction.

Ensuite, la gestion du déferlement doit faire l'objet d'investigations plus complètes. Le réel r fixant la largeur de la zone dans laquelle les effets dispersifs sont supprimés doit lui aussi être ajusté en fonction du problème. De plus, la considération d'ordres polynomiaux élevés peut favoriser l'apparition d'instabilités au niveau des zones de transition GN/NSW, pouvant rapidement se propager et s'amplifier, et à terme entraîner l'activation du limiteur sur l'ensemble du domaine. Il se pose donc à ce niveau un problème de couplage relativement complexe. Il conviendrait donc de travailler à une amélioration de cette stratégie, en envisageant par exemple d'enrichir le critère de détection et/ou d'assurer une meilleure communication entre les deux modèles.

A terme, l'objectif réside naturellement dans l'extension du schéma proposé sur maillages non structurés, avec l'intégration éventuelle du modèle à 3 paramètres [70] pour améliorer le domaine de validité du système. Une discrétisation Volumes Finis a récemment été proposée [184], et une version dG actuellement à l'étude.

Publications

Ces travaux on fait l'objet des publications suivantes :

[-1-] A. Duran, F. Marche, Q. Liang. On the well-balanced numerical discretization of shallow water equations on unstructured meshes. *J. Comput. Phys.* 235:565-586 - 2013.

[-2-] A. Duran, F. Marche. Recent advances on the discontinuous Galerkin method for shallow water equations with topography source terms. In press, `http://www.sciencedirect.com/science/article/pii/S0045793014002369` - 2014.

Les papiers ci-dessous sont en cours de révision :

[-3-] A. Duran. A robust and well-balanced scheme for the Shallow Water system with friction source term on unstructured meshes - Février 2014.

[-4-] C. Berthon, A. Duran, F. Marche, R. Turpault. Asymptotic Preserving scheme for the Shallow Water equations with source terms on unstructured meshes - Décembre 2013.

[-5-] A. Duran, F. Marche. Discontinuous-Galerkin discretization of a new class of Green-Naghdi equations - Mars 2014.

Bibliography

[1] R. Abgrall. On essentially non-oscillatory schemes on unstructured meshes: Analysis and implementation. *J. Comp. Phy.*, 114:45–58, 1994.

[2] V. Aizinger and C. Dawson. A discontinuous galerkin method for two-dimensional flow and transport in shallow water. *Adv. Wat. Res.*, 25:67–84, 2002.

[3] B. Alvarez and D. Lannes. A nash-moser theorem for singular evolution equations. application to the serre and green-naghdi equations. *Indiana Univ. Math. J.*, 57:97–131, 2008.

[4] V.R. Ambati. Flooding and drying in discontinuous Galerkin discretizations of shallow water equations. In *European Conference on Computational Fluid Dynamics*, 2006.

[5] K. Anastasiou and C.T. Chan. Solution of the 2d shallow water equations using the finite volume method on unstructured triangular meshes. *Int. J. Numer. Meth. Fluids*, 24:1225–1245, 1997.

[6] N. Crnjaric-Zic ans S. Vukovic and L. Sopta. Balanced finite volume weno and central weno schemes for the shallow water and the open-channel flow equations. *J. Comp. Phys.*, 200:512–548, 2004.

[7] D. Aregba-Driollet, M. Briani, and R. Natalini. Asymptotic high order preserving schemes for 2 $\times$ 2 dissipative hyperbolic systems. *SIAM J. Numer. Anal.*, 46:869–894, 2008.

[8] P. Arminjon, M.C. Viallon, and A. Madrane. A finite volume extension of the lax-friedrichs and nessyahu-tadmor schemes for conservation laws on unstructured grids. *Int. J. Comp. Fluid Dyn.*, 9:1–22, 1998.

[9] D.N. Arnold, F. Brezzi, B. Cockburn, and L.D. Marini. Unified analysis of discontinuous Galerkin methods for elliptic problems. *SIAM J. Numer. Anal.*, 39(5):1749–1779, 2002.

[10] E. Audusse, F. Bouchut, M.O. Bristeau, R. Klein, and B. Perthame. A fast and stable well-balanced scheme with hydrostatic reconstruction for shallow water flows. *SIAM J. Sci. Comput.*, 25:2050–2065, 2004.

[11] E. Audusse and M.O. Bristeau. Transport of pollutant in shallow water - a two time steps kinetic method. *Math. Mod. and Num. Anal.*, 37:389–416, 2003.

[12] E. Audusse and M.O. Bristeau. A well balanced positivity preserving "second-order" scheme for shallow water flows on unstructured meshes. *J. Comput. Phys.*, 206:311–333, 2005.

[13] F. Aureli, P. Mignosa, and M. Tomirotti. Dam-break flows in presence of abrupt bottom variations. In *In: Proc. XXVIII IAHR Congr., Graz, Austria*, pages 163–171, 1999.

[14] C. Bardos, A.Y. Le Roux, and J-C. N'ed'elec. First order quasilinear equations with boundary conditions. *Comm. Part. Diff. Eq.*, 4:1017–1034, 1979.

[15] T. Barth and P.O. Fredericksson. Higher order solution of the euler equations on unstructured grids using quadratic reconstruction. In *Proceedings of the AIAA 28th Aerospace Sciences Meeting 90-0013*, 1990.

[16] T. Barth and D. Jespersen. The design and application of upwind schemes on unstructured meshes. In *Proceedings of the AIAA 27th Aerospace Sciences Meeting 89-0366*, 1989.

[17] F. Bassi and S. Rebay. A high-order accurate discontinuous finite element method for the numerical solution of the compressible Navier−Stokes equations. *J. Comput. Phys.*, 131:267–279, 1997.

[18] S. Beji and J.A. Battjes. Experimental investigation of wave propagation over a bar. *Coast. Engrg.*, 19:151–162, 1993.

[19] F. Benkhaldoun, I. Elmahi, and M. Seaid. A new finite volume method for flux-gradient and source-term balancing in shallow water equations. *Comp. Meth. App. Mech. Eng.*, 199:3324–3335, 2010.

[20] A. Bermudez and M.-E. Vazquez. Upwind methods for hyperbolic conservation laws with source terms. *Comput. & Fluids*, 23:1049–1071, 1994.

[21] C. Berthon. Robustness of MUSCL schemes for 2D unstructured meshes. *J. Comput. Phys.*, 218:495–509, 2006.

[22] C. Berthon, P. Charrier, and B. Dubroca. An hllc scheme to solve the m1 model of radiative transfer in two space dimensions. *J. Sci. Comput.*, 31:347–389, 2007.

[23] C. Berthon, J. Dubois, B. Dubroca, T.-H. Nguyen-Bui, and R. Turpault. A free streaming contact preserving scheme for the m1 model. *Adv. App. Math. Mech.*, 2:259–285, 2010.

[24] C. Berthon and F. Foucher. Efficient well balanced hydrostatic upwind schemes for shallow water equations. *J. Comput. Phys.*, 231:4993–5015, 2012.

[25] C. Berthon, P. LeFloch, and R. Turpault. Late-time/stiff-relaxation asymptotic-preserving approximations of hyperbolic equations. *Math. Comp.*, 82:831–860, 2013.

[26] C. Berthon and F. Marche. A positive preserving high order VFRoe scheme for shallow water equations: a class of relaxation schemes. *SIAM J. Sci. Comput.*, 30:2587–2612, 2008.

[27] C. Berthon, F. Marche, and R. Turpault. An efficient scheme on wet/dry transitions for shallow water equations with friction. *Comput. & Fluids*, 48:192–201, 2011.

[28] C. Berthon and R. Turpault. Asymptotic preserving hll schemes. *Num. Meth. Part. Diff. Eq.*, 27:1396–1422, 2011.

[29] S. Bianchini, B. Hanouzet, and R. Natalini. Asymptotic behavior of smooth solutions for partially dissipative hyperbolic systems with a convex entropy. *Commun. Pure Appl. Math.*, 60:1559–1622, 2007.

[30] F. Bianco, G. Puppo, and G. Russo. High-order central schemes for hyperbolic systems of conservation laws. *SIAM J. Sci. Comput.*, 21:294–322, 1999.

[31] H.B. Bingham, P.A. Madsen, and D.R. Fuhrman. Velocity potential formulations of highly accurate Boussinesq-type models. *Coast. Eng.*, 56:467–478, 2009.

[32] O. Bokhove. Flooding and drying in finite-element discretizations of shallow-water equations. part 2: Two dimensions, 2003. Imported from MEMORANDA.

[33] O. Bokhove. Flooding and drying in discontinuous galerkin finite-element discretizations of shallow-water equations. *J. Sci. Comput.*, 22:47–82, 2005.

[34] A. Bollermann, S. Noelle, and M. Lukacova-Medvidova. Finite volume evolution Galerkin methods for the shallow water equations with dry beds. *Commun. Comput. Phys.*, 10:371–404, 2011.

[35] P. Bonneton. Modelling of periodic wave transformation in the inner surf zone. *Ocean Engrg.*, 34(10):1459–1471, 2007.

[36] P. Bonneton, E. Barthélemy, F. Chazel, R. Cienfuegos, D. Lannes, F. Marche, and M. Tissier. Recent advances in Serre / Green - Naghdi modelling for wave transformation, breaking and runup processes. *Eur. J. Mech. B/Fluids*, 30:589–597, 2011.

[37] P. Bonneton, F. Chazel, D. Lannes, F. Marche, and M. Tissier. A splitting approach for the fully nonlinear and weakly dispersive Green - Naghdi model. *J. Comput. Phys.*, 230:1479–1498, 2011.

[38] F. Bouchut. Entropy satisfying flux vector splittings and kinetic bgk models. *Numer. Math.*, 94:623–672, 2003.

[39] F. Bouchut. *Nonlinear stability of finite volume methods for hyperbolic conservation laws, and well-balanced schemes for sources*. Frontiers in Mathematics. Birkhauser, 2004.

[40] F. Bouchut, H. Ounaissa, and B. Perthame. Upwinding of the source term at interfaces for euler equations with high friction. *Comput. Math. App.*, 53:361–375, 2007.

[41] F. Bouchut, J. Le Sommer, and V. Zeitlin. Frontal geostrophic adjustment and nonlinear wave phenomena in one-dimensional rotating shallow water. part 2. high-resolution numerical simulations. *J. Fluid Mech.*, 514:35–63, 2004.

[42] S.F. Bradford and B.F. Sanders. Finite-volume model for shallow-water flooding of arbitrary topography. *J. Hydr. Engrg.*, 128:289–298, 2002.

[43] M.-O. Bristeau and B. Coussin. Boundary conditions for the shallow water equations solved by kinetic schemes. *INRIA Report RR-4282*, 2001. http://www.inria.fr/RRRT/RR-4282.html.

[44] A.R. Brodtkorb, M.L. Sætra, and M. Altinakar. Efficient shallow water simulations on GPUs : Implementation, visualization, verification and validation. *Comput. & Fluids*, 55:1–12, 2012.

[45] P. Brufau, M.E. Vazquez-Cendon, and P. Garcia-Navarro. A numerical model for the flooding and drying of irregular domains. *Int. J. Numer. Meth. Fluids.*, 39:247–275, 2002.

[46] S. Bryson, Y. Epshteyn, A. Kurganov, and G. Petrova. Well-balanced positivity preserving central-upwind scheme on triangular grids for the Saint-Venant system. *ESAIM Math. Model. Numer. Anal.*, 45:423–446, 2011.

[47] C. Buet and S. Cordier. An asymptotic preserving scheme for hydrodynamics radiative transfer models: numerical scheme for radiative transfer. *Numer. Math.*, 108:199–221, 2007.

[48] C. Buet and B. Després. Asymptotic preserving and positive schemes for radiation hydrodynamics. *J. Comput. Phys.*, 215:717–740, 2006.

[49] C. Buet, B. Després, and E. Franck. Design of asymptotic preserving finite volume schemes for the hyperbolic heat equation on unstructured meshes. *Numer. Math.*, 122:227–278, 2012.

[50] T. Buffard, T. Gallouet, and J.M. Hérard. A naive godunov scheme to solve the shallow water equations. *CR Acad. Sci. Paris*, 326:385–390, 1998.

[51] T. Buffard, T. Gallouet, and J.M. Hérard. A sequel to a rough godunov scheme: application to real gases. *Comput. & Fluids*, 29:813–847, 2000.

[52] S. Bunya, E.J. Kubatko, J.J. Westerink, and C. Dawson. A wetting and drying treatment for the runge–kutta discontinuous galerkin solution to the shallow water equations. *Comput. Meth. Appl. Mech. Engrg.*, 198:1548–1562, 2009.

[53] A. Burbeau, P. Sagaut, and Ch.-H. Bruneau. A problem-independent limiter for high-order runge–kutta discontinuous Galerkin methods. *J. Comput. Phys.*, 169:111–150, 2001.

[54] J. Burguete and P. Garcia-Navarro. Efficient construction of high-resolution tvd conservative schemes for equations with source terms : application to shallow water flows. *Int. J. Numer. Meth. Fluids*, 37:209–248, 2001.

[55] J. Burguete, P. Garcia-Navarro, and J. Murillo. Friction term discretization and limitation to preserve stability and conservation in the 1d shallow-water model: Application to unsteady irrigation and river flow. *Int. J. Numer. Meth. Fluids*, 58:403–425, 2008.

[56] V. Caleffi, A. Valiani, and A. Bernini. Fourth-order balanced source term treatment in central WENO schemes for shallow water equations. *J. Comput. Phys.*, 218:228–245, 2006.

[57] S. Camarri, M.V. Salvetti, B. Koobus, and A. Dervieux. A low-diffusion muscl scheme for les on unstructured grids. *Comput. & Fluids*, 33:1101–1129, 2004.

[58] G. Carrier and H. Greenspan. Water waves of finite amplitude on a sloping beach. *J. Fluid Mech.*, 2:97–109, 1958.

[59] M. Castro, J. Gonzales, and C. Pares. Numerical treatment of wet/dry fronts in shallow flows with a modified roe scheme. *Math. Mod. Meth. Appl. Sci.*, 16:897–931, 2006.

[60] M. Castro, A. Milanes, and C Pares. Well-balanced numerical schemes based on a generalized hydrostatic reconstruction technique. *Math. Mod. Meth. Appl. Sci.*, 17:2055–2113, 2007.

[61] M.J. Castro, J.A. Lopez-Garcia, and C. Pares. High order exactly well-balanced numerical methods for shallow water systems. *J. Comput. Phys.*, 246:242–264, 2013.

[62] M. Cathala. Asymptotic shallow water models with non smooth topographies. *http://hal.archives-ouvertes.fr/hal-00804047*, 2013.

[63] L. Cea and M.E. Vázquez-Cendón. Unstructured finite volume discretization of bed friction and convective flux in solute transport models linked to the shallow water equations. *J. Comput. Phys.*, 231:3317–3339, 2012.

[64] C. Cercignani. *The Boltzmann equation and its applications*. Applied Mathematical Sciences 67. New York. Springer-Verlag, 1988.

[65] E.M. Chaabelasri, N. Salhi, I. Elmahi, and F. Benkhaldoun. High order well balanced scheme for treatment of transcritical flow with topography on adaptive triangular mesh. *Phys. Chem. News*, 53:119–128, 2010.

[66] C. Chalons, F. Coquel, E. Godlewski, P.-A. Raviart, and N. Seguin. N. seguin Godunov-type schemes for hyperbolic systems with parameter dependent source. the case of euler system with friction. *Math. Model. Methods Appl. Sci.*, 20:2109–2166, 2010.

[67] T.-J. Chang, K.-H. Chang H.-M. Kao, and M.-H. Hsu. Numerical simulation of shallow-water dam break flows in open channels using smoothed particle hydrodynamics. *J. Hydro.*, 408:78–90, 2011.

[68] H. Chanson. Analytical solution of dam break wave with flow resistance. application to tsunami surges. *XXXI Congress, IHAR*, pages 3341–3353, 2005.

[69] G. Chavent and J. Jaffré. Mathematical models and finite elements for reservoir simulation. *Studies in Mathematics and its applications, North Holland, Amsterdam*, 1986.

[70] F. Chazel, D. Lannes, and F. Marche. Numerical simulation of strongly nonlinear and dispersive waves using a Green - Naghdi model. *J. Sci. Comput.*, pages 105–116, 2011.

[71] G.Q. Chen, C.D. Levermore, and T.P. Liu. Hyperbolic conservation laws with stiff-relaxation terms and entropy. *Comm. Pure Appl. Math.*, 47:787–830, 1995.

[72] Q. Chen, J.T. Kirby, R.A. Dalrymple A.B. Kennedy, and A. Chawla. Boussinesq modeling of wave transformation, breaking, and runup. I: 2D. *J. Waterway Port Coast. Ocean Eng.*, 126:48–56, 2000.

[73] S. Chippada, C.N. Dawson, M.L. Martinez, and M.F. Wheeler. A Godunov-type finite volume method for the system of shallow water equations. *Comput. Meth. App. Mech. Engrg.*, 151:105–129, 1998.

[74] R. Cienfuegos, E. Barthélemy, and P. Bonneton. A fourth-order compact finite volume scheme for fully nonlinear and weakly dispersive Boussinesq-type equations. I: Model development and analysis. *Int. J. Numer. Meth. Fluids*, 51(11):1217–1253, 2006.

[75] R. Cienfuegos, E. Barthélemy, and P. Bonneton. A fourth-order compact finite volume scheme for fully nonlinear and weakly dispersive Boussinesq-type equations. Part II: Boundary conditions and validation. *Int. J. Numer. Meth. Fluids*, 53:1423–1455, 2007.

[76] R. Cienfuegos, E. Barthélemy, and P. Bonneton. Wave-breaking model for Boussinesq type equations including roller effects in the mass conservation equation. *J. Water. Port. Coast. Oc. Eng.*, 136:10–26, 2010.

[77] B. Cockburn and C.-W. Shu. The Local Discontinuous Galerkin method for time-dependent convection-diffusion systems. *SIAM J. Numer. Anal.*, 141:2440–2463, 1998.

[78] B. Cockburn and C.-W. Shu. The Runge-Kutta discontinuous Galerkin method for conservation laws V. *J. Comput. Phys.*, 141:199–224, 1998.

[79] B. Cockburn and C.-W. Shu. Runge-Kutta discontinuous Galerkin methods for convection-dominated problems. *J. Sci. Comput.*, 16:173–261, 2001.

[80] F. Coquel and B. Perthame. Relaxation of energy and approximate riemann solvers for general pressure laws in fluid dynamics. *SIAM J. Numer. Anal.*, 35:2223–2249, 1998.

[81] P.H. Cournède, C. Debiez, and A. Dervieux. A Positive MUSCL Scheme for Triangulations. Technical Report RR-3465, INRIA, 1998.

[82] D.T. Cox. Experimental and numerical modelling of surf zone hydrodynamics. *Univ. of Delaware, Newark*, 1995.

[83] P. Crispel, P. Degond, and M.-H. Vignal. An asymptotic preserving scheme for the two-fluid euler-poisson model in the quasi-neutral limit. *J. Comput. Phys.*, 223:208–234, 2007.

[84] S.F. Davis. Simplified second-order godunov-type methods. *SIAM J. Sci. Stat. Comput*, 9:445–473, 1988.

[85] T.A. Davis and I.S. Duff. An unsymmetric-pattern multifrontal method for sparse LU factorization. *SIAM J. Matrix Anal. and App.*, 18:140–158, 1997.

[86] C. Dawson and V. Aizinger. A discontinuous Galerkin method for three-dimensional shallow water equations. *J. Sci. Comput.*, 22-23:245–267, 2005.

[87] A.J.C. de Saint Venant. Théorie du mouvement non-permanent des eaux, avec application aux crues des rivières et à l'introduction des marées dans leur lit. *C.R. Acad. Sc. Paris*, 73:147–154.

[88] P. Degond, F. Deluzet, A. Sangam, and M.-H. Vignal. A numerical scheme for a viscous shallow water model with friction. *J. Comput. Phys.*, 228:3540–3558, 2009.

[89] O. Delestre. *Simulation du ruissellement d'eau de pluie sur des surfaces agricoles*. PhD thesis, 2010.

[90] O. Delestre, C. Lucas, P.-A. Ksinant, F. Darboux, C. Laguerre, T.N.T. Vo, F. James, and S. Cordier. A compilation of shallow water analytic solutions for hydraulic and environmental studies. *Int. J. Num. Meth. Fluids.*, 72:269–300, 2013.

[91] O. Delestre and F. Marche. A numerical scheme for a viscous shallow water model with friction. *J. Sci. Comput.*, 48:41–51, 2011.

[92] A.I. Delis and N.A. Kampanis. Numerical flood simulation by depth averaged free surface flow models. In *Environmental Systems - Encyclopedia of Life Support Systems (EOLSS)*, 2009.

[93] A.I. Delis and T. Katsaounis. Relaxation schemes for the shallow water equations. *Int. J. Num. Meth. Fluids*, 41:695–719, 2003.

[94] A.I. Delis and M. Kazolea. A well-balanced finite volume scheme for extended Boussinesq equations on unstructured meshes. In *Fifth International Conference on Advanced Computational Methods in Engineering (ACOMEN 2011)*, 2011.

[95] M.W. Dingemans. Comparison of computations with Boussinesq-like models and laboratory measurements. *Delft Hydr.*, Report H-1684.12, 32, 1994.

[96] K. Djadel, A. Ern, and S. Piperno. A discontinuous Galerkin method for the shallow water equation with bathymetric source terms and dry areas. In *European Conference on Computational Fluid Dynamics*, 2006.

[97] N. Dodd. Numerical model of wave run-up, overtopping, and regeneration. *J. Waterw., Port, Coast. Ocean Eng.*, 124:73–81, 1998.

[98] B. Dubroca and J.-L. Feugeas. Entropic moment closure hierarchy for the radiative transfer equation. *C. R. Acad. Sci. Paris*, 329:915–920, 1999.

[99] A. Duran. A robust and well balanced scheme for the 2d saint-venant system on unstructured meshes with friction source term. *Submitted*, 2014.

[100] D. Dutykh, R. Poncet, and F. Dias. The VOLNA code for the numerical modelling of tsunami waves: generation, propagation and inundation. *Eur. J. Mech. - B/Fluids*, 30:598–615, 2011.

[101] E.Audusse, M.-O. Bristeau, and B. Perthame. Kinetic Schemes for Saint-Venant Equations with Source Terms on Unstructured Grids. Rapport de recherche RR-3989, INRIA, 2000. Projet M3N.

[102] B. Einfeldt. On godunov type methods for gas dynamics. *SIAM J. Numer. Anal.*, 25:294–318, 1988.

[103] A.P. Engsig-Karup, J.S. Hesthaven, H.B. Bingham, and P.A. Madsen. Nodal DG-FEM solution of high-order Boussinesq-type equations. *J. Engrg. Math.*, 56:351–370, 2006.

[104] A.P. Engsig-Karup, J.S. Hesthaven, H.B. Bingham, and T. Warburton. DG-FEM solution for nonlinear wave-structure interaction using Boussinesq-type equations. *Coast. Eng.*, 55:197–208, 2008.

[105] K. Erduran. Further application of hybrid solution to another form of Boussinesq equations and comparisons. *Int. J. Numer. Meth. Fluids*, 53:827–849, 2007.

[106] A. Ern and J.-L. Guermond. Discontinuous Galerkin methods for Friedrichs' systems. i. general theory. *SIAM J. Numer. Anal.*, 44(2):753–778, 2006.

[107] A. Ern and J.-L. Guermond. Discontinuous Galerkin methods for Friedrichs' systems. ii. second-order elliptic pdes. *SIAM J. Numer. Anal.*, 44(6):2363–2388, 2006.

[108] A. Ern, S. Piperno, and K. Djadel. A well- balanced Runge-Kutta discontinuous Galerkin method for the shallow-water equations with flooding and drying. *Int. J. Numer. Meth. Fluids*, 58:1–25, 2008.

[109] C. Eskilsson and S.J. Sherwin. An hp/spectral element model for efficient long-time integration of Boussinesq-type equations. *Coast. Engrg.*, 45:295 – 320, 2003.

[110] C. Eskilsson and S.J. Sherwin. A triangular spectral/hp discontinuous Galerkin method for modelling 2D shallow water equations. *Int. J. Numer. Meth. Fluids*, 45:605–623, 2004.

[111] C. Eskilsson and S.J. Sherwin. Discontinuous Galerkin spectral/hp element modelling of dispersive shallow water systems. *J. Sci. Comp.*, 22 - 23:269–288, 2005.

[112] C. Eskilsson and S.J. Sherwin. Spectral/hp discontinuous Galerkin method for modelling 2D Boussinesq equations. *J. Comput. Phys.*, 212:566–589, 2006.

[113] C. Eskilsson, S.J. Sherwin, and L. Bergdahl. An unstructured spectral/hp element model for enhanced Boussinesq-type equations. *Coast. Engrg*, 53(947–963), 2006.

[114] E. Franck. *Construction et analyse numérique de schémas "asymptotic preserving" sur maillages non structurés. Application à l'équation de transport et aux systèmes de Friedrichs.* PhD thesis, 2012.

[115] O. Friedrich. Weighted essentially non-oscillatory schemes for the interpolation of mean values on unstructured grids. *J. Comput. Phys.*, 144:194–212, 1998.

[116] J.M. Gallardo, C. Parés, and M Castro. On a well-balanced high-order finite volume scheme for shallow water equations with topography and dry areas. *J. Comput. Phys.*, 227:574–601, 2007.

[117] T. Gallouët, J.M. Hérard, and N. Seguin. On the use of some symetrizing variables to deal with vacuum. *Calcolo*, 40:163–194, 2003.

[118] T. Gallouët, J.M. Hérard, and N. Seguin. Some approximate godunov schemes to compute shallow-water equations with topography. *Comput. & Fluids*, 32:479–513, 2003.

[119] T. Gallouët and T. Masella. A rough godunov scheme. *C. R., Math., Acad. Sci. Paris*, 323:77–83, 1996.

[120] P. Garcia-Navarro and M.E. Vazquez-Cendon. Some considerations and improvements on the performance of Roe's scheme for 1d irregular geometries. *Internal Report 23, Departamento de Matematica Aplicada, Universidade de Santiago do Compostela*, 1997.

[121] D.L. George. *Finite Volume methods and adaptative refinement for tsunami propagation and inundation*. PhD thesis, 2006.

[122] J.-F. Gerbeau and B. Perthame. Derivation of viscous saint-venant system for laminar shallow water numerical validation. *Disc. Contin. Dyn. Syst. Ser. B*, 1:89–102, 2001.

[123] J.-M. Ghidaglia and F. Pascal. On boundary conditions for multidimensional hyperbolic systems of conservation laws in the finite volume framework. Technical report, CMLA, ENS Cachan, 2002.

[124] J.-M. Ghidaglia and F. Pascal. The normal flux method at the boundary for multidimensional finite volume approximations in cfd. *Eur. J. Mech. B/Fluids*, 24:1–17, 2005.

[125] F.X. Giraldo, J.S. Hesthaven, and T. Warburton. Nodal high-order discontinuous Galerkin methods for the spherical shallow water equations. *J. Comput. Phys.*, 181:499–525, 2002.

[126] P. Glaister. Prediction of supercritical flow in open channels. *Comput. Math. Appl.*, 24:69–75, 1992.

[127] M.F. Gobbi, J.T. Kirby, and G. Wei. A fully nonlinear Boussinesq model for surface waves. Part 2. Extension to $O(kh)^4$. *J. Fluid Mech.*, 405:181–210, 2000.

[128] E. Godlewski and P.-A. Raviart. *Numerical approximation of hyperbolic systems of conservation laws*. Applied Mathematical Sciences, vol.118, Springer-Verlag, 1996.

[129] S.K. Godunov. A difference method for numerical calculation of discontinuous equations of hydrodynamics. *Mat. Sb.*, pages 271–300, 1959.

[130] L. Gosse. A well-balanced flux-vector splitting scheme designed for hyperbolic systems of conservation laws with source terms. *Comput. Math. Appl.*, 39:135–159, 2000.

[131] L. Gosse. A well-balanced scheme using non-conservative products designed for hyperbolic systems of conservation laws with source terms. *Math. Mod. Meth. Appl. Sci.*, 11:339–365, 2001.

[132] L. Gosse and A.-Y. LeRoux. A well balanced scheme designed for inhomogeneous scalar conservation laws. *C.R. Acad. Sci. Paris Sér. I Math.*, 323:543–546, 1996.

[133] L. Gosse and G. Toscani. An asymptotic-preserving well-balanced scheme for the hyperbolic heat equations. *C. R. Acad. Sci. Paris*, 334:337–342, 2002.

[134] L. Gosse and G. Toscani. Space localization and well-balanced schemes for discrete kinetic models in diffusive regimes. *SIAM J. Numer. Anal.*, 41:641–658, 2003.

[135] S. Gottlieb, C.-W. Shu, and E. Tadmor. Strong stability preserving high order time discretization methods. *SIAM Review*, 43:89–112, 2001.

[136] N. Goutal and F. Maurel. Dam-break wave simulation. In *Proceedings of the 2nd workshop, HE-43/97/016/B, France*, 1997.

[137] A.E. Green and P.M. Naghdi. A derivation of equations for wave propagation in water of variable depth. *J. Fluid Mech.*, 78:237–246, 1976.

[138] J.M. Greenberg and A.Y. Leroux. A well-balanced scheme for the numerical processing of source terms in hyperbolic equations. *SIAM J. Numer. Anal.*, 33:1–16, 1996.

[139] J.M. Greenberg, A.Y. Leroux, R. Bataille, and A. Noussair. Analysis and approximation of conservation laws with source terms. *SIAM J. Numer. Anal.*, 34:1980–2007, 1997.

[140] S. Guibourg. Modélisation numérique et expérimentale des houles bidimensionnelles en zone cotière, phd thesis. *Université Joseph Fourier-Grenoble I, France*, 1994.

[141] Y. Guo, R. Liu, Y. Duan, and Y. Li. A characteristic-based finite volume scheme for shallow water equations. *J. Hydro., Ser. B*, 21:531–540, 2009.

[142] A. Harten, B. Engquist, S. Osher, and S.R.Chakravarthy. Uniformly high order accurate essentially non-oscillatory schemes iii. *J. Comp. Phys.*, 71:231–303, 1987.

[143] A. Harten, P.D. Lax, and B. Van Leer. On upstream differencing and godunov-type schemes for hyperbolic conservation laws. *SIAM Review*, 25:35–61, 1983.

[144] H. Hassan, K. Ramadan, and S.N. Hanna. Numerical solution of the rotating shallow water flows with topography using the fractional steps method. *App. Math.*, 1:104–117, 2010.

[145] S. Hibberd and D.H. Peregrine. Surf and run-up on a beach: a uniform bore. *J. Fluid. Mech.*, 95:323–345, 1979.

[146] H. Hoteit, P. Ackerer, R. Mosé, J. Erhel, and B. Philippe. New two-dimensional slope limiters for discontinuous Galerkin methods on arbitrary meshes. *Int. J. Numer. Meth. Fluids*, 61:2566–2593, 2004.

[147] J. Hou, F.Simons, M. Mahgoub, and R. Hinkelmann. A robust well-balanced model on unstructured grids for shallow water flows with wetting and drying over complex topography. *Comput. Meth. Appl. Mech. Engrg.*, 257:126–149, 2013.

[148] J. Hou, Q. Liang, F. Simons, and R. Hinkelmann. A stable 2d unstructured shallow flow model for simulations of wetting and drying over rough terrains. *Comput. & Fluids*, 82:132–147, 2013.

[149] S-C. Hsiao and T-C. Lin. Tsunami-like solitary waves impinging and overtopping an impermeable seawall: Experiment and rans modeling. *Coast. Eng.*, 57:1–18, 2010.

[150] K. Hu, C.G. Mingham, and D.M. Causon. Numerical simulation of wave overtopping of coastal structures using the non-linear shallow water equations. *Coast. Eng.*, 41:433–465, 2000.

[151] M.E. Hubbard and N. Dodd. A 2d numerical model of wave run-up and overtopping. *Coast. Eng.*, 47:1–26, 2002.

[152] M.E. Hubbard and P. Garcia-Navarro. Flux difference splitting and the balancing of source terms and flux gradients. *J. Comput. Phys.*, 165:89–125, 2000.

[153] X. Li J.-F. Remacle, S. Soares-Frazão and M.S. Shephard. An adaptive discretization of shallow-water equations based on discontinuous Galerkin methods. *Int. J. Numer. Meth. Fluids*, 52:903–923, 2006.

[154] A. Jameson. Analysis and design of numerical schemes for gas dynamics, 1: artificial diffusion, upwind biasing, limiters and their effect on accuracy and multigrid convergence. *Int. J. Comp. Fluid Dyn.*, 4:171–218, 1985.

[155] E. Jamois. *Interaction houle-structure en zone côtière*. PhD thesis, 2005.

[156] G. Jiang and C.W. Shu. Efficient implementation of weighted eno schemes. *J. Comput. Phys.*, 126:202–228, 1996.

[157] G. Jiang and E. Tadmor. Nonoscillatory central schemes for multidimensional hyperbolic conservation laws. *SIAM J. Sci. Comput*, 19:1892–1917, 1998.

[158] S. Jin. Efficient asymptotic-preserving (ap) schemes for some multiscale kinetic equations. *SIAM J. Sci. Comput.*, 21:441–454, 1999.

[159] S. Jin. A steady-state capturing method for hyperbolic systems with geometrical source terms. *M2AN*, 35:631–645, 2001.

[160] S. Jin and M. A. Katsoulakis. Relaxation approximations to front propagation. *J. Diff. Equations*, 138:380–387, 1997.

[161] S. Jin and D. Levermore. Numerical schemes for hyperbolic conservation laws with stiff relaxation terms. *J. Comput. Phys.*, 126:449–467, 1996.

[162] S. Jin and Z. Xin. The relaxation scheme for systems of conservation laws in arbitrary space dimension. *Comm. Pure Appl. Math.*, 45:235–276, 1995.

[163] T. Katsaounis, B. Perthame, and C. Simeoni. Upwinding sources at interfaces in conservation laws. *Appl. Math. Lett.*, 17:309–316, 2004.

[164] M. Kawahara and T. Umetsu. Finite element method for moving boundary problems in river flow. *Int. J. Numer. Meth. Fluids*, 6:365–386, 1986.

[165] M. Kazolea, A.I. Delis, I.K. Nikolos, and C.E. Synolakis. An unstructured finite volume numerical scheme for extended 2DBoussinesq-type equations. *Coast. Eng.*, 69:42–66, 2012.

[166] M. Kazolea, A.I. Delis, and C.E. Synolakis. Numerical treatment of wave breaking on unstructured finite volume approximations for extended Boussinesq-type equations. *J. Comput. Phys.*, in press, 2014.

[167] A.B. Kennedy, Q. Chen, J.T. Kirby, and R.A. Dalrymple. Boussinesq modeling of wave transformation, breaking, and runup. I: 1 D. *J. Waterway Port Coast. Ocean Eng.*, 126:39–47, 1999.

[168] K.Erduran, S. Ilic, and V. Kutija. Hybrid finite-volume finite-difference scheme for the solution of Boussinesq equations. *Int. J. Numer. Meth. Fluids*, 49:1213–1232, 2005.

[169] G. Kesserwani and Q. Liang. A discontinuous Galerkin algorithm for the two-dimensional shallow water equations. *Comput. Meth. Appl. Mech. Engrg.*, 199:3356–3368, 2010.

[170] G. Kesserwani and Q. Liang. Well-balanced RKDG2 solutions to the shallow water equations over irregular domains with wetting and drying. *Comput. & Fluids*, 39:2040–2050, 2010.

[171] G. Kesserwani and Q. Liang. Locally limited and fully conserved RKDG2 shallow water solutions with wetting and drying. *J. Sci. Comput.*, 50:120–144, 2012.

[172] B. Koobus, S.F. Wornom, S. Camarri, M.V. Salvetti, and A. Dervieux. Nonlinear V6 schemes for compressible flow. Rapport de recherche, 2008.

[173] L. Krivodonova. Limiters for high-order discontinuous galerkin methods. *J. Comput. Phys.*, 226:879–896, 2007.

[174] L. Krivodonova, J. Xin, J.-F. Remacle, N. Chevaugeon, and J.E. Flaherty. Shock detection and limiting with discontinuous Galerkin methods for hyperbolic conservation laws. *App. Num. Math.*, 48:323–338, 2004.

[175] S. N. Kružkov. First order quasilinear equations in several independent variables. *Math. USSR Sb.*, 10:217–243, 1970.

[176] E.J. Kubatko, S. Bunya, C. Dawson, and J.J. Westerink. Dynamic p-adaptive runge–kutta discontinuous galerkin methods for the shallow water equations. *Comp. Meth. App. Mech. Eng.*, 198:1766–1774, 2009.

[177] E.J. Kubatko, J.J. Westerink, and C. Dawson. hp discontinuous galerkin methods for advection dominated problems in shallow water flow. *Comp. Meth. App. Mech. Eng.*, 196:437–451, 2006.

[178] A. Kurganov and D. Levy. A third-order semidiscrete central scheme for conservation laws and convection-diffusion equations. *SIAM J. Sci. Comput.*, 22:1461–1488, 2000.

[179] A. Kurganov and D. Levy. Central-upwind schemes for the saint-venant system. *Math. Mod. Num. Anal.*, 36:397–425, 2002.

[180] A. Kurganov and G. Petrova. A third-order semi-discrete genuinely multidimensional central scheme for hyperbolic conservation laws and related problems. *Numer. Math.*, 88:683–729, 2001.

[181] A. Kurganov and G. Petrova. A second-order well-balanced positivity preserving central-upwind scheme for the saint-venant system. *Commun. Math. Sci.*, 5:133–160, 2007.

[182] D. Lannes. *Water waves: mathematical analysis and asymptotics*. Amer. Mathematical Society, 2013.

[183] D. Lannes and P. Bonneton. Derivation of asymptotic two-dimensional time-dependent equations for surface water wave propagation. *Phys. Fluids*, 21:016601, 2009.

[184] D. Lannes and F. Marche. A new class of fully nonlinear and weakly dispersive green-naghdi models for efficient 2d simulations. Programme LEFE MANU, January 2014.

[185] C. Lattanzio and D. Serre. Convergence of a relaxation scheme for hyperbolic systems of conservation laws. *Numer. Math.*, 88:121–134, 2001.

[186] P. D. Lax. Hyperbolic systems of conservation laws and the mathematical theory of shock waves. *Conference Board of the Mathematical Sciences Regional Conference Series in Applied Mathematics. SIAM, Philadelphia*, 11, 1973.

[187] R.J. Leveque. Balancing source terms and flux gradients in high-resolution godunov methods: the quasi-steady wave-propagation algorithm. *J. Comput. Phys.*, 146:346–365, 1998.

[188] R.J. Leveque. *Finite-Volume Methods for Hyperbolic Problems*. Cambridge Texts in Applied Mathematics, 2002.

[189] R.J. Leveque and M. Pelanti. A class of approximate riemann solvers and their relation to relaxation schemes. *J. Comput. Phys.*, 172:572–591, 2001.

[190] D. Levy, G. Puppo, and G. Russo. Compact central weno schemes for multidimensional conservation laws. *SIAM J. Sci. Comput.*, 22:656–672, 2000.

[191] M. Li, P. Guyenne, F. Li, and F. Xu. High order well-balanced CDG-FE methods for shallow water waves by a Green-Naghdi model. *J. Comput. Phys.*, 257:169–192, 2014.

[192] Y.S. Li and R. Liu. The discontinuous Galerkin finite element method for the 2d shallow water equations. *Math. Comput. Sim.*, 56:223–233, 2001.

[193] Y.S. Li, S.X. Liu, Y.X. Yu, and G.Z. Lai. Numerical modeling of Boussinesq equations by finite element method. *Coast. Eng.*, 37:97–122, 1999.

[194] Q. Liang and A.G.L. Borthwick. Adaptive quadtree simulation of shallow flows with wet–dry fronts over complex topography. *Comput. & Fluids*, 38:221–234, 2009.

[195] Q. Liang and F. Marche. Numerical resolution of well-balanced shallow water equations with complex source terms. *Adv. Water Res.*, 32:873–884, 2009.

[196] P.L. Lions and G. Toscani. Diffusive limit for finite velocity Boltzmann kinetic models. *Rev. Mat. Iberoamericana*, 13:473–513, 1997.

[197] H.L. Liu and G. Warnecke. Convergence rates for relaxation schemes approximating conservation laws. *SIAM J. Numer. Anal.*, 37:1316–1337, 2000.

[198] P.L.-F. Liu, Y.-S. Cho, M.J. Briggs, U. Kanoglu, and C.E. Synolakis. Runup of solitary waves on a circular island. *J. Fluid Mech.*, 320:259–285, 1995.

[199] X. Liu, D. Osher, and S. Chan. Weighted essentially non-oscillatory schemes. *J. Comp. Phys.*, 115:200–212, 1994.

[200] M. Lukacova-Medvidova, S. Noelle, and M. Kraft. Well-balanced finite volume evolution Galerkin methods for the shallow water equations. *J. Comput. Phys.*, 1:122–147, 2007.

[201] H. Luo, J.D. Baum, and R. Lohner. A hermite weno-based limiter for discontinuous galerkin method on unstructured grids. *J. Comput. Phys.*, 225:686–713, 2007.

[202] D.R. Lynch and W.G. Gray. Finite element simulation of flow in deforming regions. *J. Comput. Phys.*, 36:135–153, 1980.

[203] D. Handorf M. Lauter, F.X. Giraldo and K. Dethloff. A discontinuous galerkin method for the shallow water equations in spherical triangular coordinates. *J. Comput. Phys.*, 227:10226–10242, 2008.

[204] P.A. Madsen, H.B. Bingham, and H. Liu. A new Boussinesq method for fully nonlinear waves from shallow to deep water. *J. Fluid Mech.*, 462:1–30, 2002.

[205] P.A. Madsen, H.B. Bingham, and H.A. Schaffer. Boussinesq-type formulations for fully nonlinear and extremely dispersive water waves: derivation and analysis. *Proc. R. Soc. A*, 459:1075–1104, 2003.

[206] P.A. Madsen, R. Murray, and O.R. Sørensen. A new form of the Boussinesq equations with improved linear dispersion characteristics. *Coast. Eng.*, 15(4):371–388, 1991.

[207] P.A. Madsen and O.R. Sørensen. A new form of the Boussinesq equations with improved linear dispersion characteristics. Part 2: A slowing varying bathymetry. *Coast. Eng.*, 18:183–204, 1992.

[208] P. Marcati and A. Milani. The one-dimensional Darcy's law as the limit of a compressible Euler flow. *J. Diff. Eq.*, 84:129–146, 1990.

[209] F. Marche. *Theoretical and numerical study of shallow water models. Applications to nearshore hydrodynamics*. PhD thesis, 2005.

[210] F. Marche. Derivation of a new two-dimensional viscous shallow water model with varying topography, bottom friction and capillary effects. *Eur. J. Mech./B-Fluid*, 26:49–63, 2007.

[211] F. Marche, P. Bonneton, P. Fabrie, and N. Seguin. Evaluation of well-balanced bore-capturing schemes for 2D wetting and drying processes. *Int. J. Numer. Meth. Fluids*, 53:867–894, 2007.

[212] J.M. Masella, I. Faille, and T. Gallouet. On an approximate godunov scheme. *Int. J. Comput. Fluid. Dyn.*, 12:133–149, 1999.

[213] O. Le Métayer, S. Gavrilyuk, and S. Hank. A numerical scheme for the Green-Naghdi model. *J. Comput. Phys.*, (229):2034–2045, 2010.

[214] D. Mitsotakis, B. Ilan, and D. Dutykh. On the Galerkin/finite-element method for the Serre equations. *J. Sci. Comput.*, 2014.

[215] J. Murillo and P. Garcia-Navarro. Augmented versions of the hll and hllc riemann solvers including source terms in one and two dimensions for shallow flow applications. *J. Comput. Phys.*, 231:6861–6906, 2012.

[216] J. Murillo, P. Garcia-Navarro, and J. Burguete. Time step restrictions for well-balanced shallow water solutions in non-zero velocity steady states. *Int. J. Numer. Meth. Fluids*, 60:1351–1377, 2009.

[217] J. Murillo, P. Garcia-Navarro, J. Burguete, and P. Brufau. The influence of source terms on stability, accuracy and conservation in two-dimensional shallow flow simulation using triangular finite volumes. *Int. J. Numer. Meth. Fluids*, 54:543–590, 2007.

[218] K.D. Watson N. Kobayashi, G.S. Desilva. Wave transformation and swash oscillation on gentle and steep slopes. *J. Comput. Res.*, 94:951–966, 1989.

[219] R.D. Nair, S.J. Thomas, and R.D. Loft. A discontinuous galerkin global shallow water model. *Mont. Weather Rev.*, 133:876–888, 2004.

[220] H. Nessyahu and E. Tadmor. Non-oscillatory central differencing for hyperbolic conservation laws. *J. Comput. Phys.*, 87:408–463, 1990.

[221] I.K. Nikolos and A.I. Delis. An unstructured node-centered finite volume scheme for shallow water flows with wet/dry fronts over complex topography. *Comput. Meth. Appl. Mech. Engrg.*, 198:3723–3750, 2009.

[222] S. Noelle, N. Pankratz, G. Puppo, and J.R. Natvig. Well-balanced finite volume schemes of arbitrary order of accuracy for shallow water flows. *J. Comput. Phys.*, 213:474–499, 2006.

[223] S. Noelle, Y. Xing, and C.-W. Shu. High-order well-balanced finite volume weno schemes for shallow water equation with moving water. *J. Comput. Phys.*, 226:29–58, 2007.

[224] O. Nwogu. Alternative form of Boussinesq equations for nearshore wave propagation. *J. Waterway. Port. Coastal. Ocean Eng.*, 119:618–638, 1993.

[225] C.F. Ollivier-Gooch. High-order eno schemes for unstructured meshes based on least-squares reconstruction. In *AIAA, paper 97-0540*, 1997.

[226] J. Orszaghova, A.G.L. Borthwick, and P.H. Taylor. From the paddle to the beach − A Boussinesq shallow water numerical wave tank based on Madsen and Sørensen's equations. *J. Comp. Phys.*, 231:328–344, 2012.

[227] H.T. Özkan-Haller and J.T. Kirby. A Fourier-Chebyshev collocation method for the shallow water equations including shoreline runup. *App. Oc. Rch.*, 19:21–34, 1997.

[228] R. Comblen V. Legat P.-E. Bernard, J.-F. Remacle and K. Hillewaert. High-order discontinuous galerkin schemes on general 2d manifolds applied to the shallow water equations. *J. Comput. Phys.*, 228:6514–6535, 2009.

[229] J.D. Pearce and J.G. Esler. A pseudo-spectral algorithm and test cases for the numerical solution of the two-dimensional rotating Green-Naghdi shallow water equations. *J. Comput. Phys.*, 229:7594–7608, 2010.

[230] D.H. Peregrine. Long waves on a beach. *J. Fluid Mech.*, 27:815–827, 1967.

[231] B. Perthame. *An introduction to kinetic schemes for gas dynamics. An introduction torecent developments in theory and numerics for conservation laws.* L.N. in Comput. Sc. and. Eng., 5, D.Kroner, M. Ohlberger and C. Rohde eds, Springer, 1998.

[232] B. Perthame. *Kinetic formulations of conservation laws*. Oxford University Press, 2002.

[233] B. Perthame and Y. Qiu. A variant of van leer's method for multidimensional systems of conservation laws. *J. Comput. Phys.*, 112:370–381, 1994.

[234] B. Perthame and C.W. Shu. On positivity preserving finite volume schemes for Euler equations. *Numer. Math.*, 73:119–130, 1996.

[235] B. Perthame and C. Simeoni. A kinetic scheme for the Saint-Venant system with a source term. *Calcolo*, 38:201–231, 2001.

[236] J. Qiu and C.W. Shu. On the construction, comparison, and local characteristic decomposition for high-order central weno schemes. *J. Comp. Phys.*, 183:187–209, 2002.

[237] J. Qiu and C.W. Shu. Hermite weno schemes and their application as limiters for runge–kutta discontinuous galerkin method: one dimensional case. *SIAM J. Sci. Comp.*, 193:115–135, 2003.

[238] J. Qiu and C.W. Shu. A comparison of troubled-cell indicators for runge–kutta discontinuous galerkin methods using weighted essentially nonoscillatory limiters. *SIAM J. Sci. Comp.*, 27:995–1013, 2005.

[239] K. D. Devine R. Biswas and J. E. Flaherty. Parallel, adaptive finite element methods for conservation laws. *App. Num. Math.*, 14:255–283, 1994.

[240] B. Perhame R. Botchorishvili and A. Vasseur. Equilibrium schemes for scalar conservation laws with stiff sources. *Math. Comp.*, 72:131–157, 2003.

[241] S. Rhebergen, O. Bokhove, and J.J.W. Van Der Vegt. Discontinuous galerkin finite element methods for hyperbolic nonconservative partial differential equations. *J. Comput. Phys.*, 227:1887–1922, 2008.

[242] M. Ricchiuto, R. Abgrall, and H. Deconinck. Application of conservative residual distribution schemes to the solution of the shallow water equations on unstructured meshes. *J. Comput. Phys.*, 222:287–331, 2007.

[243] M. Ricchiuto and A. Bollermann. Stabilized residual distribution for shallow water simulations. *J. Comput. Phys.*, 228:1071–1115, 2009.

[244] M. Ricchiuto and A.G. Filippini. Upwind residual discretization of enhanced Boussinesq equations for wave propagation over complex bathymetries. *J. Comput. Phys.*, in press, 2014.

[245] P.L. Roe. Approximate riemann solvers, parameter vectors and difference schemes. *J. Comp. Phys.*, 43:357–372, 1981.

[246] V. Roeber and K.F. Cheung. Boussinesq-type model for energetic breaking waves in fringing reef environments. *Coast. Eng.*, 70(0):1 – 20, 2012.

[247] B. Rogers, M. Fujihara, and A. Borthwick. Adaptive Q-tree Godunov-type scheme for shallow water equations. *Int. J. Numer. Meth. Fluids*, 35:247–280, 2001.

[248] G. Russo. Central schemes for conservation laws with application to shallow water equations. *in Trends and applications of mathematics to mechanics : STAMM 2002, S. Rionero and G. Romano (Editors), Springer-Verlag Italia SRL*, pages 225–246, 2005.

[249] J. Sampson, A. Easton, and M. Singh. Moving boundary shallow water flow above parabolic bottom topography. *ANZIAM J (EMAC 2005)*, 21:373–387, 2006.

[250] R. Saurel and R. Abgrall. A simple method for compressible multifluid flows. *SIAM J. Sci. Comput.*, 21:1115–1145, 1999.

[251] D. Schwanenberg and M. Harms. Discontinuous Galerkin finite-element method for transcritical two- dimensional shallow water flows. *J. Hydr. Engrg.*, 130:412–421, 2004.

[252] N. Seguin. *Modélisation et simulation numérique des écoulements diphasiques.* PhD thesis, 2002.

[253] F. Serre. Contribution à l'étude des écoulements permanents et variables dans les canaux. *Houille Blanche*, 6:830–872, 1953.

[254] F. Shi, J.T. Kirby, J.C. Harris, J.D. Geiman, and S.T. Grilli. A high-order adaptive time-stepping tvd solver for Boussinesq modeling of breaking waves and coastal inundation. *Oc. Mod.*, 43-44:36–51, 2012.

[255] C.W. Shu. Total-variation-diminishing time discretizations. *SIAM J.Sci.Statist.Comput.*, 9:1073–1084, 1988.

[256] C.W. Shu and S. Osher. Efficient implementation of essentially non oscillatory shock capturing schemes. *J. Comp. Phys.*, 77:439–471, 1988.

[257] J. Singh, M.S. Altinakar, and Y. Ding. Two-dimensional numerical modeling of dam-break flows over natural terrain using a central explicit scheme. *Adv. Wat. Res.*, 34:1366–1375, 2011.

[258] S. Soares-Frazão and V. Guinot. A second-order semi-implicit hybrid scheme for one-dimensional Boussinesq-type waves in rectangular channels. *Int. J. Num. Meth. Fluids*, 58:237–261, 2008.

[259] S. Soares-Frazão and G. Testa. In *Proceedings of the 3rd CADAM Workshop, Milan, Italy*.

[260] O. Sørensen, H.A. Schäffer, and P. Madsen. Surf zone dynamics simulated by a Boussinesq type model. III. Wave-induced horizontal nearshore circulation. *Coast. Engrg.*, 33:155–176, 1998.

[261] O.R. Sørensen, H.A. Schaffer, and L.S. Sørensen. Boussinesq-type modelling using an unstructured finite element technique. *Coast. Engrg.*, 50:181–198, 2004.

[262] I. Suliciu. On modelling phase transitions by means of rate-type constitutive equations, shock wave structure. *Int. J. Engrg. Sci.*, 28:829–841, 1990.

[263] I. Suliciu. Some stability-instability problems in phase transitions modelled by piecewise linear elastic or viscoelastic constitutive equations. *Int. J. Engrg. Sci.*, 30:483–494, 1992.

[264] C.E. Synolakis. The runup of solitary waves. *J. Fluid Mech.*, 185:523–545, 1981.

[265] P.A. Tassi, O. Bokhove, and C.A. Vionnet. Space discontinuous galerkin method for shallow water flows kinetic and hllc flux, and potential vorticity generation. *Adv. Wat. Res.*, 30:998–1015, 2007.

[266] W.C. Thacker. Some exact solutions to the nonlinear shallow water wave equations. *J. Fluid Mech.*, 107:499–508, 1981.

[267] P.G. LeFloch M.D. Thanh. The riemann problem for the shallow water equations with discontinuous topography. *Commum. Math. Sci.*, 5:865–885, 2007.

[268] M. Tissier, P. Bonneton, F. Marche, F. Chazel, and D. Lannes. A new approach to handle wave breaking in fully non-linear Boussinesq models. *Coast. Engrg.*, 67:54–66, 2012.

[269] M. Tonelli and M. Petti. Hybrid finite volume- finite difference scheme for 2dh improved Boussinesq equations. *Coast Engrg.*, 56(5-6):609–620, 2009.

[270] M. Tonelli and M. Petti. Finite volume scheme for the solution of 2d extended Boussinesq equations in the surf zone. *Oc. Engrg.*, 37:567–582, 2010.

[271] M. Tonelli and M. Petti. Shock-capturing Boussinesq model for irregular wave propagation. *Coast. Engrg.*, 61:8–19, 2012.

[272] E.F. Toro. *Riemann solvers and numerical methods for fluid dynamics*. Springer, Berlin, 1997.

[273] E.F. Toro, M. Spruce, and W. Speare. Restoration of the contact surface in the HLL Riemann solver. *Shock waves*, 4:25–34, 1994.

[274] C.J. Trahan and C. Dawson. Local time stepping in Runge Kutta discontinuous Galerkin finite element methods applied to the shallow-water equations. *Comp. Meth. App. Mech. Engrg.*, 217:139–152, 2012.

[275] S. Tu and S. Aliabadi. A slope limiting procedure in discontinuous galerkin finite element method for gasdynamic applications. *Int. J. Numer. Anal. Model.*, 2:163–178, 2005.

[276] B. Van-Leer. Towards the ultimate conservative difference scheme. V - A second-order sequel to Godunov's method. *J. Comput. Phys.*, 135:227–248, 1997.

[277] J.J.W. Van Der Vegt and H. Van Der Ven. Space-time discontinuous galerkin finite element method with dynamic grid motion for inviscid compressible flows. *J. Comput. Phys.*, 182:546–585, 2002.

[278] V. Venkatakrishnan. On the accuracy of limiters and convergence to steady state solutions. In *AIAA, paper 93-0668*, 1993.

[279] J.P. Vila. Simplified godunov schemes for 2 $\times$ 2 systems of conservation laws. *SIAM J. Numer. Anal.*, 23:1173–1192, 1986.

[280] S. Vukovic and L. Sopta. Eno and weno schemes with the exact conservation property for one-dimensional shallow water equations. *J. Comput. Phys.*, 179:593–621, 2002.

[281] J.-W. Wang and R.-X. Liu. A comparative study of finite volume methods on unstructured meshes for simulation of 2D shallow water wave problems. *Math. Comput. Sim.*, 53:171–184, 2000.

[282] Y. Wang, Q. Liang, G. Kesserwani, and J.W. Hall. A 2d shallow flow model for practical dam-break simulations. *J. Hydr. Res.*, 49:307–316, 2011.

[283] G. Wei and J. Kirby. Time-dependant numerical code for extended boussinesq equations. *J. Waterway*, 121:251–261, 1995.

[284] E. Tadmor X.-D. Liu. Third order nonoscillatory central scheme for hyperbolic conservation laws. *Num. Math.*, 79:397–425, 1998.

[285] Y. Xing. Exactly well-balanced discontinuous galerkin methods for the shallow water equations with moving water equilibrium. *J. Comput. Phys.*, 257:536–553, 2014.

[286] Y. Xing and C.-W. Shu. High order finite difference WENO schemes with the exact conservation property for the shallow water equations. *J. Comput. Phys.*, 208:206–227, 2005.

[287] Y. Xing and C.-W. Shu. High order well-balanced finite volume weno schemes and discontinuous galerkin methods for a class of hyperbolic systems with source terms. *J. Comput. Phys.*, 214:567–598, 2006.

[288] Y. Xing and C.-W. Shu. A new approach of high order well-balanced finite volume WENO schemes and discontinuous Galerkin methods for a class of hyperbolic systems with source terms. *Commun. Comput. Phys.*, 1:100–134, 2006.

[289] Y. Xing, C.-W. Shu, and S. Noelle. On the advantage of well-balanced schemes for moving-water equilibria of the shallow water equations. *J. Sci. Comp.*, 48:339–349, 2011.

[290] Y. Xing and X. Zhang. Positivity-preserving well-balanced discontinuous Galerkin methods for the shallow water equations on unstructured triangular meshes. *J. Sci. Comp.*, 57:19–41, 2013.

[291] Y. Xing, X. Zhang, and C.-W. Shu. Positivity-preserving high order well-balanced discontinuous Galerkin methods for the shallow water equations. *Adv. Wat. Res.*, 33:1476–1493, 2010.

[292] Y. Xu and C.-W. Shu. Local Discontinuous Galerkin methods for high-order time-dependent partial differential equations. *Commun. Comput. Phys.*, 7(1):1–46, 2010.

[293] X. Ying and S. Wang. Improved hll scheme for 1d dam-break flows over complex topography. *Archives of Hydro-Engineering and Environmental Mechanics*, 57:31–41, 2010.

[294] X. Ying, S. Wang, and A. Khan. Numerical simulation of flood inundation due to dam and levee breach. In *World Water and Environmental Resources Congress, 2003*, pages 1–9.

[295] J.A. Zelt. *Tsunamis: the response of harbors with sloping boundaries to long wave exitation*. Tech. Rep. KH-R-47 1986; California Institute of Technology, 1986.

[296] J.A. Zelt. The run up of nonbreaking and breaking solitary waves. *Coast. Eng.*, 15:205–246, 1991.

[297] J.A. Zelt and F.A. Raichlen. A lagrangian model for waveinduced harbour oscillations. *Coast. Eng.*, 213:203–225, 1990.

[298] X. Zhang and C.-W. Shu. On maximum-principle-satisfying high order schemes for scalar conservation laws. *J. Comput. Phys.*, 229(9):3091 – 3120, 2010.

[299] X. Zhang, Y. Xia, and C.-W. Shu. Maximum-principle-satisfying and positivity-preserving high order discontinuous Galerkin schemes for conservation laws on triangular meshes. *J. Sci. Comp.*, 50:29–62, 2012.

[300] X. Zhong and C.-W. Shu. A simple weighted essentially nonoscillatory limiter for runge–kutta discontinuous galerkin methods. *J. Comput. Phys.*, 232:397–415, 2013.

[301] J. G. Zhou, D. M. Causon, D. M. Ingram, and C. G. Mingham. Numerical solutions of the shallow water equations with discontinuous bed topography. *Int. J. Numer. Meth. Fluids.*, 38:769–788, 2002.

[302] J.G. Zhou, D.M. Causon, and C. G. Mingham. The surface gradient method for the treatment of source terms in the shallow-water equations. *J. Comput. Phys.*, 168:1–25, 2001.

[303] J. Zhu, J. Qiu, C.-W. Shu, and M. Dumbser. Runge–kutta discontinuous galerkin method using weno limiters ii: Unstructured meshes. *J. Comput. Phys.*, 227:4330–4353, 2008.

[304] J. Zhu, J. Zhong, J. Qiu, and C.-W. Shu. Runge–kutta discontinuous galerkin method using a new type of weno limiters on unstructured meshes. *J. Comput. Phys.*, 248:200–220, 2013.

[305] C. Zoppou and S. Roberts. Numerical solution of the two dimensional unsteady dam break. *App. Math. Mod.*, 24:457–475, 2000.